The design and commissioning of an enclosed jet-in-hot-coflow setup for the investigation of flameless combustion

MSc Thesis

Thimo van den Berg

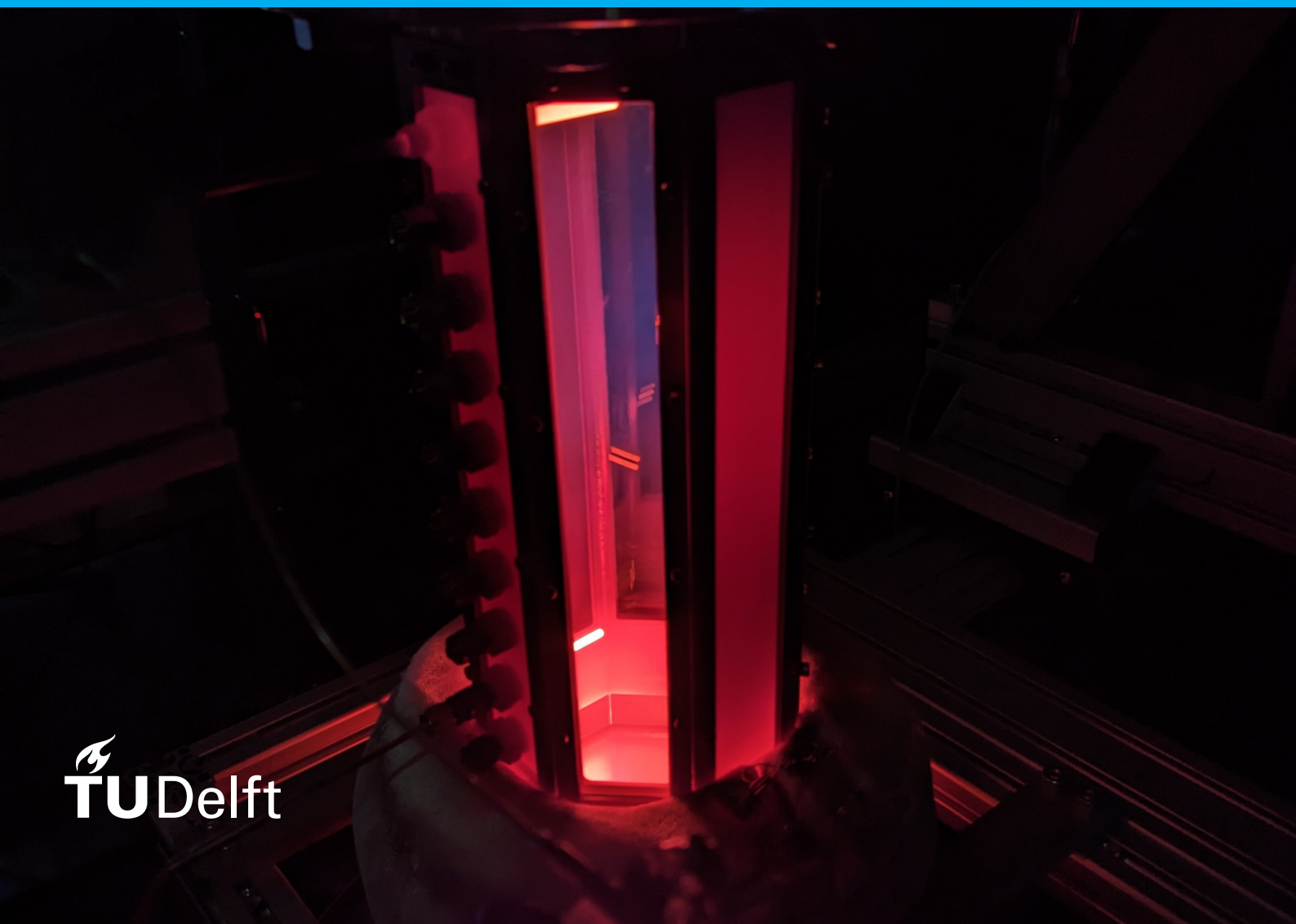

TU Delft

The design and commissioning of an enclosed jet-in-hot-coflow setup for the investigation of flameless combustion

MSc Thesis

by

Thimo van den Berg

to obtain the degree of Master of Science
at the Delft University of Technology,
to be defended publicly on Thursday July 20, 2023 at 14:00.

Student number: 4441354

Thesis committee:		
	Prof. Dr. ir. A. Gangoli Rao,	TU Delft, supervisor
	Prof. Dr. D.J.E.M. Roekaerts,	TU Delft
	Dr. ir. W.J. Baars,	TU Delft
	ir. R.P. Sampat,	TU Delft, daily supervisor

TU Delft

Preface

With the completion of this master's thesis, I will be graduating from the faculty of aerospace engineering at TU Delft. I have studied at this faculty since 2015 when I started my bachelor's. Since then I have learned so much both on an academic and professional level, but also on a personal level. I have had amazing opportunities during my time at the TU to apply the knowledge I gained during my studies in practice. This combination of practical and theoretical facets is something I wanted to continue to pursue with my master's thesis, and I am very grateful for being given the opportunity to design a flameless combustion setup and then be allowed to have it built and perform experiments with it.

I would like to thank Arvind Gangoli Rao and Rishikesh Sampat for giving me this opportunity and supervising me during my thesis. Your input during our meetings has made me a better scientist and engineer. I would like to especially thank my daily supervisor Rishikesh for the countless hours he spent in the lab performing experiments with me, helping me get my setup operational and for his input in the long discussions we've had about the design of the setup and the interpretation of the various results.

Furthermore, I would like to thank Jos van Meurs, and Gerard van de Sande for their practical input into the combustor design, and building and installing the system in the combustion lab. Additionally, I would like to thank all the people in the combustion group for watching my progress presentations and for their feedback. I also want to thank the faculty members and the technicians of the high-speed laboratory: Henk-Jan, Frits, Dennis and Peter for their help in procuring equipment and enabling me do to my experiments. Special thanks also to Yoram Hoogterp for helping me out during the PIV campaign.

I would like to thank all the people of room NB 1.01 for creating a both fun and productive working atmosphere. Finally, I would like to thank my friends and family for their support during this project.

Thimo van den Berg
Delft, July 2023

Abstract

Flameless combustion is a combustion regime which results in drastically lower NO_x emissions. NO_x has been found to influence global warming through its interactions with ozone chemistry and, exposure to this gas has been found to have adverse health effects in humans. A jet-in-hot-coflow setup is a combustor which is used in literature to study flameless combustion. It is well suited for studying flame morphology and the coflow composition can easily be changed. In most of these setups, the reaction zone is uncontained, allowing for ambient air to entrain into the region of interest. Furthermore, there is currently a lack of emissions data over a wide range of operating conditions.

This project included the engineering, design, and development of an enclosed jet-in-hot-coflow setup as well as an analysis of the flow field and combustion characteristics through experiments. Measurements were done using PIV, suction probe gas analyzer, thermocouples, and chemiluminescence imaging. Experiments were done with methane-air mixtures in the central jet and the coflow consisted of hot burnt products of methane-air combustion with the addition of external diluents such as CO_2 and N_2. One of the most interesting results was that NO_x reburning was observed in the reaction zone produced by the central jet, which was found to be correlated to the CO concentration in the combustion chamber. The addition of CO_2 and N_2 as diluents in the coflow resulted in a longer combustion zone and reduced temperatures in the combustion chamber, leading to decreased NO_x production, and increased reburning. Further, the impact of oxygen concentration, equivalence ratio, and coflow temperature on product species formation was also analysed. The results indicate that combustion zone growth and temperature effects are balanced for lower jet speeds, while for others, the effects of increasing combustion zone size and distribution with increasing equivalence ratio result in reburning becoming more dominant. Improvements are recommended, such as redesigning the central jet cooling assembly, integrating a secondary burner inside the mixing duct, implementing a pre-heating system for temperature control, and using high-speed imaging techniques for capturing flame development and ignition behaviour.

Contents

List of Figures

List of Tables

1 Introduction

The devastating effects of climate change are becoming increasingly clear. It is now more important than ever to find ways of reducing harmful emissions. Electrification using clean energy is often hailed as the solution, but this is not (yet) feasible for every application. For this reason, combustion still remains relevant for aviation. Therefore, research into cleaner forms of combustion is paramount. The current trend in aero engines is to use higher pressure ratios and combustion temperatures as this increases the efficiency [Yin and Gangoli Rao, 2017]. This does result in higher NO_x emissions as can be seen from Figure 1.1. In this figure, the NO_x emissions are plotted as a function of the pressure ratio based on historical data. While NO_x is not a greenhouse gas itself it does indirectly have both warming and cooling effects. An increase in temperature is realised through the enhancement of the production of ozone [Lee et al., 2009]. This effect is especially strong in aviation, where due to its altitude of emissions, NO_X can lead to a three times greater production of O_3 as compared to sea-level emissions [Hoor et al., 2009]. Additionally, NO_x also has a cooling effect due to its role in reducing ambient methane; though the overall effect results in heating [Lee et al., 2009].

Aside from affecting global warming NO_x emissions also have adverse health effects. Nitric oxides emissions play a role in the secondary formation of $PM_{2.5}$, particulate matter smaller than 2.5 micrometres. These particles can penetrate deep into the lungs and can be absorbed into the bloodstream. Both these small particles and NO_x itself have been linked to causing or exacerbating asthma, COPD, and cardiovascular diseases [U.S. EPA L U - U S Environmental Protection Agency, 2016][Feng et al., 2016]. To protect the health of the general public the emissions of these gasses should be minimised or even completely prevented. For all these reasons the European Union has set the goal of reducing NO_x emissions of aviation by 90% as compared to a typical new aircraft sold in 2000 [European Commission and Directorate-General for Mobility and Transport and Directorate-General for Research and Innovation, 2011]. This ACARE goal is displayed in Figure 1.1 as the greyed-out area.

Flameless combustion could be one of the technologies employed to reduce nitric oxides emissions. This regime is in general achieved by diluting the reactants with flue gasses down to a degree where the overall volumetric oxygen concentration is between 10 and 3% [Medwell and Dally, 2012a]. The flame is then sustained by heating the reactants to above their self-ignition temperature. This results in a more distributed flame, with a more uniform temperature distribution and overall lower temperatures. Since the thermal pathway for NO_x production plays a major role in the overall NO_x emissions of aero engines the reduction in temperature results in this pathway being severely inhibited [Warnatz et al., 2006]. The dilution achieves this reduction in temperature in three ways: By mixing in additional gasses the overall heat capacity of the mixture is increased. Dilution also reduces the rate of reactions by making it less likely for two reacting molecules to collide in the right way [Perpignan et al., 2018]. Finally, the diluents also alter what reactions take place by directly participating in them. Either by acting as a third body or by decomposing and altering the available pool of radicals [Park et al., 2002].

1.1. Relevance and research objective

As will be discussed in chapter 2 there is no clear consensus on what flameless combustion is. There are multiple definitions in use with varying degrees of overlap. In general flameless combustion is

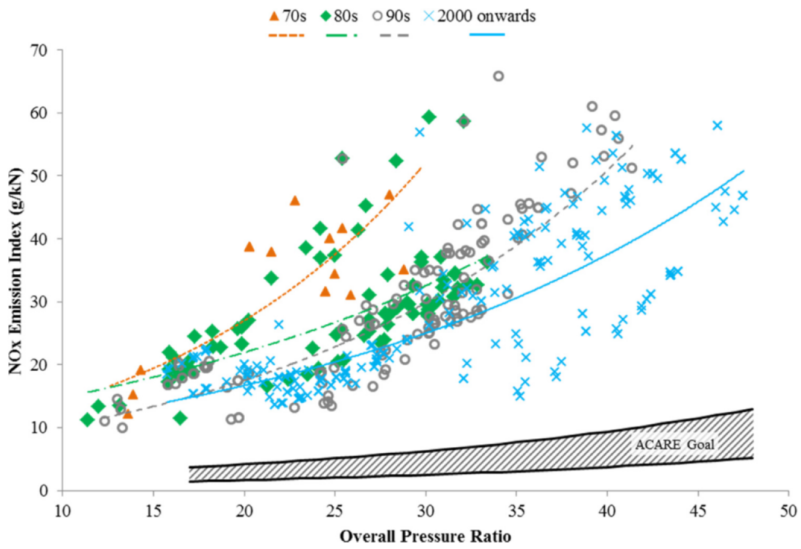

Figure 1.1: Variation of overall pressure ratio with NO_x emissions index for aero engines over time. Data from ICAO Aircraft Emissions Databank [ICAO, 2016]. Data for the ACARE goal European Commission and Directorate-General for Mobility and Transport and Directorate-General for Research and Innovation, 2011. Figure taken from Perpignan et al., 2018

achieved by diluting the reactants with flue gasses down to an oxygen concentration of between 10 and 3% [Medwell and Dally, 2012a], but even within this range different types of behaviour are observed. Additionally, data on emissions is lacking especially in combination with flame morphology measurements [Perpignan et al., 2018]. All previously built jet-in-hot-coflow setups are unenclosed, allowing lab air to influence the region of interest. Though, the jet-in-hot-coflow burner design is well suited for studying flame morphology and having control over the diluent composition. To be able to take accurate gas measurements the combustion chamber should be sealed off from the ambient air. As will be discussed in chapter 2 the gas composition of the diluent mixture can have a significant effect on the progression of combustion. Though, current combustion models were not designed with the presence of large volumes CO_2 and H_2O before ignition [Sabia and de Joannon, 2020]. For this reason, more emissions data is needed for validation in a wide range of operating conditions.

The main objective of the thesis will therefore be defined as:

> "To study the effect of vitiation on the formation of product species, and stability of flameless combustion, by designing an enclosed jet-in-hot-coflow burner and analysing methane combustion in flameless operation by diluting it with hot vitiated gasses at various equivalence ratios, operating temperatures and dilution levels."

1.2. Research questions

The research objective can be broken down into sub-questions, these questions are presented below.

"How does dilution with hot vitiated gasses influence the physical characteristics of the combustion zone at various oxygen concentrations, equivalence ratios, and coflow temperatures?"
- Various experiments have shown that the oxygen concentration, flue gas inlet temperature and equivalence ratio can lead to different types of behaviour and shape of the flame. Experiments by Oldenhof et al., 2010 and Medwell et al., 2008 found that for a non-premixed flame at a coflow oxygen concentration of around 9% the flame appears to be lifted and is more luminous, as compared to a flame with a 3% oxygen concentration in the coflow. At the low oxygen concentration, the flame is attached to the jet exit by a faint outline. At higher oxygen concentrations of 9% ignitions occur through the formation of ignition kernels, which grow, and then merge as they convect downstream [Oldenhof et al., 2010]. Different types of behaviour are also observed with changing jet velocity. In the higher oxygen range, the lift-off height of the flame decreases with increasing jet velocity at certain temperatures [Medwell and Dally, 2012b].

Furthermore, Sabia, Sorrentino, et al., 2015 found regions where different types of dynamic behaviour

are observed depending on the diluent composition, inlet temperature and equivalence ratio. This was found to be caused by competition between pyrolitic/ endothermic reactions and exothermic reactions. In flameless combustion, the dilution reduces the rates of reaction which creates a more delicate balance between different reaction branches.

"In what way does dilution with hot vitiated gasses influence the formation of secondary product species at various oxygen concentrations, equivalence ratios, and coflow temperatures?" - The effect of the operating conditions on the emissions of gasses like NO_x are of interest. [Park et al., 2002] found that dilution with CO_2 and H_2O changed the production of NO_x through the prompt pathway, by altering the rate of formation of CH. Dilution with nitrogen only resulted in a general depression of all pathways. H_2O dilution was also found to enhance NO_x reburning compared to CO_2. Additionally, Song et al., 2019 found that the addition of NO_x resulted in different behaviours depending on the inlet temperature of the reactants. At low temperatures, NO_x addition had a catalytic effect while at higher temperatures they would be reburned.

"What are the operational limits of the designed setup and what are the characteristics of the flow field inside the combustor?" - Since this is a new burner it is important to quantify its characteristics. This burner will have an enclosure of an octagonal shape, it is important to understand the behaviour of the flow in the combustion chamber to be able to accurately interpret the gas measurements that will be taken. Furthermore, the operational limits of the device need to be understood before a proper test plan can be formed.

1.3. Structure of the report

In chapter 2 some background information will be provided on flameless combustion. What terms are used, what definitions are used in literature, as well as the ignition behaviour and effects of diluents will be discussed. Then in chapter 3 the design of the enclosed jet-in-hot-coflow setup will be discussed. In chapter 4 the formulas used to design the experimental campaign in chapter 7 will be discussed. In chapter 5 the heat transfer model used for the design of the combustor will be detailed. Then in chapter 6 the flow field inside the combustion chamber will be investigated using a particle image velocimetry campaign. In chapter 7 the results from the commissioning campaign and the followup campaign will be discussed. In chapter 8 the research questions will be answered and recommendations for further research will be provided.

2

Background

Flameless combustion is a combustion regime where the combustion temperature has been lowered by, in general, diluting the reactants with flue gasses. These gasses are usually exhaust gasses from the combustion process being recirculated back into the combustion zone [Perpignan et al., 2018]. Reducing the flame temperature results in lower NO_x emissions, as the main production pathway for NO_x production is highly temperature dependent, [Warnatz et al., 2006]. Though as will be discussed in this chapter NO_x emissions are also be reduced in other ways [Park et al., 2002].

In this chapter the state of the art on flameless combustion will be discussed. First starting with the definition. In the literature, various terms are used to refer to more-or-less the same domain, these will be discussed in the first section. Furthermore, several definitions are used to refer to the same domain these will also be analysed. More background on the several ways in which NO_x can be produced will also be provided. Then, the ignition behaviour of flameless combustion will be discussed, in particular in reference to flames in jet-in-hot-coflow setups. Dynamic behaviour is also observed under certain conditions. This will be analysed, as well as the effect of different diluents on this dynamic behaviour and on the temperature and emissions from the flame. Then, the effect of jet momentum and premixing will be discussed. Finally, a summary of the state of the art will be given.

2.1. Definition of Flameless combustion

While there has been a notable amount of research on the subject of flameless combustion there is no clear consensus on what flameless combustion is. Also, the name flameless combustion is not universally used to describe the regime. In literature, other terms can be found which refer to more or less the same kind of combustion. Cavaliere and De Joannon, 2004 provides a good summary of these various definitions. Flameless combustion can be considered a type of high-temperature air combustion, or Hi-TOC. Where air is preheated to achieve higher thermodynamic efficiencies. However simply increasing the reactant temperature increases NO_x emissions, as pointed out by Wünning and Wünning, 1997. These authors coined the term FLOX, or flameless oxidation, which refers to a combustion process in which exhaust gas is recirculated into the combustion zone leading to lower flame temperatures. Other terms used to refer to flameless combustion include mild combustion and colourless distributed combustion, or CDC [Perpignan et al., 2018]. The differences or overlap between these terms is not entirely clear. The terms FLOX, flameless combustion and CDC indicate a reduction or complete lack of visible radiation emitting from the flame. However, reductions in flame luminosity are not necessarily linked to lower emissions [Li et al., 2011]. In general, these terms describe a combustion process where the flame temperature has been lowered significantly to such a degree that the flame is not able to sustain itself without the reactants being preheated to above their self-ignition temperature. Usually, the flame temperature is reduced by highly diluting the reactants with inert gasses, most often by recirculating exhaust gasses. However, low oxygen concentrations are not always required for example in the work of Khalil and Gupta, 2017 who were able to achieve a reduction in flame temperature with a gas mixture of pure oxygen, between 40% down to 21% volume, and the rest of carbon dioxide. These authors referred to this domain as colourless distributed combustion. The lack of a robust definition

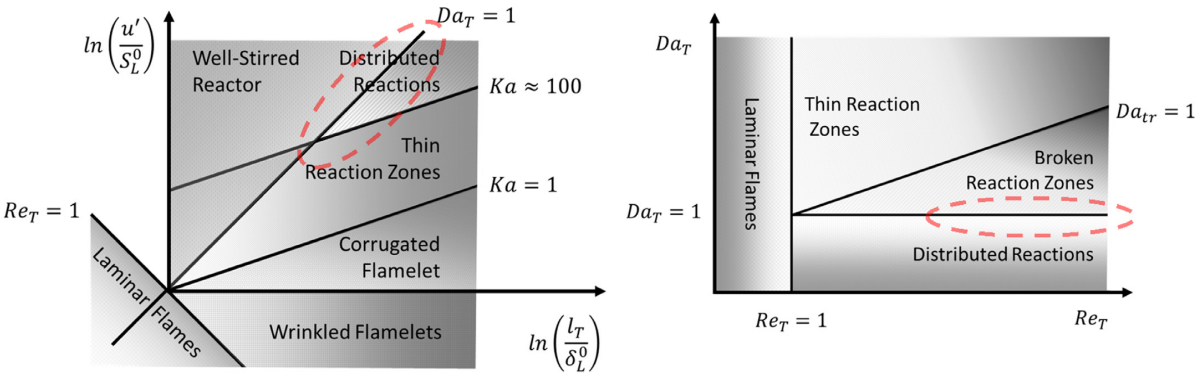

Figure 2.1: Combustion diagram for premixed (left) and non-premixed flames (right). The region demarcated by the red dotted line is where flameless combustion can be found. Taken from Perpignan et al., 2018.

makes it hard to determine which phenomena are inherent to flameless combustion, or are related to some other similar domain.

In Figure 2.1 a combustion diagram is shown for both premixed and non-premixed combustion. For premixed combustion, the natural log of turbulent fluctuations over the laminar flame speed is on the Y-axis, and the X-axis has the natural log of the ratio of turbulent integral length scale over the laminar flame thickness. The non-premixed diagram has the Damköhler number Da on the Y-axis and the Reynolds number Re on the X-axis. The domains in these diagrams are separated based on the Reynolds, Damköhler and Karlovitz numbers [Warnatz et al., 2006]. The Damköhler number is defined as the ratio of the flow time scale over the chemical time scale. The Karlovitz number is the ratio of the chemical time scale over the Kolmogorov time scale, which is the time scale of the smallest eddies in the flow. A large Karlovitz number means that small-scale eddies can enter the flame front and increase the local diffusive transport leading to a thicker flame front. The subscript T and L refer to the integral time scale and integral length scale respectively. The integral length scale is the size of the largest eddies in the flow, while the timescale is the time scale associated with these eddies.

In Figure 2.1 in the premixed case the encircled area indicates the location of flameless combustion. It can be found in the distributed reactions zone, at a Da of around one, a high Karlovitz number and a high Reynolds number. Dilution is thought to reduce the rate of reactions, increasing the chemical time scale and leading to thickened and broadened reaction zones [Perpignan et al., 2018]. Although, Perpignan et al., 2018 point out that there is still a large amount of uncertainty surrounding the degree to which flameless combustion is dependent on the Karlovitz number due to the difficulties of achieving a broad range of conditions experimentally or using DNS. The increased turbulence intensities at high Reynolds numbers have been reported to aid in reaching flameless conditions [Derudi et al., 2007].

2.1.1. Recirculation definition

Besides the different terms used to describe flameless combustion, there are also different definitions. The most simple one is the recirculation definition for FLOX by Wünning and Wünning, 1997. Whether flameless combustion was achieved depends purely on the recirculation rate of flue gasses. That recirculation rate is defined using Equation 2.1, in which K_v is the recirculation rate, $\dot{M}_E$ the mass flow of recirculated flue gasses, $\dot{M}_F$ the fuel mass flow and $\dot{M}_A$ the air mass flow rate. Experiments by the authors generated a stability diagram, which is shown in Figure 2.2. The X-axis is the recirculation rate, the Y-axis is the furnace temperature In this diagram there are three separate regions, region A is the stable regime for diffusive flames, in region B the flame is unstable and was observed to lift off and blow out, and in region C, at higher recirculation rates, the flameless regime was reached and the flame was observed to be stable again. The flame was not visible and did not produce sound when operating in region C.

$$K_v = \frac{\dot{M}_E}{\dot{M}_F + \dot{M}_A} \tag{2.1}$$

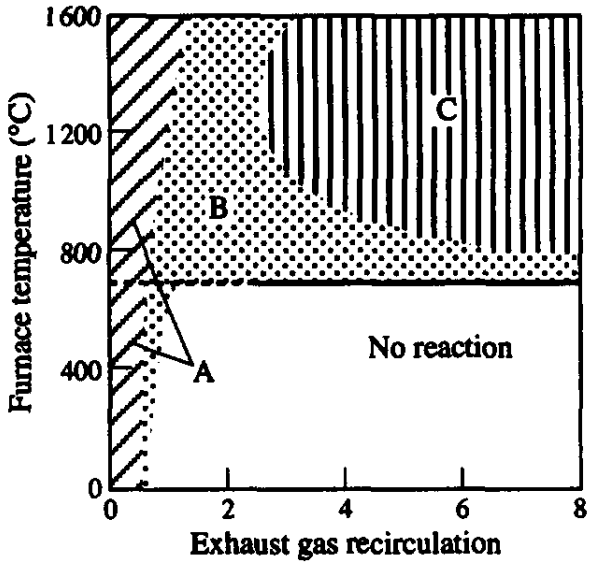

Figure 2.2: Stability diagram FLOX [Wünning and Wünning, 1997]

2.1.2. PSR definition

Another simple definition is the one proposed by Cavaliere and De Joannon, 2004. This definition defines a combustion process as flameless if the increase in temperature in a perfectly stirred reactor is smaller than the self-ignition temperature ($\Delta T < T_{si}$), where the change in temperature is defined as the difference between the maximum temperature in the combustor and the inlet temperature $\Delta T = T_{max} - T_{in}$. Additionally, the reactant inlet temperature has to be higher than the self-ignition temperature ($T_{in} > T_{si}$). This definition is referred to as the perfectly stirred reaction (PSR) definition, it is the most used definition in literature [Perpignan et al., 2018]. Although, as Perpignan et al., 2018 point out, this definition poses difficulties when flameless combustion is achieved using recirculation. The reactant inlet temperature will be below the self-ignition temperature, which means this cannot be considered flameless following this definition; defining the inlet temperature based on a perfect mixture of the fresh incoming reactants and the recirculated gas is also not accurate as the gasses don't mix completely before igniting.

2.1.3. Ignition based definition

Experiments performed inside the flameless domain following the PSR definition have shown different types of ignition behaviour. At oxygen concentrations of about 5% - 12% ignition kernels are observed [Oldenhof et al., 2010, Medwell and Dally, 2012b]. These kernels grow in size as they move downstream away from the fuel nozzle and then form a continuous flame front. Below these kernels, a faint outline of OH was observed [Medwell et al., 2008], which indicates even below this point some kind of pre-ignition is taking place. At lower oxygen concentrations the flame was observed to be attached, but the entire flame itself appears much fainter [Medwell et al., 2008]. The ignition behaviour in this region is more slow and gradual. The flamelet definitions only define flames in which this gradual ignition behaviour is observed as flameless.

Ignition and extinction phenomena are often discussed using the S-shaped curve. For premixed combustion, this temperature curve is plotted as a function of the Damköhler number, while for non-premixed flamelets it is a function of the inverse of the scalar dissipation rate. Normally this curve takes the shape of an S, where there is a distinct ignition and quench point. The low branch refers to slow reaction rates and low temperatures, the upper branch refers to faster reaction rates and higher temperatures. Increasing the Damköhler number, or decreasing the scalar dissipation at the ignition point results in a jump in temperature to the upper branch, at the quenching point a decrease in Da or increase of the scalar dissipation results in a jump to the lower branch. Under some conditions this S-shape does not exist, there are no distinct ignition and quench points. When this happens reactants shift monotoni-

cally from a burned to an unburned state. This definition has been used to separate gradually igniting flameless combustion from the combustion in which ignition kernels are found.

Premixed

Oberlack et al., 2000 derive the ignition definition for lean premixed combustion. Equation 2.2 gives the ignition and quenching temperature in the s-shaped diagram. In this equation Q^* is the normalised heat of combustion $\left(Q^* = \frac{QY_{F_u}}{c_P W_F T_u}\right)$, Y_{F_u} is the unburned fuel mass fraction, c_P the specific heat at constant pressure, W_F the molar mass of the fuel, and T_u the unburned reactant temperature. E^* is the normalised activation energy $\left(E^* = \frac{E}{\mathcal{R}T_u}\right)$, with the universal gas constant $\mathcal{R}$. The fact that only the fuel mass fraction is used in this formulation means that it is only valid for lean mixtures. Figure 2.3 shows the s-shape curve for different values of the normalised activation energy E^*, with on the x-axis the Damköhler number, and on the y-axis the normalised steady temperature $\left(T_S^* = \frac{T}{T_u}\right)$. The ignition and quench point only exist if the result from Equation 2.2 is real, when the resulting temperature is complex the quench and ignition points do not exist anymore. Looking at the equation it can be seen that the result is complex if the inside of the square root is negative, which is achieved if the condition in Equation 2.3 is met. Looking at the definition for Q^* and E^*, an increase in inlet temperature would lead to a decrease in normalised activation energy and an increase in the right hand term. A higher inlet temperature would then also allow for a larger heat of combustion while still maintaining monotonic combustion.

$$T_{I,Q} = \frac{(2+Q^*)E^* \pm \sqrt{[E^*Q^* - 4(1+Q^*)]E^*Q^*}}{2(E^*+Q^*)} \tag{2.2}$$

$$E^* < 4\frac{1+Q^*}{Q^*} \tag{2.3}$$

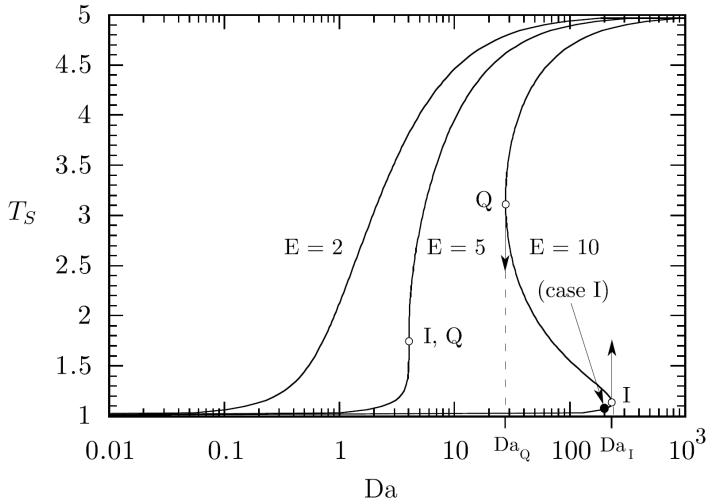

Figure 2.3: S-shaped curve for a PSR, with Q^* = 4 with various E [Oberlack et al., 2000]

Non-premixed

For non-premixed flames the monotonic ignition criterion was derived by Evans et al., 2017, based on the formulation for the ignition and quench temperature by Pitsch and Fedotov, 2001. The normalised ignition and quenching temperature can be computed using Equation 2.4. The normalised temperature is defined as $\theta = \left(T - T_{st,u}\right) / \left(T_{st,b} - T_{st,u}\right)$, where the subscript st refers to stoichiometric conditions, the subscript u to the unburned state, and the subscript b to the burned state. β is the activation temperature ratio $\beta = \frac{E_{eff}}{\mathcal{R}T_{st,b}}$, with the universal gas constant $\mathcal{R}$, and the stoichiometric burned temperature $T_{st,b}$. Finally, α is the heat release parameter defined as $\alpha = \Delta T_{st}/T_{st,b}$. When Equation 2.4 is real the

quench and ignition temperature exists, when the result is complex there are no distinct quench and ignition temperature; as can be seen in the equation the result is complex if ξ is negative. The definition for ξ is given in Equation 2.5.

$$\theta_{st} = 1 - \frac{1 + (3 + \beta)\alpha \pm \zeta^{1/2}}{2\,(\alpha^2 + (1 + \beta)\alpha)}, \quad \theta_{st,ex} \geq \theta_{st,\,ign} \tag{2.4}$$

$$\zeta = \left(\beta^2 + 6\beta + 1\right)\alpha^2 - (6\beta - 2)\alpha + 1 < 0 \tag{2.5}$$

In Figure 2.4 the S-shape curve is shown for a methane flame with activation energy E = 150 kJ/kg, β = 8.03 and a fuel inlet temperature of 300K [Pitsch and Fedotov, 2001]. The X-axis is the natural logarithm of the scalar dissipation rate. Pitsch and Fedotov, 2001 varied the Zeldovich and Damköhler numbers and the heat release parameter α. The authors increased the Zeldovich number by increasing the activation temperature ratio (β) this resulted in a reduction in both quenching and ignition scalar dissipation rate, but the reduction in ignition point was further than the reduction in the quenching point. A change in the Damköhler number simply resulted in a shift of the curve. The strongest response can be seen when altering the heat release parameter α; an increase led to a very strong reduction in the scalar dissipation rate for the ignition point and a slight increase for the quenching point. The heat release parameter is a function of the change in temperature at stoichiometry. A higher inlet temperature, or a lower change in temperature both result in a smaller value for α, which will result in the quench and ignition point coming closer together. A smaller β will also result in these points coming closer together and eventually disappearing. Changing the Damköhler number does not bring the points closer together, and can therefore also not be found in Equation 2.5.

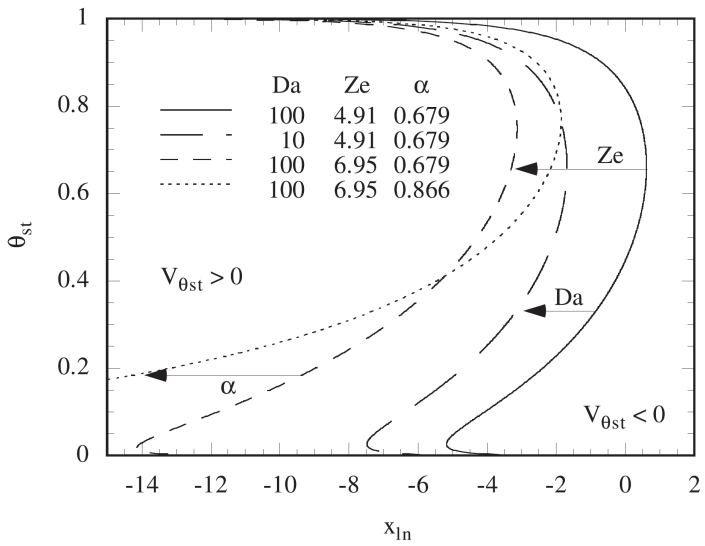

Figure 2.4: S-shaped curve for non-premixed combustion [Pitsch and Fedotov, 2001]

2.2. Nitric oxide production

To better understand the relevance of these definitions the NO_x formation pathways need to be understood first. There are multiple ways to produce NO_x as part of a combustion process with a nitrogen-free hydrocarbon fuel. The first production pathway is thermal or Zeldovich NO_x [Zeldovich, 1946]. The three main reactions are shown in Equation 2.6, Equation 2.7, and Equation 2.8. This reaction is referred to as the thermal mechanism as it is very temperature dependent. The reaction in Equation 2.6 is rate limiting due to the strong triple bond of nitrogen; the nitrogen radicals produced by the first reaction are needed in the other reactions [Warnatz et al., 2006]. Below 1700K this reaction rate of the first reaction is too low to have any meaningful effect according to Warnatz et al., 2006.

$$O + N_2 \rightarrow NO + N \tag{2.6}$$
$$N + O \rightarrow NO + O \tag{2.7}$$
$$N + OH \rightarrow NO + H \tag{2.8}$$

The second pathway is prompt, or Fenimore NO_x [Fenimore, 1971]. Fenimore observed NO concentrations close to the downstream side of a premixed flame front higher than is predicted by the slow thermal NO_x mechanism. This effect was only observed when burning hydrocarbons. This production mechanism is very fast and is therefore referred to as prompt. Production occurs through C_2H_2 and CH radicals and is, therefore, most active under rich conditions. The rate-limiting reaction $CH + N_2 \rightarrow HCN + N$ has much lower activation energy than the rate-limiting reaction for thermal NO_x, therefore prompt NO_X is also produced at temperatures below 1000K [Warnatz et al., 2006].

Another often overlooked pathway is production via nitrous oxide N_2O [Warnatz et al., 2006]. This NO produced through this mechanism is often very small, but when the thermal and prompt NO_x production pathways are suppressed this pathway can become the dominant one. As the reaction, given in Equation 2.9, is a three-body reaction, higher pressures promote production through this pathway. Furthermore, since the activation energy of this reaction is quite low it can proceed at low temperatures as well. The nitrous oxide then reacts with either a hydrogen or oxygen radical as shown in Equation 2.10 and Equation 2.11 [Glarborg et al., 2018].

$$N_2 + O + M \rightarrow N_2O + M \tag{2.9}$$
$$N_2O + O \rightarrow NO + NO \tag{2.10}$$
$$N_2O + H \rightarrow NO + NH \tag{2.11}$$

Even more recently production of NO though the NNH pathway has been identified [Bozzelli and Dean, 1995]. NNH is a very short-lived molecule. It quickly decomposes back to N_2 and H, but the formation reaction is also really quick therefore equilibrium or near-equilibrium concentrations of NNH are still achieved. The molecule can then react with a free oxygen radical to form $NNHO^*$, which decomposes to NH and NO [Bozzelli and Dean, 1995]. This pathway is enhanced when hydrogen is added to the mixture, especially in lean conditions [Iavarone and Parente, 2020].

As Iavarone and Parente, 2020 points out there is still a large amount of uncertainty surrounding the kinetics of this pathway, and the heat of formation of the NNH radical is still debated. The rate constant for the limiting reaction in Equation 2.12 is still not well determined either. Values reported in the literature vary by more than an order of magnitude.

$$N_2 + H \rightarrow NNH \tag{2.12}$$
$$NNH + O \rightarrow NH + NO \tag{2.13}$$

The main way in which NO_x production is decreased in flameless combustion is due to the decrease in flame temperature and thus the reduction in the thermal production of NO_x. The PSR definition and both ignition definitions are also valid above an inlet temperature of 1700K, the size of the domain grows even for the ignition definitions. That means that while the combustion process might be flameless, and or with a gradual ignition, following these definitions, the NO_x production might still be high if the reaction temperature is high enough.

Dilution does not only affect the production of NO through a reduction in temperature. While the diluents are often referred to as inert they do in fact play a role in the progression of reactions. Park et al., 2002 found in their numerical study of a methane-air counterflow diffusion flame that, when adding either CO_2 or N_2 from 0 to 10% volume, prompt NO_x production was suppressed. In the case of N_2 all pathways are restrained, likely just as an effect of dilution. When CO_2 was supplied the path $CH_3 \rightarrow CH_2 \rightarrow CH_2O$ is enhanced, reducing the amount of CH formed from CH_2. As the reaction of CH with N_2 is the rate-limiting step of NO production through the prompt pathway [Warnatz et al., 2006], the reduced availability of CH will result in a reduction in prompt NO formation. Additionally, CH is also produced via the C2 route, $C_2H2 \rightarrow CH_2 \rightarrow CH$ and another C1 pathway. Both of these are also weakened due to the addition of CO_2.

2.3. Discussion on the definitions

Evans et al., 2017 created a diagram with the PSR definition and the premixed and non-premixed ignition definitions, for various normalised temperature increases and inlet temperatures. This diagram is displayed in Figure 2.5 From this diagram it can be seen that these definitions do not fully overlap, and have different trends with increasing inlet temperature. The PSR definition is bound by the requirement for the inlet temperature to be above the self-ignition temperature. Following both these definitions flameless combustion can also be achieved below the self-ignition temperature, but the flame has to be continuously ignited to be able to sustain it. de Joannon et al., 2012 noted suppression of pyrolysis and flame thickening in this region below the self-ignition temperature in their simulation. This means that the ignition definitions are not just a subset of flameless combustion following the PSR definition. Each of the different definitions also has a different trend. The PSR definition has a decreasing trend in the maximum allowed normalised temperature with increasing inlet temperature, while both ignition definitions show increasing trends. The non-premixed line gradually becomes less steep with increasing inlet temperature, but the premixed definition increases seemingly without bounds. This is interesting considering the effect of temperature on NO_x production.

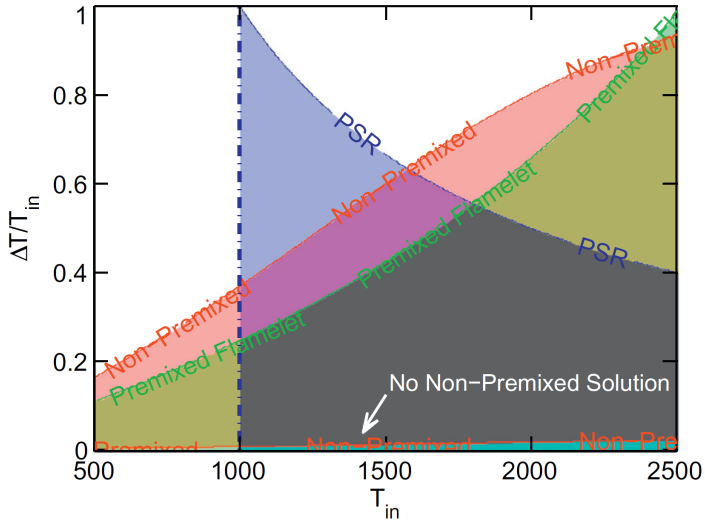

Figure 2.5: Comparison of different FC definitions, with T_{si} = 1000K, $E_{eff} = 1.67 \cdot 10^8$J/kmol and $T_{in} = T_{st,u}$ [Evans et al., 2017]

There are also other definitions out in the literature, which have not been discussed so far. Kumar et al., 2002 define a flame as flameless if the normalised temperature variance is low. However exact bounds using this definition have not been found [Cheong et al., 2021]. Another definition for non-premixed mild combustion by Cheong et al., 2021 is based on the spatial separation of regions of positive heat release rate and negative heat release rate or the lack of negative heat release rate. The aim of such a definition is to verify that flameless combustion has been achieved rather than predicting under which conditions it will be achieved. The problem with this definition is that it is very dependent on the fuel used. Under diluted conditions the negative HRR region of a methane flame was suppressed, Cheong et al., 2021 did not observe any negative HRR when burning hydrogen either diluted on undiluted, while when burning propane the negative HRR spatially separates from the positive HRR.

2.4. Behaviour of flameless combustion

In this section, the behaviour of flameless combustion will be discussed. Starting with the ignition behaviour, then the dynamic behaviour observed under some inlet temperatures and equivalence ratio will be treated. The effect of adding diluents like CO_2, H_2O, N_2 and NO_x will be discussed and the effect of premixing will also be analysed.

2.4.1. Ignition in jet-in-hot-coflow setups

As discussed in the definition section different ignition behaviours are observed in flameless combustion. In general, ignition occurs through autoignition [de Joannon et al., 2012], however, flames with depressed pyrolysis and broad reaction zones have also been found below the self-ignition temperature where the flame had to be continuously ignited. These flames are also referred to as quasi-mild [Wang et al., 2014].

Within the set of flames which ignite through self-ignition different behaviour is observed based on the oxygen concentration. Between 5%-12% oxygen volume ignition kernels occur and the flame appears lifted [Medwell and Dally, 2012b]. At lower oxygen concentrations between 3% and 5% the flame is attached to the jet exit [Medwell et al., 2008]. Medwell et al., 2008 experimented with different coflow conditions in the Adelaide jet-in-hot-coflow burner. The coflow oxygen concentration was varied from 3% to 9% of the volume. In the central jet, various fuel compositions were also used: pure ethylene, ethylene-hydrogen at a 1:1 volume ratio, ethylene-air at a 1:3 ratio, and ethylene-nitrogen at a 1:3 ratio. For all these fuel compositions the flame was attached to the jet exit by a faint outline at 3% oxygen concentration. In the 9% oxygen cases all, except the hydrogen case were lifted and were more luminous. For the three fuel compositions which showed a lifted flame the lift-off height was also observed to decrease with increasing jet Reynolds between a Reynolds range of 5,000 and 10,000.

Similarly, experiments by Oldenhof et al., 2010 in the Delft JHC also showed a decrease in lift-off height with increasing jet Reynolds between $Re = 3,000$ and $5,000$ at a coflow oxygen mass percentage of 8.4% and 9.5%. In the central jet, three fuel mixtures were used; Dutch natural gas and two mixtures approximating Dutch natural gas: Mixture one consists of nitrogen and methane, and mixture two of nitrogen, methane and a small percentage of ethane. The conventional non-diluted flame showed a clear continuous flame front at the bottom, but when a vitiated coflow was supplied small flame pockets were observed. These grew as they convected downstream and then merged into a continuous flame front. These ignition kernels were also observed in the 9% O_2 cases by Medwell et al., 2008. The location at which these flame pockets were formed fluctuated, so the definition of lift-off height chosen by Oldenhof et al., 2010 is that there is a 50% chance of finding a flame at this downstream location.

Medwell and Dally, 2012b produced a regime diagram showing the general location where these different types of ignition behaviour are observed. This diagram is shown in Figure 2.6. The authors also performed experiments on the Adelaide JHC burner under various coflow conditions. In the central jet pure methane is provided as the fuel, and a secondary burner produces a hot coflow of flue gasses. This secondary burner is provided with a mixture of natural gas, hydrogen, air and nitrogen. The hydrogen-natural gas ratio is kept constant at a volumetric ratio of 1.3:1. The oxygen concentration is controlled by altering the ratio of nitrogen to air provided to the secondary burner while keeping the fuel flow rate constant. By not altering the fuel flow rate the volumetric concentration of H_2O and CO_2 are maintained at 10% and 3% respectively. The lift-off height was determined based on visual observation, analysis of photographs and CH^* chemiluminescence.

Medwell and Dally, 2012b only found a decrease in lift-off height when the coflow temperature was 1400K in the Reynolds range between about 4,000 and 10,000. This was observed even at a coflow oxygen concentration of 3%, which according to Figure 2.6 should be in the mild regime. The authors note that flames at 1400K typically had the highest lift-off height at various coflow oxygen conditions. The point at which an increase in Reynolds number produced a decrease in lift-off is also the transition point from a laminar to a turbulent jet. Visually, the flames looked different based on the coflow oxygen concentration. The authors note that the 3% O_2 flames are much less luminous than the flames in the 6% O_2 cases.

An interesting trend was observed in the lift-off height when altering the coflow temperature and coflow oxygen concentration. When increasing the oxygen concentration from 3% with a coflow temperature of 1300 K an increase in lift-off height is observed. After 6% oxygen concentration, the lift-off height reduces again. The 12% coflow oxygen case has the lowest lift-off height. Similarly, increasing the temperature leads to an increase in lift-off height, with a peak at 1400 K, 1300 K and 1300 K for the 3, 6 and 9% coflow oxygen cases respectively. An increase in lift-off height is indicative of reduced reactivity, one would expect the reactivity to increase with increasing oxygen concentration and temperature. The authors draw similarities with the unstable regime observed by Wünning and Wünning, 1997 which can be seen in Figure 2.2. An unstable regime was found between the regular diffusion stabilised flames

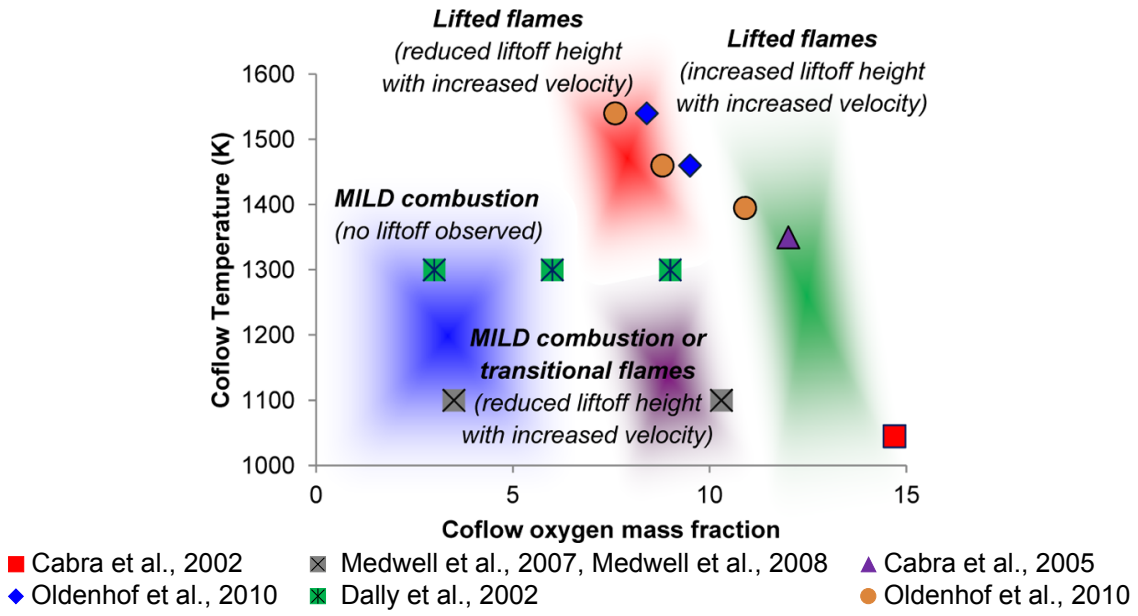

Figure 2.6: Regime diagram showing the location where different types of ignition behaviour can be found. Taken from Medwell and Dally, 2012b

and the mild regime. Medwell and Dally, 2012b state that the behaviour of increased lift-off height with increasing temperature and oxygen concentration is analogous to the transition between these two stable regions. It seems that the temperature and oxygen concentration change has some effect on mixing and the chemical kinetics which cannot be inferred from the data presented by these authors and would warrant further research over a wide range of operating conditions.

2.4.2. Dynamic behaviour

Not only changes in the oxygen concentration influence the ignition behaviour of flameless combustion. Sabia, Sorrentino, et al., 2015 performed a numerical simulation of methane-oxygen diluted with 90% CO_2 in a perfectly stirred reactor. The inlet temperature and equivalence ratio were changed, at adiabatic and non-adiabatic conditions. From this, a regime map with different types of behaviour was produced, with on the Y-axis the equivalence ratio expressed as the C/O ratio, and on the X-axis the reactant inlet temperature. The diagram for non-adiabatic conditions is shown in Figure 2.7a and for adiabatic conditions in Figure 2.8.

In non-adiabatic conditions five distinct regions were found. At low temperatures, no reaction was observed. Increasing the temperature leads to a regime with multiple ignitions, one with damped temperature oscillations, one with undamped periodic oscillations and a steady stationary combustion regime. In Figure 2.7b a temperature-time plot is shown of these four reactive regimes. In the multiple ignition regime, a spike in temperature is observed, after which the temperature drops back to the inlet temperature. At the peak temperature in this regime, all fuel is converted. Reactants do not occur until a sufficient amount of reactants have re-entered the combustor, resulting in a period which is larger than the flow residence time. In the damped oscillation regime, the temperature eventually converges to a fixed value. In the periodic oscillation regime, the temperature keeps oscillating around a temperature higher than the inlet temperature. In the steady regime, an initial spike in temperature is observed after which the temperature returns to a fixed value.

In adiabatic conditions all the same behaviours, but the multiple ignition regime, were observed. Comparing the two maps it can be seen that the dynamic regimes have shrunken in size, while the steady regime has grown in size. The fact that dynamic behaviour is observed indicates that it is not just caused by heat losses, but also due to competition between pyrolytic/ endothermic reactions and exothermic reactions. Under mild conditions the reactions are generally slower, there seems to be a delicate balance between competing reactions at certain conditions. This makes the reaction sensitive to external perturbations, like heat losses. The authors found that different chemical-kinetic models resulted in

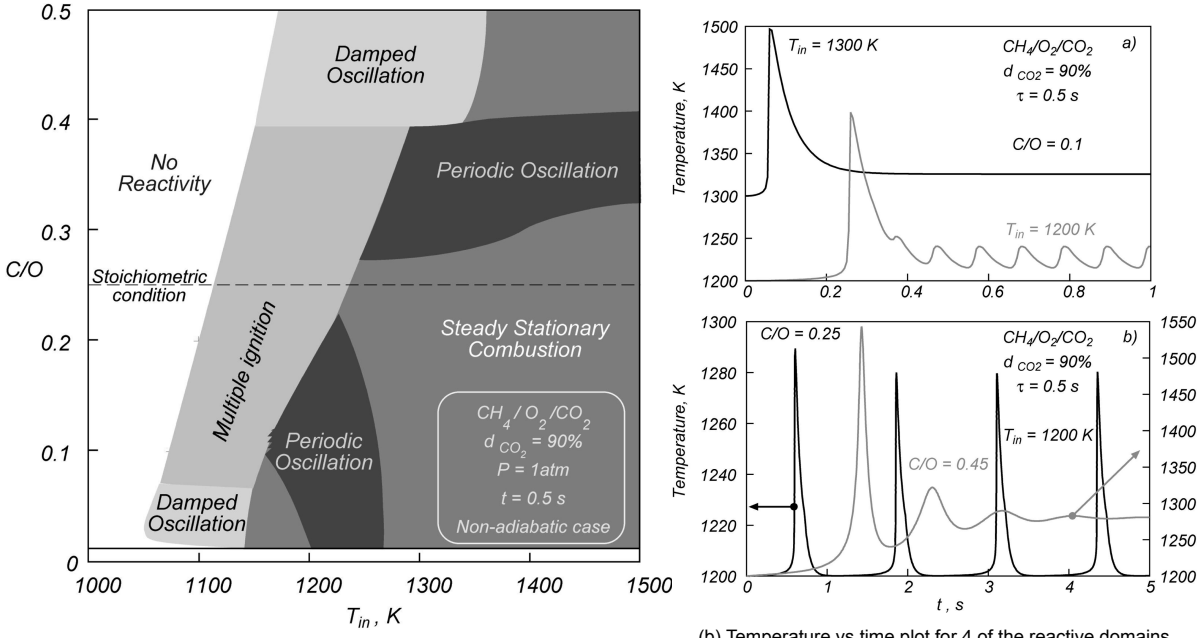

(a) Regime map for different inlet temperatures and equivalence ratios

(b) Temperature vs time plot for 4 of the reactive domains

Figure 2.7: Numerically simulated PSR of methane-oxygen with 90% carbon-dioxide dilution in non-adiabatic conditions [Sabia, Sorrentino, et al., 2015]

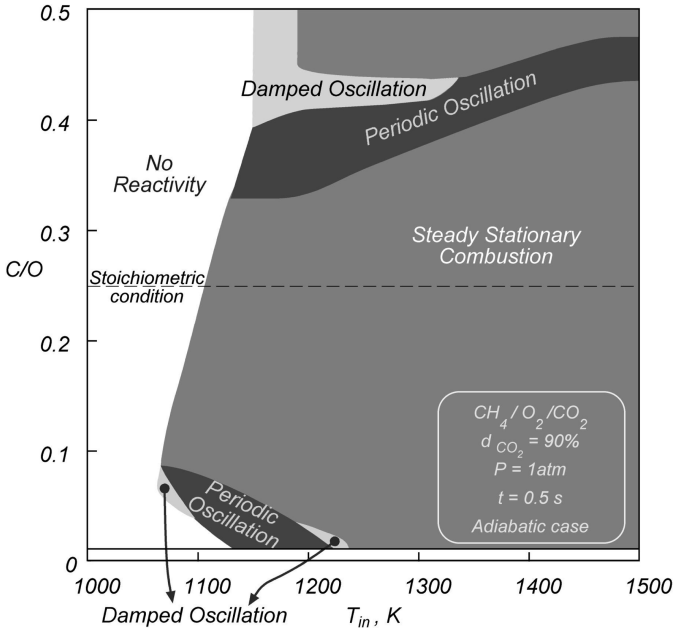

Figure 2.8: Regime map for different inlet temperatures and equivalence ratios, based on numerically simulated PSR of methane-oxygen with 90% carbon-dioxide dilution in adiabatic conditions [Sabia, Sorrentino, et al., 2015]

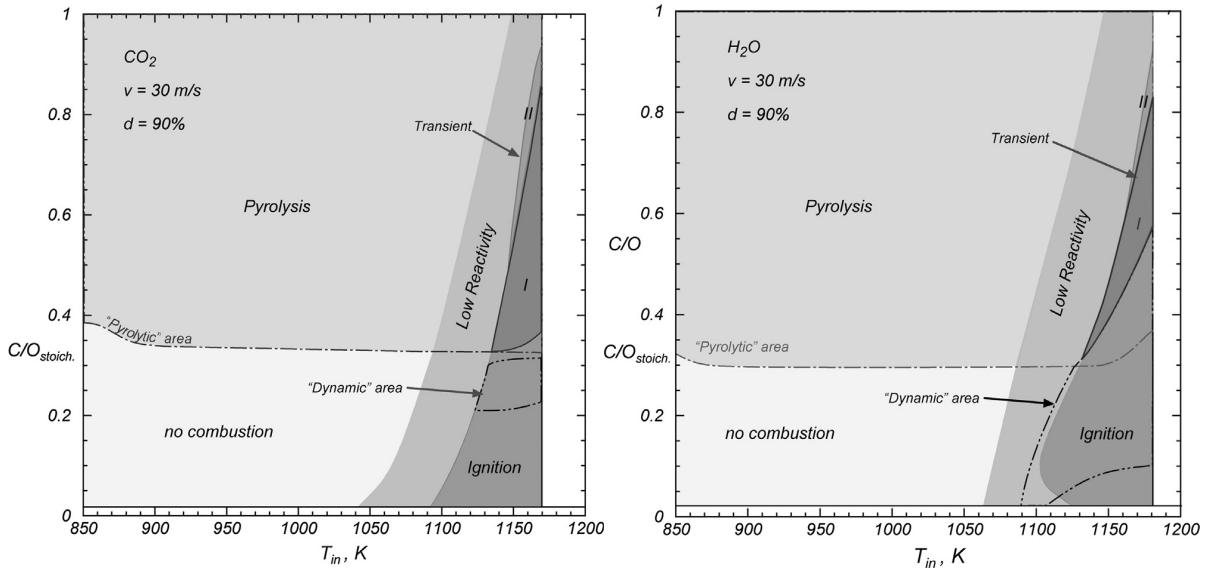

(a) Dilution with CO_2 (b) Dilution with H_2O

Figure 2.9: Stability diagrams obtained from experiments with the tubular flow reactor burning propane with a 10% oxygen and 90% diluent mixture [Sabia, Lubrano Lavadera, et al., 2015]

different shapes of the regimes as well as differences in ignition delay, and amplitude and frequency of the temperature oscillations.

Sabia, Lubrano Lavadera, et al., 2015 also observed regions with different behaviour based on the inlet temperature and equivalence ratio. These authors completed both experiments and numerical simulations on the combustion of propane and oxygen diluted with 90-97% CO_2 or H_2O. The setup used is a tubular flow reactor at atmospheric pressure. The regimes maps obtained with 90% dilution are shown in Figure 2.9. Though the authors tested at higher dilution levels they found that this did not result in the same oxidation regimes, and only lowered the temperatures achieved inside the combustor. The authors observed five regimes as well: The no combustion region in which there was no temperature change between the inlet and the inside of the combustor. A pyrolysis region in which the temperature in the combustor was lower than the inlet temperature. A low reactivity region in which the observed temperature increase is less than 10K. An ignition region in which the temperature increase exceeded 10K. A dynamic region in which the temperature profile was recorded to flip periodically. Finally, a transient region in which the mixture ignites and stabilises at a first reactive state, but then later spontaneously switches to another final stationary state.

The dynamic region observed when diluting with water is larger than when carbon dioxide is used. This is due to a delicate competition between oxidation, pyrolysis and recombination reactions. The authors found from numerical simulations that water dilution promoted dynamic behaviour mainly due to its higher third-body collision efficiency. This results in a dampening of the oxidation routes and promotes recombination reactions.

2.4.3. Effect of Diluents

As already seen in the previous section different diluents can have different effects. Park et al., 2002 used GRI v2.11 to analyse the effect of CO_2, H_2O and N_2 addition for a methane-air counterflow flame. The diluent is added to the air stream from 0 to 10% volume. While these diluent concentrations might not be high enough for this flame to be considered flameless the trends observed in these results might still shed light on what trends can be observed.

Park et al., 2002 found that increasing the diluent flow rate resulted in reduced peak temperatures. The largest reduction in temperature is observed when CO_2 is used as the diluent, followed by H_2O and then N_2. The authors state that water has the highest specific thermal capacity by mass, at almost double that of CO_2 or N_2, followed by N_2 and CO_2. Although it is important to note that this is different when looking at the specific thermal capacity per mole; Then CO_2 has the highest specific thermal capacity,

followed by H_2O and then N_2 [Chase, 1998]. Since the diluents are added as a volume one might argue that comparison using the thermal capacity per mole would be more suitable. Nevertheless, the authors state that the reduction in temperature is not purely caused by changes in the overall thermal capacity of the gasses. All diluents resulted in lower reactive species concentrations, leading to fewer reactive collisions. However, each of the diluents can decompose as well which alters the available radical pool. The authors state that water can decompose into H, O_2 and HO. While carbon dioxide might break down into CO which will then react at a higher rate with hydrogen radicals reducing their availability [Westbrook and Dryer, 1984].

Park et al., 2002 also found that these diluents also affected the production of NO_x through the prompt pathway. Prompt NO_x is mainly formed due to the interaction between CH and N_2. N_2 was found to repress the global activity of all pathways, but does not induce any relative change between pathways. Adding CO_2 strengthens that pathway $CH_3 \rightarrow CH_2 \rightarrow CH_2O$ reducing CH formation from CH_2. The C2 and other C1 pathways to CH formation are also weakened. The addition of water resulted in a strengthening of the C1 and C2 pathways due to the increased availability of the chain carrier radicals OH and H. On the other hand dilution water did result in enhanced NO consumption, compared to carbon dioxide.

Finally, the authors conclude that all diluents decrease the temperature due to an increase in total thermal capacity. While carbon-dioxide was found to also chemically decrease the temperature by inhibiting branching reactions, and water on the other hand chemically increases the temperature due to an increase in chain carrier radicals. From the perspective of reducing NO production CO_2 was found to be most potent, followed by H_2O and finally N_2. CO_2 and H_2O dilution resulted in the greatest NO reduction due to their modification of the reaction pathways.

Sorrentino et al., 2016 compared the behaviour of N_2 and CO_2 dilution in a cyclonic burner using propane. The oxygen concentration was set at 6%. The oxidiser stream contained pure oxygen and either N_2 or CO_2 as diluent. The inlet temperature of the oxidiser stream and equivalence ratio were varied. In Figure 2.10 the temperature change in the combustor is plotted as a function of the C/O ratio, for either N_2 or CO_2 dilution at different oxidiser inlet temperatures. The ΔT in these plots is defined as the maximum temperature observed in the combustor minus the inlet temperature. What can be noted first is that N_2 resulted in a greater temperature increase than CO_2, except in the low inlet temperature case of 975K. Here, the addition of CO_2 resulted in a greater temperature increase. The authors cite Sabia, Lubrano Lavadera, et al., 2015 who found that at lower temperatures CO_2 promotes radical branching due to its higher third body collision efficiency with the reaction $H_2O_2 + M \rightarrow 2OH + M$; while at intermediate temperatures CO_2 promotes methyl recombination which inhibits the ignition process. The inhibitory effect of CO_2 is even more pronounced at higher temperatures above 1200K, as CO_2 decomposes into CO, which then consumes hydrogen radicals as stated earlier [Westbrook and Dryer, 1984].

In fuel-rich conditions no combustion was possible below an inlet temperature of 900K. Moving towards leaner conditions the minimum ignitable inlet temperature increases. When the flow is diluted with N_2 this temperature is higher than when using CO_2 as carbon dioxide enhances ignition at low temperatures as discussed in the previous paragraph. At temperatures above the minimum ignitable limit, a low reactivity region is identified, where an increase in temperature of less than 10K was observed. Increasing the inlet temperature further leads to a stable regime where the ΔT is larger than 10K. This transition between low reactivity and stable combustion occurred at an inlet temperature of around 1000K. This transition is not dependent on the equivalence ratio when diluting with CO_2 due to its enhancing effect at these temperatures. When diluting with N_2 the transition occurs at a slightly higher temperature in rich conditions.

The earlier cited paper by Sabia, Lubrano Lavadera, et al., 2015 looked at the effect of H_2O dilution when burning propane. The authors found that water mainly acts as a third body species. In low temperatures at around 900 K it was found to boost branching reactions by causing the decomposition of hydrogen peroxide with the reaction $H_2O_2 + M \rightarrow 2OH + M$. At intermediate temperatures (T_{in} > 1000) water slows the reaction process by promoting methyl recombination reactions by acting as a third body. However, at the same time, it reacts with the methyl radicals converting them to methane and OH through the reaction $CH_3 + H_2O \rightarrow CH_4 + OH$ at a similar reaction rate as the recombination route. At higher temperatures, between 1200K and 1350K, this reaction is the main source of OH radicals.

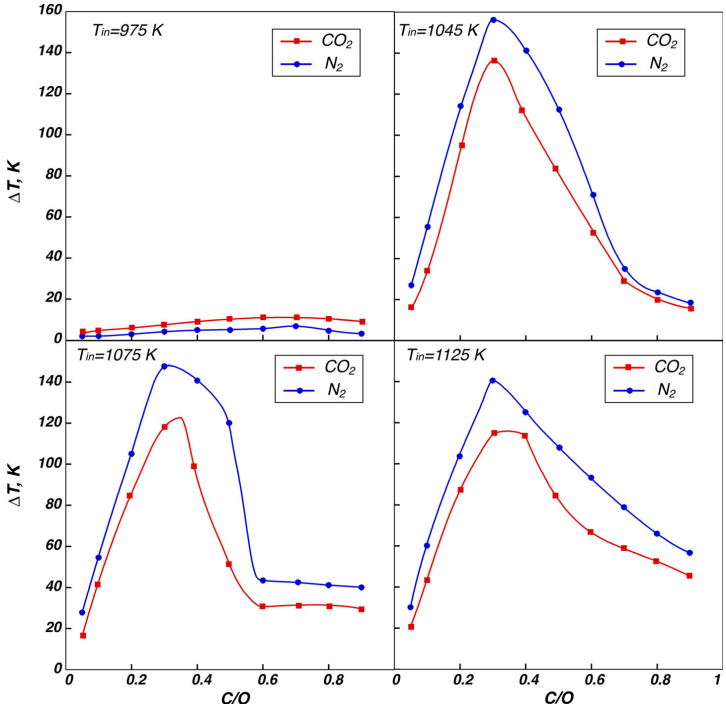

Figure 2.10: Combustion of propane; ΔT as a function of C/O at different inlet temperatures, for either 94% CO_2 or N_2 as diluent and 6% O_2 [Sorrentino et al., 2016]

Additionally, at intermediate temperatures, water enhances the production of HO_2, which reacts with methyl radicals to form CH_3O. Methoxide then decomposes feeding the oxidation channel by producing large amounts of H radicals. At high temperatures, water reduces the reactivity by consuming O and H radicals required for branching reactions. At low temperatures, water increases reactivity, while at intermediate to high temperatures water was found to decrease reactivity.

Sabia and de Joannon, 2020 points out that big uncertainties on the kinetic parameters still remain. In Sabia, Lubrano Lavadera, et al., 2015 it is stated that there is a discrepancy between the numerical simulation and the experimental results. The presence of CO_2 prior to combustion is not something that was considered when current models were developed. These gasses are usually only present after oxidation so they would interact with fewer species closer to the equilibrium point. As was seen in this section CO_2 and H_2O can alter the ignition process. They both increase reactivity at low temperatures but decrease it at moderate to high temperatures. Sabia and de Joannon, 2020 also note that there is currently a lack of validation data available to improve these models in the low to intermediate temperature range.

Recent work by Kazangas et al., 2021 looked at the influence of NO_x, and SO_x on the ignition of methane flames. While their work was mainly focused on NO_x addition in the context of marine engines with exhaust gas recirculation, their simulations were performed using methane and are still valid for flameless combustion in general. A PSR simulation at pressures ranging from 7.2 bar to 90 bar and equivalence ratios ranging from 0.5 to 2, and temperatures ranging from 1200- 1620k was performed. Four different detailed chemistry models were assembled and compared to JSR and shock tube data, from this, the best-performing model was selected. The addition of NO and NO_2 were found to decrease the ignition delay significantly with increasing concentration, while the effect of SO_x addition was negligible. At intermediate pressures, NO_2 addition yields a greater decrease in ignition delay as compared to NO, while at higher pressures the difference between them decreases. The reduction in ignition delay is non-linear with the slope becoming flatter with increasing NO, NO_2 addition.

A rate of production analysis was performed to identify how NO_x addition influences the chemical kinetics, specifically its influence on the OH radical pool. OH production was enhanced by both the introduction of NO and NO_2 mainly through production of CH_2O, then converted to HO_2, which is finally converted into 2 OH molecules. It was found that NO_2 addition yielded two magnitudes higher

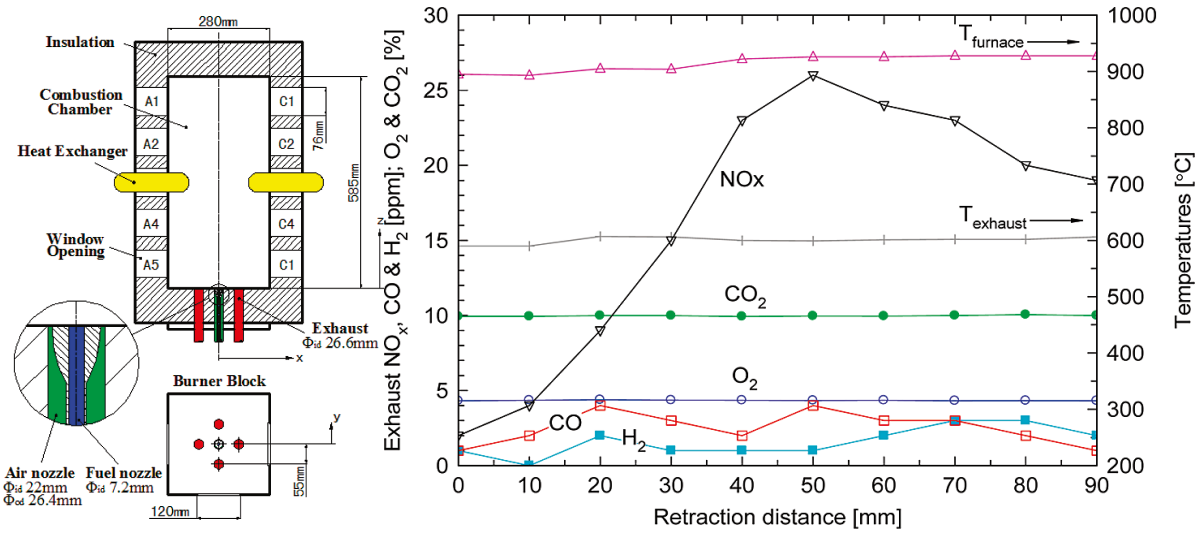

(a) Schematic of the furnace used by Mi et al., 2009

(b) Exhaust gas composition as a function of fuel nozzle retraction, with a heat input of 10kW and an equivalence ratio of $\phi = 0.77$ [Mi et al., 2009]

Figure 2.11

production of CH_3O as compared to NO addition at a pressure of 15 bar and equivalence ratio of 0.5.

Similar results were found by Song et al., 2019. At low temperatures of 850K, the addition of NO_x accelerated the reactions by producing H radicals. NO and NO_2 were found to have a catalytic effect and were not consumed but recycled back into NO and NO_2. Only at higher temperatures NO_x reburning would occur and the concentration of NO and NO_2 would be lower at the exit. From Glarborg et al., 1998 the reaction: $CH_3 + NO \rightarrow H_2CN + OH$ and $CH_3 + NO \rightarrow HCN + H_2O$ and the reaction of $HCCO$ with NO were responsible for the consumption of NO_x. All these pathways eventually progress further to form HCN; high concentrations of this species might be a good indicator if reburning is occurring. Song et al., 2019 observed a rise in HCN starting at around 1175K, while in Glarborg et al., 1998 the concentration peaked at around 1400K.

2.4.4. Effect of premixing

Most jet-in-hot-coflow setups operate in non-premixed conditions. However, it is interesting to look at the effect of premixing on flameless combustion. Medwell et al., 2008 looked at the ignition behaviour of JHC flames with additional gasses added to the fuel. Ethylene was used pure, or mixed with air, nitrogen or hydrogen. By comparing the N_2 or air diluted case the effect of premixing can be established. The composition of the fuel stream is 75% nitrogen or air, and 25% volume ethylene. When adding air this results in a central jet equivalence ratio of 4.8. The partially premixed flame showed the highest formaldehyde levels. Earlier work by McEnally and Pfefferle, 1999 had already shown that for partially premixed methane flames the formaldehyde concentrations are at least 5 times higher than for non-premixed flames. Additionally, higher temperatures were observed in the partially premixed flame. No difference in the lift-off height was observed between the N_2 or air addition. The jet without any additives in the central jet had the lowest lift-off height. The OH concentrations are also observed to be similar.

Mi et al., 2009 directly analysed the effect of premixing on mild combustion. Different levels of premixing were achieved by altering the retraction distance of a retractable nozzle. Natural gas flows through the nozzle which is placed in the centre of a larger tube through which air flows. Retracting the nozzle inside of the air duct gives time for the natural gas and air to mix before emerging into the combustion chamber, thus increasing the level of premixing. An additional case where the air was added directly to the fuel nozzle was also tested. The reactants enter the combustion chamber at the bottom, and then also have to leave the combustion chamber at the bottom. In Figure 2.11a a schematic of the burner design is shown.

Mi et al., 2009 first used CFD to ascertain the effect of jet momentum on the combustion regime. The authors found that a lower jet momentum leads to flames becoming visible, resulting in higher tem-

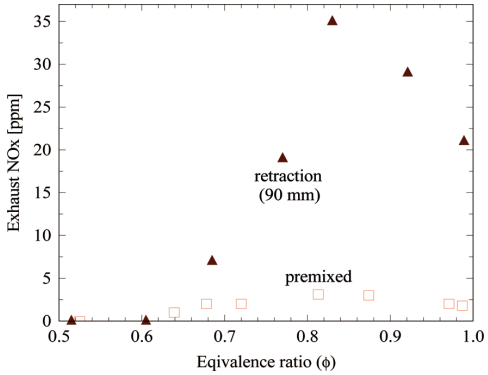

Figure 2.12: NO_x emissions at various equivalence ratios for different levels of premixing [Mi et al., 2009]

perature peaks and higher NO_x emissions. These findings were then also supported by experimental observations. A critical momentum rate was found below which mild combustion could not be established, as the recirculation rate of the gasses is influenced by the jet momentum. What the critical jet momentum rate is depends on the geometry of the setup. When the reactants were partially premixed the required jet momentum to establish flameless combustion was reduced. Above this critical momentum, a change in jet momentum did not result in significant changes to the stability or emissions from the flame.

In Figure 2.11b the exhaust gas composition measurements are shown as a function of the retraction distance. The CO_2, CO and H_2 concentrations remain fairly constant, while the NO_x concentration increases from 2ppm to 26ppm and then decreases to 19ppm with increasing nozzle reaction. It should be noted that when the nozzle is retracted the jet momentum also decreases. Although, for all cases, the jet momentum remains above the computed critical jet momentum rate. Even though the NO_x emissions are observed to change the fact that the maximum NO_x emissions do not correlate to the minimum jet momentum makes the authors conclude that the jet momentum does not have a significant influence on the performance of mild combustion.

In Figure 2.12 the NO_x concentration is plotted as a function of the equivalence ratio. The 90 mm retraction case is the furthest the nozzle could be retracted and is therefore the highest level of partial premixing. In the premixed case, the air and natural gas are mixed inside the central jet pipe. For the retracted nozzle the measured NO_x concentrations show a relatively large variation from about 0 ppm on the lean side up to just above 35 ppm at an equivalence of 0.84. The fully premixed jet shows a relatively small variation. It is important to note that the fully premixed jet has a much higher jet momentum than the retracted nozzle. Comparing the NO_x concentration between the least retracted case in Figure 2.11b and the premixed case in Figure 2.12 it can be seen that the NO_x concentration is very similar. Therefore, it can be concluded that, for this burner, when the jet momentum is sufficiently high the level of premixing does not have a significant effect on the NO_x emissions.

2.5. Summary of the state of the art

In this chapter, some literature about flameless combustion is discussed. In the first section, the different definitions for flameless combustion are compared. There is still no consensus on what flameless combustion is. There are also several terms in use with varying degrees of overlap. The early definition of flameless combustion by Wünning and Wünning, 1997 is based on the recirculation rate. The PSR definition is based on the inlet temperature and the change in temperature inside the combustor. The flamelet definitions are based on the ignition behaviour. Flames which monotonically shift from unburned to burned are defined as flameless, and flames that do not are not. These different definitions also show different trends with inlet temperature as can be seen in Figure 2.5. Low NO_x emissions are the reason why flameless combustion is a combustion regime of interest. NO_x production through the Zeldovich pathway is very temperature dependent [Warnatz et al., 2006]. This is currently not incorporated into these definitions, the inlet temperature can increase without any limit. So at these higher temperatures, higher NO_x emissions can also be expected even though the regime might be considered flameless following these definitions.

Dynamic behaviour was also observed. This was found to be caused by both heat transfer and competition between pyrolytic/ endothermic reactions and exothermic reactions. Dilution leads to a temperature decrease but also changes the radical pool, which results in different reaction pathways becoming strengthened or weakened. CO_2 or H_2O can act as a third body species, which can have both beneficial effects; like aiding in the decomposition of hydrogen peroxide into OH, or can inhibit reactivity by enhancing recombination reactions of methyl [Sabia, Lubrano Lavadera, et al., 2015] [Sorrentino et al., 2016].

The results from the kinetic models do not always match well with experimental results. Sabia and de Joannon, 2020 point out that these models were not developed with the presence of CO_2 or H_2O before combustion. There is currently also a lack of validation data to improve the models, especially at low and intermediate temperatures. Most jet-in-hot-coflow burners are unenclosed, and therefore no emissions data is collected on these setups. Perpignan et al., 2018 point out that modelling would benefit from data combining flame morphology and structure with emissions measurements.

3

Combustor design

Since the jet-in-hot-coflow setups in literature are unenclosed an enclosed setup will be designed. The jet-in-hot-coflow configuration has been shown to be well-suited for attaining the conditions required for flameless combustion to occur. This configuration also has a single flame in the centre which means the flame structures can be observed without interference from other flames, and the conditions in the coflow can be easily adapted to study the effects of different diluents.

3.1. Requirements

To be able to answer the research questions set out in chapter 1 the new design has to meet some requirements.

- The combustor needs to be able to operate at various oxygen concentrations. The regime diagram by Medwell and Dally, 2012b specifies that true flameless combustion occurs at oxygen concentrations below 5% mass fraction. The combustor shall be able to operate in this regime and also in the transitional regime above a mass fraction of 5% oxygen.
- The combustor needs to be built from material that can withstand the temperatures and oxidative conditions in the mixing duct and the combustion chamber. The heat transfer calculations in chapter 5 predict very high wall temperatures, so a material has to be selected which can withstand this.
- The combustor also needs to be able to provide a mixture of hot flue gasses and additional inert diluents to observe the behaviour of flameless combustion under these varying conditions. The temperature of this mixture needs to be high enough for the methane-air mixture of the main burner to ignite.
- The coflow mixture needs to be uniform and well-mixed before entering the combustion chamber. Having uniform boundary conditions makes it easier to model the combustor, and thus the obtained data from experiments can be used for more detailed numerical analysis.
- The combustor design must allow for both visual observation of the flame, for example, to apply laser-based diagnostics, but also allow for in situ measurements without external lab air entering the combustion chamber.
- The combustor needs to interface with the currently existing lab equipment.
- The combustor shall be operated safely without damaging itself, any persons, or other equipment around the setup.

3.2. Other setups in literature

Creating an overview of different jet-in-hot-coflow setups in literature can aid in making design decisions. These setups have been proven to work, they can thus serve as a basis for this new design. In Table 3.1 an overview is given of the geometric properties of other burner designs, the enclosed

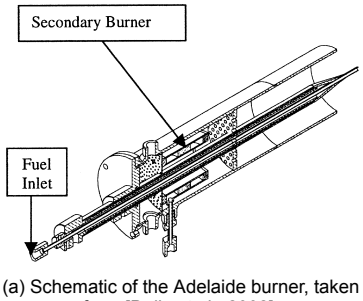

(a) Schematic of the Adelaide burner, taken from [Dally et al., 2002].

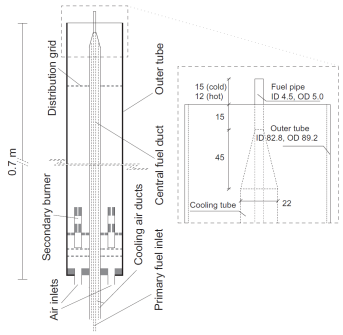

(b) Schematic of the Delft jet-in-hot-coflow burner, taken from [Oldenhof et al., 2011].

Figure 3.1

jet-in-hot-coflow setup designed in this thesis is also listed for comparison. h_{max} is the maximum measurement location downstream of the jet exit up until where the authors state that the coflow shields the central jet region from interference by ambient air. The maximum measurement height listed in the table for the enclosed jet-in-hot-coflow setup is based on the height of the windows in the combustion chamber; gas measurements can be taken further downstream.

The Adelaide burner

The Adelaide burner is a jet-in-hot-coflow burner built by the University of Adelaide [Dally et al., 2002]. A secondary burner is integrated inside the coflow annulus. The flue gasses produced by the secondary burner mix with the cold nitrogen and air which is added through two ports at the bottom of the setup. The cold nitrogen and air will also cool the secondary burner. A cooling jacket surrounds the central jet. Since this burner is an open setup ambient air is found to start influencing the jet region about 100 mm downstream from the jet exit. The burner is mounted in a wind tunnel to delay the entrainment of lab air as much as possible. A schematic of the burner is presented in Figure 3.1a.

The Delft Jet-in-hot-coflow burner

The Delft jet-in-hot-coflow burner is based on the Adelaide burner [Oldenhof et al., 2011]. A partially premixed ring burner is integrated into the annulus of the coflow and provides hot flue gasses. Additional air is added to the coflow through ports at the bottom of the setup. A screen is inserted, 110 mm upstream from the jet exit, into the coflow to cool the gasses. The central jet is surrounded by a cooling jacket, just like the Adelaide burner. In Figure 3.1b a schematic of the combustor is shown.

DLR jet-in-hot-coflow burner

The DLR-JHC is built to investigate the ignition behaviour of flameless combustion by burning hydrogen in short pulses [Arndt et al., 2012]. The coflow provided by a lean premixed hydrogen flat flame stabilised on a water-cooled bronze sinter matrix. The sinter matrix is located 8 mm upstream from the jet exit plane. The combustion chamber is surrounded by a quartz glass tube with a height of 120mm, which prevents ambient air from interacting with the combustion zone. In Figure 3.2a a schematic of this setup is shown.

The Cabra burner

The Cabra burner is a jet-in-hot-coflow setup, with a coflow provided by a lean premixed hydrogen flame stabilised on a perforated disk located 70 mm upstream of the jet exit [Cabra et al., 2005]. A schematic of the burner is shown in Figure 3.2b.

Piloted premixed jet burner

This burner is designed by [Dunn et al., 2007]. The central jet in this burner is surrounded by two coflows; one small pilot burner with an inner diameter of 23.5 mm surrounds the central jet. The flame of the pilot burner is anchored on a base plate placed 7 mm upstream from the jet exit. Another coflow

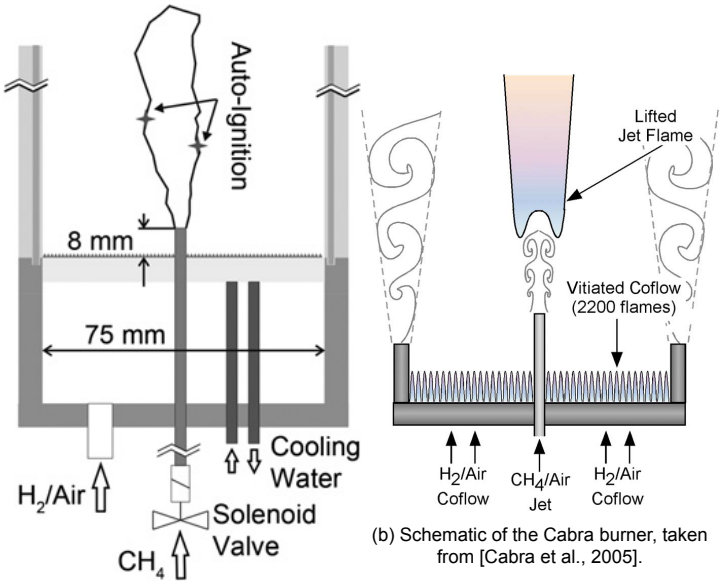

(a) Schematic of the DLR-JHC, taken from [Arndt et al., 2012].

(b) Schematic of the Cabra burner, taken from [Cabra et al., 2005].

Figure 3.2

with a diameter of 197 mm surrounds the pilot burner. This flame is anchored on a perforated brass disk which is placed 70 mm upstream from the jet exit plane. A schematic of this burner is shown in Figure 3.3b.

The distributed flameless combustion burner

This burner is designed by [Duwig et al., 2012]. A four-armed star shape is placed inside the central jet tube 20 mm upstream from the jet exit. This shape generates a streamwise vortex, which promotes the entrainment of hot gasses from the coflow. It is water-cooled to prevent preheating of the fuel mixture. The central jet is surrounded by a McKenna burner, which generates a laminar planar flame 2 mm upstream from the jet exit. A picture of the setup and a schematic of the central jet is shown in Figure 3.3a.

Burner	D nozzle [mm]	D annulus [mm]	h_{max} measurement [mm]	h_{max}/D_{jet}
Adelaide [Dally et al., 2002]	4.25	82	~100	23.53
Cabra [Cabra et al., 2005]	4.57	210	320	70
DJHC [Oldenhof et al., 2010]	4.5	82.8	160	35.56
DLR-JHC [Arndt et al., 2016]	2	75	120	60
DFC [Duwig et al., 2012]	1.5	60	30	20
PPJB [Dunn et al., 2007]	4	197	240	60
Enclosed JHC	3	120	300	100

Table 3.1: Geometric properties of Jet-in-hot-colflow burner designs found in literature, including the enclosed jet-in-hot-coflow burner designed in this thesis.

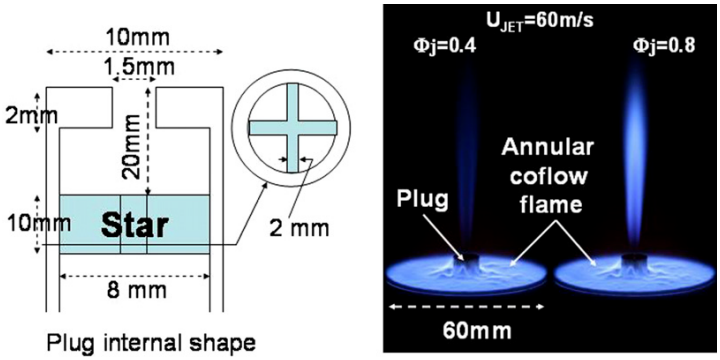

(a) Picture of the distributed flameless combustion burner and a schematic of the star in the central jet, taken from [Duwig et al., 2012].

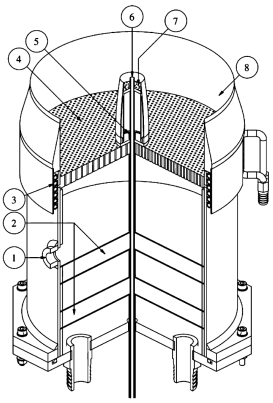

Balloon number	Description
1	Flashback over-pressure sensing port
2	Glass bead filled cavities
3	Cooling water coil
4	Coflow perforated baseplate
5	Pilot mixture feed exit
6	Central jet exit
7	Pilot perforated baseplate
8	Coflow collar

(b) Diagram of the piloted premixed jet burner, taken from [Dunn et al., 2007].

Figure 3.3

3.3. Design considerations

In this section, the design driving requirements are discussed. These requirements are used to size the combustion chamber and mixing ducts.

3.3.1. Chamber sizing

It is important to attain optical access to the combustion zone in the combustion chamber. The easiest way to do this is to use a quartz glass cylinder as the chamber containment. The disadvantage of using a cylinder is that it will cause distortions in the light coming out of the chamber. Especially when looking at the regions near the walls. Using a rectangular shape would resolve this as the glass plates are not curved, but this shape comes with its own disadvantages. The sharp corners would induce secondary flow structures to form [Pirozzoli et al., 2018]. In a pentagon none of the sides are parallel. This will likely result in the laser light reflecting off of the glass or frame interfering with measurements. The next best shape is the octagon. All sides of which are parallel to each other. It is now also possible to place a camera at a perfect right angle with the laser sheet and the glass windows.

A disadvantage of higher-order regular polygons is that the frame-to-window ratio becomes worse. The minimum frame size is fixed and determined by the size of the smallest bolts available. The width of the combustion chamber is therefore largely driven by the size of the windows. Larger windows are desirable as they allow for observation of a larger area. However, since the volume flow rate is limited a wider combustion chamber will also slow down the bulk flow velocity, increasing the difference between the jet velocity which might lead to an increase in recirculation in the chamber. Furthermore, a larger diameter of the mixing ducts is also not advantageous as this increases the outside surface area resulting in more heat loss in the ducts to the environment. A slower bulk velocity here also results in a larger residence time allowing for more heat to be transferred out of the flow.

The primary region of interest is the central jet of the combustor. Here the coflow gasses will be entrained, and the fuel-air mixture will be self-ignited. To determine the minimum size of the windows the maximum jet width in the region of interest should be determined. It was found that the spreading rate of a self-similar turbulent jet is linear. The spreading rate and velocity decay are even found to be completely independent of the Reynolds number [Pope, 2013]. The jet half-width $r_{1/2}$ can be computed using the empirical relation in Equation 3.1 [Panchapakesan and Lumley, 1993]. Where S is an empirically found constant, x_0 is the distance to the virtual origin, and x is the downstream distance from the jet exit. The virtual origin is the point where the linear jet width is predicted to be 0. However, since the jet spread is only linear in the self-similar region this virtual origin lays slightly downstream

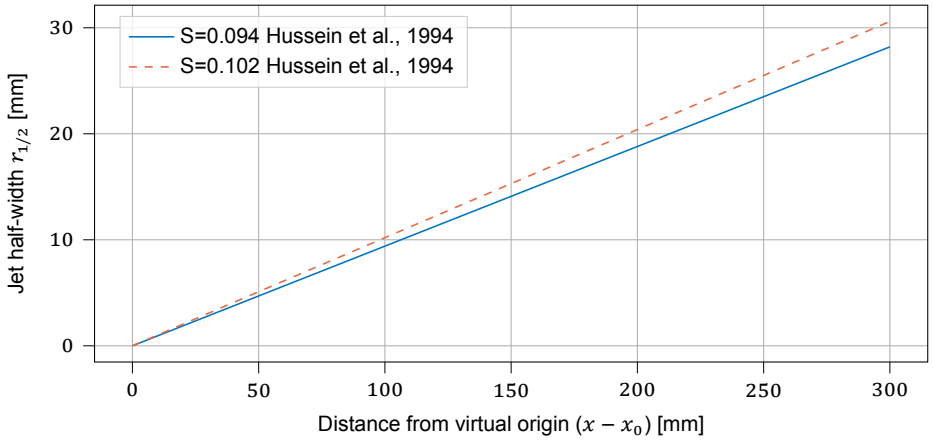

Figure 3.4: The jet width as predicted from Equation 3.1 for two different values of S as a function of downstream distance

from the jet exit plane. Pope, 2013 gives three values for S, the smallest one of 0.094 and the largest one of 0.102 are both from Hussein et al., 1994, with the first one obtained from hot-wire velocimetry and the second one from LDA. The value $S = 0.096$ found by Panchapakesan and Lumley, 1993 is in good agreement with the previous two values.

$$r_{1/2} = S\,(y - y_0) \tag{3.1}$$

The jet half-width is plotted for the maximum and minimum S as a function of the distance from the virtual origin in Figure 3.4. The maximum measurement height of other jet-in-hot coflow setups is $h/D = 70$ as seen in Table 3.1. With a jet diameter of 3mm this results in $h = 210mm$ for this combustor. Looking at Figure 3.4 the jet width is slightly over 20mm at this downstream location. With a window width of $40mm$, virtually the entirety of the jet is visible in the region of interest.

3.3.2. Foam disks

Since the coflow duct is relatively large the flow rate will be slow. The flow will likely be in the laminar domain. This is a problem, as in the mixing duct the flue gasses from the pilot burners should mix with the diluent gas. To aid in this foam disks will be placed in the tube. These foam disks will cause a pressure drop in the tube. This pressure loss is estimated in this section.

The pressure drop for an incompressible flow per meter of porous media can be obtained from Forchheimer's equation, given in Equation 3.2 [Innocentini et al., 1999]. In this equation, v_s is the fluid velocity, L the thickness of the porous medium, μ the viscosity and ρ the density. k_1 and k_2 are constants only dependent on the properties of the medium itself. The equations for k_1 and k_2 for a porous medium made of spheres, cylinders, etc. are given in Equation 3.3 and Equation 3.4 respectively, where ϵ is the porosity of the material and d_p the particle diameter. The foam disks do not contain loose particles but consist of a web-like structure. In literature, the particle diameter is often replaced by the pore, or cell diameter [Innocentini et al., 1999], which is often measured using enlarged photographs. The relation between the pore diameter and the particle size is shown in Equation 3.5, as defined by Innocentini et al., 1999

$$\frac{\Delta P}{L} = \frac{\mu}{k_1} v_s + \frac{\rho}{k_2} v_s^2 \tag{3.2}$$

$$k_1 = \frac{\epsilon^3 d_P^2}{150\,(1-\epsilon)^2} \tag{3.3}$$

$$k_2 = \frac{\epsilon^3 d_p}{1.75\,(1-\epsilon)} \tag{3.4}$$

$$d_p = 1.5 \frac{1-\epsilon}{\epsilon} d_c \tag{3.5}$$

The foam used in this combustor setup is a silicone carbide foam, with 30 pores per inch (PPI). The porosity of the material ϵ is 80%. The pore diameter is usually measured using enhanced photographs of the foam, but this data is not available for the obtained material. The cell diameter can be estimated using the porosity and the pores per inch. By assuming the variance in the pore diameter is small the pore diameter can be computed by calculating the average number of pores in a cube with sides of one inch. Then computing the average pore diameter using the porosity of the material. The formula for this is given in Equation 3.6.

$$d_c = \left(\frac{6\epsilon \left(25.4E-3\right)^3}{\pi \cdot ppi^3} \right)^{1/3} \tag{3.6}$$

Using Equation 3.6 to find d_c for the ceramic foam and then plugging this into the equations for k_1 and k_2 results in $k_1 = 1.14E-8m^2$, and $k_2 = 5.35E-4m^2$. In the mixing tube, the temperature will vary, but it is expected to be around 1200°C. At this temperature and atmospheric pressure, the air has a dynamic viscosity of $\mu = 52.06E-6Pa \cdot s$[Engineering Toolbox, 2003a]. The density at this temperature is $\rho = 0.240kg/m^3$. The flow velocity is very low in the mixing duct; it varies between about 0.4 - 2.7 m/s. Each disk is about 25mm in thickness, which results in a maximum pressure drop of ΔP = 0.0064 bar.

3.3.3. Mixing duct sizing

Ideally, the mixing ducts would have the same diameter as the combustion chamber, with the same shape. A hexagonal duct with this specific internal diameter would have to be welded, which is time-consuming. Cylindrical stainless steel or Inconel tubes are readily available at about the right size. The mixing duct should also be able to house the ceramic foam disks. The mixing duct should be long enough for the diluent and the flue gasses to become well-mixed. Since the flow rate is very low the flow will be laminar, which increases the length required. To generate some swirl in the flow the diluent will be introduced radially with an offset from the centre line of the mixing duct. An exact estimate of the required mixing length is hard to compute. Additionally, a longer mixing duct will increase the heat losses. Therefore, the mixing duct length is set at about 4 hydraulic diameters. This results in a length of 400 mm.

Three foam disks will be placed in the mixing duct to generate turbulence and enhance mixing. The easiest way to attach these disks is to place them between flanges. A small pocket can be created inside the flange to hold a foam disk. The mixing duct is split into two sections. The foam disks can then be placed between the coflow attachment and the bottom mixing duct, between the bottom and top mixing duct and between the top mixing duct and the combustion chamber.

Inconel tubes are available in nominal pipe sizes. Using an available standard pipe size reduces the price and manufacturing time required, as opposed to manufacturing octagonal ducts. Because the mixing tube is split into two sections it is possible to manufacture the coflow attachment and bottom mixing duct using a nominal pipe, and manufacturing the top mixing duct section in the same size as the combustion chamber. As the combustion chamber has an inner diameter of 120mm the closest available nominal pipe size is NPS 4, which has an outer diameter of 114.3mm [Engineers edge, 2020]. The wall thickness is 3.048mm, which results in an inner diameter of 108.204mm. A smaller as opposed to a bigger diameter is preferred since a smaller tube will have less surface area for heat to escape from.

To accommodate the diameter and geometry change between the bottom and top mixing duct the inside of one of the flanges will be machined to create a smooth transition from a circular inner diameter of 108.2mm, to an octagonal shape with an inner diameter of 120mm.

3.3.4. Central jet sizing

The reactants for the main burner flow through the central jet into the combustion chamber. The jet emanating from the tube then entrains the hot coflowing gasses causing the mixture to self-ignite. In literature, the Reynolds number of this jet has been shown to influence the flame as discussed in section 2.4. Ricou and Spalding, 1961 found that the ratio of the jet mass flow to the entrained mass flow to the central jet mass flow to be independent of the jet Reynolds number only above a Reynolds

Reference	Jet velocity [m/s]	Jet Re [-]	Jet T [K]	Jet composition	Jet D [mm]	Burner
Ye et al., 2016	44	10,000	413	59% Air 41% Ethanol	4.6	Adelaide
Medwell et al., 2008	17.5	10,000	**305**	C_2H_6	4.6	
Cabra et al., 2005	100	28,000	320	33% CH_4 66% Air 1% H_2	4.57	Cabra
Oldenhof et al., 2010	**68.21**	9,500	450	15% N_2 85% CH_4	4.5	Delft JHC
Arndt et al., 2012	100	13,000	**281**	Methane	2	DLR

Table 3.2: Central jet specifications from various combustor setups. The values in bold are calculated based on the information in the paper.

number of approximately 25,000. They found that the local mass flow rate in the jet is a function of the downstream location, as shown in Equation 3.7. In this equation $\dot{m}_{jet}$ is the central jet mass flow rate, K_1 the entrainment constant, M the excess momentum flux, ρ_1 the density of the surrounding gas and x the downstream distance.

$$\dot{m}_{jet} = K_1 x \sqrt{M \rho_1} \tag{3.7}$$

Unlike most other experiments conducted in jet-in-hot coflow setups in this combustor the fuel will be premixed. To achieve flameless conditions the reactants have to entrain a sufficient amount of diluents before the flame ignites. Mi et al., 2009 found that when the jet momentum was low higher temperature peaks and NO_x emissions were observed, as well as the flame becoming more visible. The authors found that when the jet momentum was above a combustor-specific critical jet momentum rate above which flameless combustion could be established. Above this jet momentum rate, the level of premixing does not greatly influence the flame in their setup. They also noted that this critical momentum rate is lower for premixed flames as compared to non-premixed flames.

In Table 3.3 some jet velocities, Reynolds numbers, jet diameters and jet composition for various setups are tabulated for reference. The values in bold are calculated based on the information available in the paper. In Figure 3.5a and Figure 3.5b the jet Reynolds number and velocity for a pipe with 3mm in diameter is shown as a function of the flow rate. Dimotakis, 2000 states that there is a fundamental difference in mixing behaviour between jets with a Reynolds number below and above 10,000. Below this point, the author states that the jet cannot be considered a fully developed turbulent flow. To maintain the fastest rate of entrainment and the fastest rate of mixing the jet Reynolds number should therefore be kept above this mixing transition Reynolds number. Assuming the jet reaches a temperature of about 300 degrees Celsius and a minimum flow rate of about 40 lnpm then the Reynolds requirement is met with a 3mm nozzle diameter. This is a similar size as the other setups shown in Table 3.2.

3.3.5. Material selection

To be able to ignite the flame in the combustion chamber the reactants have to be above the self-ignition temperature of the gas mixture. The gasses in the mixing duct will need to be sufficiently hot to ignite the central jet mixture. The walls of the combustion chamber, mixing ducts and central jet need to be able to withstand this heat. From the heat transfer calculations in chapter 5 the maximum expected wall temperature of the mixing duct is about 1350K, that of the central jet 1250K. The mixing duct will also be surrounded by a layer of insulation, while the central jet will be cooled with cooling air. The gas mixture in the coflow is hot and will contain oxygen and carbon dioxide which can oxidise the mixing duct and central jet cooling material [British Stainless Steel Association, n.d.].

Stainless steel alloys are made to withstand the temperatures required for this setup. These alloys contain high concentrations of chromium which when exposed to oxygen at high temperatures form a chromium-rich oxide (Cr_2O_3) layer which protects the underlying steel from oxidising [British Stainless Steel Association, n.d.]. Additionally, nickel had also been found to aid in increasing the material's

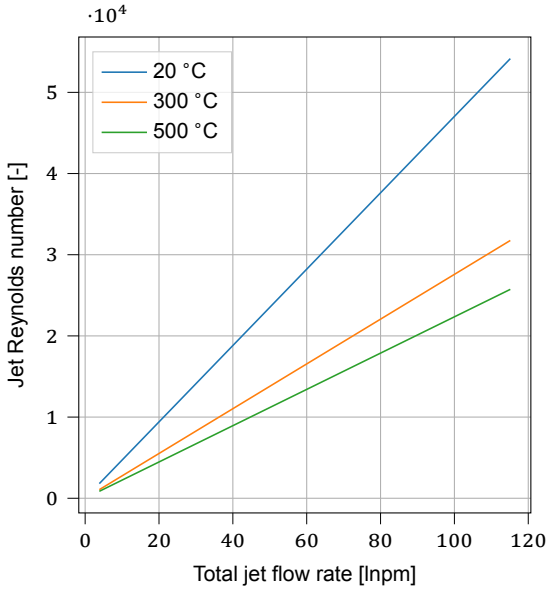

(a) Jet Reynolds number as a function of flow rate for a jet diameter of 3mm, at different jet temperatures.

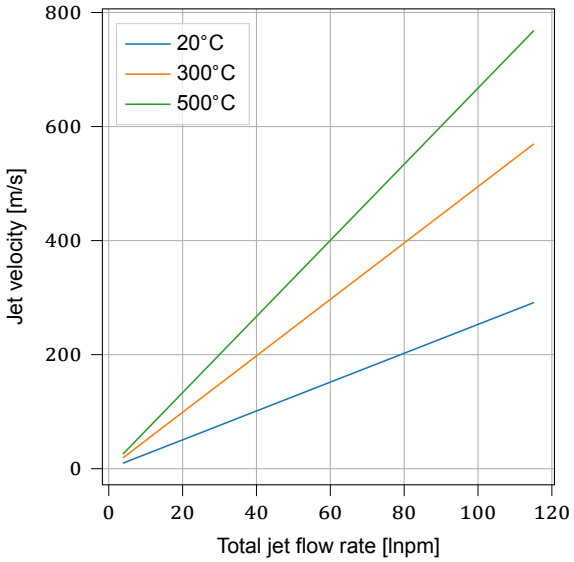

(b) Jet velocity as a function of flow rate for a jet diameter of 3mm, at different jet temperatures.

Figure 3.5

resistance to oxidising conditions at high temperatures. Stainless steel 310 has a high chromium concentration and therefore offers very good resistance to oxidation with a maximum temperature of 1150 $^{\circ}C$ for continuous service and 1035$^{\circ}C$ for intermittent service [AZO Materials, n.d.]. This difference in temperature is that the protective oxidative layer might crack during cyclic temperature changes, as will be the case for this combustor, which will then increase the rate of oxidation.

Another alloy able to withstand high-temperature oxidative environments is inconel. This is a nickel alloy with added chromium, which offers superior resistance to oxidation over stainless steel 310. Its maximum operating temperature is 1095 $^{\circ}C$ [Special Metals Corporation, 2008].

While Inconel offers a superior maximum operating temperature and resistance to oxidation it is more expensive and harder to obtain than stainless steel 310. From the heat transfer calculations, Inconel only seems required for the mixing duct. While stainless steel will suffice for the central jet and combustion chamber. The central jet can also be actively cooled so maximum temperature can be reduced by increasing the cooling rate if required. While the mixing duct will be placed under insulation to minimise heat losses. High-temperature resistance is thus more critical for the mixing duct, justifying the additional cost of Inconel 600.

3.4. Thermal Buckling calculations

As a metal heats up it will expand. If there is a temperature difference in the metal parts of the material will want to expand to different extents. This will cause internal stress and might lead the object to buckle and deform. In this section, the expected internal stress due to the temperature difference on the inside and outside of the setup will be calculated and compared to the calculated critical buckling force.

The formula for thermal expansion is given in Equation 3.8. With α being the linear thermal expansion coefficient, ΔT the change in temperature and L the length of the material. From thermal calculations, it is found that the temperature difference between the inside and outside of the combustor is about 8.5 kelvin. For stainless steel 310 the average linear thermal expansion coefficient between 200$^{\circ}C$ and 800$^{\circ}C$ is about 18.5 $\mu m/(m \cdot K)$ [thyssenkrupp Materials Ltd, 2017]. The length of the material is 366mm. From this, the difference in thermal expansion is 5.8E-5 m. The stress this causes is then calculated with Equation 3.9. The Young's modulus of stainless steel AISI 310 is 200 GPa [Heanjia Super-Metals Co. Ltd, n.d.]. The stress obtained is then 11.51 MPa. The combustion chamber consists of eight panels, looking at the horizontal cross-section of each of these panels there are two

trapeziums on either side of the quartz panel. The force will be computed assuming these pillars transfer the force independently; in reality, they will be welded together and so will likely be more resistant to buckling. These trapeziums have an area of 5.4E-5 m^2, which results in a force of 0.62 kN due to thermal expansion.

$$\epsilon = \alpha \cdot \Delta T \cdot L \tag{3.8}$$

$$\sigma = E\epsilon \tag{3.9}$$

The formula for the critical buckling force is shown in Equation 3.10 as taken from Megson, 2012. Here E is the Young's modulus of the material, I is the area moment of inertia, K is the clamping factor and L is the unsupported length of the beam. The panels will be welded on both sides and K is therefore equal to 0.5. The area moment of inertia for a trapezium is given in Equation 3.11 [Lemonis, 2020]. The trapezium has a side $a \approx 2mm$, a side $b \approx 7mm$ and a height $h = 12mm$, the area moment of inertia is, therefore, 5.81E-10 m^4. With an unsupported length of 366 mm, the critical force follows as 34.2 kN. The critical force is several times larger than the expected force, and therefore thermal buckling is not expected to occur. Additionally, this result for the critical force is likely an underestimation as it considers each panel independently. In reality, these panels will be welded together and will therefore likely be stronger.

$$P_{cr} = \frac{\pi^2 EI}{(KL)^2} \tag{3.10}$$

$$I_{xx} = \frac{h^3}{12}(3a + b) - \frac{(a + b)\,h}{2}\left(\frac{h}{3}\frac{(2a + b)}{(a + b)}\right)^2 \tag{3.11}$$

3.5. Insulation

Heat losses in the mixing duct should be minimised. To achieve this the mixing ducts will be isolated. Since the combustor gets very hot the insulation material should be able to withstand high temperatures and be flame resistant. Some materials used for insulation pose health risks to people when working with them. In particular, insulation containing ceramic fibres can be hazardous when disturbed, though they're often used in high-temperature applications [FNV, 2010]. When inhaled these fibers cannot be broken down quickly resulting in an increased chance of developing certain diseases like silicosis or certain types of cancer [FNV, 2010]. The insulation material chosen for the combustor is made from alkaline earth silicates. These fibres are not classified as carcinogenic and are therefore safe to use [Brown and Harrison, 2014]. AES fibres might undergo crystallisation under high temperatures above 900 $^\circ C$ which could produce potentially dangerous crystalline silica. However, experiments show that devitrified AES fibres are weakened allowing the body to clear the fibres if they end up in the lungs [Brown and Harrison, 2014] [RS Components SAS, 2020]. Additionally, only a very thin layer of the insulation material might be exposed to sufficiently high temperatures for devitrification to take place which means that the dust which could potentially be inhaled does not contain any detectable crystalline silica [RS Components SAS, 2020].

Five insulation blankets are ordered. The outside of the blankets is made from pumice, while the inside is made from AES. Two blankets will be placed around the two mixing ducts between the flanges. Two additional blankets will go over the flanges for the coflow attachment and the flanges between the two mixing ducts. These outer blankets will also cover the inner insulation blankets. An additional blanket is placed around the bottom combustion chamber flange as well. A photograph of the setup with blankets is provided in Figure 3.6a

3.6. Cooling

The combustor has two independent cooling systems. The exhaust gasses from the combustor are transported outside via a flexible hose, but this hose cannot handle high temperatures. Therefore, cooling air is mixed in at the exhaust just before the gasses enter the exhaust duct. This cooling air is injected radially through eight holes each 8mm in diameter in the flange above the combustion chamber. As will be discussed in subsection 3.6.1 the bend in the exhaust tube results can have effects on the flow

field inside the combustor, additionally the cooling air should not entrain into the combustion chamber as this would defeat the purpose of having an enclosure. For these reasons, a pressure drop is induced between the combustion chamber and the exhaust duct, by reducing the area of the exhaust. This will isolate the two sections and prevent cooling air from flowing upstream. An abrupt change in diameter might create unwanted flow structures inside the combustion chamber so this change is made gradual using a conical exhaust. Two concentric cones are used; the exhaust gas flows through the inside of the first cone. The cooling flange with radial holes is placed on top of the first cone, on top of which the outermost cone is placed. In Figure 3.6b the concentric cone structure can be seen. The cooling air thus flows between the two concentric cones, and will then mix with the exhaust at the top of the cone.

The central jet is also cooled with air. The aim is to keep the fuel-air mixture cold enough not to ignite in the central jet, and maintain a constant temperature of the central jet gasses between experiments. The main reactant pipe is placed at the centre, and around this two concentric pipes are placed. Inside the inner pipe, air will flow up next to the reactant tube. This is to keep the reactants at the lowest temperature. At the top the air will move to the outer pipe and will flow down, cooling the outer cooling jacket. The cooling air then exits the combustor at the bottom. The fuel pipe has an inner diameter of 3 mm and an outer diameter of 5mm. The inner cooling pipe has an inner diameter of 8 mm and an outer diameter of 12mm. This leaves 3mm of space for cooling air to flow around the central fuel line. An attachment is made on this tube for cooling air to enter into the space between the fuel pipe and this pipe. The outer cooling jacket has an inner diameter of 26 mm and an outer diameter of 30mm. The fuel pipe is not cooled for the entire length of the mixing duct. It is unprotected for about 90mm to prevent vortexes from forming around the cooling structure and interfering with the flame in the combustion chamber. Furthermore, the top of the cooling jacket is a conical section with an angle of 8 degrees. This makes the transition in diameter from the cooling jacket to the unprotected fuel pipe smooth.

The entire central jet cooling assembly is welded together onto a plate at the bottom. This plate has an attachment for the cooling air to exit. The plate is bolted onto the coflow attachment at the bottom of the mixing ducts. The entire cooling assembly can thus be replaced without requiring a new coflow attachment to be built.

3.6.1. Exhaust upstream influence

Particle image velocimetry (PIV) will be applied in this setup. This means the system will be seeded with titanium oxide particles, which can block the ATEX exhaust system installed in the lab. A flexible duct will therefore be connected to the exhaust side of the setup. This duct will bend in one direction which has shown in previous experiments to influence the upstream flow conditions in the combustion chamber. In order to isolate the combustion chamber from the flexible duct a cone will be placed between the cooling flange and the combustor exhaust flange. The pressure drop over this cone needs to be sufficiently large, at least a couple of millibars.

The pressure drop is modelled by assuming the cone acts like an orifice plate, Equation 3.12 gives the pressure drop of over an orifice [Miller, 1996]. C_d is the discharge coefficient, β is the ratio between the hole diameter and the tube diameter, and ρ and $\dot{m}$ are the density and mass flow rate respectively.

$$\Delta P = \left(\frac{\dot{m}}{\frac{C_d \cdot A_2}{\sqrt{1-\beta^4}}} \right)^2 \frac{1}{2\rho} \tag{3.12}$$

Several flow conditions are considered. The pressure drop should be sufficiently high when using the system at the lowest possible setting as computed by the heat transfer model in chapter 5. Selecting a hole size of 15mm, and a discharge coefficient of $C_d = 0.6$ results in a pressure drop of 3-119 mbar. Selecting a hole size of 20mm results in a pressure drop of 1-38 mbar. A 15mm hole in the orifice plate results in a higher pressure drop under minimal flow rate conditions and is therefore better. If the pressure drop under high flow conditions turns out to be too high during experiments the hole size can always be increased.

3.6.2. Cone cross-section check

Since the cooling air has to flow between the two cones there should be enough space for the flow not to choke. To check if there is enough room for air the flow between the outside of the cone and the

cross-sectional area between the cone and the wall of the cooling flange has to be computed.

$$A_{octagon} = 2D^2\left(\sqrt{2}-1\right) \tag{3.13}$$

Both the inner and outer cones have an angle of about 15 degrees. The gap at the centre of the hole between the flange and the inner cone is $t_t = 12 \cdot 10^{-3} \tan(15)$. The flow area in the annulus between the cooling flange inner wall and the inner cone is computed with $A_{outer\ octagon} - A_{inner\ octagon}$, where the area of the octagon is computed from the diameter D using Equation 3.13. From this, the area is found to be $1.244 \cdot 10^{-3} m^2$, which is larger than the combined area of the inlet holes in the cooling exhaust of $0.4 \cdot 10^{-3} m^2$. The inlet is thus still the limiting factor. As the air leaves the inlet hole it needs to spread around, to check if there is enough area for this we should check if the flow is able to get away from the hole. At the top the distance between the cooling flange and the inner cone is $t_t = 16e - 3\tan 15 \approx 4.3mm$. The area right above the hole is thus about $8 \cdot 4.3 = 34.4mm^2$. The gap at the bottom of the hole is $t_b = 8e - 3\tan 15 \approx 2.1mm$. The area on either side of the hole is thus $\frac{8(4.3-2.1)}{2} + 8 \cdot 2.1 \approx 25.6mm^2$, the total area the flow to flow through on the side and on top is $25.6 \cdot 2 + 34.4 = 85.6mm^2$, this is much more than the area of one inlet hole of $50.27mm^2$. This thus also does not limit the flow of cooling air. There is a sufficiently large area in the gap between the cone and the cooling flange for the cooling air to flow.

3.7. Equipment

Table 3.3 shows an overview of the mass flow controllers installed in the combustion lab with their minimum and maximum flow rates. The left-hand side of the table shows the design flow rate range.

Purpose	Min [lnpm]	Max [lnpm]	Flow controller	Min [lnpm]	Max [lnpm]
Main Air	14.04	42.13	FCV-012	10	500
Main Fuel	1.83	3.65	FCV-013	1.76	85
Pilot Air	16.85	134.8	FCV-005	10	500
Pilot Fuel	1.83	14.61	FCV-014	1.76	85
Diluent	20.22	111.97	FCV-008/ 003	20	1000
Cooling Exhaust	N/A	N/A	FCV-001	300	15,000
Cooling Central Jet	N/A	N/A	FCV-011	60	3000

Table 3.3: Flow rates for the baseline measurements, with selected mass flow controllers and their min max flow rates

The setup will also be equipped with various thermocouples, an overview of the data acquisition equipment is tabulated in Table 3.4. The thermocouples are used to monitor the temperature of the setup for safety and control and some will be used for data collection. The thermocouples on the central jet cooling line and fuel line will serve a dual purpose; they will be used to monitor the central jet temperature and they will be used to validate the heat transfer model. Two thermocouples will be placed on the outside to monitor the material temperature. One on the coflow attachment and one on the bottom mixing duct, the hottest parts of the combustor. In case the material gets too hot a safe shutdown can be performed before any permanent damage is caused. A flexible duct is attached to the exhaust of the combustor. This tube cannot get too hot. Therefore, cooling air is mixed into the exhaust flow. A thermocouple will be used to monitor this temperature and in case it gets to hot increase the cooling flow rate. Finally, an S-type thermocouple will be inserted into the combustion chamber to take measurements of the flame temperature.

ID Nr	Quantity	Sub component	Component	Material
1	1	Cooling Flange	Cooling Flange	Stainless steel 310
2	1	DN150 Octagonal Flange	Combustion chamber	Stainless steel 310
3	8	Combustor frame		
4	1	Thin octagonal flange		
N/A	8	Windows		Quartz
5	1	Thick octagonal flange	Octagonal mixing duct	Inconel 600
6	8	Octagonal duct plate		
7	1	Circ to octagonal flange		
8	2	Thick circular flange	Cylindrical mixing duct	Inconel 600
9	1	Duct		
10	1	Coflow attachment	Coflow attachment	Stainless steel 310
11	1	Cooling exit	Jet cooling assembly	Stainless steel 310
12	1	Cooling jacket		
13	1	Cooling channel		
14	1	Fuel pipe		
15	8	Window plate	Window plate	Stainless steel 310
16	1	Inner cooling cone	Inner cooling cone	Stainless steel 310
17	1	Outer cooling cone	Outer cooling cone	Stainless steel 310

Table 3.5: Overview of the components and sub-components of the combustor that will be produced.

Description	max. T [K]	Placement	Type	ID	Purpose
Cooling air inlet	300	Into Gas	K-type	TC-CJ-IN	Data
Cooling air exit	600	Into Gas	K-type	TC-CJ-OUT	Data
Fuel line inlet temperature	300	Into Gas	K-type	TC-MF-IN	Data
Fuel line exit temperature	600	Into Gas	K-type	TC-MF-OUT	Control/ Data
Coflow temperature	1500	Into Gas	K-type	TC-CO	Control/ Data
Coflow Attachment wall temperature	1500	Material	K-type	TC-WAL-1	Control
Mixing Duct wall temperature	1500	Material	K-type	TC-WAL-2	Control
Combustion flow temperature	1700	Into Gas	S-type	TC-COMB	Data
Combustor exit temperature	1000	Into Gas	K-type	TT-005	Control
Gas analyser	1500	Into Gas	N/A	GA-001	Data

Table 3.4: Overview of DAQ placement and purpose

Furthermore, two Honeywell-Kromschröder pilot burners of the model ZMI-16B200R are used to produce the hot flue gasses. This burner can produce 1 to 2 kW of power with natural gas according to its specifications, but from experience, the operational limit can be pushed to at least 4 kW per burner. These burners are inserted at the bottom of the combustor setup in the coflow attachment.

In Table 3.5 an overview of all components that will be produced is shown. The coflow attachment at the bottom of the combustor is the part where the pilot burners, central jet cooling assembly and the pipes for added N_2/ CO_2 will be connected. An overview of the entire combustor assembly is shown in Figure 3.6b with bubbles corresponding to the ID numbers in the table. The engineering drawings for each of these parts are also provided in Appendix D. The ID numbers in Table 3.5 and Figure 3.6b are written in parenthesis behind the part name on the engineering drawings. The size and shape of the components of the setup are listed in Table 3.6.

The process and instrumentation diagram for the entire setup and its interface with the lab is provided in Appendix C.

Component	Shape	Inner diameter [mm]	Height [mm]
Combustion chamber	Octagonal	120	395 (windows: 300)
Top mixing duct	Octagonal	120	199
Bottom mixing duct	Cylindrical	108.2	260
Coflow attachment	Cylindrical	108.2	69

Table 3.6: Sizes and shapes of certain components of the enclosed jet-in-hot-coflow setup.

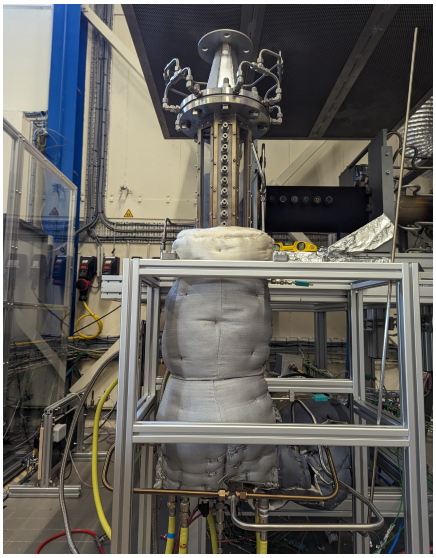

(a) Photograph of the fully assembled combustion setup with insulation blankets around the mixing ducts

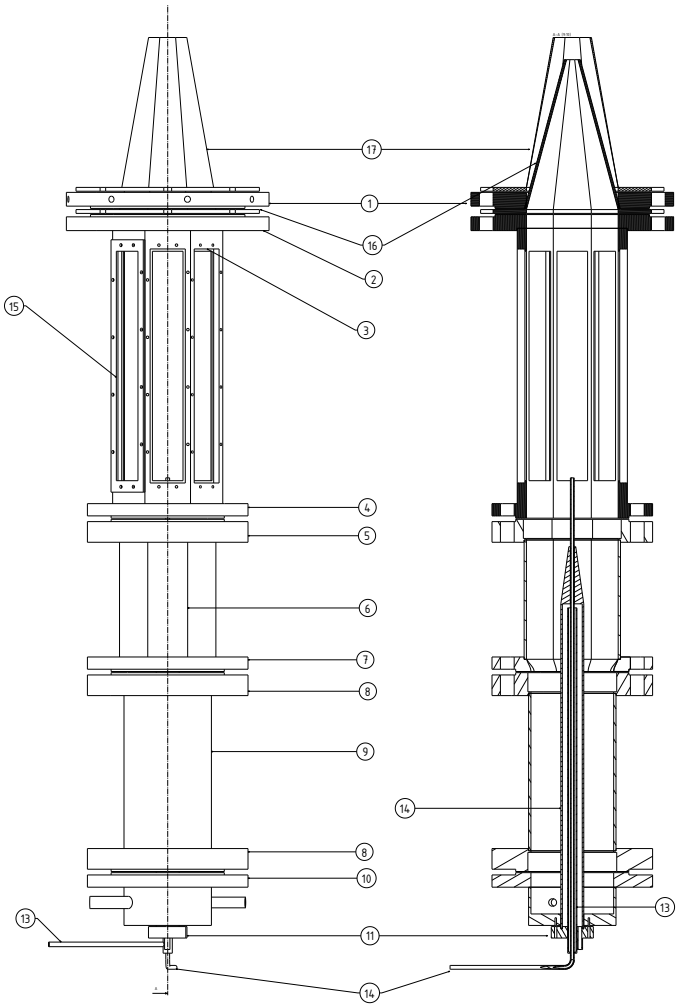

(b) Full combustor assembly with ID numbers

Figure 3.6

4

Dilution flow rate calculation

In this chapter, the calculation for the flow rates is explained. The diluent is a combination of the exhaust of the pilot burner the added diluent and the nitrogen from the air being added in the central jet. The objective is to achieve similar concentrations of gasses at different equivalence ratios and oxygen concentrations. In section 2.4 the various ignition behaviours observed at different oxygen concentration was discussed. The goal of the experimental campaign is to operate in both the mild domain and the transitional domain as described in Figure 2.6. Ideally, one would change one parameter without affecting the others. Unfortunately, the oxygen concentration, pilot burner power, equivalence ratio, coflow temperature, added diluent flow rate, and main burner power and equivalence ratio are all connected. For example, when changing the equivalence ratio the oxygen concentration will also change, changing the diluent flow rate changes the temperature. There are several strategies considered to maintain similar operating conditions between cases. In Table 4.1 an overview is given of the considered operating options.

4.1. Considered operating strategies

Fixed pilot	The pilot burner exhaust is a fixed percentage of the total coflow + oxidiser composition
Fixed added diluent	The added diluent (CO_2 or N_2) is a fixed percentage of the coflow + oxidiser composition
Pure oxygen as oxidiser	Instead of air pure oxygen is used as the oxidiser. This eliminates the nitrogen from the oxidiser in the coflow
Pilot as a percentage of diluent	The pilot burner exhaust is a fixed percentage of the diluent excluding the N_2 in the air
Fixed coflow and central jet flow rate	The total volume flow rate in the coflow and central jet are fixed, any changes to the central jet equivalence result in a different power setting, and any changes to the diluent change the pilot burner operating settings.

Table 4.1: List of evaluated options for flow rates

In the fixed pilot case the pilot burner flue gasses make up a fixed percentage of the total gas mixture. This is advantageous since the mixing temperature of the coflow and the central jet will remain very similar when altering the oxygen concentration by altering the diluent flow rate. The disadvantage of this strategy is that the composition of the coflow will not remain the same when the oxygen concentration is changed. The pilot burner will have a fixed equivalence ratio, so the exhaust of the pilot burners will not provide oxygen for the central jet to burn, additional air is therefore added to the coflow. This air contains nitrogen and so with a change in oxygen concentration by altering the total diluent flow rate the ratio of nitrogen from the air and the extra added diluent will change.

Alternatively, pure oxygen can be used. This would result in a constant coflow composition, but this would require major changes to the combustion lab so this is not really an option.

The added diluent flow rate can also be fixed, but this would be even less favourable. The mixing temperature would change and the coflow composition would still change.

Keeping the pilot burner as a fixed percentage of the diluents excluding the nitrogen in the air would also change the coflow composition, but then the ratio of radicals in the flue gas to the inert added diluent would remain the same. In the previous examples, it was considered that the air for the main burner would be mixed into the coflow, but it is also possible to mix it in the central jet. This would remove the issue of changing coflow conditions completely. For the initial design of the combustor, this option was chosen. With the central jet being premixed. The heat transfer calculations presented in chapter 5 were computed using this strategy as well.

In this case the main burner power is fixed at a specified power, and the equivalence ratio varied. The flow rate of diluents is then computed based on the specified oxygen concentration and the flow rate of air for the main burner. Now the flow rate of flue gasses is set at a fixed percentage of the diluent flow rate (excluding the nitrogen in the central jet), and the rest of the coflow is made up out of the added diluent, either N_2 or CO_2. The pilot burners will operate at an equivalence of 1.0, from this combined with the total flue gas flow rate the pilot burner fuel and airflow rate can be computed.

In the end, as shall be discussed in chapter 7, this strategy would not work out. During commissioning the heat transfer out of the mixing duct was much higher than predicted by the heat transfer model. Adding any inert diluent greatly reduced the operating temperature. Operating with a constant added diluent rate is not an option. Additionally, the pilot burners were less flexible than originally anticipated. They operate outside of their design maximum power setting and thus are very susceptible to blow-off when the equivalence ratio was changed. They were found to be most stable at a range of 0.87 to 0.99. Operating at stoichiometry is thus also not an option as initially planned. Therefore a new operating strategy was created, which will be discussed in the next paragraphs.

4.2. Employed operating strategy

NO_x formation is a very slow process therefore the time the gasses send in the combustion chamber greatly influences the NO_x concentration [Warnatz et al., 2006]. In the other scenarios discussed the jet and coflow velocities would change depending on the central jet equivalence ratio and the requested oxygen concentration. This would have resulted in varying residence time, which would have made comparing the NO_x concentration between cases difficult. In the commissioning campaign and the second campaign that followed after it was decided to keep the central jet and coflow normal volume flow rate constant. The power in the central jet would not remain constant anymore but will increase with increasing equivalence ratio. There might still be a slight difference in jet velocity due to a difference in heat capacity and expansion between air and methane, but this difference will be small. When a diluent is added to the coflow the flue gas flow rate has to be reduced. To maintain a constant oxygen concentration the pilot burner equivalence will be changed when diluent is added.

$$CH_4 + \frac{2}{0.21\phi}\left(0.21O_2 + 0.79N_2\right) \rightarrow 1CO_2 + 2H_2O + \frac{2}{\phi}\frac{0.79}{0.21}N_2 + \left(\frac{2}{\phi} - 2\right)O_2 \tag{4.1}$$

The volume ratio of fuel to air is computed based on the central jet equivalence as shown in Equation 4.2. In Equation 4.1 the reaction of methane with air is shown for lean combustion. From this equation, it can be seen that the stoichiometric fuel-to-air ratio is $0.21/2$. The volume flow rate of air and methane can then be computed based on the set total volume flow rate as seen in Equation 4.3 and Equation 4.4.

$$\frac{\dot{V}_{main\ fuel}}{\dot{V}_{main\ air}} = \phi_{cj} \frac{0.21}{2} \tag{4.2}$$

$$\dot{V}_{air\ main} = \frac{\dot{V}_{cj}}{\left(\frac{\dot{V}_{main\ fuel}}{\dot{V}_{main\ air}} + 1\right)} \tag{4.3}$$

$$\dot{V}_{methane\ main} = \dot{V}_{cj} \frac{\dot{V}_{main\ fuel}}{\dot{V}_{main\ air}} \tag{4.4}$$

The oxygen concentration in the flue gasses $X_{O_2\ flue}$ can then be computed based on the specified oxygen concentration in the coflow $X_{O_2\ coflow}$, the total coflow volume flow rate $\dot{V}_{coflow}$ and the added diluent flow rate $\dot{V}_{diluent\ added}$ as shown in Equation 4.5. With this, the pilot equivalence ratio can be computed with Equation 4.6. The volume flow rate of pilot fuel and air is then obtained using the same equations as the main burner air and methane.

$$X_{O_2\ flue} = X_{O_2\ coflow} * \frac{\dot{V}_{coflow}}{\dot{V}_{coflow} - \dot{V}_{diluent\ added}} \tag{4.5}$$

$$\phi_{pilot} = \frac{2}{0.21} \frac{0.21 - X_{O_2\ flue}}{2 + X_{O_2\ flue}} \tag{4.6}$$

5

Heat transfer calculations

In the mixing duct the pilot burner flue gasses and the added diluent mix. The mixing duct is long to leave sufficient time for this to happen. The fuel and oxidiser for the main burner will flow through the central jet, which is placed in the centre of the mixing duct. To prevent the heat from the surrounding gasses from transferring to the fuel-air mixture a cooling jacket is placed around the central jet. The heat transfer from the coflow to the central jet and from the coflow to the surrounding air and metals need to be characterised to predict required cooling flows, expected maximum metal temperatures, and to predict the coflow temperature when it finally emerges in the combustor. In this chapter, the equations for this model are derived, and a sensitivity study of various parameters is presented.

5.1. The model

The schematic drawing in Figure 5.1 shows a cut-through of the mixing duct and cooling jacket. Each colour denotes a separate gas flow. In the centre, the premixed methane-air mixture flows through the central jet and is shown in green. Surrounding that cooling air flows through the cooling jacket, shown in blue. Finally, the area shown in orange is the hot coflow in the mixing duct. To make the formulation of a set of equations easier the 3 flows are split into 4 different tubes. Tube A is the coflow, tube B is the outer cooling duct in which the air flows downward in the cooling jacket, tube C is the inner cooling tube where the air flows upwards, and tube D is the upwards-flowing methane-air mixture of the central jet.

The cooling flow through the cooling jacket is similar to that of flow through a heat exchanger, however, an algebraic solution to the heat transfer equations is not readily available for this problem. In most heat exchanger problems radiation is disregarded, it might, however, be important to account for in this case due to the expected high wall temperatures and the high water and CO_2 concentration in the coflow. Convection and conduction are both linear equations so this problem can quickly be solved using linear algebra without requiring any kind of iteration. Radiation cannot be solved using linear algebra, besides the estimation of the emissivity and reflectivity of the gas mixture are dependent on the wall temperature, as will be discussed in section 5.4. To compute these values a good initial guess of the wall temperature can decrease the time required for convergence of the model. Solving the convection and conduction equations without radiation using linear algebra is computationally quite cheap. Outputs from this model can then serve as a good initial guess for the more complex model. The flow chart in Figure 5.2 details the complete process for solving the gas and wall temperatures. For the radiation model, the energy balance will be solved by using an iterative process.

5.2. The linear model

The tubes will be split up into streamwise segments each with a height of Δx. In each of these segments, the change in enthalpy in the flow is calculated based on the heat transfer from the walls of the ducts. In Equation 5.1, Equation 5.2, Equation 5.3 and Equation 5.4 the equations for the change in gas temperature is duct A, B, C and D is given, in which U is the combined heat transfer coefficient per unit area, P is the perimeter of the tube, and the subscript i refers to the segment number.

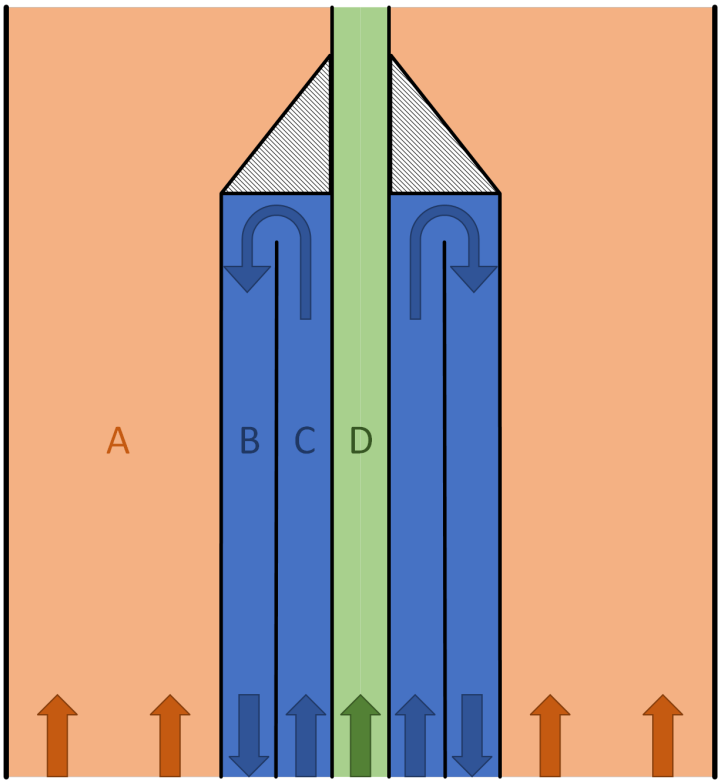

Figure 5.1: Schematic cut-through of the mixing duct, cooling jacket and central jet. (Not to scale)

$$C_{P_{coflow}} \cdot \dot{m}_{coflow} \left(T_{A,i} - T_{A,i-1}\right) = (U \cdot P)_{amb} \left(T_{amb} - T_{A,i}\right) \Delta x + (U \cdot P)_{AB} \left(T_{B,i} - T_{A,i}\right) \Delta x \tag{5.1}$$

$$C_{P_{air}} \cdot \dot{m}_{cooling} \left(T_{B,i-1} - T_{B,i}\right) = (U \cdot P)_{AB} \left(T_{A,i} - T_{B,i}\right) \Delta x + (U \cdot P)_{BC} \left(T_{C,i} - T_{B,i}\right) \Delta x \tag{5.2}$$

$$C_{P_{air}} \cdot \dot{m}_{cooling} \left(T_{C,i} - T_{C,i-1}\right) = (U \cdot P)_{BC} \left(T_{B,i-1} - T_{C,i-1}\right) \Delta x + (U \cdot P)_{DC} \left(T_{D,i-1} - T_{C,i-1}\right) \Delta x \tag{5.3}$$

$$C_{P,\ central\ jet} \dot{m}_{central\ jet} \left(T_{D,i} - T_{D,i-1}\right) = (U \cdot P)_{DC} \left(T_{C,i-1} - T_{D,i-1}\right) \Delta x \tag{5.4}$$

These equations are linear and can thus be converted into matrix form. Matrix A contains all the coefficients, T all the gas temperatures and C contains all constants. The size of matrix A is 4Nx4N, where N is the number of segments along the length of the mixing duct. positions 0 up to N are for tube C, positions N to 2N are for tube B, positions 2N to 3N are for tube D and finally positions 3N to 4N are for tube A.

$$[A][T] = [C] \tag{5.5}$$

$$A = \begin{bmatrix} a_{0,0} & \cdots & a_{0,3N-1} \\ \vdots & \ddots & \vdots \\ a_{3N-1,0} & \cdots & a_{3N-1,3N-1} \end{bmatrix} \tag{5.6}$$

$$T = \begin{bmatrix} T_{C,i} & \cdots & T_{C,N-1} & T_{B,i} & \cdots & T_{B,N-1} & T_{D,i} & \cdots & T_{D,N-1} & T_{A,i} & \cdots & T_{A,N-1} \end{bmatrix}^T \tag{5.7}$$

$$C = \begin{bmatrix} c_{0,0} \\ \vdots \\ c_{3N-1} \end{bmatrix} \tag{5.8}$$

$$a_{i,\ i-1} = \frac{-C_{P,air}\dot{m}_{cooling}}{dx} + (U \cdot P)_{BC} + (U \cdot P)_{CD} \tag{5.9}$$

$$a_{i,\ i} = \frac{C_{P,air}\dot{m}_{cooling}}{dx} \tag{5.10}$$

$$a_{i,\ N+i-1} = -(U \cdot P)_{BC} \tag{5.11}$$

$$a_{i,\ 2N+i-1} = -(U \cdot P)_{CD} \tag{5.12}$$

$$c_i = 0 \tag{5.13}$$

The boundary conditions need to be set for each tube; for tubes A, C and D the inlet temperature is given. For tube A the inlet temperature is defined based on the mixing temperature of the pilot burner and the diluent gasses. For tubes C and D the inlet temperature is assumed to be equal to the lab temperature. The boundary condition for tube B is set at the top of the mixing duct. The gas temperature at the end of tube C is equal to the temperature of the gas flowing into tube C.

$$a_{0,0} = 1 \,\&\, c_0 = T_{inlet} \tag{5.14}$$

$$a_{2N,2N} = 1 \,\&\, c_{2N} = T_{inlet} \tag{5.15}$$

$$a_{3N,3N} = 1 \,\&\, c_{3N} = T_{mixing} \tag{5.16}$$

$$a_{N,2N-1} = 1 \,\&\, a_{N,N-1} = -1 \tag{5.17}$$

The combined heat transfer and perimeter can be obtained from Equation 5.18 for concentric tubes [Mills, 2014]. The first and last parameters are the convection components on either side of the tube surface, while the middle term describes the heat transfer through the central tube. r_o and r_i refer to the radius of the tube, with the subscript o referring to the outer radius of the tube and the subscript i referring to the inner radius of the tube. The coefficient of convective heat transfer h must fist be calculated. This can be done using Equation 5.19, in which Nu is the Nusselt number, k the conductive heat transfer coefficient and D_H the hydraulic diameter. The Nusselt number is a function of the Reynolds number and Prandtl number, relations for the Nusselt number in a duct with either laminar or turbulent flow are given in Equation 5.20, Equation 5.21 and Equation 5.22, Equation 5.23 respectively [Mills, 2014].

$$\frac{1}{U \cdot P} = \frac{1}{h_{c,i} \cdot 2\pi r_i} + \frac{ln(r_o/r_i)}{2\pi k} + \frac{1}{h_{c,o} 2\pi r_o} \tag{5.18}$$

$$h = \frac{\mathrm{Nu} \cdot k}{D_H} \tag{5.19}$$

$$f = \frac{64}{Re_D} \qquad \text{for } \mathrm{Re}_D < 2300 \tag{5.20}$$

$$\mathrm{Nu}_D = 3.66 + \frac{0.065(D/L)\mathrm{Re}_D\mathrm{Pr}}{1 + 0.04\left[(D/L)\mathrm{Re}_D\mathrm{Pr}\right]^{2/3}} \qquad \text{for } \mathrm{Re}_D < 2300 \tag{5.21}$$

$$f = \left(0.79 \ln Re_{D_h} - 1.64\right)^{-2} \qquad \text{for } 10^4 < \mathrm{Re}_{D_h} < 10^6 \tag{5.22}$$

$$\mathrm{Nu}_{D_h} = \frac{(f/8)\left(\mathrm{Re}_{D_h} - 1000\right)\mathrm{Pr}}{1 + 12.7(f/8)^{1/2}\left(\mathrm{Pr}^{2/3} - 1\right)} \qquad \text{for } 3000 < \mathrm{Re}_{D_h} < 10^6 \tag{5.23}$$

The temperature can then easily be solved for by multiplying matrix C with the inverse of matrix A. This yields the gas temperatures in all four ducts. The wall temperatures can be computed using Equation 5.24.

$$[T] = [C][A]^{-1} \tag{5.24}$$

5.3. Natural convection

So far only forced convection has been considered. Natural convection occurs on the outside of the setup, as it can be assumed that there is no forced airflow in the lab. The magnitude of natural convection depends on the surface temperature, in the simple linear model a small dummy value was used in place of the natural convection for this reason. The book by Boetcher, 2014 gives a good overview of various relations for natural convection found in the literature for cylinders in different orientations. As is pointed out in the book experimentally defining the natural convection is difficult since it is hard to isolate the natural convection phenomena from other factors like radiative and conductive losses. The model by Kreith et al., 2011 reports the average Nusselt number of a vertical cylinder as given in Equation 5.25 for laminar Rayleigh numbers between 10^5 and 10^9. For turbulent flow, the Nusselt number is reported in Equation 5.26, for Rayleigh numbers between 10^9 and 10^{12}. The Rayleigh number can be found by multiplying the Grashof number with the Prandtl number. The Grashof number is the ratio of the buoyancy force over the viscous force, its formula is given in Equation 5.27[Çengel and Ghajar, 2015]; g is the gravitational acceleration, β the coefficient of volume expansion ($\beta = 1/T$ for ideal gasses), T_s is the surface temperature, T_∞ is the fluid temperature far from the surface, L_c the characteristic length and ν the kinematic viscosity of the fluid. The Nusselt number given by these formulas is the average over the entire length of the cylinder, therefore the Grashof number is defined based on the entire length of the cylinder as well.

$$Nu_L = 0.555\,(Gr_L Pr)^{1/4} \qquad \text{for } 10^5 \leq Gr_L Pr \leq 10^9 \tag{5.25}$$

$$Nu_L = 0.0210\,(Gr_L Pr)^{2/5} \qquad \text{for } 10^9 \leq Gr_L Pr \leq 10^{12} \tag{5.26}$$

$$Gr_L = \frac{g\beta\,(T_S - T_\infty)\,L^3}{\nu^2} \tag{5.27}$$

5.4. The combined radiation model

The initial model does not account for the effects of radiation on heat transfer between either the gasses and the walls of the tubes and between the walls. Gasses absorb and emit radiation at specific wavelengths, the absorptivity is very discontinuous and as such gasses can usually not be considered a grey body. However, for most engineering applications, where high precision is not required, reasonable results have been achieved by assuming gasses to be grey and calculating the emissivity and absorptivity based on an averaging process [Çengel and Ghajar, 2015]. The emissivity and absorptivity still depend on geometry, the temperature of the gasses and the gas composition. Not all gasses will be assumed to participate in the radiation exchange; O_2 and N_2 are assumed not to participate; while H_2O and CO_2 are assumed to participate. Hottel, 1954 created charts for the mixture of H_2O and CO_2 in non-participating gasses based on temperature, pressure and mean beam length.

$$\dot{Q}_{net} = \frac{\epsilon_s + 1}{2} A_s \sigma \left(\epsilon_g T_g^4 - \alpha_g T_s^4\right) \tag{5.28}$$

$$\alpha_{CO_2} = C_{CO_2} \left(\frac{T_g}{T_s}\right)^{0.65} \epsilon_{CO_2} \tag{5.29}$$

$$\alpha_{H_2O} = C_{H_2O} \left(\frac{T_g}{T_s}\right)^{0.45} \epsilon_{H_2O} \tag{5.30}$$

$$\alpha_{gas} = \alpha_{CO_2} + \alpha_{H_2O} \tag{5.31}$$

Since CO_2 and H_2O can only be found in the mixing duct, and the cooling channels only contain air, it is assumed that only the gas in the mixing duct radiates and absorbs radiation and the gasses in the cooling channels are assumed to be completely transparent. In the mixing, there will be both radiation exchange with the gasses and between the inner mixing duct wall and the outer wall of the cooling jacket. Inside the cooling channels, there will only be radiation transfer between each wall.

The radiation between two enclosed grey opaque surfaces 1 and 2 can be calculated based on the combined view factor and emissivity coefficient F_{12}. For two concentric infinitely long tubes the formula for this combined coefficient is given in Equation 5.32 Mills, 2014. The net energy transfer from wall 1 to wall 2 is then given by Equation 5.33.

$$F_{12} = \frac{\epsilon_1}{1 + \left(\frac{\epsilon_1 A_1}{\epsilon_2 A_2}\right)(1 - \epsilon_2)} \tag{5.32}$$

$$\dot{Q}_{rad,\,12} = \sigma A_{wall\ 1} F_{12} \left(T^4_{wall\ 1} - T^4_{wall\ 2}\right) \tag{5.33}$$

Since radiation is not linear the combined model cannot be solved using linear algebra. Instead for each section, the heat balance has to be solved. The enthalpy change of the gasses inside the tube needs to be equal to the heat transfer out of the fluid. For the outer coflow duct these include the convection to the outer coflow duct and the outer cooling jacket as well as the radiation transfer from the gas to both of these surfaces. For the flows in the cooling jacket and the fuel line, the only heat transfer from the fluid is through convection. The convection to the wall needs to be balanced with the conduction through the wall, the radiation between the walls and the radiation from the gas to the walls in the case of the coflow duct. The conduction through the wall then needs to be balanced on the other side of the wall with the convection and radiation heat transfer occurring on the other side of the wall.

$$C_P\,(T_{i-1} - T_i) - Q_{conv} - Q_{rad,\,gas} = 0 \tag{5.34}$$

$$Q_{cond} - Q_{conv} - Q_{rad,\,wall} - Q_{rad,\,gas} = 0 \tag{5.35}$$

By generating a set of equations and defining the relations between these equations they can be solved by a root-finding method. From the linear model, an initial guess based purely on conduction and convection was found. The same segments will be used to solve the heat balance in this model. Starting at the bottommost segment the temperature of the fluid and of the walls is found by utilising the modified Powell method as implemented in the SciPy function *scipy.optimize.root()*. This is done for each segment along the length of the mixing duct. Not all flows in the cooling duct flow upwards, the outer flow of the cooling jacket flows downwards. To know the temperature of this flow the temperature of the flow at the end of the inner cooling tube needs to be known which is also dependent on the temperature in the outer cooling jacket. Due to this dependency simply solving for the temperature in each segment from the bottom upwards is not enough, several iterations of this process will be required to obtain a fully converged temperature distribution. Additionally, the equations for the natural convection are based on the average wall temperature of the insulation along the entire mixing duct; to compute this average temperature the temperature in each segment also needs to be resolved. Convergence is set based on the change in the fuel temperature at the of the fuel tube between each iteration. If this difference between iterations is smaller than 10^{-5} the model is said to have converged. The schematic in Figure 5.2 shows this entire process.

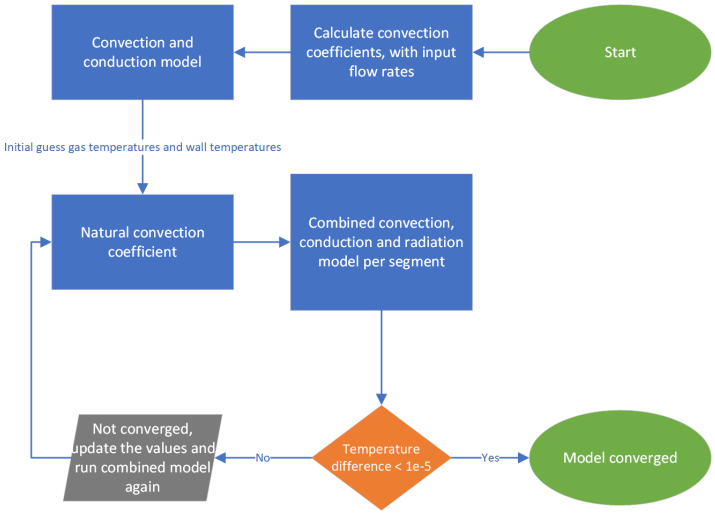

Figure 5.2: Flow chart of the heat transfer mode.

So far only the section of the mixing duct in which the fuel tube is protected by the cooling jacket is considered. However, the final segment of the cooling jacket is unprotected to prevent the coflow from separating at the end of the cooling jacket and to give time for any disturbances in the coflow to dissipate before reaching the combustion chamber. The coflow will lose some heat over this segment and the fuel mixture will become hotter, to get accurate predictions for the coflow and fuel mixture temperatures as they enter the combustion chamber the heat transfer equations should be solved for this final section as well. To simplify the model the conical section is ignored; it is assumed that the cooling jacket ends and after that, the central tube is unprotected from the coflow. Then the same approach is used for this part of the mixing duct as the other parts of the setup. However, so far the internal conduction parallel to the flow direction has been ignored. Due to this sudden change in heat transfer to the wall, there will be a jump in the wall temperature. To resolve this the internal conduction is also calculated, but only for the central fuel tube; it was most significant for this tube due to its large impact on the final fuel mixture temperature. Adding the internal conduction to the outer tube wall and insulation only resulted in a 3 K change in final coflow exit temperature but lead to a 10-fold increase in time to convergence.

$$\dot{Q}_{cond,\,top} = k_{steel}\pi\left(r_{out}^2 - r_{in}^2\right) * \left(\frac{T_{wall,\,out,\,i} + T_{wall,\,in,\,i}}{2} - T_{wall,\,i+1}\right)/dx \tag{5.36}$$

$$\dot{Q}_{cond,\,bottom} = k_{steel}\pi\left(r_{out}^2 - r_{in}^2\right) * \left(T_{wall,\,i-1} - \frac{T_{wall,\,out,\,i} + T_{wall,\,in,\,i}}{2}\right)/dx \tag{5.37}$$

$$T_{wall,\,i\pm1} = \frac{T_{wall,\,out,\,i\pm1} + T_{wall,\,in,\,i\pm1}}{2} \tag{5.38}$$

In each segment the internal conduction is calculated as coming from the bottom and top based on the average temperature in the other segment and this segment. The energy flow from the top is given by Equation 5.36 and the energy flow from the bottom segment is given by Equation 5.37, the average segment temperature is given by taking the average of the outer and inner wall temperature as shown in Equation 5.38.

5.5. Sensitivity analysis & verification

In order to verify the model and assess to which degree which parameter influences the model output a sensitivity analysis will be performed. In Table 5.1 all the input values for the model are tabulated. Many of these values are a function of temperature; however to simplify the model it was assumed that they are constant. For Air two different values are used, one for hot air as can be found in the coflow, and one for cold air which can be found in the cooling channels and the ambient air. Additionally, the gas composition influences these parameters, but since this is a simple first estimate model it is not

required, it is therefore assumed that the gasses in the coflow can be modelled as just regular air, and the gas in the central jet is pure methane.

Variable	Symbol	Value	Unit	Comments	Source
Conductivity of Stainless Steel	k_{steel}	24.5	$[\frac{W}{mK}]$	Steel 310 at 800 C	Engineering Toolbox, 2019
Conductivity of inconel	$k_{inconel}$	27.5	$[\frac{W}{mK}]$	Inconel 600 at 800 C	Special Metals Corporation, 2008
Conductivity of Cold Air	$k_{Air,\ Cold}$	2.81E-02	$[\frac{W}{mK}]$	Air at 50C	Engineering Toolbox, 2009
Conductivity of Hot Air	$k_{Air,\ Hot}$	8.11E-02	$[\frac{W}{mK}]$	Air at 1000 C	Engineering Toolbox, 2009
Conductivity of Methane	$k_{methane}$	3.45E-02	$[\frac{W}{mK}]$	Methane at 28C	Engineering Toobox, 2018
Conductivity of insulation	$k_{insulation}$	0.48	$[\frac{W}{mK}]$		RS, n.d.
Prandtl number of Cold Air	$Pr_{Air,\ Cold}$	0.7	[-]	Air between about 340K and 600 K	Engineering Toolbox, 2018a
Prandtl number of Hot Air	$Pr_{Air,\ Hot}$	0.74	[-]	Air between about 1000K and 1500K	Engineering Toolbox, 2018a
Prandtl number of methane	$Pr_{methane}$	0.725	[-]	Methane between 0C and 100C	Engineering Toolbox, 2018b
Kinematic viscosity Cold Air	$\nu_{Air,\ Cold}$	1.79E-05	$[m^2/s]$	Air at 50C	Engineering Toolbox, 2003a
Kinematic viscosity Hot Air	$\nu_{Air,\ Hot}$	1.73E-04	$[m^2/s]$	Air at 1000C	Engineering Toolbox, 2003a
Kinematic viscosity Methane	$\nu_{Methane}$	1.74E-05	$[m^2/s]$	Methane at 28C	
Emssivity of Steel	ϵ_{Steel}	0.69	[-]	Rolled 310	Special Metals Corporation, 2008
Emssivity of Inconel	$\epsilon_{Inconel}$	0.82	[-]	Inconel 600 at 980 C	Klein Tools, n.d.
Emissivity of the Insulation	$\epsilon_{insulation}$	0.6	[-]	Guess; No good data	
Emissivity of Coflow Gas	ϵ_{coflow}	0.095-0.045	[-]	Calculated using Hottel's method	Hottel, 1954
Heat capacity of air	$C_{P_{Air}}$	1.30E+03	[J/kg]		
Heat capacity of methane	$C_{P_{Methane}}$	2.23E+03	[J/kg]		

Table 5.1: Table of input parameters of the heat transfer model

In Table 5.2 the conductivity, Prandtl number, kinematic viscosity and emissivity of the different fluid and materials considered in the heat transfer model are shown. To assess the effect of these values on the model they are each individually increased by 10% and decreased by 10%, the change in the

maximum material temperature and the change in fuel tube exit temperature are then recorded. The response will be used to verify that the model responds in an expected way, and to assess how much each variable affects the model output.

			10% Increase			10% Decrease		
Variable	Units	Value	Value	ΔT_{max}	ΔT_{fuel}	Value	ΔT_{max}	ΔT_{fuel}
k_{steel}	$\left[\frac{W}{m \cdot k}\right]$	24.5	26.95	-89 mK	-41.7 mK	22.05	109 mK	32.9 mK
$k_{inconel}$	$\left[\frac{W}{m \cdot k}\right]$	27.5	30.25	-5.6 mK	-4.2 mK	24.75	6.8 mK	5.2 mK
$k_{Air,\ Cold}$	$\left[\frac{W}{m \cdot k}\right]$	2.81E-02	3.01E-02	-3.9 K	-1.6 K	2.5E-02	4.1 K	1.7 K
$k_{Air,\ Hot}$	$\left[\frac{W}{m \cdot k}\right]$	8.11E-02	8.9E-02	3.5 K	1.1 K	7.3E-02	-3.7 K	-1.2 K
$k_{Methane}$	$\left[\frac{W}{m \cdot k}\right]$	3.45E-02	3.8E-02	-28.1 mK	3.0 K	3.1E-02	32.2 mK	-3.6 K
$k_{insulation}$	$\left[\frac{W}{m \cdot k}\right]$	0.480	0.528	-6.4 K	-4.8 K	0.432	6.6 K	5.1 K
$Pr_{Air,\ Cold}$	[-]	0.7	0.77	-1.7 K	-0.61 K	0.63	1.9 K	0.67 K
$Pr_{Air,\ Hot}$	[-]	0.74	0.814	1.2 K	0.37 K	0.666	-1.2 K	-0.40 K
$Pr_{Methane}$	[-]	0.73	0.803	-15.7 mK	1.7 K	0.657	18.1 mK	2.0 K
$\nu_{Air,\ Cold}$	$\left[\frac{m^2}{s}\right]$	1.79E-05	1.97E-05	3.2 K	1.4 K	1.61E-05	-3.6 K	-1.6 K
$\nu_{Air,\ Hot}$	$\left[\frac{m^2}{s}\right]$	1.73E-04	0.00019	-1.1 K	-0.364 K	0.000155	1.3 K	0.413 K
$\nu_{Methane}$	$\left[\frac{m^2}{s}\right]$	1.74E-05	1.91E-05	22.4 mK	-2.5 K	1.57E-05	-24.0 mK	2.6 K K
ϵ_{Steel}	[-]	0.69	0.759	-7.3 K	6.6 K	0.621	7.5 K	-6.9 K
$\epsilon_{Inconel}$	[-]	0.82	0.902	5.2 K	0.54 K	0.738	-5.4 K	-0.59 K
$\epsilon_{insulation}$	[-]	0.6	0.66	-0.490 K	-0.515 K	0.54	0.536 K	0.571 K

Table 5.2: Variable sensitivity analysis at an operating condition of $\phi = 0.8$, $\%_{O_2} = 3\%$ and $T_{coflow} = 1593K$; ΔT_{max} is the change in maximum material temperature and ΔT_{fuel} the change in fuel mixture exit temperature.

A change in the metal conductivity of the stainless steel and the inconel have a very small effect on the final fuel mixture temperature or the maximum metal temperature. The wall thickness for all tubes is relatively small, the thickness of the mixing duct wall is 2mm, while the thickness of the walls inside the cooling assembly can be as small as 1mm, this means that the temperature difference between the inside and outside of these tubes is going to be quite small, so a 10% variation in conductivity does not change the temperature too much. The largest difference is observed when altering the steel conductivity. The cooling jacket assembly will be made from steel, so a variation in conductivity of this steel directly translates into how well it is able to cool the central fuel line, and interestingly also influences the material temperature of the mixing duct; the larger conductivity likely leads to a lower material temperature on the outside of the cooling jacket, which then results in larger radiative heat transfer from the inner wall of the mixing duct.

Variation of the gas conductivity has a larger effect on both the fuel exit temperature and the maximum material temperature. Looking at the formula for the convective heat transfer coefficient given in Equation 5.19 explains why; a 10% change in gas conductivity results in a change in 10% change in the convective heat transfer coefficient. A 10% change in air conductivity already results in a temperature difference of a couple of degrees kelvin. The air conductivity is specified separately for cold and hot air, where the cold value is obtained Using the same value for both the hotter and relatively colder air streams would thus affect the temperatures notably. As expected altering the methane conductivity influences the fuel exit temperature most significantly, whereas the maximum material temperature of the mixing duct only sees a small change.

Further as expected, an increase in the cold air conductivity results in a decrease in the maximum material temperature and fuel temperature due to the increase in cooling effectiveness, a 10% decrease in

conductivity has the opposite result. An increase in the hot air conductivity results in a higher material temperature and fuel exit temperature due to the increase in heat losses from the coflow to the wall and cooling structure/ fuel pipe. An increase in the methane conductivity leads to a decrease in the maximum material temperature and an increase in the fuel exit temperature; the increase in the convective heat transfer coefficient leads to an increase in heat transfer towards the methane very slightly cooling the mixing duct. Naturally, the conductivity of the insulation influences both the maximum material temperature and the fuel temperature most out of all the conductive heat transfer coefficients. An increase in conductivity leads to higher heat losses and therefore lower temperatures.

The Prandtl number can be found in the relations for the Nusselt number and thus influences the convective heat transfer coefficient indirectly but in a similar fashion to the gas conductivity; an increase in conductivity results in an increase in convection. However, the change in temperature is smaller than the change observed when altering the conductivity.

The kinematic viscosity also influences convection, but even more indirectly than the Prandtl number. The Reynolds number is a variable in the calculation of the Nusselt number for forced convection, the Reynolds number is a function of kinematic viscosity. For natural convection, the Grashof number is calculated using the kinematic viscosity. However, an increase in viscosity leads to a decrease in Reynolds and Grashof number and thus also a decrease in convective heat transfer. As expected the results in Table 5.2 reflect this; the sign of the temperature change is the opposite of that observed with the Prandtl and conductivity change. The order of magnitude change of the kinematic viscosity for hot air and for methane is similar to the corresponding Prandtl numbers. For cold air however, the order of magnitude is slightly larger and similar to the order of the gas conductivity. The cold air kinematic viscosity also influences the natural convection through the Grashof number in which the kinematic viscosity is squared resulting in a larger influence.

An increase in the emissivity of steel 310 results in an increase in heat transfer from the mixing duct to the cooling jacket, increased the radiation absorbed by the cooling jacket from the gas in the mixing duct and increases the radiation heat transfer internally in the mixing assembly; this is confirmed in Table 5.2 where a 10% increase of the emissivity leads to a -7.3K change in material temperature and an increase of 6.6K in the fuel exit temperature. An increase in Inconel emissivity also increases the heat transfer from the mixing duct to the cooling jacket and increases the heat transfer from the coflow to the mixing duct wall. The heat transfer from the gas to the wall seems to have a larger effect on the maximum wall temperature than the increase in radiation from the mixing duct to the cooling jacket as the maximum wall temperature increases by 5.2K. The Inconel emissivity has a smaller effect on the fuel exit temperature than the steel emissivity; the fuel exit temperature only increases by 0.54K. The insulation emissivity influences the temperature to a lesser degree as the other two emissivities due to the difference between the outer insulation temperature and the lab ambient temperature being small.

Most variables seem to have a small influence over the final fuel and material temperature, the maximum percentile change is 1.5% for the fuel mixture and 0.5% for the maximum material temperature. The metal conductivity does not have a great influence on the temperatures either due to the small wall thickness. Insulation conductivity does play a significant role. The gas conductivity also influences the temperatures due to its influence on the convective heat transfer. The hot and cold values for the conductivity, Prandtl number and kinematic viscosity have therefore been split into two different variables.

The behaviour of the model in response to alterations in the variables is in line with expectations as well. No behaviour was observed which might indicate the model was not properly implemented. Additional verification is done by comparing the heat loss over the boundary of the model as compared to the heat loss observed in the coflow. The enthalpy change in the cooling air in the cooling assembly plus the enthalpy change in the fuel line and the convection and radiation losses on the outside of the setup should be equal to the enthalpy change in the coflow. A difference of only 0.04% was found between the values, this small discrepancy can easily be explained by discretisation errors in the model.

In Figure 5.3a and Figure 5.3b the gas temperatures in the coflow and in the cooling assembly have been plotted along the length of the mixing duct. The dotted line is used for results from the combined radiation and convection model, while the solid line is used for results from the simpler convection model. T_A refers to the temperature coflow gasses, T_B is the temperature of the cooling air in the

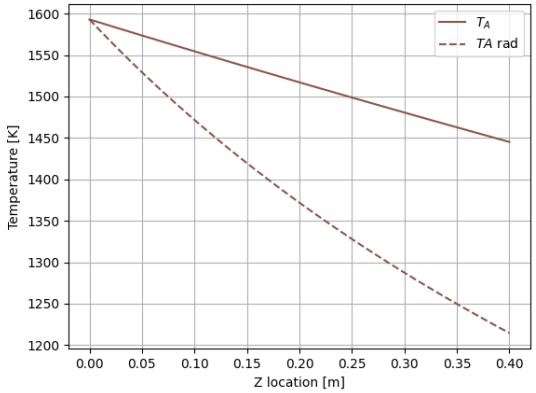

(a) Comparison between pure convection and combined model for the coflow

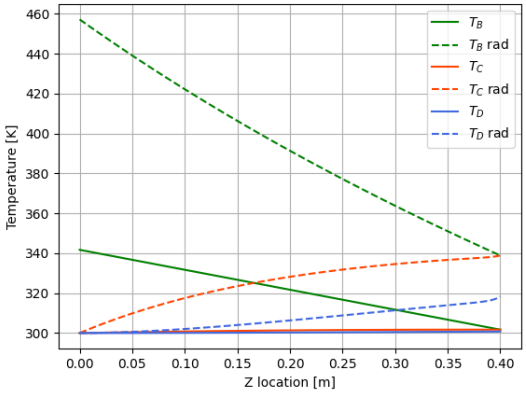

(b) Comparison between pure convection and combined model for the gasses in the cooling assembly

Figure 5.3: Comparison of convection and radiation heat transfer at ϕ = 0.8, $\%_{O_2}$ = 3% and T_{coflow} = 1593K

outer tube of the cooling assembly, T_C refers to the cooling air in the inner tube, and T_D refers to the methane-air mixture. Figure 5.1 shows a cut through of the assembly with the flow letters indicated fro visualisation. The linear model predicts a higher coflow temperature since it underestimates the energy loss in the coflow, the difference is almost 250 kelvin. The convection model also predicts a lower temperature for all gasses in the cooling assembly. The exit temperature of the outer cooling flow (T_B) is almost 120 kelvin higher in the radiation model. The convection model also predicts that the fuel mixture and the inner cooling flow only heat up a couple of degrees, however, the radiation model shows a clear increase in both these temperatures.

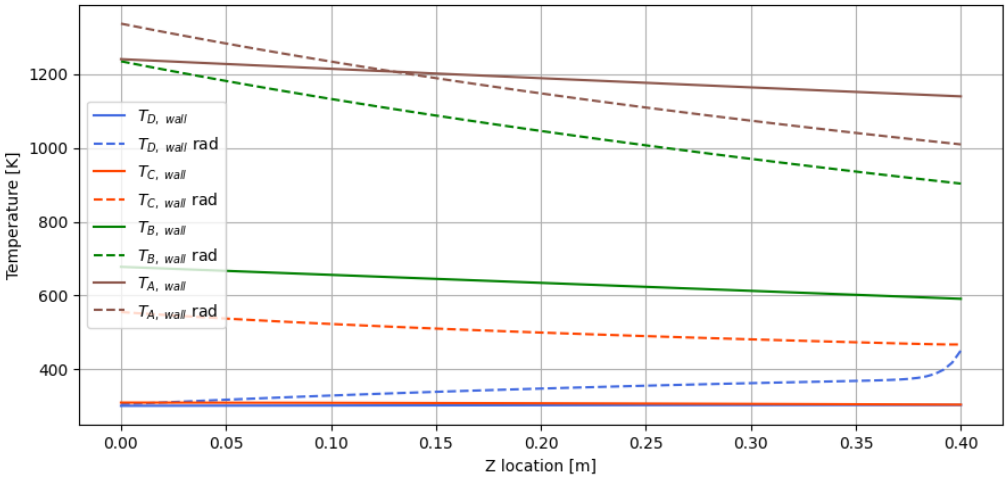

Figure 5.4: Comparison of the wall temperatures from the linear model and the radiation model. at ϕ = 0.8, $\%_{O_2}$ = 3% and T_{coflow} = 1593K

The diagram in Figure 5.4 shows the wall temperatures as obtained from the linear model with a solid line and the one obtained from the radiation model with dashed lines. In the cooling assembly, the wall temperatures are significantly higher than the radiation model, especially the outer cooling jacket wall is a lot hotter. Radiation from the mixing duct wall to the cooling jacket wall increases the wall temperature, additionally radiation from the coflow gas mixture in the mixing duct to the cooling jacket and the mixing duct increase both temperatures as well. Due to radiation heat transfer from the mixing duct wall to the cooling jacket, the mixing duct wall temperature is generally lower in the radiation model

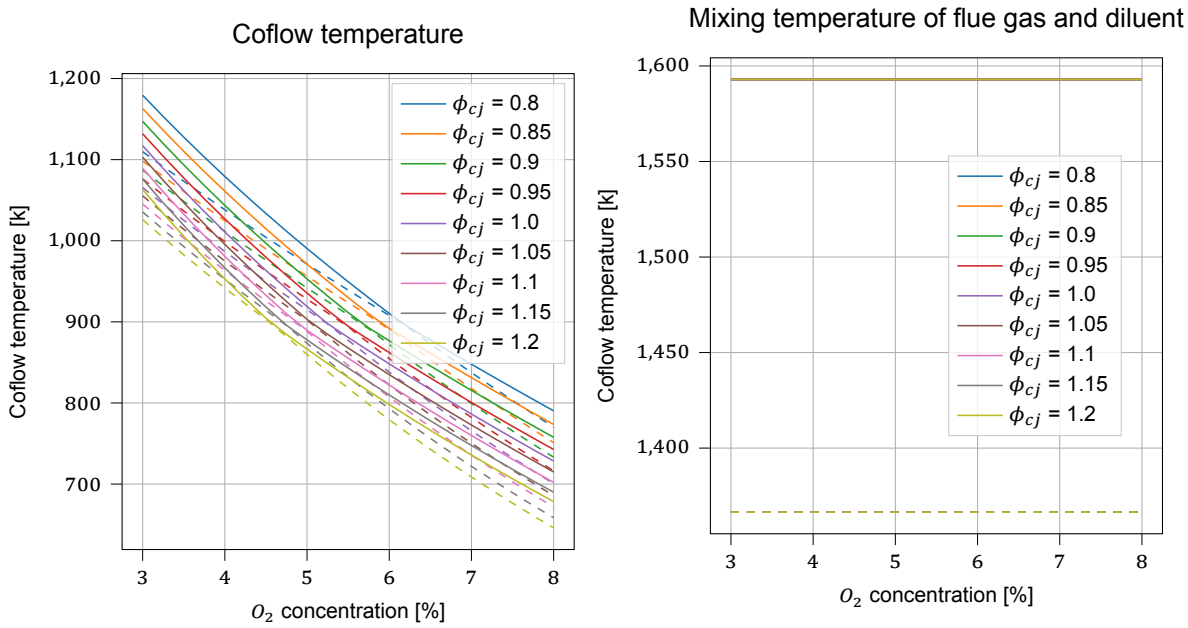

(a) Temperature of the coflow when it reaches the combustion chamber

(b) Mixing temperature of the pilot burner exhaust and the diluent.

Figure 5.5: The Dashed line is when CO_2 is used, the solid line is for N_2

than the linear model, but at the beginning of the mixing duct, the wall temperature is higher due to radiation from the flow to the wall.

5.6. Results

In Figure 5.5a the predicted temperature for the coflow when it enters the combustion chamber is shown as a function of the oxygen concentration. The solid line is for nitrogen, the dashed line shows the prediction when nitrogen is used. These predictions are made for the operating range in Table 5.3, where the pilot burner flue gasses are a fixed percentage of the coflow compositions. At a higher oxygen concentration, the flow rate of the coflow is lower, and therefore the power output of the pilot burners is also lower. In Figure 5.5b the mixing temperature of the pilot burner exhaust and the added diluent is shown. Since the pilot burner exhaust is a fixed percentage of the coflow mixture the temperature will remain the same regardless of the oxygen concentration. There is a significant difference in temperature between the nitrogen-diluted case and the carbon-dioxide-diluted case, but this difference is a lot smaller when it reaches the combustion chamber. The higher temperature of nitrogen drives a higher heat transfer rate, which results in a greater energy loss as compared to CO_2.

	Min	Max
Main power [kW]	2	2
Oxygen concentration [%]	3.0	8
Equivalence ratio [-]	0.8	1.2
Fraction pilot coflow [-]	0.58	0.58
Pilot equivalence [-]	1.0	1.0
Cooling central jet [lnpm]	186	186

Table 5.3: Operating conditions

In Figure 5.6a and Figure 5.6b the maximum material temperature for the mixing duct and for the outer central jet tube are shown. Both show a small change in temperature with a change in oxygen concentration. Likely due to differences in the predicted Nusselt number based on changes in the flow rate. Finally, the temperature of the quartz plates in the combustion chamber is computed and shown in Figure 5.7.

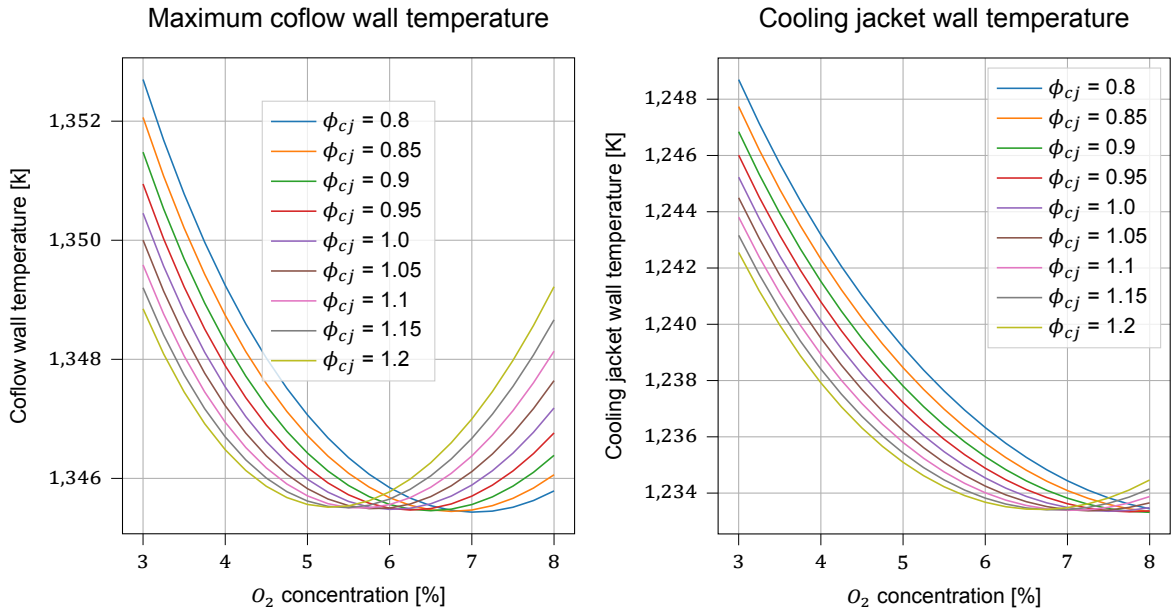

(a) Predicted maximum mixing duct temperature

(b) Predicted maximum cooling jacket wall temperature

Figure 5.6

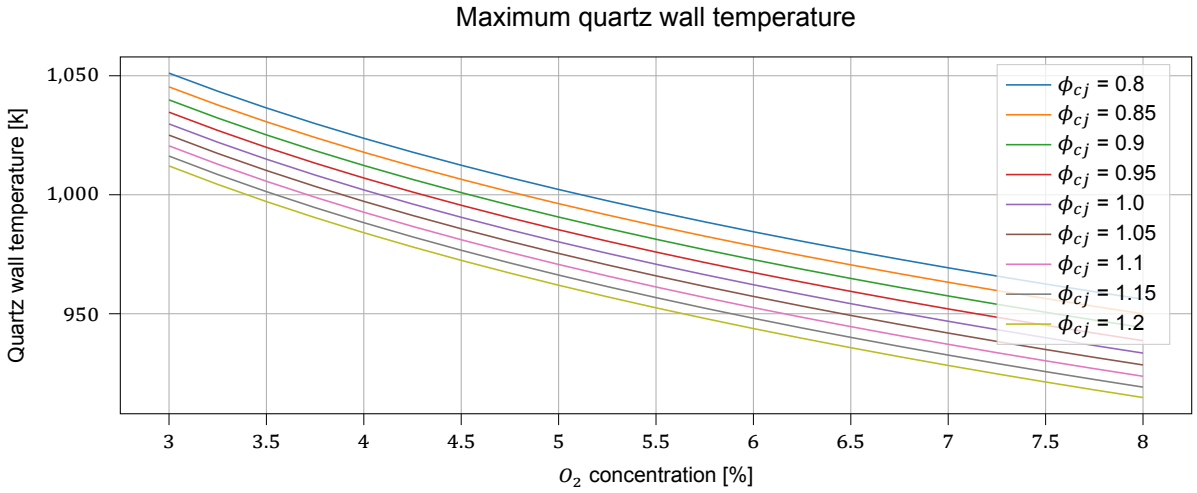

Figure 5.7: Predicted maximum quartz temperature in the combustion chamber.

The temperature of the walls is quite high. This indicates that high-temperature-resistant alloys should be used to manufacture these parts. The quartz temperature is a bit lower than the predicted maximum wall temperatures and falls below the maximum temperature for quartz glass of 1100°C [Shin-Etsu Quartz Products, n.d.]. The temperature of the coflow is a bit low. Only at low oxygen concentration is the coflow temperature high enough to get ignition.

In the end this model has a very large uncertainty, so the predicted coflow temperature might be higher or lower in real life. A major assumption in this model is that the flow is well-mixed at all times. Over the entire radius, the same temperature is assumed. In reality, the temperature profile will be parabolic. At the mixing duct wall and the cooling jacket wall, the temperature will be lower than in the centre of the duct. This will potentially result in a lower heat loss in the coflow. Additionally, internal heat transfer in the material of the mixing duct and the cooling jacket has not been taken into account. This might lower the maximum material temperature, but might also result in a lower coflow temperature as the temperature difference between the wall and flow will be higher. Additionally, any radiation coming from the pilot flame has been completely ignored. The predictions for the Nusslet number are also very uncertain. This model serves as an initial prediction for the conditions in the combustor, which will primarily be used to make design decisions. During the commissioning of the setup changes to the operational domain might have to be made. Furthermore, since the predicted material temperature is so high the wall temperature of the coflow attachment and of the mixing duct wall will be monitored to prevent them from being damaged.

6

Flow field characterisation

A series of cold flow tests were performed as part of the commissioning process. The aim of this experiment is to characterise the flow in the combustor. The flow coming out of the coflow needs to be uniform and well mixed. To verify this, stereo particle image velocimetry (SPIV) was applied in different configurations. In this chapter this experiment will be discussed by first looking at the theoretical background for PIV, then at the experimental objectives, the different PIV camera configurations used, and finally the results from the campaign will be presented and analysed.

6.1. Particle image velocimetry

By adding particles to the flow the flow direction and speed can be obtained from their displacement. PIV is a non-intrusive measurement technique which uses tracer particles, either added or already occurring in the flow, to capture the flow field. Unlike other velocimetry methods, like hot wire anemometry, no probe is inserted into the flow which otherwise might have caused disturbances. PIV can also capture a large area instantaneously. A PIV setup uses a laser sheet to illuminate these particles and one, or more, cameras to capture the state of the flow at two sequential times. The captured frames are then subdivided into smaller interrogation windows. The displacement is then obtained by analysing the average particle displacement inside this window, yielding a velocity vector.

If a single camera is used the out-of-plane velocity, or velocity component normal to the laser sheet plane, cannot be measured. Stereoscopic PIV solves this by using two cameras, using a similar method to how humans perceive depth. In this cold flow experiment, stereo PIV was used. Since the diluent is introduced into the mixing duct at an offset from the centre it might cause a small swirl to form. In the vertical viewing angles, this will be the out-of-plane velocity, which cannot be resolved using regular PIV.

6.1.1. Particles

The disadvantage of PIV is that it is an indirect measurement technique. The flow is not measured directly, but rather the effect of the flow on the particles. Therefore, care should be taken to make sure that particles are able to follow the flow in order to get accurate results [Raffel et al., 2007].

A major source of discrepancy between the flow and particle motion is due to a difference in the gravitational force caused by the difference in density between the flow and the tracer particles. By assuming the particles are spherical and in a viscous flow at low Reynolds number stokes law can be applied to the particles. Setting the stokes drag equal to the force of gravity due to the density difference yields the equation for the slip velocity in Equation 6.1 [Tropea et al., 2007].

$$V_{slip} = \frac{d_p^2 \left(\rho_p - \rho_f\right)}{18\mu} \frac{dV}{dt} \tag{6.1}$$

In which d_p is the particle diameter, ρ_p and ρ_f respectively the particle and flow density and μ the dynamic viscosity. The particle response to a sudden change in flow velocity follows an exponential

change in velocity. The relaxation time for a velocity change is shown in Equation 6.2, assuming $\rho_p >> \rho_f$ [Tropea et al., 2007].

$$\tau_p = d_p^2 \frac{\rho_p}{18\mu} \tag{6.2}$$

This equation is only valid for a constant deceleration is constant and stokes drag applies. If these assumptions cannot be made, the relaxation time becomes much harder to solve. This unit however still is a good metric for evaluating how well a choice of tracer particle follows flow deviations [Raffel et al., 2007]. The stokes number as given in Equation 6.3 is defined as the ratio of the relaxation time to the characteristic flow time scale [Tropea et al., 2007]. A tracer particle is said to have an acceptably short relaxation time if the stokes number is smaller than 0.1, resulting in an error smaller than 1%.

$$S_k = \frac{\tau_p}{\tau_f} \tag{6.3}$$

For the cold flow experiment DEHS oil was used. An approximation for the density of this oil is $\rho_p \approx 10^3 kg/m^3$, with a mean particle diameter of $1-3\mu m$ [Tropea et al., 2007]. Taking $\mu = 18.13e-6\ Pa\ s$ [Engineering Toolbox, 2003a], and assuming $1\mu m$ for the particle diameter then yields a response time of $\tau_p \approx 3.04\mu s$. For the flow time scale we can use the Kolmogorov time scale, the time scale of the smallest flow features in turbulent flow. The Kolmogorov time scale is defined in Equation 6.4 [Warnatz et al., 2006]. Where ν is the kinematic viscosity and ϵ is the turbulence dissipation rate.

$$\tau_f = \left(\frac{\nu}{\epsilon}\right)^{1/2} \tag{6.4}$$

Friehe et al., 1972 showed that the turbulence dissipation of a jet can be found with Equation 6.5, for a self-similar jet with a Reynolds range of $10^4 < Re_{jet} < 5 \cdot 10^5$ and a range for distance from the nozzle of $20 \leq x/D \leq 70$. In this equation U_j is the jet exit velocity, D is the jet diameter, c is a constant which is 48 and x is the distance from the nozzle.

$$\epsilon = \frac{U_j^3}{D} c \left(\frac{x}{D}\right)^{-4} \tag{6.5}$$

With a jet velocity of 111 m/s and a jet diameter of 3mm the turbulence dissipation at $x/D = 20$ is $\epsilon = 13.7 \cdot 10^4 m^2/s^4$. With a kinematic viscosity of air at $20°C$ of $\nu = 15.06e-6\ m^2/s$ the Kolmogorov time scale is found to be $\tau_f = 10.49\mu s$. With this, the stokes number can be found to be $S_k = 0.3$. This means that while it doesn't meet the criterion of 0.1 it is very close.

The tracer particles should also scatter a sufficient amount of light for them to be tracked. Spherical particles with a larger but similar diameter than the laser light wavelength can be assumed to undergo Mie scattering [Tropea et al., 2007]. The wavelength used by the laser is 532 nm, and the tracer particle size is about 1-3μm. The scattering behaviour of such particles can be determined by the Mie parameter q, as given in Equation 6.6 [Tropea et al., 2007]. In this equation, d_p is the particle diameter and λ is the laser light wavelength. When this q is larger than one peaks in the scattering intensity will start to form in different radial directions. In Figure 6.1 an example of a scattering function is shown. The largest peak is found at 180 degrees from the light, this is called forward scatter. A smaller peak forms at 0 degrees with respect to the light source, this is called backscatter. The smallest amount of scatter is found at about 90 degrees, this is called side scatter and is the angle most often used due to practical reasons [Tropea et al., 2007]. Ideally one would position their camera setup to take advantage of the forward scatter. The ratio between the forward and backward scatter also increases rapidly with increasing q.

$$q = \frac{\pi d_p}{\lambda} \tag{6.6}$$

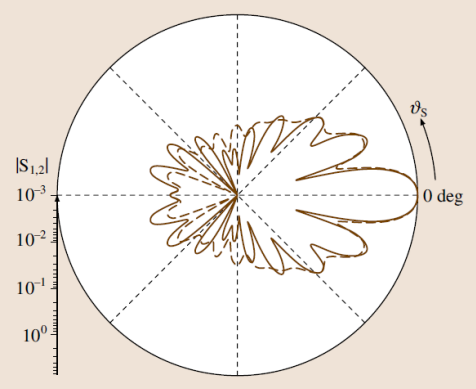

Figure 6.1: An example of a scattering function for a Mie parameter value of 10 computed for a water droplet in air. Data from Albrecht et al., 2003 image taken from Tropea et al., 2007

6.1.2. Laser

In PIV double pulsed lasers are used which produce two short pulses for the two successive frames to capture. The working principle of PIV requires that the flow is imaged twice with a small Δt. In each of these images, the particles should be illuminated for a short time to make sure the particles appear as dots and not stripes. For this reason, the laser needs to produce a pulse of time δt for which the criteria $\delta t \ll \frac{d_\tau}{vM}$ holds [Tropea et al., 2007]. Where d_τ is the particle diameter projected on the imaging sensor, M is the magnification and v is the velocity of the flow.

A thin sheet of light is created from the laser light using lenses. Spherical lenses expand or contract the light in all directions, and cylindrical lenses do this in one direction. The sheet should be a couple of mm thick usually in the order of 1% of the field of view width or height [Tropea et al., 2007]. The beam waist is the point at which the laser sheet is thinnest. In this region, the sheet thickness and energy density change the most rapidly. The waist should therefore not be placed in the field of view, ideally beyond the measurement region [Tropea et al., 2007]. The sheet profile needs to be as parallel as possible. This is even more important for stereo PIV with high out-of-plane velocities as a changing sheet thickness in the measurement domain means particles leave the laser sheet after different intervals in the domain.

6.1.3. Imaging & Timing

Imaging is usually performed with a digital sensor, either CMOS or CCD, and a lens to focus the light on the sensor. Two important parameters of the lens are its focal length f and its f-stop $f^\#$. The f-stop is defined as the focal length divided by the aperture diameter and is a measure of how much light is collected. The f-stop also influences the depth of field. With a higher f-stop resulting in a greater depth of field. Depending on the distance to the imaging plane and the focal length a value for image magnification M_0 is obtained. This is defined as the distance between the lens and the sensor (image distance Z_0) over the distance between the lens to the object (object distance z_0). The diameter of the imaged particle on the sensor d_τ can then be found using Equation 6.7. Here d_p is the particle diameter, and d_s is the diffraction-limited spot diameter. This is an optical effect which occurs when imaging very small or very distant objects. As light of one of these objects is captured a small so-called Airy disc is formed on the imaging plane with diameter d_s surrounded by diffraction rings with decreasing brightness. d_s can be found using Equation 6.8, in which λ is the wavelength of light from the laser [Tropea et al., 2007]. In practice, the value of the diffraction diameter is much larger than the diameter based on the magnification, so it is usually safe to assume that the imaged particle size is the same as the diffraction-limited spot diameter ($d_\tau \approx d_s$). This also means that variations in particle diameter are usually not very important and the imaged particles have a fairly uniform diameter.

$$d_\tau = \left(d_s^2 + M_0 d_p^2\right)^{1/2} \tag{6.7}$$

$$d_s = 2.44\,(1 + M_0)\,f^\# \lambda \tag{6.8}$$

The focal depth of the camera can be determined using Equation 6.9 [Tropea et al., 2007]. As can be seen from this equation the focal depth is lowest when the f-stop is in the lowest setting. For this

reason, focusing using the scheimpflug was performed at the lowest f-stop setting. Then when the entire FOV was in focus the f-stop was changed to the desired setting for measurements.

$$\delta_z = 4\left(1 + \frac{1}{M_0}\right)^2 f^{\#^2}\lambda \tag{6.9}$$

When the projected particle size on the imaging sensor is smaller than one pixel an effect called peak locking occurs [Tropea et al., 2007]. The sub-pixel displacement of the particle cannot be discerned, which greatly decreases the minimum observable particle displacement. Ideally, the imaged particle should cover 2-3 pixels. By means of Gaussian peak interpolation can the sub-pixel displacement then be obtained. Therefore, the f-stop should be selected in such a way that the diffraction-limited spot diameter d_s is about 2-3 pixels in size.

In stereo PIV two cameras are used to capture the same field of view. Tropea et al., 2007 states that there are two methods for positioning the cameras: the translation method and the angular method. In the translation method, the object and the image plane remain parallel to keep magnification constant. If the cameras are only translated the overlap in their field of view is smaller and the measurement domain thus smaller as well. By angling the cameras such that they are viewing the same plane a larger measurement domain is obtained. To be able to focus the entire object plane a scheimpflug is used. This scheimpflug is a lens that can be rotated. To focus the whole object plane the scheimpflug should be rotated such that the object plane, the imaging plane and the scheimpflug plane all intersect at one point. A disadvantage of angling the cameras with respect to the object plane is the perspective deformation it causes, but this can be corrected in software.

To get any displacement information two images need to be captured per camera. The flow displacement can be computed based on the observed displacement of particles between each frame. Computing the flow velocity based on the displacement of single particles is only possible if the displacement is less than the particle spacing. When this is the case the obtained velocity vectors are very sparse and randomly distributed. By using a higher particle density a greater resolution of resolved velocity vectors can be obtained, but in this case, single particle tracking is not possible. Instead, the entire domain is subdivided into small interrogation windows with a sufficient number of particles inside them. These windows are generally in the order of 16x16 to 128x128 pixels. The displacement is then computed based on the cross-correlation map for the particles inside the window. The particle displacement inside each of these windows should be nearly uniform, and the particle displacement relative to the window size should not be too large. If the displacement is big then there will not be enough particle pairs between each captured frame [Tropea et al., 2007].

An important factor is also the timing between the two frames. The timing should be chosen such that the in-plane displacement in the integration window is smaller than the window size, but it should be large enough that there is at least a displacement of more than 0.1 pixels. Otherwise, no displacement will be detected. Additionally, the particles can also move perpendicular to the laser sheet. The displacement of the particles should be smaller than a quarter of the laser sheet thickness, as otherwise too many would move out of view between frames [Tropea et al., 2007]. This also means that it is not possible to simultaneously capture fast and slow-moving flow.

6.2. Experimental objectives

The three main objectives of this campaign are:

- Investigate the flow uniformity
- Investigate the influence of the jet on the flow in the combustion chamber.
- Investigate the effect of the porous foam disks in the mixing duct on the flow field in the combustion chamber.

Stereo PIV was chosen as the measurement technique due to the need for measuring the flow velocity in three axes. The diluent is added at an offset from the centre line at the coflow attachment, which would produce a slight swirling motion in the flow. The foam disks are supposed to aid in dissipating this swirl before the flow reaches the combustion chamber. A good overview of the complete flow field is

needed to assess the flow uniformity in the combustion chamber. Therefore, hot-wire velocimetry was not suitable. Additionally, this setup has been designed with laser-based flow measurement techniques in mind. This PIV campaign will also facilitate as an evaluation of the feasibility of utilising lasers on the setup.

6.3. The setup

A Quantel Evergreen 200 532nm Nd:YAG laser was used to produce the laser sheet. The light of the laser was transformed into a sheet of about 1mm thickness using three lenses: a cylindrical lens with $f = -75mm$, a cylindrical lens of $f = 75mm$ and a spherical lens with $f = -30mm$. Two Imperx Bobcat IGV-B1610 CCD cameras (1628x1236, px:$4.4\mu m$) were used to capture the flow. Each of these cameras was equipped with an AF Nikkor lens. For most cases a 35mm lens was used, only the vertical enclosed - two-window view a 105mm lens was used. A 532nm bandgap filter was placed on each lens to filter out the background light. Additionally, two scheimplfugs were placed between the camera and the lens. This made it possible to rotate the camera lens to get the entire field of view in focus, by satisfying the scheimpflug condition. The coordination between the camera and the laser was done using a LaVision programmable timing unit. The tracer particles were generated using a PIVTEX Aerosol Generator (PIVpart45) which used DEHS oil. The SPIV system was calibrated using a type 10 LaVision 3D calibration plate. This plate was placed in the middle of the combustion chamber and aligned with the location of the laser sheet. A photograph is then taken of the calibration plate using both cameras. The PIV processing software DaVis will then match up the dots on the calibration plate in the photograph to their known locations.

Since this is a cold flow test only air is provided to the setup. The seeding is added to through the diluent connection. Three silicon carbide foam disks are placed in the mixing ducts. One at the bottom between the coflow attachment and the cylindrical mixing duct, one between the cylindrical mixing duct and the octagonal mixing duct and one between the octagonal mixing duct and the combustion chamber. In the enclosed configuration, a 3D-printed cone, made from PLA, is placed on top of the setup. This prevents ambient air from being entrained into the combustion chamber. In the reacting experiments, the PLA cone is replaced with a steel cone manufactured from welded steel plates.

Several viewing configurations were used to observe the flow. Both with an enclosure and without an enclosure. In Table 6.1 an overview of the different configurations which were tested is shown. In the subsections below each of the configurations will be discussed in more detail.

Configuration	Utility
Open horizontal	Visualse if there is a swirl in the flow
Open vertical	Visualse the entrainment of lab air into the region of interest
Closed single window	Study the flow field in an enclosed configuration
Closed two windows	Study the flow field without interference from the window frame

Table 6.1: Overview of the tested configurations

Open horizontal

The first configuration is unenclosed, with a horizontal laser sheet. Measurements with a horizontal laser sheet are only possible when the setup is unenclosed, as the frame would otherwise block the light. The two PIV cameras are placed above the setup looking down. Each camera is on the other side of the setup, and on the centre line. The horizontal laser sheet is placed about 4-5mm from the jet exit plane. A schematic of the setup is shown in Figure 6.2 and a photo of the laser light illuminating the tracer particles in Figure 6.3.

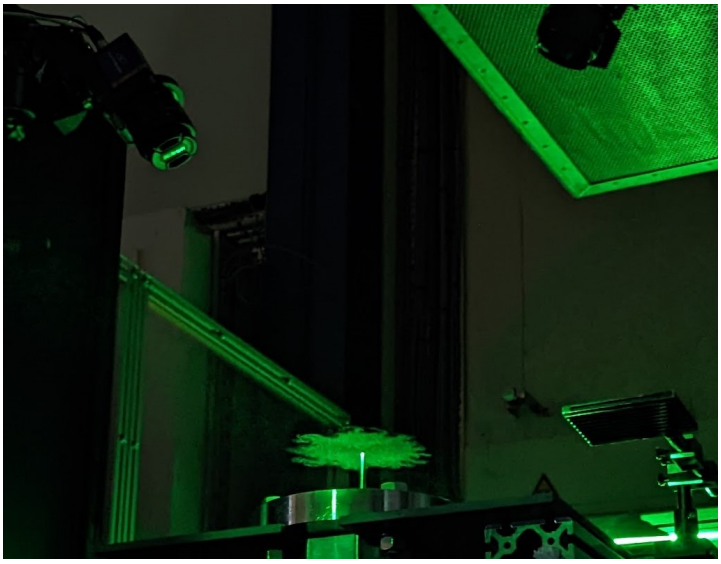

Figure 6.3: Photo of the laser light eluminating the tracer particles in the open horizontal configuration.

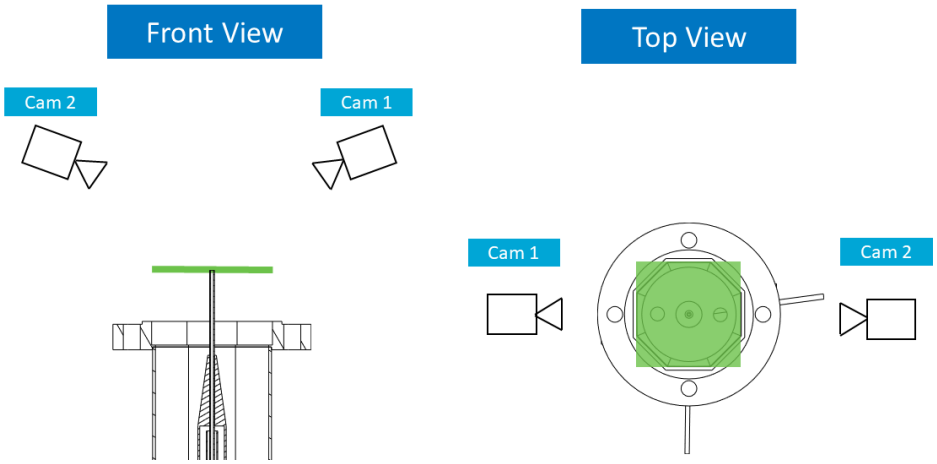

Figure 6.2: Diagram of the open horizontal configuration. The green region indicates the approximate field of view.

Open vertical

In the vertical open configuration, the setup was also not enclosed, but the laser sheet rotated vertically. The cameras are moved in front of the setup, still positioned on either side, but now at the same height as the field of view. The field of view is the entire width of the coflow, it starts about 5mm above the jet exit plane and ends at about 87mm above the jet exit plane. The cameras are now also each observing a different side of the laser sheet. In Figure 6.4 the setup is shown schematically. It was observed that the unseeded ambient lab was relatively quickly entrained into the coflow. To still be able to perform PIV measurements a smoke generator was used to add seeding to the lab air surrounding the setup. In Table 6.2 the timing, lens focal length and number of images captured per case are shown for this configuration.

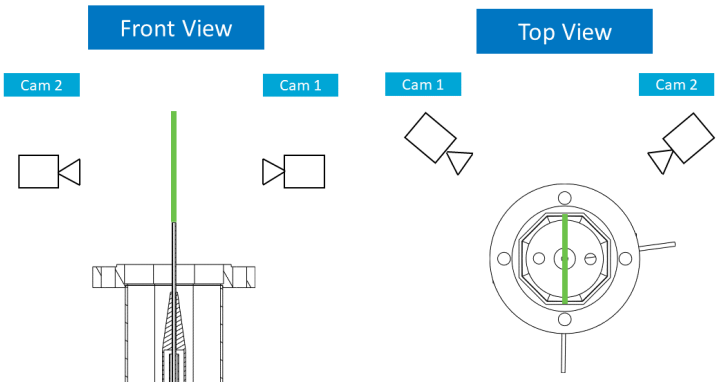

Figure 6.4: Diagram of the open vertical configuration. The green line indicates the approximate FOV.

ΔT [μ s]	20
f-stop [-]	8
Lens focal length [mm]	35
Number of images [-]	290

Table 6.2: Setup details for the open vertical configuration.

Closed vertical - single window

As can be seen in Figure 6.5 in this configuration both cameras are on the same side of the setup, and positioned one above the other. Both cameras are looking through the same window; both cameras can also see through the windows on the left and right of the window in the centre. The entire width of the combustion chamber cannot be seen as the frame partially blocks the field of view. The field of view is positioned about 21mm from the jet exit plane and extends up to about 120 mm. In Table 6.3 the timing, lens focal length and number of images captured per case are shown for this configuration.

Additionally, some issues were encountered when performing the stereo calibration in this field of view. The calibration plate was not large enough to be seen in both side windows. It would only be visible in one side window. Furthermore, the dot-finding algorithm was not able to pick up on the dots which were visible in the side window. This is caused by the difference in refraction which is not something the calibration algorithm can account for. The resulting combined image was not very well aligned in the side windows. There is thus a small calibration error when looking at data in the side windows.

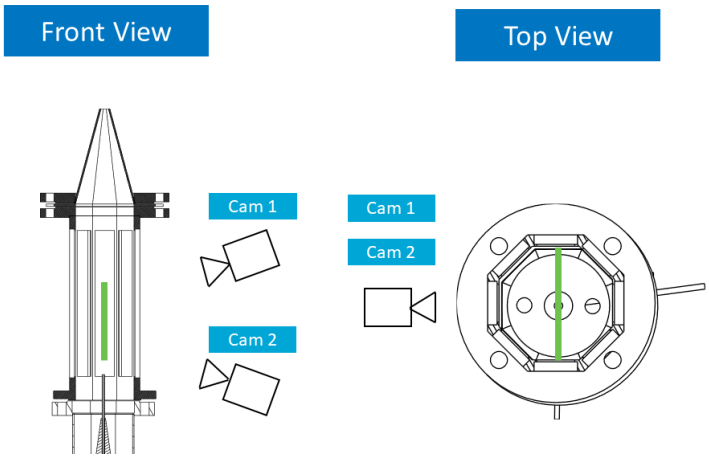

Figure 6.5: Diagram of the closed vertical single window view configuration. The green line indicates the approximate FOV.

	Jet	Jet off
ΔT [μ s]	20	2500
f-stop [-]	8	
Lens focal length [mm]	35	
Number of images [-]	100	

Table 6.3: Setup details for the closed vertical - single window configuration.

Closed vertical - two windows

If it can be assumed that the flow is axisymmetric then only one-half of the combustor has to be observed to know what the flow field looks like. In this configuration, shown in Figure 6.6, both cameras are again placed on either side and slightly in front of the setup. Each camera looks through a different window to slightly more than half the combustion chamber. This ensures that we can still see the entirety of the jet. The field of view in the direction of the flow is now also a bit smaller. Starting at 58mm till about 92mm from the jet exit plane. Furthermore, the setup has also been rotated 90 degrees with respect to the other configurations. Now the pilot burners are on the same line as the laser sheet. Whereas previously the pilot burners did not intersect with the laser sheet at all. In Table 6.4 the timing, lens focal length and number of images captured per case are shown for this configuration.

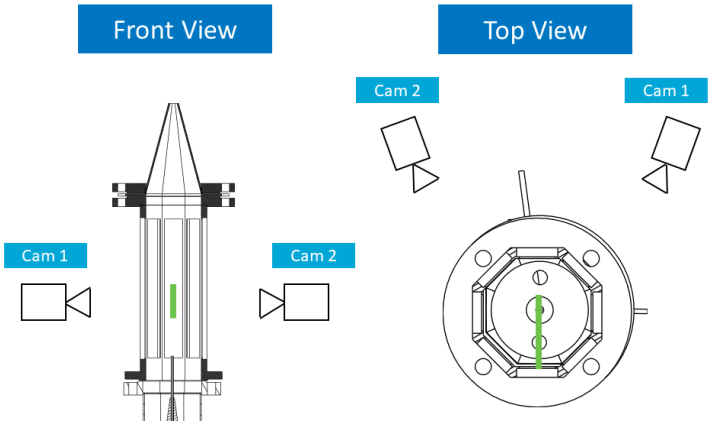

Figure 6.6: Diagram showing the position of the PIV cameras with respect to the setup in the two windows configuration. The green line indicates the approximate location of the FOV. (Note that the setup is rotated 90 degrees w.r.t. the other configurations.)

	Jet	Jet on, coflow focus	jet off
ΔT [μ s]	1.5	100	750
f-stop [-]	11		
Lens focal length [mm]	105		
Number of images [-]	800		

Table 6.4: Setup details for the closed vertical - two window configuration

6.4. Testing and processing procedure

In this section, the setup procedure, calibration of the system, timing of the laser and camera, and the processing of the images are described.

6.4.1. Calibration procedure

The setup and calibration procedure was as follows. The cameras are placed in roughly the correct position. The cameras are then translated and rotated such that the desired field of view is obtained and the observed area of each camera overlaps. We also made sure the cameras are parallel to the ground using a level, except in cases where the camera had to look up or down. We then taped pieces of paper with text in a very small font onto the calibration plate. The calibration plate was then placed at

the location of the laser sheet. The scheimpflugs and focus of the cameras were adjusted till the entire FOV was in focus. The small text made it easier to see if this was achieved. The focusing was done at the smallest f-stop as this is when the focal depth is smallest. Once this was done the PIV system was calibrated in DaVis using a type 10 3D calibration plate. The f-stop was then increased to the desired value to ensure a sufficient depth-of-field and ensure that the particle images were sufficiently large on the camera's imaging sensor.

6.4.2. Flow rates

To be able to meet the campaign objectives three flow settings were chosen to yield results representative of the entire planned experimental domain. The central jet was supplied with a high or low flow rate. In the coflow a fixed flow rate for the pilot burners was chosen, and a fixed flow rate for the diluent. Both pilot burners could be open, one could be closed or they could both be turned off. When only one of the pilot burners was open the flow rate to the pilot burners was halved such that the flow rate through each burner remains constant. Since the seeding was added to the diluent flow it could not be turned off. An overview of the flow rates, computed bulk velocities and Reynolds numbers is given in Table 6.5

	Central jet			Coflow		
Case	Flow rate [lnpm]	Bulk velocity [m/s]	Re [-]	Flow rate [lnpm]	Bulk velocity [m/s]	Re [-]
Baseline	38.38	97.12	19,354	232.04	0.35	2,577
Single pilot	38.38	97.12	19,354	178.00	0.24	2,244
High jet	47.07	119.11	23,736	232.04	0.35	2,925

Table 6.5: Overview of operating cases for the vertical enclosed - two window field of view. Bulk velocities and Reynolds calculated at 20°C.

Not all these conditions were tested for every configuration. In the open horizontal and vertical configuration only the baseline case was acquired. In the two enclosed configurations, all specified flow rates were tested. In the closed vertical - two window view configuration all specified conditions were tested with and without the top foam disk to find the effect of the top foam disk on the flow.

6.4.3. Timing

As mentioned in subsection 6.1.3 the selection of the time between consecutive frame captures depends on the flow velocity and interrogation window size. The in-plane image particle displacement should be smaller than the window size, the out-of-plane displacement smaller than a quarter of the laser sheet thickness and the displacement should also be larger than 0.1 pixels. This makes it difficult to simultaneously capture the central jet and the coflow. In Table 6.6 the timing used for different configurations is displayed. The jet timing refers to measurements which were taken when the jet was on, the coflow timing refers to cases when there is no jet, or to cases where the focus was on the coflow. In the two window configuration measurements of the same cases with jet were taken with both 1.5 and 100 μs. Using 100 μs allows for better observation of the flow coflow region when the jet is on.

	Open	Enclosed	
Configuration	Vertical	Single window	Two window
Jet timing [μs]	20	20	1.5
Coflow timing [μs]	N/A	2500	100 or 750

Table 6.6: ΔT used for each configuration

Originally, 4 μs was set as ΔT for the enclosed - two window view cases with jet. This however resulted in a timing mismatch between the laser and the camera system. During the second exposure of the camera, the laser light would not be on, resulting in that frame not containing any data. The timing issue was resolved by specifying a negative 2.5 μs offset in DaVis. However, during post-processing, it was noticed that the jet velocity from this frame did not match the jet velocity obtained from the single

window frame. DaVis still uses a ΔT of 4 μs and ignores the timing offset. As the actual timing was now 1.5 μs all velocities obtained from the processing done by DaVis have to be multiplied by $4/1.5$ and the Reynolds stresses have to be multiplied by $(4/1.5)^2$.

6.4.4. Processing

Processing of the images was done in version 8.4.0 of DaVis. For every case, a self-calibration was first performed, an initial run to correct for the light sheet misalignment and then also an additional run to correct for additional disparities. Then a background subtraction was performed using 11 images. The PIV processing was done in multi-pass mode with decreasing window size. The initial single pass has a 64x64 window size, with 50% overlap and the smallest window is 24x24 pixels with 75% overlap and is done in two passes.

6.5. Error estimation

There are several sources of errors that can influence the PIV results. Benedict and Gould, 1996 derived formulas for the uncertainty estimation of turbulence data using large sample theory. The authors provide equations for the variance for a list of different properties encountered in turbulence research. These formulas are only valid if the experimental data is independent. The standard deviation of the average flow velocity is obtained using Equation 6.10, where $\langle u'^2 \rangle$ is the RMS value of the velocity fluctuations. The standard deviation of the RMS of the velocity fluctuations can be obtained from Equation 6.11. For the Reynolds shear stress the standard deviation is obtained from Equation 6.12, where $R_{u'v'}$ is obtained from Equation 6.13. To obtain a 95% confidence interval the results from these equations have to be multiplied with a z-factor of 1.96.

$$\sigma_{\overline{u}} = \frac{\sqrt{\overline{\overline{u'^2}}}}{\sqrt{N}} = \frac{\langle u'^2 \rangle}{\sqrt{N}} \tag{6.10}$$

$$\sigma_{\langle u'^2 \rangle} = \frac{\sqrt{\overline{\overline{u'^2}}}}{\sqrt{2N}} = \frac{\langle u'^2 \rangle}{\sqrt{2N}} \tag{6.11}$$

$$\sigma_{\overline{u'v'}} = \sqrt{\frac{1 + R_{u'v'}^2}{N}} \sqrt{\overline{u'^2}} \sqrt{\overline{v'^2}} = \sqrt{\frac{1 + R_{u'v'}^2}{N}} \langle u'^2 \rangle \langle v'^2 \rangle \tag{6.12}$$

$$R_{u'v'} = \frac{\overline{u'v'}}{\sqrt{\overline{\overline{u'^2}}} \sqrt{\overline{\overline{v'^2}}}} = \frac{\overline{u'v'}}{\langle u'^2 \rangle \langle v'^2 \rangle} \tag{6.13}$$

6.6. Results

In this section, the results obtained from the PIV campaign are discussed. First, the results from the unenclosed configurations are discussed. Then the flow uniformity in the combustion chamber is analysed. Finally, the jet properties of the jet are investigated.

6.6.1. Unconfined entrainment of lab air

In the unenclosed vertical case, lab air was found to quickly entrain into the coflow/ central jet region. A frame of the observed seeding by camera 2 is shown in Figure 6.7a. At about $x/d = 25$ the lab air can be seen to reach the central jet region. If combustion was taking place, the lab air would have had an influence on it at that point. The central jet region is also visible at the bottom centre of the frame. Since the central jet is unseeded it needs to entrain seeding from the coflow to be visible. Therefore the seeding density is visibly lower in this region.

To be able to see the flow surrounding the coflow a smoke generator was placed under the setup. By running the smoke generator for a couple of seconds and then waiting for the smoke to spread a sufficiently high concentration of particles in the air surrounding the setup was obtained. In Figure 6.7b the flow field obtained from measurements at the baselines case is shown. Since the flow rate of the coflow is so slow a small draft in the lab is seen to be influencing the flow field surrounding the jet. On

the left side, the flow can even be seen to be slowly drifting to the left, while on the right side, some flow can also be seen to be moving left instead of being sucked into the jet. This effect of the ambient air on the coflow was also observed in the horizontal laser sheet configuration.

The open horizontal configuration did not offer any other interesting results. When the jet was turned off the effect of the lab air currents on the coflow was very clear. Additionally, when the top foam disk was not present the PIV results were of lower quality. Possibly, due to lab air entraining into the mixing duct at the top resulting in unseeded pockets of air.

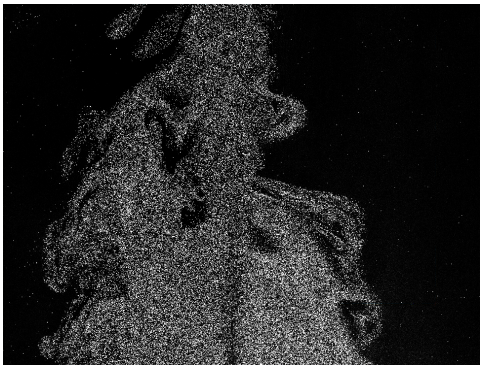

(a) Image from the second camera in the unenclosed vertical configuration, with time subtract applied. $x/d \approx 5-34$ The unseeded lab air can be seen to entrain fast. (contrast increased for clarity)

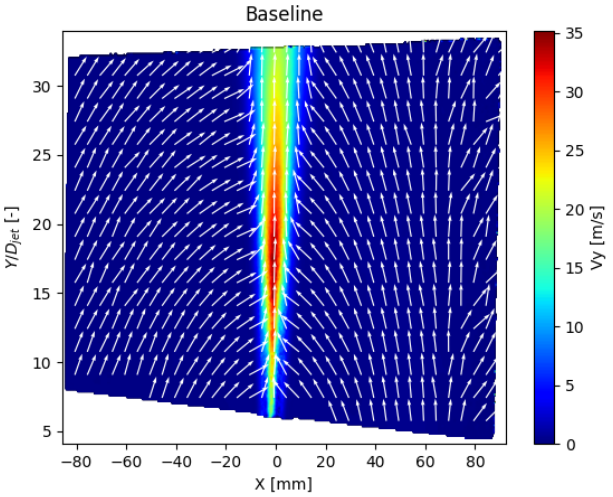

(b) The processed flow field for the baseline case in the vertical open view

Figure 6.7

6.6.2. Flow uniformity

The flow coming out of the mixing duct needs to be uniform and well mixed. The diluent attachment is off-centre in the mixing duct which will cause a rotation in the flow. The foam disks are there to destroy this rotation, and to increase mixing. In Figure 6.8a the vertical flow velocity is shown for the baseline case, with the jet, and both pilot burners open. The vectors shown in the plot show interesting behaviour in the coflow. To better visualise this the maximum and minimum velocities have been set at ± 0.5 m/s such that the velocity differences in the coflow become visible. This is shown in Figure 6.8b. The jet in the centre has a much higher vertical velocity and therefore appears as a single-coloured inverted cone. Looking at the flow on either side of the central jet it is obvious that the flow is not symmetric. There is even some downward flow observed on the top left side. The overall flow velocity is also lower on the left side as compared to the right side. The downward flow is the result of a recirculation zone of which only the bottom part is observed in this frame.

In Figure 6.9a, the vertical velocity is displayed for the case without a jet. The flow is also asymmetric in this case; The flow rate on the right side is still faster than on the left side. Unlike the case with jet, all flow is upwards, there is no recirculation observed. In Figure 6.9b the left pilot burner is closed, halving the flow rate through the pilot burners. The asymmetry is more pronounced in this case. The relative difference between the flow rate seen on the left and right side is bigger as compared to the case where both pilot burners are open. It is important to note that this field of view does not intersect with the pilot burners, but is at a 90-degree offset, as is shown in Figure 6.5. The right-hand side observed in Figure 6.9b is thus not right above the only pilot burner which is turned open.

The combustor has three disks in the mixing ducts, one at the bottom and one at the top of the circular duct, and one at the top of the octagonal duct just before the combustion chamber. In the enclosed two window view, all cases were run, both with this top disk installed and without it, to see how these disks influence the flow. Figure 6.10a and Figure 6.10b show the case with no jet and flow running through both pilot burners, the first one is with the top disk in place, the second one is without the top disk. On the Y-axis the distance from the jet exit plane is normalised with the jet diameter. The x-axis gives

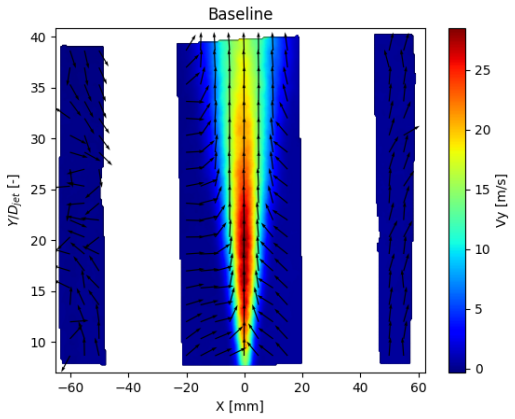

(a) Baseline case

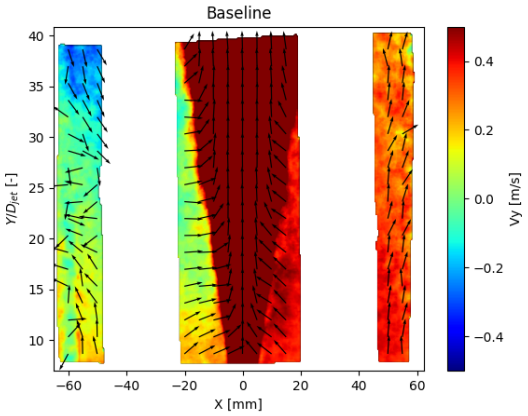

(b) Baseline, with the max and minimum displayed vertical flow velocity set at ± 0.5 m/s

Figure 6.8: Flow field of the vertical velocity from the closed vertical - single window view at baseline operating conditions.

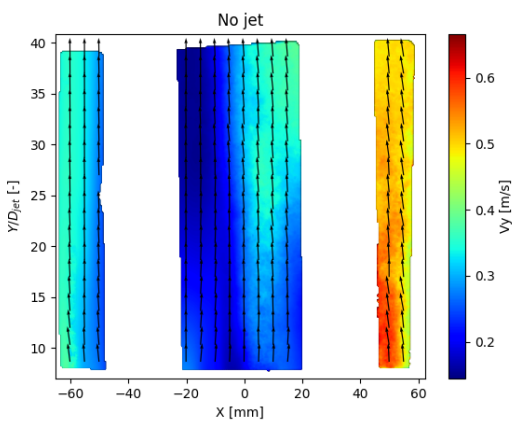

(a) Case with jet turned off and both pilot burners on.

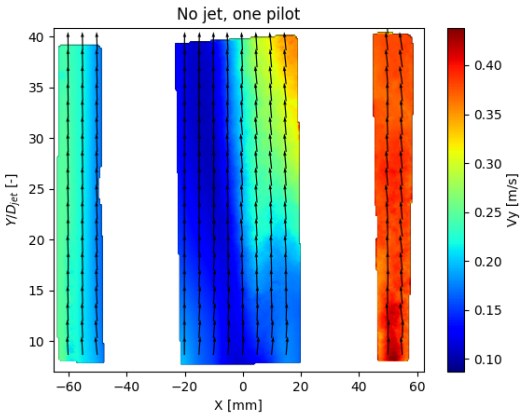

(b) Case with the jet turned off, with flow through only the right pilot burner.

Figure 6.9: Flow field from the closed vertical - single window view

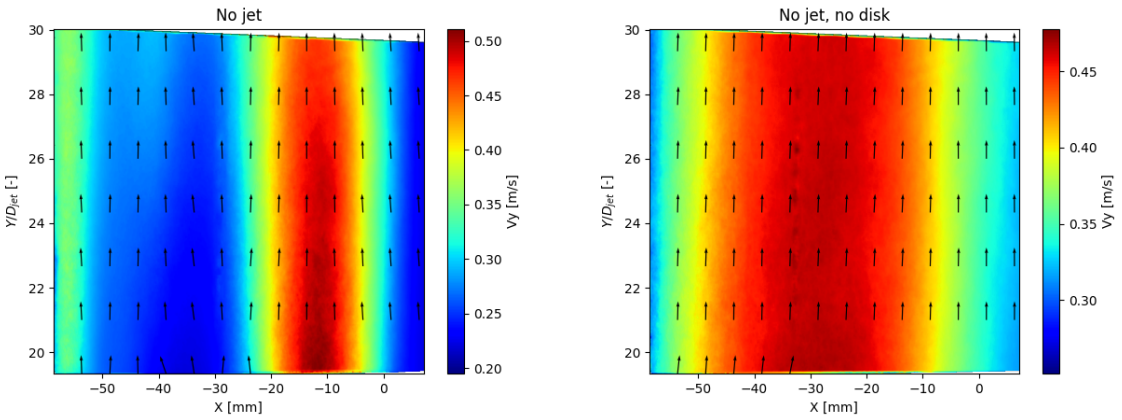

(a) Case with top foam disk

(b) Case without top foam disk

Figure 6.10: Flow field from the closed vertical - two window view, both images are of the case without jet

the distance from the central jet. This position is calculated using the average position of the peaks of the jet in all cases where there is a jet. As can be seen, only slightly more than the left-hand side of the combustion chamber can be seen. In the case with the top disk, an area of faster-moving air can be seen. It looks like there is a jet, it is however not on the location of the central jet but rather about 12mm to the side of it. In the case without the disk, the faster flow is spread out over a larger area. More interestingly the flow velocity in this area is about the same as the velocity in the fast-moving flow in Figure 6.10a even though the total mass flow rate is exactly the same in both figures. This is even easier to see when the vertical velocity is plotted at two distinct locations: at the bottom and top of the frame, for both cases, as is done in Figure 6.11.

Figure 6.11 shows the velocity of the coflow in the case when the central jet is turned off. On the Y-axis the vertical velocity is given, and on the X-axis the distance from the central jet, the same as in Figure 6.10. For each case two lines are plotted, one at the bottom of the frame at $Y/D_{jet} = 20.0$ and one at the top of the frame at $Y/D_{jet} = 28.0$. As observed earlier the peak in coflow velocity is similar in magnitude between the case with and without disk, the peak width is very different, however. Without disk, the coflow velocity distribution is as expected: a parabolic shape with a dip at the wall around $x = -60mm$ and a dip in the centre due to the wake from the central jet. When the disk is present there is a narrow jet at around $x = -12mm$, apart from in this area the flow velocity is much lower. In the jet, the velocity decays as the flow moves downstream. This is also observed when there is no foam disk. In the area between about $x = -20mm$ and $x = -60mm$, the velocity increases downstream. The flow wants to return to a parabolic shape, and the jet decays, which accelerates the surrounding flow. Both in the case with and without disk an increase in downstream velocity is observed on the right-most side of the plot. This is the result of the wake from the central jet decaying. Interestingly, however, the minimum in this wake area seems to be outside the observed area more to the right. It does not correspond to $x = 0mm$, which is where the central jet is located when it is turned on.

Since the mass flow rates are the same the momentum in the flow should be similar both when the disk is present and isn't. The general equation for momentum is given in Equation 6.14, where p is the momentum, M the mass and v the velocity. This equation will be used to compute the momentum of a volume of gas. The PIV data is given in discrete data points, which means we can use this to grab one vertical slice of data and compute the absolute momentum of this slice. Since we only have one side of the combustor, and data only for a thin slice in the z direction we have to assume the flow is axisymmetric. The volume can then be segmented into small octagons with height ΔY and thickness ΔX, it is then assumed that for each of these segments, the velocity is the same in the circumference. Using the equation for the perimeter of an octagon $P = 16R\left(\sqrt{2}-1\right)$ the mass of small volume ΔM can be computed with Equation 6.15. Where ΔX is the width of the volume, δY is the height and ρ is the density of the gas. By summing all sections from the centre at $X = 0$ to the wall the momentum of a slice of flow with height ΔY can be computed. The formula for which is given in Equation 6.16. The same spacing for Y is used in both cases.

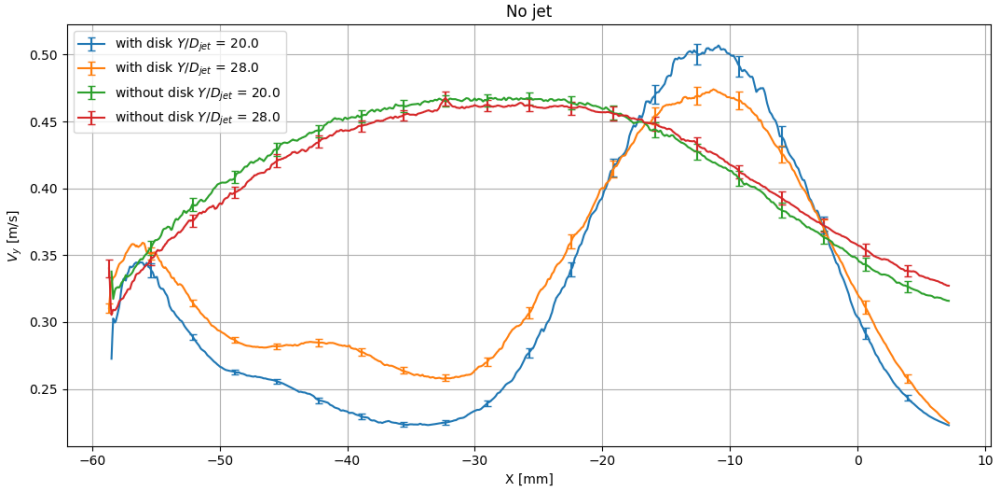

Figure 6.11: Flow field from the closed vertical - two window view, no jet case. Comparison of case with and without disk at two downstream locations

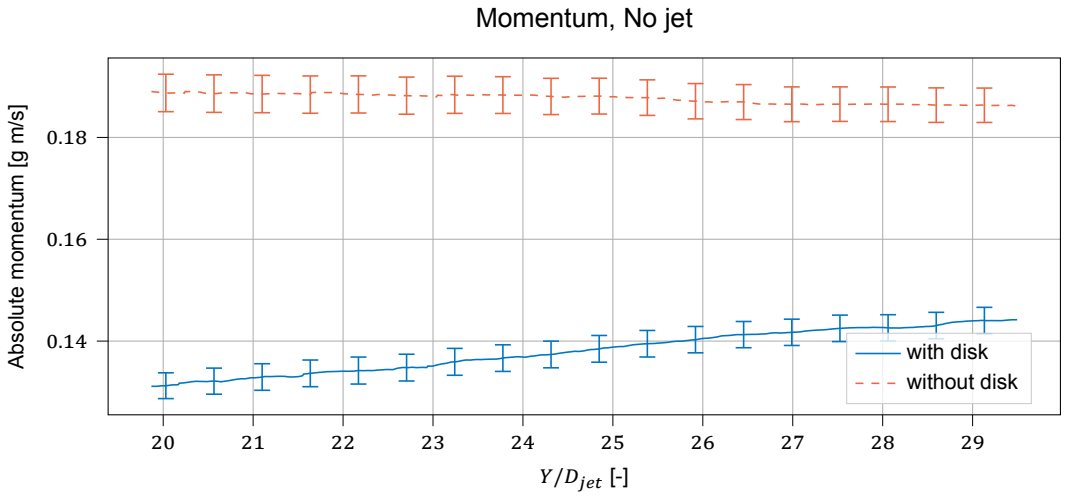

Figure 6.12: Absolute momentum from the closed vertical - two window view. in the no jet case both with and without the top foam disk. With statistical 95% confidence interval

$$\vec{p} = M\vec{V} \tag{6.14}$$

$$\Delta M = \Delta Y \Delta X 8X \left(\sqrt{2} - 1\right) \rho \tag{6.15}$$

$$\rightarrow |p| = \sum_{i=1}^{i=n} \Delta Y \left(x_i - x_{i-1}\right) x_{i-1} 16 \left(\sqrt{2} - 1\right) \rho |V| \tag{6.16}$$

The momentum at different Y-positions is plotted in Figure 6.12. The momentum is expected to drop due to friction as the flow moves downstream. The line of the case without disk is then as expected, the momentum decreases. The case with the disk shows an increase in momentum. Furthermore, the momentum is a lot lower than in the case without the disk. Since there is no momentum being added to the flow at this point the only reason why this line shows an increasing trend is that the flow is not axisymmetric. The flow rate is higher somewhere outside the field of view. Which matches the observations from the single window field of view. The fact that the case without disk does show a decay means the flow might be symmetric or close to it.

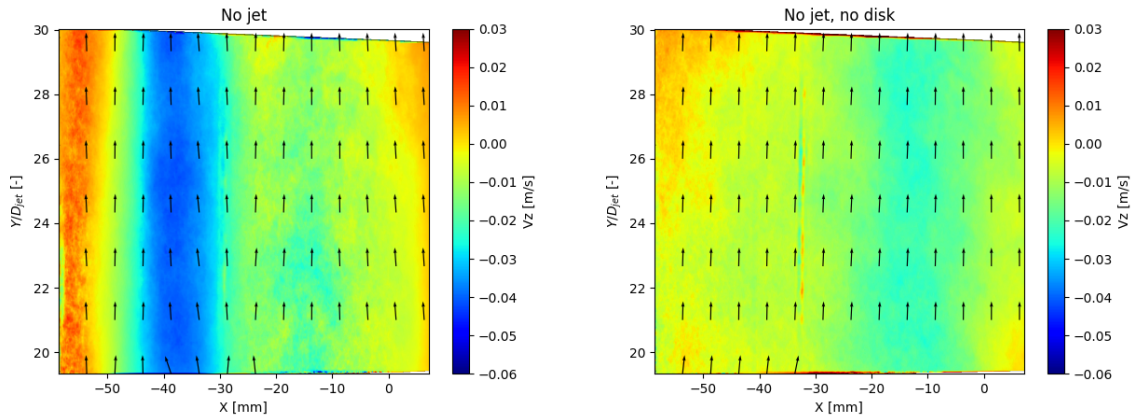

(a) With top disk

(b) Without top disk

Figure 6.13: Flow field in the Z-direction from the closed vertical - two window view, no jet case.

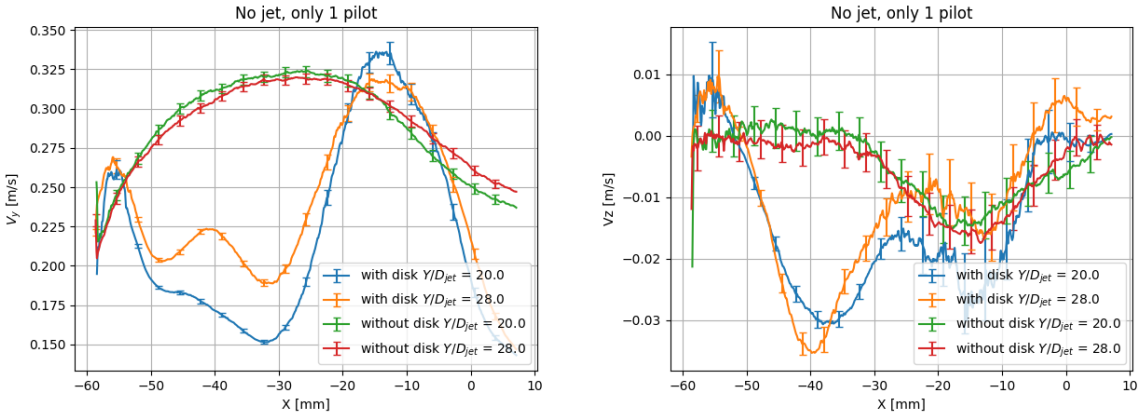

(a) Vertical velocity

(b) Out-of-plane velocity

Figure 6.14: Line plots of the vertical and out-of-plane velocity from the closed vertical - two window view, with the jet turned off and left pilot burner closed.

In the out of plane flow field, in Figure 6.13, a substantial difference in flow velocity can be seen. When the top disk is present the flow moves relatively fast into the page between $x = -45mm$ and $x = -30mm$. No such area is seen anywhere in the case without the top disk. Apart from this single region, the velocities are similar in both cases. The foam disk may induce a swirl but that is hard to confirm without seeing the other side of the flow field,d. In the single window field of view.

The same pattern is seen when one of the pilot burners is turned off. In Figure 6.14 two line plots are shown for the vertical and out-of-plane velocity for the case with no jet and only one pilot burner open. Looking at the vertical velocity plot the shapes of the lines are very similar to the case when both pilot burners have air flowing through them. In the slower-moving region of the case with disk present, there is a hump at $Y/D_{jet} = 28$ which is more pronounced when only one pilot is operational than when both are operational. At a lower Y-location, this hump does not exist. The X-location of this hump ($X \approx -40mm$) matches very well with the downwards peak seen in Figure 6.14a. In this area both the z and y velocity components are increasing when moving downstream. While it is more prominent when one pilot burner is turned off the hump in the vertical velocity field and the corresponding increase in out-of-plane velocity is also observed when both pilot burners are open.

It is thus clear that the foam disk has an undesired effect on the flow. The foam disks were included with the intention of generating turbulence to enhance mixing and cancel out the swirl induced by the diluent flow. The silicon carbide, of which the disks are made, is very brittle. Therefore there is no tight

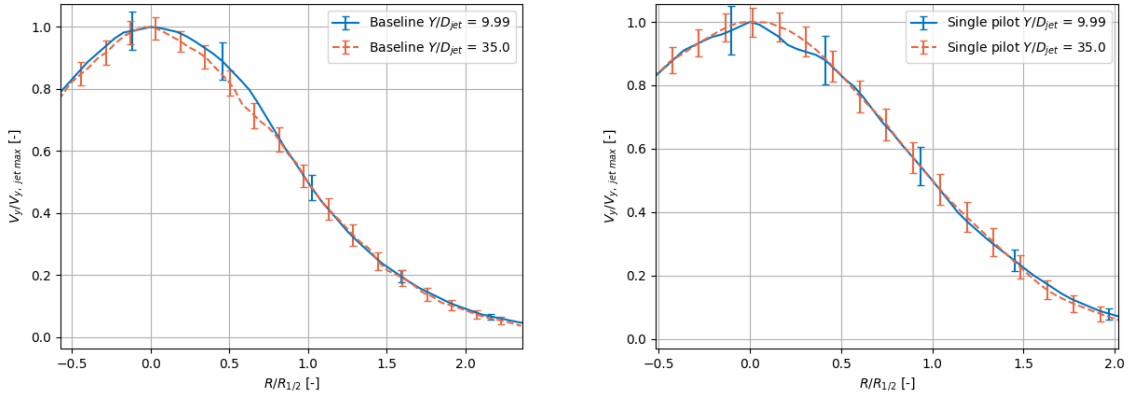

(a) Baseline (b) Single pilot

Figure 6.15: Self-similarity of the central jet in two cases, from the closed vertical - single window view.

fit between the disk and the central jet tube. Air is able to pass between the disk and the tube. This might explain the non-uniformity. The air seeping through creates an area of fast-moving air disturbing the uniformity. The same seepage occurs on the other two disks located in the circular mixing duct. These disks were present for all measurements, but when the top disk wasn't present the flow looks very uniform. The length of the octagonal mixing duct is thus long enough for the non-uniformities to dissipate. The top disk is therefore redundant and can be removed.

6.6.3. The jet

In a self-similar jet, the normalised shape of the jet is independent of the downstream location. The variables by which the velocity profiles, and other variables, have to be chosen such that this independence of the downstream location is achieved. The flow velocity is normalised with the local peak jet velocity $V/V_y\ jet\ max(y)$ and becomes a function of $\xi = R/R_{1/2}(Y)$. Here the jet half-width $R_{1/2}$ is a function of the downstream location and is the point at which the axial velocity is half that of the peak velocity [Pope, 2013]. In Figure 6.15 the normalised jet is plotted at two axial locations from the single window view. At the bottom of the frame ($Y/D_{jet} = 9.99$) and the top of the frame ($Y/D_{jet} = 35$) the lines overlap for both the baseline case in Figure 6.15a and the single pilot case in Figure 6.15b. The jet seems self-similar already at a $Y/D_{jet} = 9.99$. Although in literature self-similarity is expected to start about about 30 jet diameters away [Pope, 2013]. Similarly in the baseline and high jet case from the two window view the jets also seem to be self-similar as seen in Figure 6.16. However, the field of view of this frame does not go down as far, only to a $Y/D_{jet} = 19.33$.

In Figure 6.17 the Reynolds shear stress is shown for the baseline and the high jet case in the vertical enclosed two window view. On the X-axis the radius is normalised with the half-width, on the Y-axis the Reynolds shear stress is normalised with the square of the centreline velocity. If the jet was self-similar these lines should overlap [Pope, 2013], but they do not. Both in the baseline case and the high jet case a notable difference can be seen. Also looking at the Reynolds stress in the single window view (not shown) self-similarity is not achieved even when looking at 30-40 jet diameters away from the jet exit. Since this jet is not free it is possible that self-similarity is not fully achieved.

A difference in jet velocity profile is also seen when the top disk is removed as shown in Figure 6.18. In the figure on the left, the baseline case is displayed, in the middle figure the left pilot is closed and on the right, the jet velocity is set to high. The velocity profile of the jet is shown at the bottom of the frame and at the top. In all figures, the jet velocity is higher in the case with the disk as compared to the case without it. The difference is larger at $Y/D_{jet} = 20$, than at $Y/D_{jet} = 28$. The velocity peak in the case with the disk is also consistently to the left of the peak for cases without the disk. There could be a difference in entrainment rate, but it is more likely that the laser or setup shifted lightly during the removal of the foam disk. Additionally, the hole in the disk might have slightly pushed again the central jet assembly. Removing it caused the central jet to shift a bit. Comparing the locations of the velocity peaks shows an average offset of 0.33mm in the x direction. Since the jet is smaller closer to the jet exit

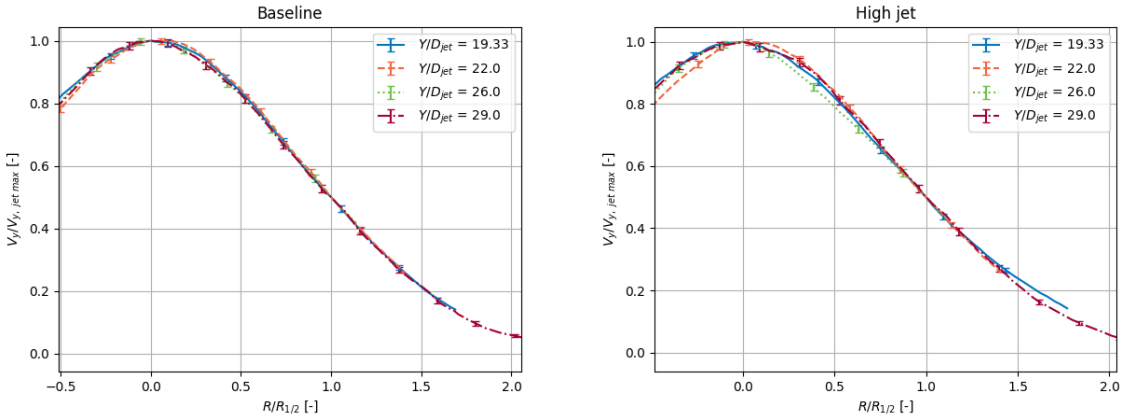

(a) Baseline (b) High jet

Figure 6.16: Self-similarity of the central jet in two cases, from the closed vertical - two window view.

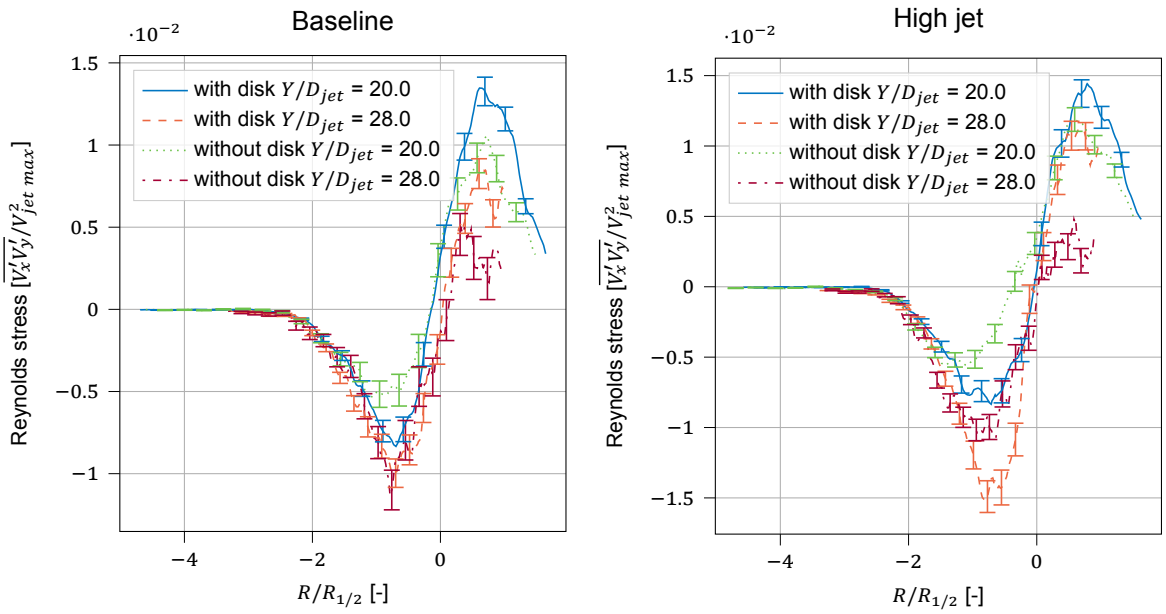

(a) Baseline (b) High jet

Figure 6.17: Reynolds shear stress self-similarity for the vertical enclosed - two window view.

plane, and the velocity gradients here are also higher, the observed lager difference in peak velocity at the bottom of the frame can logically be explained by a shift between the laser sheet and the central jet. As the jet expands the velocity gradients become smaller so a shift in the jet will also result in a smaller velocity difference observed here.

Jet expansion

For a self-similar jet, the jet expansion was found to be linear and independent of the Reynolds number [Pope, 2013]. The jet half-width can be described by the simple formula in Equation 6.17 where S is an empirically found constant, and y_0 the location of the virtual origin [Panchapakesan and Lumley, 1993]. In Figure 6.19 the jet half-width and least square fit are displayed for both the two window view and the single window view. Hussein et al., 1994 found a value of 0.094 and 0.102 for S based on hot-wire velocimetry and LDA respectively. The width of the combustion chamber and windows is based on this prediction for the spreading rate of the jet. The expansion coefficient and the location of the virtual origin are calculated using a linear least squares fit on the PIV results. In Table 6.7 these results are tabulated for each operating case and frame. For all cases the expansion coefficient is smaller than the values obtained by Hussein et al., 1994 and Panchapakesan and Lumley, 1993. In some cases the location of the virtual origin is negative. This is not something that would be expected if the jet were to be free. Although the least squares fit is relatively good, with an R^2 of around 0.9 to 0.96, there is some uncertainty in the PIV measurements which could contribute to the difference in slope and location of the virtual origin. The results do indicate that the jet expands slower than initially predicted, which does mean that the windows are of a sufficient size to be able to view the reaction zone.

$$r_{1/2}(y) = S\,(y - y_0) \tag{6.17}$$

		Baseline			Single Pilot			High jet		
Frame	Disk	S [-]	y_0 [mm]	R^2	S [-]	y_0 [mm]	R^2	S [-]	y_0 [mm]	R^2
2 window	Yes	0.088	6.21	0.95	0.093	9.14	0.90	0.087	6.13	0.93
	No	0.079	-4.82	0.94	0.080	-5.40	0.96	0.092	5.32	0.94
Single window	Yes	0.078	1.20	0.93	0.082	1.05	0.96	N/A	N/A	N/A

Table 6.7: Coefficients for the half-width expansion of the central jet for different operation conditions and frames. Data were obtained by linear regression, with the R squared displayed.

Reynolds stress

The normalised Reynolds shear stress is plotted for three operating conditions in Figure 6.20, Figure 6.21, and Figure 6.22. For each operating condition the case with the top disk, and without top disks is shown. As seen from these images the Reynolds shear stress is highest in the shear layer between the jet and the coflow. The shear stress is higher in the 'high jet' case than the baseline case, due to the higher jet velocity. Between the single pilot operational case and the baseline case, the difference is a lot smaller. In the single pilot case, the positive shear region at the bottom right of the frame is slightly stronger than the same region in the baseline case. The reduced velocity in the coflow has strengthened the shear layer slightly. A more noticeable difference is observed when comparing the cases with and without the top foam disk. In all three operating conditions, the shear stress is smaller when the top disk is removed. Lower flow velocities were also observed in Figure 6.18, where the vertical velocity is lower in cases without the top disk as compared to cases with the disk. The explanation given for this difference is an alignment issue with the location of the central jet assembly. The jet has a very small diameter, a small offset in the laser alignment will have a large effect on the obtained velocities. The suspected misalignment is not the only plausible explanation for the difference. Additionally, the relative difference in shear stress is larger as compared to the relative difference in axial velocities. The foam disks will produce turbulence, it is plausible that this increase in turbulence increases the strength of the shear layer and therefore also results in an increase in Reynolds shear stress. Furthermore, it is also possible that the leakage between the walls and the foam disk, observed in earlier, produces an annular jet resulting in an increase in shear stress.

In Figure 6.23 the normalised shear stress is plotted in the single window field of view. In this field of view, the shear stress is plotted over a larger downstream distance. Only the baseline case and the

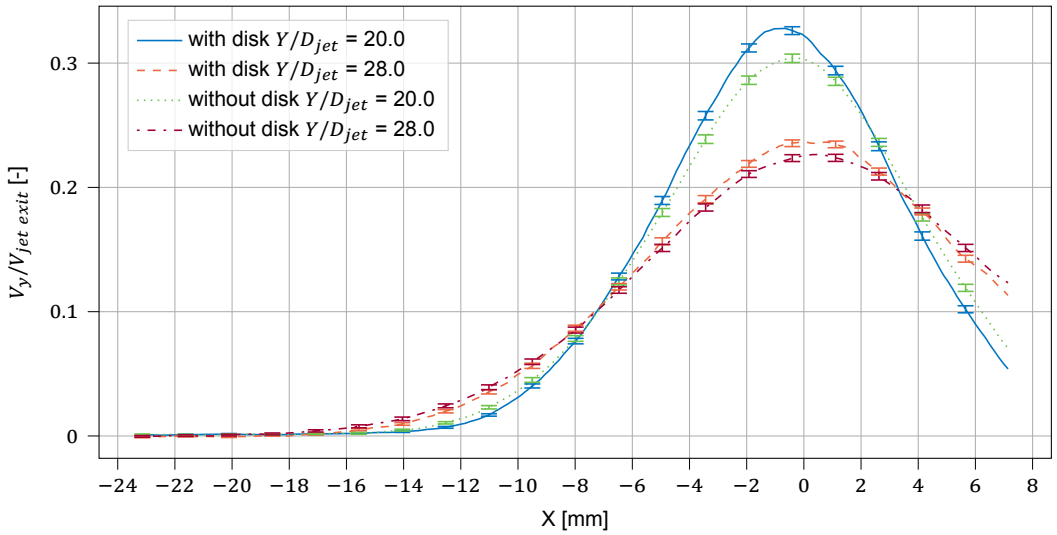

(a) Baseline case

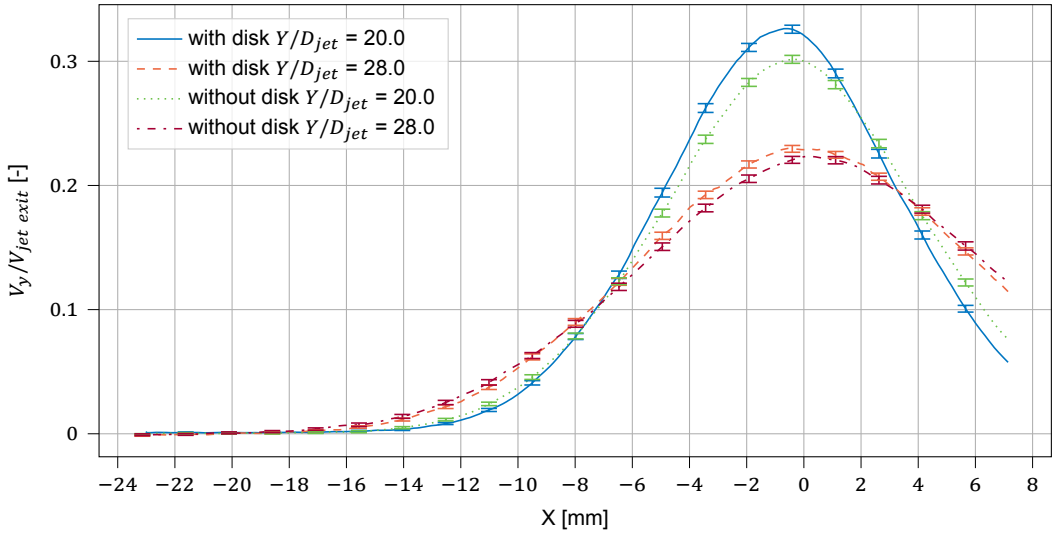

(b) Left pilot closed

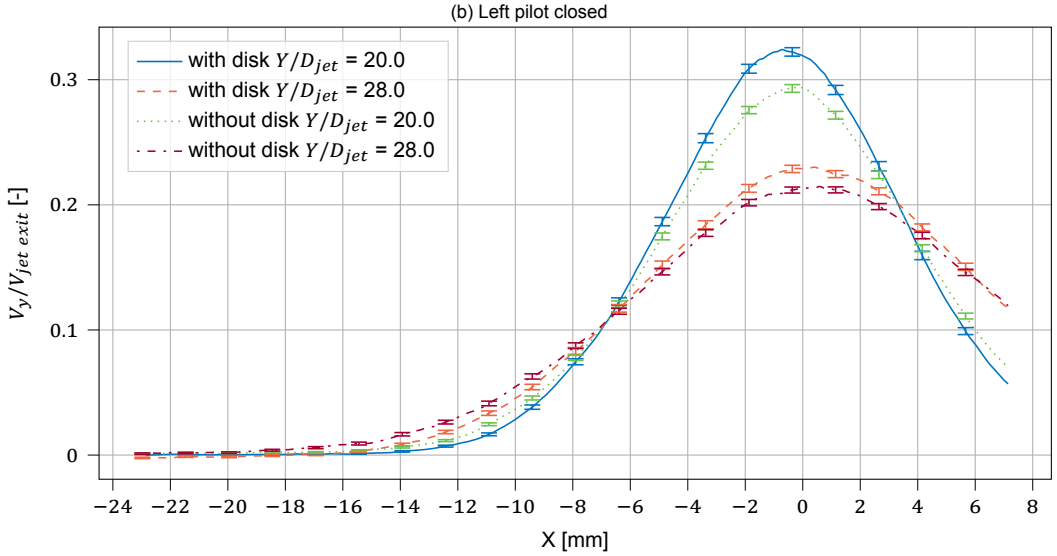

(c) High jet

Figure 6.18: Line plots of the vertical velocity for three cases with and without the top disk from the closed vertical - two window view.

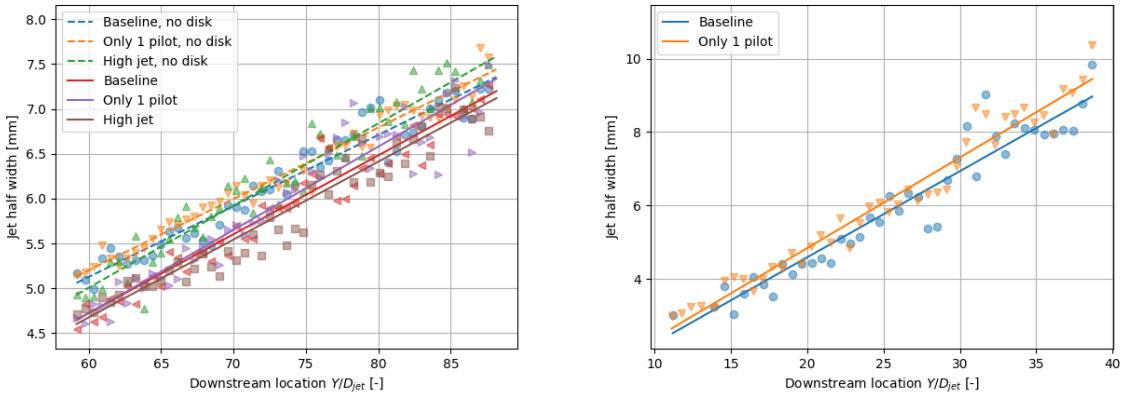

(a) Vertical enclosed - two window view

(b) Vertical enclosed - single window view

Figure 6.19: Jet half width as a function of downstream location

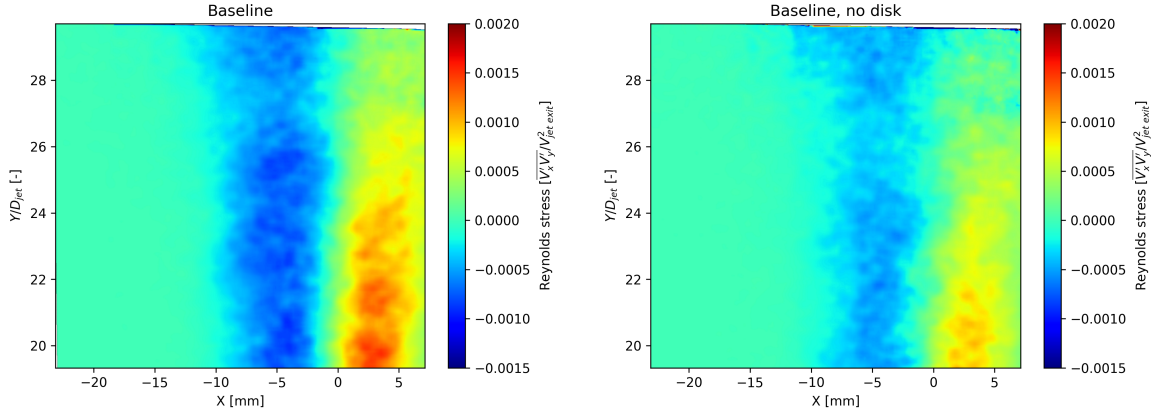

(a) With top foam disk

(b) Without top foam disk

Figure 6.20: Normalised Reynolds stress, from the enclosed vertical two windows frame. The baseline case

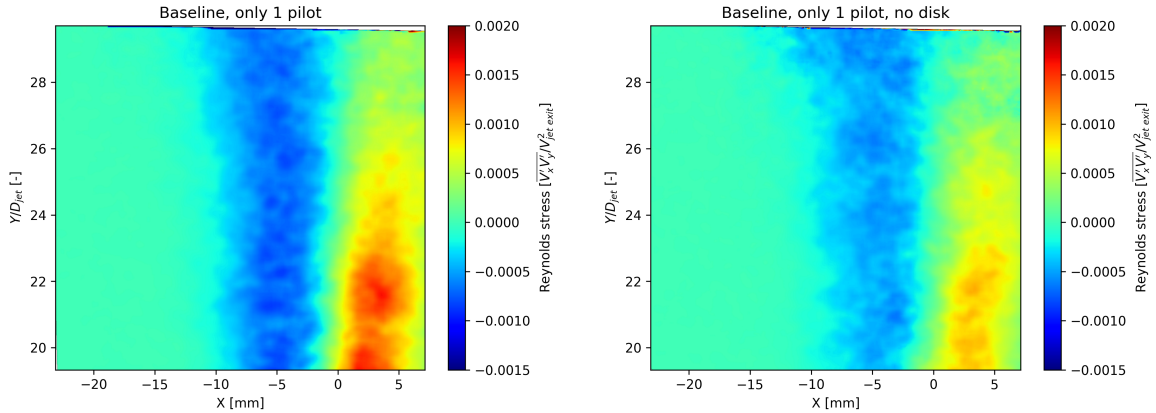

(a) With top foam disk

(b) Without top foam disk

Figure 6.21: Normalised Reynolds stress, from the enclosed vertical two windows frame. The left pilot disabled case

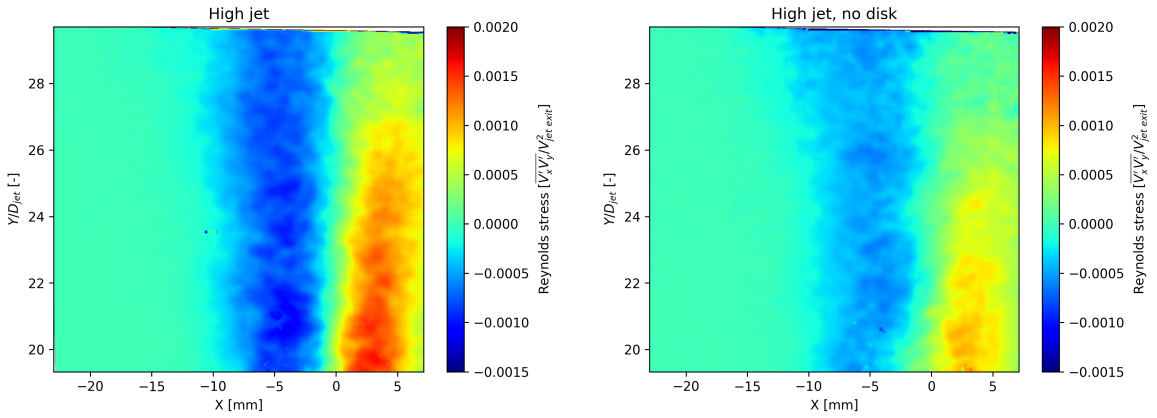

(a) With top foam disk

(b) Without top foam disk

Figure 6.22: Normalised Reynolds stress, from the enclosed vertical two windows frame. The high jet

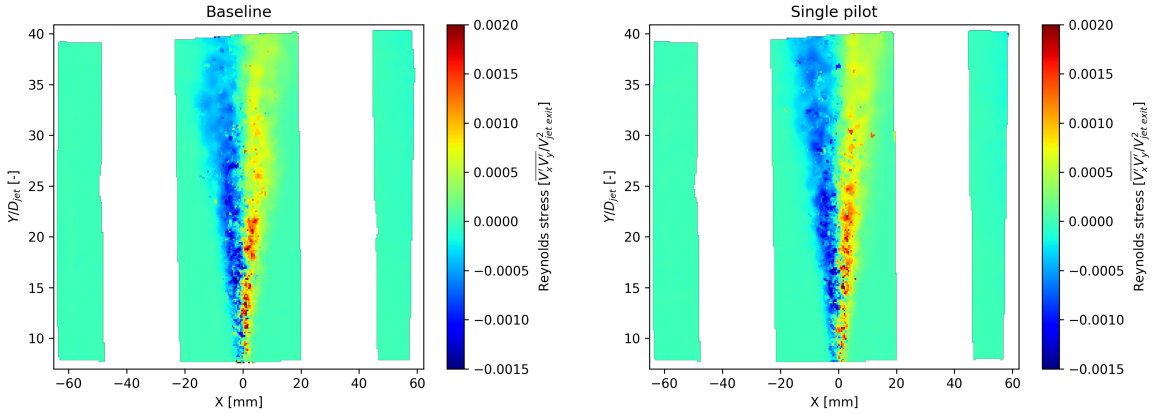

(a) The baseline case

(b) The left pilot closed

Figure 6.23: Normalised Reynolds stress, from the enclosed vertical single window frame.

one pilot operational case are available. Visually there does not appear to be any difference between the two operational conditions. In both, it can be seen that the peak of the shear stress is in the shear layer between the jet and coflow. As the jet expands downstream the area with higher shear stress also increases in size. Furthermore, the magnitude of the shear stress drops with increasing distance from the jet exit plane.

In Table 6.8 the jet decay rate for different jets is shown, obtained from a least squares interpolation of the data. In Equation 6.18 the formula for the decay rate of a self-similar jet is given as taken from Pope, 2013. Here $\frac{V_{centre}(y)}{V_{jet}}$ is the centreline velocity of the jet over the jet exit velocity, B is the decay rate constant, d_{jet} the jet diameter, y the downstream location and y_0 the location of the virtual origin. In Figure 6.24 the peak velocities and the linear interpolation are plotted.

The jet decay constants shown in Table 6.8 are higher than those reported in Pope, 2013, with $B =$ 6.06, 5.9 and 5.8, from Panchapakesan and Lumley, 1993 and Hussein et al., 1994; while the highest value reported in Ball et al., 2012 is 6.7 from Ferdman et al., 2000 which is for a jet from a pipe. This is quite close to the values obtained here and most likely resembles the conditions in this setup the closest. The outlier is the decay rate constant computed for the baseline case in the single window view with a value of 8.403. A higher value indicates a smaller rate of decay. The location of the virtual origin is also much more negative than the other values. The single pilot case yields a value for B which is much closer to the values observed in the other cases. As was seen from the data presented in previous sections this jet is not free, recirculation zones are established around the jet, and therefore

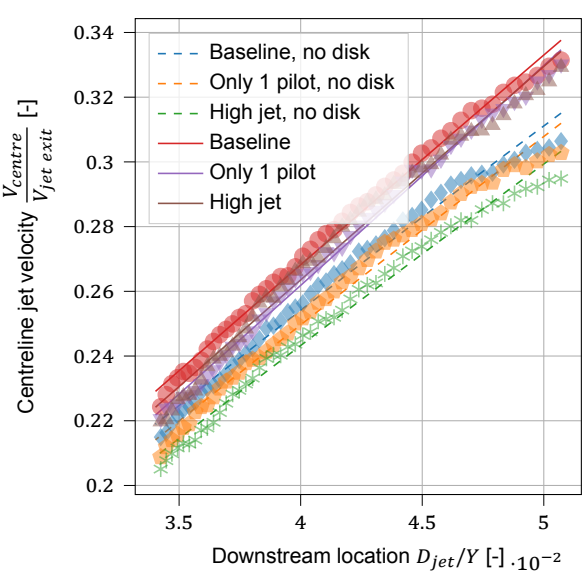

(a) Vertical enclosed - two window view

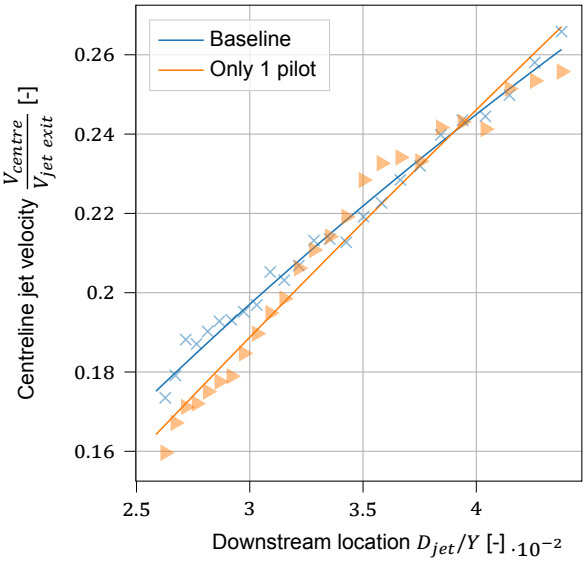

(b) Vertical enclosed - single window view

Figure 6.24: Peak velocity as a function of downstream location and linear regression of that data

the values reported in the literature may deviate from the values computed values for these cases. In the single pilot case, the flow rate in the coflow is smaller, there is therefore also less volume flow to feed the central jet. It can be seen that the decay constant is consistently higher in the single pilot cases indicating a faster jet decay. The same goes for the high jet case, also here a smaller than baseline decay rate constant is found indicating faster decay.

The fact that the value for the decay rate constant is higher in the baseline - single window view case might be due to a worse alignment of the laser sheet with the central jet. When looking at the normalised velocity in Figure 6.24 it can be seen that it is slightly lower in the single window view as compared to the two window view. If the centre of the jet is not aligned with the sheet a lower peak velocity will be obtained. The decay rate is also highest in the centre thus a misalignment would also explain the lower decay rate. Looking at Figure 6.24a the cases where the foam disk is have a lower normalised peak velocity and also a lower rate of decay. The foam disk helps centre the jet, by removing it it is possible that the jet is now on a larger angle and thus there will be a misalignment with the laser sheet.

$$\frac{V_{centre}\,(y)}{V_{jet}} = B\left(\frac{d_{jet}}{(y - y_0)}\right) \tag{6.18}$$

		Baseline			Single Pilot			High jet		
Frame	Disk	B [-]	y_0 [mm]	R^2	B [-]	y_0 [mm]	R^2	B [-]	y_0 [mm]	R^2
2 window	Yes	6.889	-2.059	0.994	6.354	2.198	0.995	6.583	0.058	0.986
	No	6.937	-6.892	0.987	6.6	-4.316	0.988	6.49	-5.039	0.988
Single window	Yes	8.403	-27.906	0.986	6.748	-7.261	0.972			

Table 6.8: Jet decay for different jets in the vertical enclosed two window view

Recirculation zone

In Figure 6.25 the coflow is shown for three different operating conditions: the baseline, the left pilot burner closed, and a case with high jet velocity. In all three figures the air is moving downwards at the top of the frame, at the bottom the flow is moving upwards. The central jet can be seen to entrain air from the coflow, in all cases as well. The downward flow is caused by a recirculation zone, of which only the bottom part is visible in this field of view. A larger area of the frame is occupied with the downward

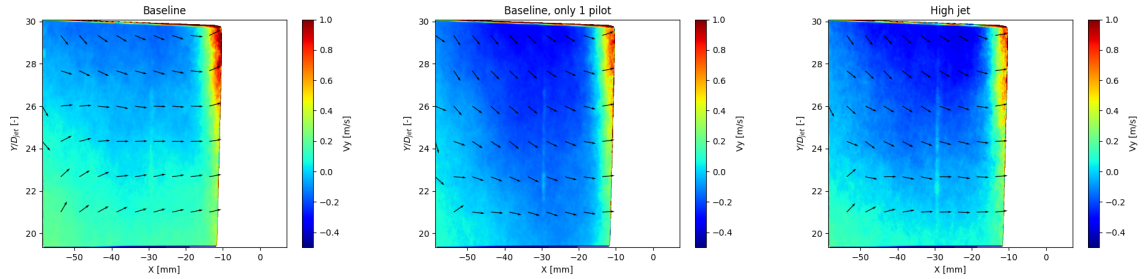

(a) Baseline (b) Left pilot off (c) High jet

Figure 6.25: The flow field in the coflow from the closed vertical - two window view.

moving flow as the coflow flow rate is decreased, as seen in Figure 6.25b. Similarly, in Figure 6.25c the area of downward moving air also increases as compared to the baseline case but not as much as observed in the decrease in coflow flow rate.

The Craya - Curtet number (C_t) describes the behaviour of turbulent jets as they enter a region of slower moving air [Harnby et al., 1985]. For a C_t above 0.75, the jet is said to be free until the jet hits the walls of the secondary container. If the Craya-Curtet number is below 0.75 recirculation zones will appear around the jet. The co-flowing fluid does not provide a high enough flow rate to feed the jet entrainment. The formula for the Craya - Curtet number is given in Equation 6.19, where V is the ratio of the jet velocity over the coflow bulk velocity in Equation 6.20, and D is the ratio of the jet diameter over the coflow diameter as in Equation 6.21.

$$C_t = \frac{(V-1)D^2 + 1}{D(V^2 - V - 0.5D^2(V-1)^2)^{0.5}} \tag{6.19}$$

$$V = \frac{V_{jet}}{V_{coflow}} \tag{6.20}$$

$$D = \frac{D_{jet}}{D_{coflow}} \tag{6.21}$$

In Table 6.9 the jet, coflow velocity and Craya-Curtet number are listed for all three cases in Figure 6.25. The lowest is seen in the one-pilot case, the recirculation zone is thus largest in this case, which corresponds to what is observed in Figure 6.25b. After that, the high-jet case has a C_t of 0.16 and the largest C_t is found in the baseline case. Since the relative change in coflow flow rate is larger than the relative change in the central jet the change in coflow has a larger effect on the recirculation zone. In all three cases, C_t is much smaller than 0.75, which means in none of the operating conditions the jet will be free. In Figure 6.26 the Craya-curtet number is plotted as a function of the velocity ratio. For this combustion setup, the critical velocity ratio is 55.7. With a coflow velocity of $0.35m/s$ as in the baseline case a jet velocity of lower than $19.5m/s$ is needed for $C_t \geq 0.75$; With the baseline jet velocity of $97.12m/s$ a coflow bulk velocity of $1.74m/s$ or higher is required.

		Baseline	One pilot	High jet
Jet velocity	[m/s]	97.12	97.12	119.11
Coflow velocity	[m/s]	0.35	0.24	0.35
Craya-Curtet number	[-]	0.17	0.12	0.14

Table 6.9: Jet, coflow velocity and Craya-curtet number for three operating conditions, with the jet and coflow at $P = 1atm$, $T = 20$°C

These numbers are all at a pressure of 1 atmosphere and a temperature of 20°C. During operation, the coflow will be significantly hotter than 20°C. The central jet is cooled but will also heat up slightly. When the gasses heat up they expand, increasing the flow velocity and therefore also altering the Craya-curtet number. Taking the most optimistic case (the baseline case), with a high coflow flow rate, low jet flow

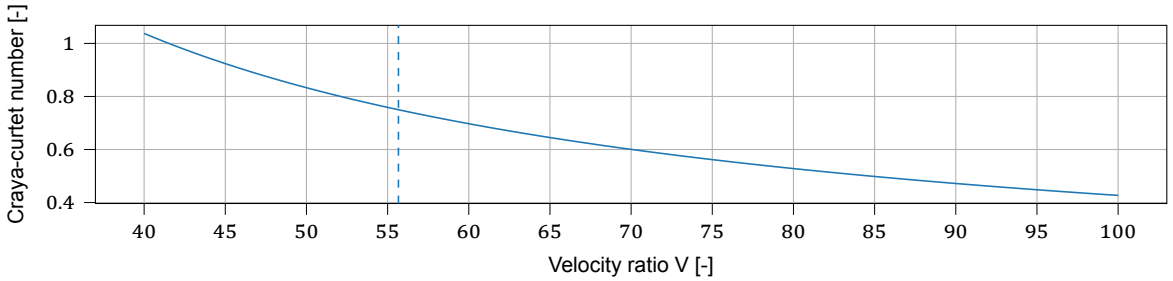

Figure 6.26: The Craya-curtet number as a function of the velocity ratio for a $D = 0.12/3$. The vertical line indicates $C_t = 0.75$

rate and assuming that the jet does not heat up at all and a coflow temperature of 1000° the C_t is 0.60. Even in this optimistic case, the C_t is short of the threshold for a free jet. All other operating conditions will have a lower coflow velocity or higher jet velocity which means that the C_t is also lower in those cases. A free jet will thus also not be achieved when the setup is actually operating. The recirculation zone will likely be a lot smaller and weaker as compared to the zone observed in the cold flow case.

6.7. Cold flow conclusions

In this chapter, the flow field in the combustor was studied using PIV. From the obtained data some conclusions can be drawn. When the combustor was not enclosed lab air was seen to quickly entrain into the central jet. From the flow field, it seems that external lab air reaches the central jet at about 25 jet diameters away from the jet exit. When the entraining lab air reaches the central jet it will start affecting the combustion. Ensuring that the jet is enclosed is thus needed in order to get meaningful results on the effect of the coflow composition.

The foam disks failed to increase flow uniformity they were counterproductive. There are 3 disks in the mixing duct. When the top disk was present, the flow was found to be non-uniform both when the jet was on and when only the coflow is present. When the top disk is removed the coflow has a nice parabolic shape with a dip near the walls due to the boundary layer and near the centre due to the wake from the central jet assembly as can be seen in Figure 6.11. Also in the z-axis, a larger velocity is observed when the top disk is present. Since the disk is quite brittle it doesn't perfectly fit around the central jet and does not fit flush with the walls either. This causes small jets to form.

Regardless of the foam disk a recirculation zone is present in the combustion chamber. The coflow does not provide enough volume flow to feed the entrainment needs of the central jet, which causes the flow to recirculate. Using the Craya-Curtet number it was shown that in none of the operating points in this experimental campaign, the coflow provided enough flow rate to prevent recirculation zones to form. Even during regular operation, where the coflow will be heated, the current operating points will give rise to a recirculation zone, though it is expected to be less strong due to the higher coflow volume flow rate caused by the higher temperatures.

To remedy this either the size of the combustion chamber or the velocity difference between the central jet and the coflow should be changed. The diameter of the combustion chamber cannot be decreased since this will result in the windows being too small to see the entire spread of the jet. Changing the central jet velocity can be achieved either by changing the diameter of the jet exit or by changing the flow rate of the central jet. Alternatively, the coflow flow rate could be increased, but this would require additional pilot burners or an alternative burner setup to produce hot flue gasses.

From the vertical velocity the jet seems to be self-similar already from a distance of about 10 jet diameters away from the jet exit. However, the Reynolds stress does not appear to be self-similar at this location yet. It is possible that the jet never fully becomes self-similar since it is not a free jet. The jet spreading and jet decay coefficients were slightly off from those reported in the literature but were still in the same range. The spreading rate was found to be smaller than the values reported in the literature, while the centreline velocity decay rate was found to be in the range of reported values in the literature with the exception of the baseline case in the single window view. Where notably higher values for the decay rate constant B were found. The most important conclusion is that the windows are big enough to see the entire spread of the jet up to the design point of 210mm.

Finally, it can be concluded the setup is suitable for PIV measurements. Since the windows are at right angles the reflections caused by the laser were minimal, and because there is no curved glass there were no distortion effects. The main disadvantage of this setup is the small window size. The entire width of the combustion chamber cannot be imaged by the PIV cameras. In this experimental campaign, two different views were used. One in which the entire width of the combustion chamber was imaged, but this meant that the frame of the combustion chamber blocked part of the field of view. In the other frame, two cameras were focused on slightly more than half the combustion chamber width. This only works if the combustion chamber can be assumed to be symmetric, which was found not to be the case when the top foam disk was present. It might be possible to view the entire width of the combustion chamber by using a wide-angle lens and placing the PIV cameras closer to the windows.

7

Combustion results

Two experimental campaigns were executed with combustion. In the first campaign, the goal was to make the setup operational. The second campaign was focused on data collection of the reaction zone. In this chapter, this commissioning campaign and this second campaign will be discussed. First, some background on the setup and configuration is given and the measurement equipment will be discussed, then an overview of the testing procedures will be given, and some problems encountered during the two campaigns and their solutions will also be discussed. Finally, the results obtained from the reaction experiments are presented and analysed.

7.1. Setup & equipment

In this section, an overview of the setup is given for the two reacting campaigns.

7.1.1. The setup

In the commissioning of the setup, various configurations were tested. With or without the cylindrical duct. In the end, this duct was removed in the second campaign. In both campaigns, the octagonal combustion chamber is equipped with four quartz glass panels and four stainless steel 310 panels positioned in an alternating pattern. One of the steel plates has probe connections attached to it. These probe connections can be used to insert a thermocouple or a gas analyser probe. A DSLR camera is placed on the side of the setup, looking through one of the quartz glass panes. A traverse system is also used to take radial gas concentration and temperature measurements.

7.1.2. Probe locations

In Figure 7.1 a schematic is shown of the configuration of the combustor during the secondary campaign. The jet is recessed 43.5mm below the bottom of the combustion chamber window. A plate with ports placed at 30 mm intervals was used for the insertion of a gas probe and an S-type thermocouple. This plate is placed in one of the combustor's window frames. During the experiment ports 1, 3, 5, 7 and 10 were used. At the top of the combustor, at the end of the exhaust cone, there is an additional gas probe connection. A tube extends a couple of times the cone exit diameter into the combustion chamber to prevent any cooling air from being sucked in. This probe is only used for exhaust gas measurements. There is a thermocouple placed above this location but cooling air is mixed in at that point, making the data useful only for monitoring purposes.

During the commissioning campaign the central jet was recessed further downwards. The exit of the central jet pipe was located 88.5mm below the bottom of the combustion chamber window.

7.1.3. Gas analyser

The gas analyser system consists of three different modules. One module measures the O_2 concentration, the other CO_2, CO and CH_4 and the other module measures the NO and NO_2 concentration. The sample gas is collected through a simple stainless steel tube which is inserted into the combustor. A thermocouple is inserted into the gas inside the tube to measure the gas temperature. The gas is

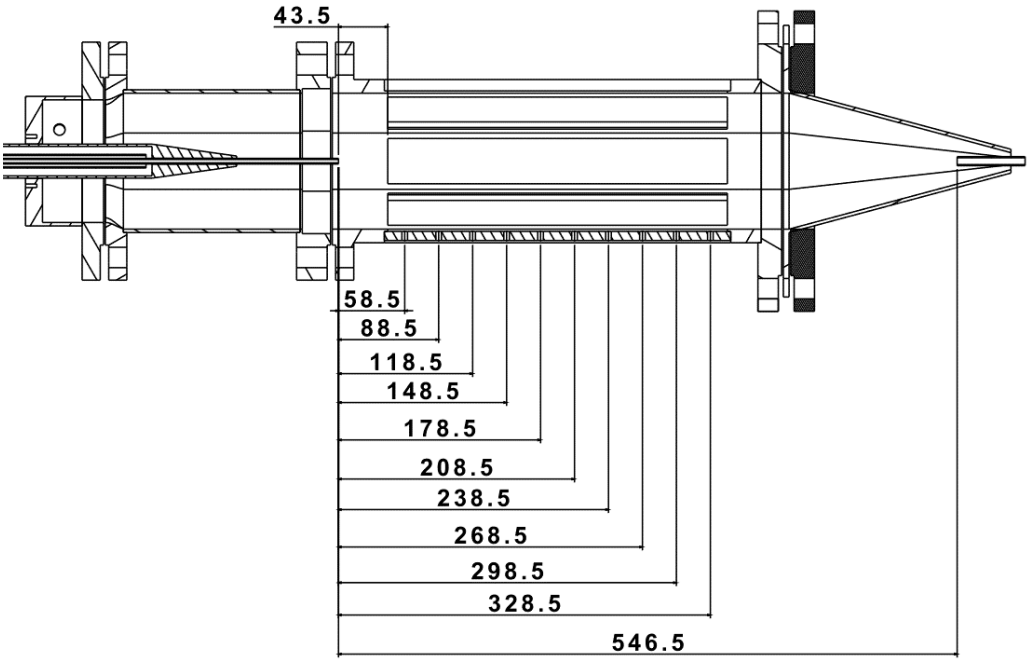

Figure 7.1: Distances in mm from the jet exit to the different measurement ports during the April campaign.

then transported to the gas analyser cabinet through a heated sample line. The temperature inside this line is kept at 180 $^{\circ}C$. This is done to prevent water from condensing out of the gas. These water droplets could absorb species from the gas mixture affecting the measured result. This is particularly a problem for NO_2 [Gluck et al., 2003]. For this reason, water is not condensed out of the gas mixture before entering the first measurement module, the Limas HW. Here the NO and NO_2 concentrations are measured. The gas is then cooled and filtered to remove some dust and water, after which it is sent to the Uras26 where CO, CO_2 and CH_4 concentration are measured. Finally, the gas is sent to the magnos28 which measures the oxygen concentration.

IR analyser

The ABB Uras26 module of the gas analyser uses the absorptivity of CO, CO_2 and CH_4 in the infrared spectrum to measure their concentration. A Non-dispersive Infrared (NDIR) photometer shines light into a cell where the sample gas is held. The gas will absorb some wavelengths of light; which wavelength depends on the species. Usually, a photodetector is then used to measure the light intensity at the end of the sample cell. However, the Uras uses an opto-pneumatic detector. This is a cell with a membrane capacitor filled with a reference gas of the species of interest. This detector cell is placed after the sample cell. After some of the light is absorbed by the species of interest in the sample cell less light will reach the detector cell. This will change the temperature of the reference gas in the detector cell, which in turn changes its pressure. The pressure change is then turned into an electrical signal by the membrane capacitor [Rüdiger et al., 2008].

$$I(\lambda) = I_0(\lambda)e^{-\alpha(\lambda)cl} \tag{7.1}$$

The absorption of light by the gas follows the Beer-Lambert law, which is given in Equation 7.1 [Popa and Udrea, 2019]. Here I is the detected intensity of light at a specific wavelength λ, I_0 is the emitted intensity, α is the wavelength-dependent gas absorption coefficient, c the gas concentration and l the light-gas interaction path length. The light path length is the sample cell length in the Uras. When the concentration of the gas of interest is very low the cell size can be increased to increase the ratio between the emitted and detected intensity. The cell length, therefore, determines the accuracy and span of the detectable gas concentration [Goselink, 2022].

UV analyser
The Limas21 HW module measures the NO and NO_2 concentration using differential UV resonance absorption spectroscopy (DUV-RAS). The advantage of using UV light is that H_2O and CO_2 do not absorb light in this spectrum and thus do not interfere with the measurement [Worthington and von-Hoersten, n.d.]. An electrode-less discharge lamp (EDL) is used as a source of UV radiation. This lamp is filled with a mixture of N_2 and O_2 at about 1 millibar pressure. A high-frequency induction is used to create a plasma in which the nitrogen and oxygen dissociate and form excited NO. When the electrons in the excited NO radicals fall back to their ground state they emit photons with a wavelength of around 226.5mm. The NO then decays back to N_2 and O_2. The NO molecule can have different rotational-vibrational states, and will thus generate an emission spectrum of different emission lines. These lines can be grouped into two categories: The cold and the hot lines.

1. The cold lines are generated with those transitions ending at rotation-vibrational quantum states in the electronic ground state which are populated by electrons of NO molecules showing a Boltzmann distribution of the rotational energy in thermodynamic equilibrium. These lines can be absorbed by the NO molecules in the sample cell.

2. The hot lines end at higher rotation-vibrational quantum states. These lines cannot be absorbed by the NO in the sample cell. This is therefore used as a reference signal.

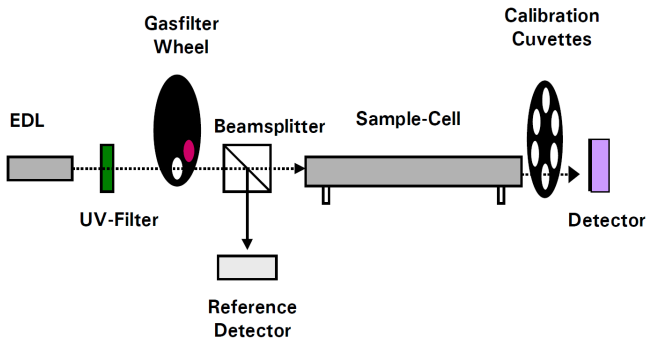

Figure 7.2: Schematic of the DUV-RAS analyser as taken from [Worthington and von-Hoersten, n.d.]

In Figure 7.2 a schematic is shown of the DUV-RAS analyser. After the EDL a UV-filter is used to select specific emission bands, the light then passes through a gas filter wheel this wheel contains a cuvette with NO which can be moved into the light stream. By moving the cuvette into the light beam the cold lines will be blocked, but the hot lines will pass through into the sample cell. Looking at the reduction in intensity in the sample cell will make it possible to account for contamination in the sample cell. When the cuvette is not in the light beam the cold lines will pass through to the sample cell and some light will be absorbed by the NO following the Beer-lambert law as given in Equation 7.1. After the gas filter wheel, the beam is split by a beam splitter, some of the light will go to a reference detector and some will go through the sample cell to the detector. By taking reference measurements zero drift due to ageing of the EDL or UV-filter can be accounted for.

The Limas can detect the NO_2 concentration simultaneously by using wavelength comparison in the 200-500nm range [ABB, 2004]. No good source on the exact methodology could be found. Previously, these UV-photometers used a molybdenum catalytic converter, to convert NO_2 into NO [Gluck et al., 2003]. By measuring the NO concentration prior and after conversion the NO_2 concentration can be deduced from the difference between the measurements.

These measurements are taken before water is removed from the gas stream due to the water solubility of NO_2 and NO [Gluck et al., 2003]. NO_2 in particular is very water soluble. It reacts with water to form HNO_2 and HNO_3 following the reaction in Equation 7.2 [Gluck et al., 2003]. NO has a more limited solubility: only 7% at 0 °C and it is insoluble at 100 °C. Condensed water in the probe or tube will absorb some of the NO_2 and give an invalid reading. Therefore the sample line is heated to 180 to prevent water from condensing.

$$NO_2 + H_2O \rightarrow HNO_2 + HNO_3 \tag{7.2}$$

Magnetic analyser
The Magnos28 module is used to determine the dry oxygen concentration. Oxygen is paramagnetic, which means it is attracted by an electric field [Systech Instruments, n.d.]. The working principle of the Magnos is of a rotating lever with two nitrogen-filled spheres at either end. This assembly is mounted in a strong magnetic field. Since the oxygen is attracted to the magnetic field it will push against the spheres creating a torque. A mirror is attached to the centre of the suspension assembly. A small light shines light at this mirror the rotation of the lever can then be measured by the location where the reflected light lands with a photo-sensor. In the Magnos28 this system has been replaced by the microwing [Egerton, 2021]. This doesn't use the glass dumbbells but integrates everything onto a circuit. It still operates on the sample principle as the dumbbell assembly.

Other gasses can interfere with the measurements as they are also either attracted or repelled by the magnetic field. CO_2 is diamagnetic, which means it is repelled by the magnetic field, but oxygen has a magnetic force that is 160 times greater than CO_2[Iwasaka, 2009]. NO is also paramagnetic and can have quite an interference effect [Systech Instruments, n.d.], it is however only present in very small concentrations and this interference is therefore not really of any concern.

In Table 7.1 an overview is shown of the three modules installed in the gas analyser, with the guaranteed measurement range included.

Uras26 (dry) IR absorption		Limas21 HW (wet) DUV-RAS		Magnos28 (dry) Paramagnetism	
Gas	Range	Gas	Range	Gas	Range
CO	0 - 1000 ppm	NO	0 - 10ppm	O_2	0 - 25 % volume
CO_2	0 - 100 % volume	NO_2	0 - 10ppm		
CH_4	0 - 50.000 ppm				

Table 7.1: Overview of the modules in the gas analyser, with their measurement principle, measurement gasses and measurement range.

7.1.4. Thermocouple temperature measurement

Thermocouples are devices used to measure the local temperature. They make use of the thermo-electric effect, where when there is a temperature difference between two points a voltage is induced. The Seeback coefficient $S(T)$ is a material property and also a function of temperature [Kasap, 2001].

If one were to try to measure the voltage difference between two ends of a cable by connecting a voltage meter to the cable made of the same material as the cable the voltages would cancel since the temperature will be equal at the connecting nodes and thus induce opposing voltages. Thermocouples, therefore, use two different metals, for example, Nickel-Chromium / Nickel-Alumel in type K thermocouples.

Thermocouples can measure temperature very accuracy and are relatively cheap and easy to operate. However, the disadvantage is that thermocouples measure the temperature of the metal and not the temperature of the gas. This makes it hard to measure temperature oscillations and local temperature fluctuations accurately Additionally the metal temperature will be influenced by heat being conducted away from the measurement head by the wires.

Several thermocouples are installed on the setup. Thermocouples are used to monitor the temperature of the material of the walls, the inlet temperature of the central jet mixture, the exhaust temperature in the cone, and the exhaust temperature at the end of the exhaust duct. An S-type thermocouple is used to collect data on the temperature in the combustion chamber. This thermocouple was also mounted on a traverse system such that radial measurements of the temperature could be taken.

7.1.5. Chemiluminescence

Chemiluminescence occurs when a product of a chemical reaction decays from an excited energy level to a lower energy level and emits light in this process. During the combustion of hydrocarbon flames

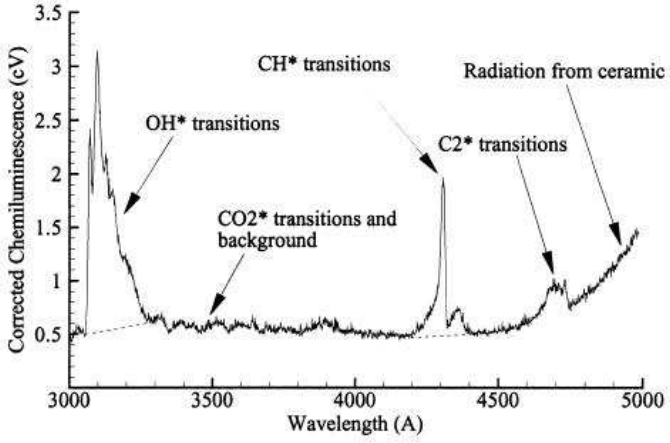

Figure 7.3: Emission spectrum of a premixed methane-air flame, taken from Haber and Vandsburger, 2003.

CH^*, OH^*, C_2^* and CO_2^* are responsible for most chemiluminescence in the visible and ultraviolet spectrum [Nori and Seitzman, 2008]. In experiments by Medwell and Dally, 2012b CH^* chemiluminescence was used to determine the lift-off height of a flame in flameless operation. A 430 nm filter was used to capture just the signal from the CH^* emissions.

In Figure 7.3 the emission spectrum of a methane-air flame is shown. As Kathrotia, 2011 states, the emissions for OH^* give a strong spectrum with a peak intensity at about 309 nm. The emissions of CH^* can be found at about 387 nm and 432 nm. While CO_2 has a very wide spectrum; it appears as a continuum, spanning from 300 nm to about 600nm. $C2^*$ emission bands are mostly seen in fuel-rich mixtures. Its emission bands are between 436 nm and 564 nm. These combined emissions give the flame a blue colour.

A CMOS camera and a 325 nm filter with a full-width-at-a-half-maximum of 50nm were used to observe the flame. However, the luminosity of the combustion zone was too low to produce an image. Instead, a Nikon D7500 DSLR camera is used to take photographs of the flame through one of the quartz windows, without a filter. For each of the measurement cases, about 292 images were taken. As will be discussed in subsection 7.6.1, the blue channel will be isolated in these images to remove background interference.

7.2. Methodology

In this section the experimental methodology is detailed. The test conditions for the commissioning and secondary campaign are discussed first, and then the calibration procedure of the gas analyser is presented. Finally, the oxygen correction methodology is stated.

7.2.1. Test matrix

Two separate campaigns were undertaken. The first campaign was part of the commissioning of the setup, a second campaign was designed based on the observations in the commissioning campaign. In the commissioning campaign, it was observed that the flame was very distributed and moved around a lot. This could have been caused by a too-fast jet velocity. The focus of the second campaign is to also look at the effect of the jet velocity. Furthermore, the effect of the oxygen concentration, central jet equivalence ratio and the effect of the additional diluent will be analysed.

In the initial campaign, the central jet volume flow rate is fixed, but the coflow flow rate was not when changing the diluent flow rate. This makes the residence time in the combustor constant between all cases, except when extra diluent was added. Since one of the main goals of these experiments is to analyse the effect of NO_x formation, and residence time can have a large effect on NO_x production. Then the equivalence ratio of the central jet was varied between the lowest possible equivalence and an equivalence of 1.15. With the main objective to look at the stability of the flame. To keep the central jet volume flow rate constant the power of the main burner would increase with increasing equivalence.

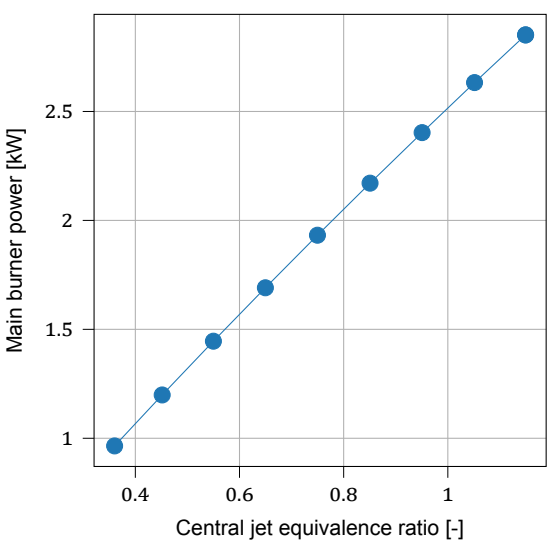

(a) Main burner power as a function of the central jet equivalence.

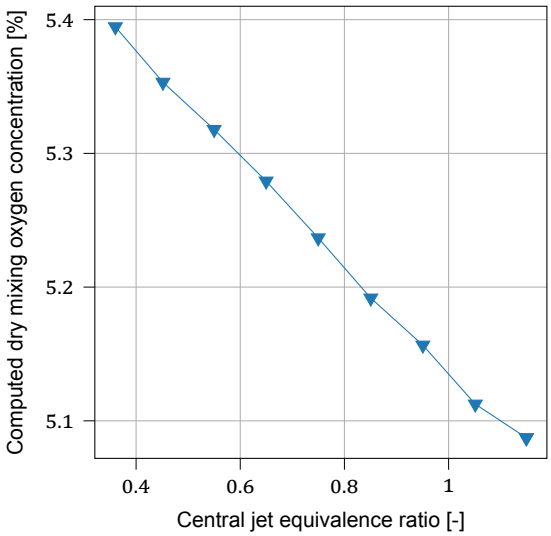

(b) Oxygen concentration of the coflow and central jet combined as a function of the central jet equivalence ratio.

Figure 7.4: Conditions for the commissioning campaign

	Flow rate [lnpm]	Velocity [m/s]		Reynolds [-]	
T_{ref} [°C]		20	300	20	300
Jet	44.4	112.3	219.7	22,307	13,769
T_{ref} [°C]		20	1000	20	1000
Coflow	203.4	0.31	1.32	4,669	1,768
Coflow + 20lnpm	223.4	0.33	1.45	4,912	1,860
Coflow + 50lnpm	253.4	0.38	1.65	5,279	1,999

Table 7.2: Flow conditions in the central jet and the coflow during the commissioning campaign

When changing the central jet equivalence the coflow conditions were kept constant. Additionally, a diluent flow of 20 and 50lnpm of nitrogen and carbon dioxide was added. The equivalence and power setting of the pilot burners remained the same. When mixing in additional diluent the central jet equivalence was kept constant at 0.85. The main burner power setting and the mixing oxygen concentration are shown in Figure 7.4a and Figure 7.4b respectively. The mixing oxygen concentration is the theoretical oxygen concentration that would be obtained if all gasses flowing into the combustion chamber were perfectly mixed. The flow rates, velocities and Reynolds numbers are given in Table 7.2, the coflow conditions and pilot burner settings are given in Table 7.3

During commissioning the initial chosen jet velocity seemed too high. The flame was too lifted and there was no continuous flame front. In the second campaign, three different jet flow rates were chosen: the volume flow rate from the commissioning campaign is the high jet case, half that volume flow rate is the low jet case and the intermediate between these two points is the base jet case. Just like in the commissioning campaign, the central jet volume flow rate is kept constant, but unlike the previous campaign, the coflow flow rate is also maintained at a constant volume flow rate. With increasing added diluent the power setting of the pilot burners was decreased. To maintain a constant oxygen concentration in the coflow the pilot burner equivalence ratio is varied as well.

	Pilot power [kW]	Equivalence	O_2 [%]	Dry O_2 [%]
No diluent	10.9	0.94	1.19	1.45
20 lnpm	10.9	0.94	1.07	1.28
50 lnpm	10.9	0.94	0.96	1.12

Table 7.3: Coflow and pilot burner settings for different added diluent flow rates in the commissioning campaign.

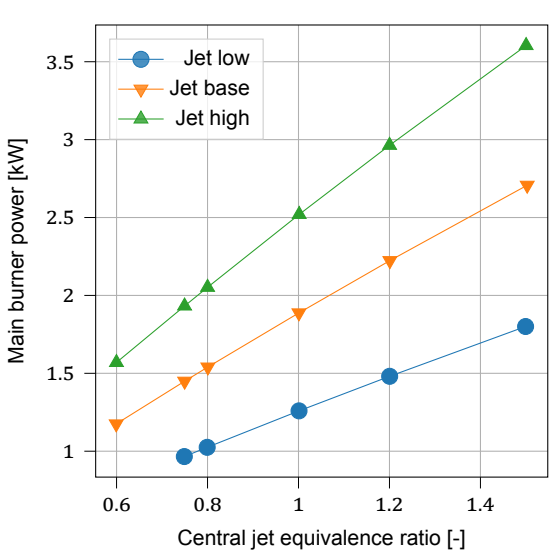

(a) Main burner power as a function of central jet equivalence ratio for the three jet flow rates.

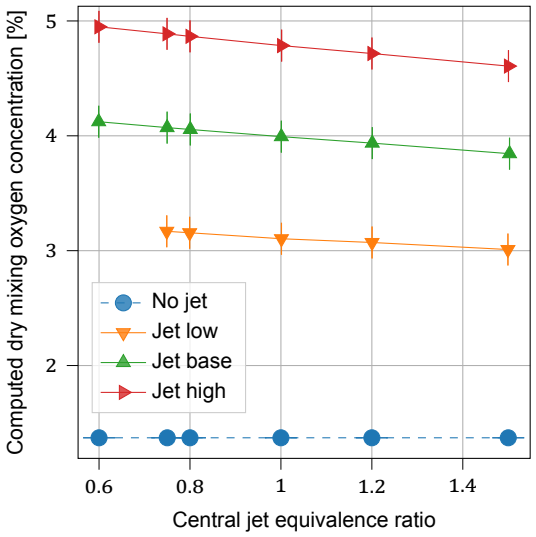

(b) Oxygen concentration of the coflow and central jet combined as a function of central jet equivalence ratio for the three jet flow rates. The no-jet case is a measurement provided as a reference for the coflow conditions

Figure 7.5: Conditions for the second campaign

In this campaign the central jet equivalence ratio was varied between 0.65 to 1.5. This lowest point was chosen based on the minimum possible flow rate of methane to the central jet, the highest equivalence was chosen such that the overall equivalence would be slightly rich for all three jet flows. Additionally, the effect of diluent was observed by supplying either 20 or 50 lnpm of N_2 or CO_2 to the coflow. When diluent was supplied the central jet equivalence was kept at 1.0. The flow rates, velocities and Reynolds numbers for the central jet and the coflow are tabulated in Table 7.4. In Table 7.5 the settings for the pilot burner are given. In Figure 7.5a the power setting of the main burner is shown as a function of the equivalence ratio. Finally, in Figure 7.5b the theoretical mixing oxygen concentration is given. This is the theoretical oxygen concentration that would be obtained if all gasses flowing into the combustion chamber were perfectly mixed.

	Flow rate [lnpm]	Velocity [m/s]		Reynolds [-]	
T_{ref} [°C]		20	300	20	300
Low jet	22.2	56.2	109.8	11,138	6,869
Base jet	33.3	84.3	164.7	16,714	10,310
High jet	44.4	112.4	219.7	22,291	13,750
T_{ref} [°C]		20	1000	20	1000
Coflow	202.8	0.3	1.321	4,647	1,760

Table 7.4: Flow conditions in the central jet and coflow for the second campaign

	Power [kW]	Equivalence	O_2 [%]	Dry O_2 [%]
No diluent	11.1	0.958	0.80	0.98
20lnpm	9.92	0.953	0.81	0.97
50lnpm	8.22	0.942	0.83	0.96

Table 7.5: Coflow conditions and pilot burner settings for different added diluent flow rates during the second campaign.

7.2.2. Calibration procedure

The gas analyser needs to be calibrated daily to get the highest degree of accuracy. In earlier experiments, an efficient calibration procedure was developed for this system [Goselink, 2022]. The system

uses a two-point calibration procedure, consisting of a zero measurement and a span measurement. The span measurement is taken by providing a known gas mixture to the analyser and specifying the concentration to the analyser. A linear calibration curve is then drawn between the two measurement points. In this calibration procedure, the cross-sensitivity and gas component correction is disabled, therefore the calibration gas mixture cannot contain any other gasses which might induce cross interference [ABB, 2009].

Four gas bottles are used in the calibration process. Each of these bottles has a specified amount of one or two target gasses. The overview in Table 7.6 lists all four gas bottles, with their contents, in the order in which they are used for calibration. The concentration in these bottles is at about 80% of each of the module's maximum span, and are certified to have a concentration margin of $\pm 2ppm$, or $5vol.\%$ [Goselink, 2022]. The oxygen zeroing is performed on bottle 3, as the manufacturer certified that this bottle did not contain any oxygen. The NO_2 zeroing is also performed twice with different calibration bottles as this value fluctuated a lot.

	Contains:	Calibrates:
Bottle 1	NO_2: 8.1 ppm N_2: balance	Span: NO_2 Zero: CO, CO_2, CH_4
Bottle 2	CO_2: 59.8 vol.% N_2 balance	Span: CO_2 Zero: NO, NO_2
Bottle 3	NO: 8.46 ppm N_2: balance	Span: NO Zero: NO_2, O_2
Bottle 4	CO: 801 ppm CH_4: 3.99 vol.% N_2: balance	Span: CO, CH_4
Lab air	Ambient air	Span: O_2

Table 7.6: Overview of the calibration bottles, listed in sequence of the calibration.

7.2.3. Oxygen correction

It is customary to present gas concentration measurements corrected for 15% oxygen concentration. This eliminates the effect of dilution on the measurement and makes it easier to compare to other cases where the oxygen concentration might have been lower. The correction is given in Equation 7.3 [Baukal and Eleazer, 1998]. The fraction 0.2095 is the concentration of oxygen in regular air, X_{O_2} is the measured oxygen concentration, and $X_{measured}$ is the measured concentration of the gas of interest.

$$X_{corrected} = X_{measured}\left(\frac{0.2095 - 0.15}{0.2095 - X_{O_2}}\right) \tag{7.3}$$

7.3. Derived quantities

Some quantities can be computed based on measured values. The methods used to do this are detailed in this section.

7.3.1. Measured equivalence ratio

The equivalence ratio can be computed from the measured flow rates in the mass flow controllers. There are three different equivalence ratios applicable in this setup. The pilot burners have a specified equivalence ratio. This can be computed using Equation 7.4. $\dot{V}_{pilot\ fuel}$ is the volume flow rate of methane towards the pilot burners, $\dot{V}_{pilot\ air}$ is the air flow rate, and $\frac{2}{0.21}$ is the stoichiometric air to methane ratio. The same equation can be used to compute the central jet equivalence ratio, but instead of using the pilot air and fuel flow rates use the ones for the central jet.

$$\phi_{pilots} = \frac{\dot{V}_{pilot\ fuel}}{\dot{V}_{pilot\ air}}\left(\frac{2}{0.21}\right) \tag{7.4}$$

Additionally, an effective equivalence ratio can be computed. Since the pilot burners are operating in the lean regime there will be some oxygen left. Taking this oxygen into account yields an effective

equivalence ratio. The formula for which is given in Equation 7.5. The second term in the denominator is the volume flow rate of oxygen left over after the combustion of the pilot burners.

$$\phi_{effective} = \frac{2\dot{V}_{fuel\ main}}{0.21\dot{V}_{air\ main} + \dot{V}_{pilot\ fuel}\left(\frac{2}{\phi_{pilots}} - 2\right)} \tag{7.5}$$

7.3.2. Central jet produced NO

It is interesting to look at how much nitric oxide the central jet is actually producing. For each coflow operating condition gas concentration measurements were taken. Combining this measurement with the measurements with jet produced or consumed amount of NO can be computed. In Equation 7.6 is X_{jet} the concentration of NO produced in the central jet, $X_{measured}$ the measured NO concentration when the jet is on, $\dot{V}_{coflow}$ and $\dot{V}_{jet}$ the total coflow and jet flow rate when the jet is on in lnpm, X_{no-jet} the measured concentration of NO when the jet is off and $\dot{V}_{no-jet}$ the coflow volume flow rate when the central jet is off in lnpm.

$$X_{jet} = \frac{X_{measured}\left(\dot{V}_{coflow} + \dot{V}_{jet}\right) - X_{no-jet}\dot{V}_{no-jet}}{\dot{V}_{jet}} \tag{7.6}$$

7.4. Error estimation

In this section, the method for estimating the error margins on the results is discussed.

7.4.1. Statistical confidence interval

It can be assumed that the temperature and gas concentration measurement fluctuations follow a normal distribution. The estimator for the standard deviation of a randomly sampled dataset is given in Equation 7.7 [Dekking et al., 2005]. N is the number of samples, x_i a discrete sample and $\overline{x}$ the average value of all samples. The lower and upper bounds of a 95% confidence interval, l_n and u_n, can then be obtained from Equation 7.8 [Dekking et al., 2005].

$$S_n = \sqrt{\frac{1}{N}\sum_{i=1}^{N}(x_i - \overline{x})^2} \tag{7.7}$$

$$l_n, u_n = \overline{x} \pm 1.96\frac{S_n}{\sqrt{N}} \tag{7.8}$$

Error bars are shown in all temperature and gas concentration plots indicating the 95% confidence interval. In some plots, the 95% confidence interval is also shown for the effective equivalence ratio. This is based on the measured flow rates. Both the thermocouple data and the gas analyser data are collected at 10 Hz. For the thermocouples 30 seconds worth of data is collected, resulting in about 300 data points for each measurement. For the gas probe, 1.5 minutes of data is collected, resulting in about 900 data points for each measurement.

7.4.2. Traverse

As will be discussed in subsection 7.6.2, a traverse system is used to collect temperature and gas concentration measurements radially at the first port of the measurement plate. The system starts at the centre of the combustion chamber, which is located approximately 62 mm from the wall, and then moves outward to the wall in one continuous movement. With the thermocouple, the gas analyser moves at about 0.62 mm/s, with the gas probe it moves at about 0.42 mm/s. Both the gas probe and the thermocouple data are collected at 10Hz. The confidence interval for each measurement point is computed by assigning a bracket around a single measurement location. All data points which are located within this bracket are used to compute the confidence interval using Equation 7.7 and Equation 7.8. This bracket is equal to the probe diameter. So for the thermocouple measurements, all data points which lay 1.5 mm on either side of a location will be counted towards this confidence interval. For the gas probe, it is 3 mm on either side. This means that for the gas probe, there are about

97 measurements inside each bracket, while for the thermocouple there are about 71 measurements inside each.

7.5. Encountered issues

During the commissioning campaign and the second campaign, some issues were encountered. In this section, those issues will be discussed.

7.5.1. Wrong mass flow controller calibration

As part of a sanity check of the flow calculations the oxygen concentration measured while heating the setup was compared to the computed oxygen concentration. A discrepancy of about 2% was observed. As further validation, the oxygen concentration was also computed using Cantera, which resulted in the same oxygen concentration as obtained from the flow rate calculations. The mass flow controller used to supply air to the pilot burner has only been calibrated on nitrogen. Since it is now supplying air the mass flow rate it reports is higher than what it is actually supplying.

To find the relationship between the measured and actual flow rate the oxygen concentration was measured in the combustion chamber while supplying different rates of air through the pilot burner and a fixed rate of nitrogen through the diluent line. All other flows were turned off. From the measured flow rate of air and nitrogen, the expected oxygen concentration can be calculated. The actual air flow rate can be back-calculated from the measured oxygen concentration. Luckily, it turns out that there is a linear relation between the measured and actual flow rates. The relation between the assigned or measured flow rare and the real flow rate is given in Equation 7.9. This function has an R^2 fit of 0.9999 with the test data. This equation is used to set the flow rates on the mass flow controller based on the required mass flow rate as computed by the control program.

$$\dot{v}_{assigned} = 1.1381\dot{v}_{real} - 0.6213 \tag{7.9}$$

At this point this mass flow controller had already been used in the cold flow campaign. This correction was applied retroactively to the data to compute the correct flow velocities.

After the second campaign it was discovered that Bronkhorst, the manufacturer of the mass flow controllers, uses a different definition for normal litre per minute. The standard definition of lnpm is based on a temperature of 20°C at 1 atmosphere in pressure; standard litre per minute is defined as 0 °C at 1 bar pressure [The Engineering ToolBox, 2004]. Bronkhorst however, defines lnpm at 0 °C and 1 atmosphere and lspm at 20 °C and also 1 atmosphere in pressure [Bronkhorst, n.d.]. This doesn't make a difference to the results for the most part as all the flow rates are scaled the same way. Problems arise in the conversion between volume flow rate and mass flow rate, like in the calculation of the volume flow rate of methane based on the power setting of the pilot burners and the main burner. This causes a small discrepancy between the specified power and results in a slightly higher power, and it changes the actual equivalence ratio.

7.5.2. Broken cooling line

When supplying cooling air to the cooling assembly the final section of the central jet pipe, which is uncooled, would immediately stop glowing. The pipe would normally glow if no gasses are supplied to the central jet line, and the cooling air is turned off. The quick response to the cooling means that air must be flowing from the cooling line into the central jet line. It is probable that the weld which connects the central fuel line on the inside of the cooling assembly to the conical section broke due to thermal stresses. As the outside of the cooling assembly heated it expanded, while the cooled central pipe did not expand. The weld is an obvious weak point and therefore broke. Ultimately this turned out not to be a problem since cooling of the central jet is not required. The stainless steel 310 is able to withstand the temperatures inside the mixing duct without a problem. It is thus not possible to control the temperature of the gasses in the central jet. Additionally, since the central jet assembly has been recessed further into the mixing duct it is not possible to measure the central jet temperature.

7.5.3. High heat losses

The heat losses in the mixing duct were higher than predicted using the heat transfer model. During the initial test foam disks were placed at the bottom of the coflow attachment and between the bottom

and top mixing duct. These plates seemed to act like heatsinks, however. The temperature below and around these plates would rise, but it would not transfer much up the mixing duct beyond the foam disks. In chapter 6 the top foam disk was found to create a non-symmetric flow. Now they also reduce the flow temperature drastically, for this reason, the disks were completely removed from the setup.

Removing all foam disks did not raise the temperature enough, an additional layer of insulation was installed on the combustor flange and the conduction between the flange and the rest of the structure. Also, this was not enough. The temperature in the combustion chamber was too low to ignite the main burner. For this reason, the bottom mixing duct was removed. This only leaves the octagonal mixing duct. An adaptor was made for the central jet assembly which made it possible to move the central jet down. Before removing the cylindrical mixing duct water would condense in the combustion chamber during startup. After the mixing duct was removed this was not the case anymore.

7.5.4. Pilot burner operational limitations

The power of pilot burners was pushed much beyond their design limit, and therefore the pilot burners had a more limited range of equivalence ratios it could operate in. A stable flame could be produced in an equivalence ratio range of 0.87 to 0.99 at a power of about 5kW for each burner.

7.5.5. Singing flame

During the commissioning of the setup, a loud sound would be produced when both pilot burners were tuned on simultaneously. The sound produced ranged from about 220-270Hz. During single burner operation, this sound could not be heard. As the burner heated up the frequency of the sound would increase. At a certain point of heating blow off would occur. Likely due to the instabilities produced by this sound. Pre-heating the setup with the electric burner did not alleviate the issue.

Both pilot burners have one common mass flow controller for air and one common controller for methane. The lines are split at a T-section just below the setup. Both burners are of the same model, and have an approximately equal pipe length after the t-section. The pressure drop and therefore also mass flow rate are expected to be equally split. The sound waves produced by the setup could however travel down the air and fuel line and periodically change the pressure drop, which would result in an oscillating mass flow rate, and continuously varying equivalence ratio. This is a plausible explanation for the instability observed when both burners are on.

By isolating the fuel and air line the instability might disappear. Getting two additional mass flow controllers would be costly and would take a lot of time. Instead, the lines can also be isolated by choking the flow after the T-section. This would prevent the sound from affecting the flow rate. By using a fixed hole size the flow rate can be controlled by altering the pressure upstream of the choking hole. The pressure range upstream of the hole can be between 2 and 8 bar, and the specified operating temperature range is -5 °C to 20 °C. The mass flow rate in choked conditions for an ideal compressible gas can be obtained from Equation 7.10 [Anderson, 2011]. By specifying the extreme conditions, the limiting maximum flow rate is at 8 bar and 20 °C, and the limiting minimum mass flow rate is at 2 bar and -5 °C.

$$\dot{m} = \frac{AP_T}{\sqrt{T_T}}\sqrt{\frac{\gamma}{R}}\left(\frac{\gamma+1}{2}\right)^{-\frac{\gamma+1}{2(\gamma-1)}} \tag{7.10}$$

The obtained minimum and maximum flow rates can be converted to power and equivalence ratio. The pilot burners should operate at an equivalence ratio of 1 during operation. By tweaking the choking diameter of the fuel and air line the plot in Figure 7.6. This plot is obtained with a diameter of 0.25mm for the fuel line and 0.9mm for the air line. All values between the lines are valid operating conditions. Higher equivalence ratios or lower power settings are possible, but the flow will not be choked in that case

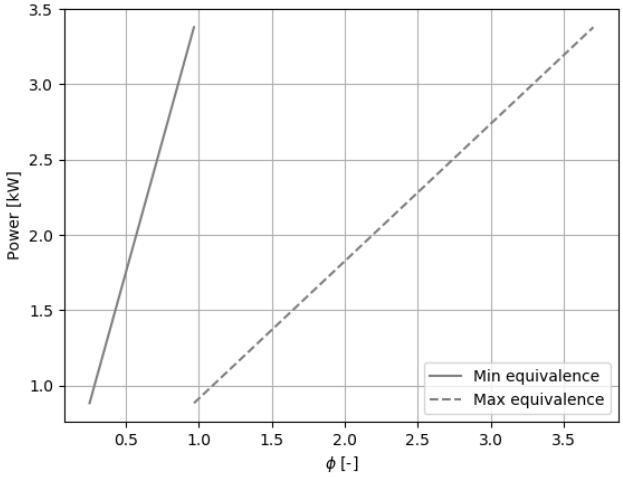

Figure 7.6: Operating range under choked conditions, with D_{fuel} = 0.25mm, and D_{air} = 0.9mm. The area between the lines are valid operating conditions for one pilot burner

To add the choking hole a T-section is filled with about 4mm of silver, the hole is then drilled into this material. The hole is thus several diameters long; the pressure drop over it might be quite notable. The Darcy-Weisbach equation in Equation 7.11 [Howell and Weathers, 1970] gives the pressure drop over a tube based on the pipe friction coefficient λ, the pipe length over diameter L/D, the density ρ and the velocity u squared. Since in all conditions, the flow will be choked the formula is re-written based on the Mach number and simplified, yielding Equation 7.16.

$$\Delta P = \lambda \frac{L}{D} \frac{\rho}{2} u^2 \tag{7.11}$$

$$P_T = \rho R T_T \rightarrow \rho = P_T/(R \cdot T_T) \tag{7.12}$$

$$u = M\sqrt{\gamma R T} \tag{7.13}$$

$$\rightarrow \Delta P = \lambda \frac{L}{D} \frac{P}{2RT_T} M^2 \gamma R T \tag{7.14}$$

$$\frac{T}{T_T} = \left(1 + \frac{\gamma - 1}{2} M^2\right)^{-1} \rightarrow \frac{T}{T_T}(M = 1) = \frac{2}{1 + \gamma} \tag{7.15}$$

$$\rightarrow \Delta P(M = 1) = \lambda \frac{L}{D} \frac{P_T \gamma}{1 + \gamma} \tag{7.16}$$

The pipe friction coefficient can be computed using the Colebrook equation given in Equation 7.17 [Colebrook, 1939], where Re is the Reynolds number based on the pipe diameter, D the diameter in mm and k the material roughness coefficient also in mm. The roughness coefficient for silver could not be found, the roughness coefficient for stainless steel is 0.015mm [Engineering Toolbox, 2003b], for drawn aluminium and copper it is an order of magnitude smaller. Using steel is thus a conservative estimate. With this, the friction coefficient for the methane choke was found to be 0.0146 at 2 bar, and 0.0143 at 8 bar.

$$\frac{1}{\sqrt{\lambda}} = -2 \log\left(\frac{2.51}{Re\sqrt{\lambda}} + \frac{k}{D} 0.269\right) \tag{7.17}$$

The pressure drop on the methane line is then found to be 0.25 bar at an inlet pressure of 4 bar, and 0.96 bar at a pressure of 8 bar. The burner only requires a pressure drop of 35 mbar, which means that at a pressure of 2 bar before the choke, there will be 1.75 bar after the choke which is enough to provide sufficient pressure for the gasses to pass through the burner.

In the end this did not alleviate the issue. The combustor is thought to act like a Sondhouse tube. This is a tube with one open end and one closed end, much like the combustor setup. Sound is

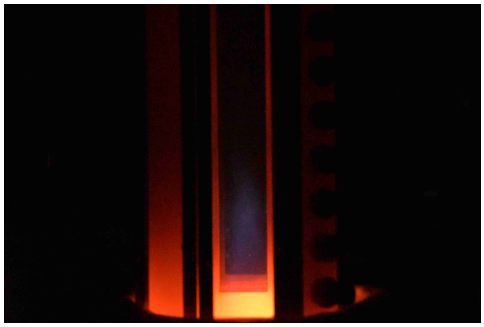

Figure 7.7: Image of the flame from the commissioning campaign for a central jet equivalence ratio of 0.55

produced when a burner is placed at the bottom of the tube. Kaneko et al., 2008 point out that there are several explanations for the underlying mechanism producing these sounds, but in general it is related to a coupling between buoyancy effects and heat transfer effects. When there is a large difference in temperature between the bottom of the tube and the top a sound will be produced. It turned out that cooling the central jet with a sufficiently high enough air flow rate stopped the sound from being produced. In the end, when the cylindrical mixing duct was removed the sound was not produced at all anymore. The temperature difference between the bottom and top of the combustor is not large enough to produce this effect. The chocked hosepillar were therefore also removed.

7.5.6. Nitrogen-dioxide measurements

The measurements of NO_2 are negative at times. It is unclear what causes this. In Equation 7.1.3 the working principle of the LIMAS gas analyser module is explained. ABB specifies that NO_2 measurements are taken using wavelength comparison, but the exact methodology could not be found. It is therefore hard to say what exactly causes this problem. A possible explanation could be that a water droplet in the probe tubing causes a pressure drop resulting in a lower density of gas and therefore also less light is absorbed by the gas, but this should then also influence the NO measurements. Furthermore, ABB specifies that they apply pressure correction using an integrated pressure sensor so the gas analyser should be able to account for this.

7.6. Results

In this section, the results from the commissioning and second campaign are discussed. First, the results from the photographs are discussed. Then the gas and thermocouple measurements are analysed. Finally, the results are summarised and discussed.

7.6.1. Visual shape of the combustion zone

A DSLR camera was placed in front of one of the windows of the combustion chamber both in the commissioning and follow-up campaign. Photos were taken at regular intervals. The flame is very faint and hard to observe as can be seen in Figure 7.7. This picture was taken during the commissioning campaign when operating the central jet at an equivalence ratio of 0.55. The glow of the metal frame is brighter than the flame; making it hard to discern, especially at the bottom of the picture. The flame is not observed in a single location but dances around. In some pictures, a flame can hardly be seen at all. The shape and location of the flame also appear to change depending on the equivalence ratio. With a low jet speed from the second campaign, the flame dances around close to the bottom of the frame. Increasing the equivalence ratio leads to a broader distribution with the highest intensity further downstream. The same trend with equivalence ratio is observed with the base and high jet speeds from the second campaign. Increasing the jet speed also results in a more distributed appearance and the brightest point being located further downstream. Oldenhof et al., 2010 describes ignition kernels forming which convect downstream and then form a more-or-less continuous flame zone. This described continuous flame zone is not observed here. Although the authors also observed ”large spatial and temporal variations in flame interface height”, which could be similar to what is observed here.

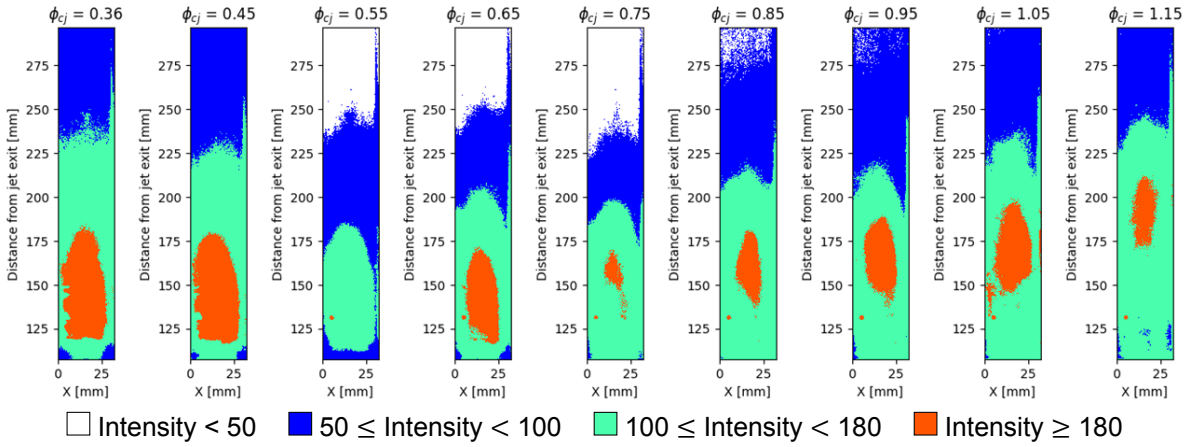

Figure 7.8: The intensity of the commissioning flame normalised with itself for different equivalence ratios. (img-avg)

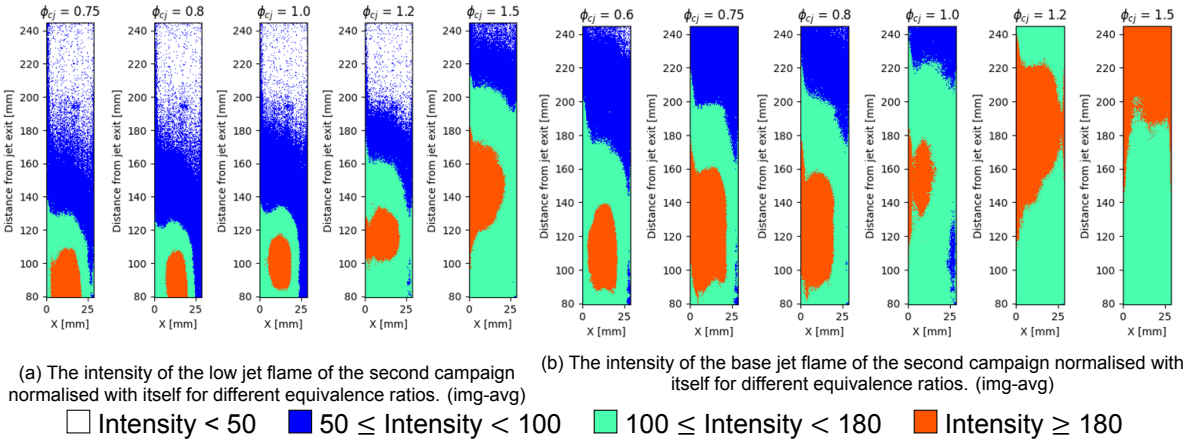

(a) The intensity of the low jet flame of the second campaign normalised with itself for different equivalence ratios. (img-avg)

(b) The intensity of the base jet flame of the second campaign normalised with itself for different equivalence ratios. (img-avg)

Figure 7.9

In order to isolate the flame from the background only the blue channel in the pictures is used, the other channels are discarded. Then the average of all of those pictures is taken for each operating point. The point where the average light intensity is highest is the point in which the flame is most often located. The average image still contains some background interference. To remove this the average is removed from each image and then the average is taken of that. Then each image is normalised with itself to create an intensity map. The pictures are taken with 8-bit colour depth, so for each colour channel, the intensity can vary between 0 and 255. Normalising the image with itself makes it such that the brightest point in the image gets assigned an intensity of 255, all other pixels are then multiplied with the same factor. For each equivalence ratio, a contour plot of the intensity is generated. For the commissioning campaign, these are all displayed next to each other in Figure 7.8.

When changing the equivalence ratio the jet velocity will remain constant. The coflow conditions also do not change. Still, the brightest area can be seen to move downstream with an increasing equivalence ratio. To better track the downstream movement of the flame a weighted centroid is calculated. For each vertical line in the photo, the intensity of the blue channel is summed over the entire width and multiplied by the distance from the bottom of the frame, this is then divided by the total sum of the intensity resulting in the downstream location of the weighted centroid. This location is plotted in Figure 7.11. As can be seen, the minimum location of the flame is observed at a central jet equivalence ratio of between 0.55 and 0.75. Both moving towards a leaner concentration and a richer concentration results in the intensity centroid moving downstream. The lowest possible equivalence ratio reached was 0.36. This was due to limitations on the minimum flow rate through the methane mass flow controller.

The same method was applied to the photographs from the second campaign. In Figure 7.9a, Fig-

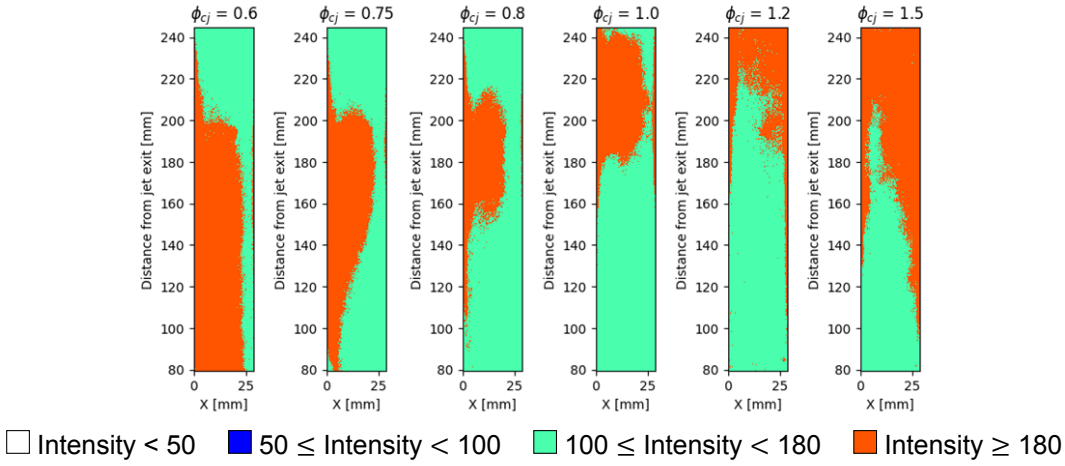

Figure 7.10: The intensity of the high jet flame of the second campaign normalised with itself for different equivalence ratios. (img-avg)

ure 7.9b and Figure 7.10 the intensity plots of the low, base and high-velocity jet in the second campaign are given. The field of view is slightly different compared to the commissioning campaign. The central jet has been moved up by about 15 jet diameters for the second campaign so this field of view is a bit lower.

The low jet velocity case here has half the normal flow per minute as compared to the commissioning campaign. The flame seemed much more compact and moved around in a smaller area as compared to the higher jet cases. This can also be seen from the comparatively smaller green and orange contour in Figure 7.9a, which is located at the bottom of the field of view. In these images, the trend of the flame moving downstream with increasing equivalence is very clear as well. The line for this case in Figure 7.11 is biased downstream for the lower equivalence ratios because part of the flame is not in the field of view in these images.

In the base jet case, which is 3/4 the flow rate of the commissioning jet, the brightest point of the flame seems to be fully in view for the low equivalence ratios. The bright region is bigger as compared to the low jet cases, which could be indicative of the flame being more distributed. Here also the high intensity region moves downstream with increasing equivalence. At the highest equivalence ratio of 1.5 the bright region seems to move beyond the field of view. Looking at the individual photographs for this case the flame that can be seen looks much more distributed and faint as compared to the low jet case. Also comparing the low to the high equivalence ratio for the base jet itself the high equivalence ratio images show a more distributed flame.

The high jet case, which has the same volume flow rate in the jet as the commissioning jet case, seems to be a lot fainter as compared to the jet base and jet low case. The intensity map from the second campaign looks different to the intensity map from the commissioning campaign, even though the conditions in these two cases are very similar. Focusing the camera on the flame was difficult as the flame was hard to see, moved around, and did not have clear edges. In the second campaign, the focus of the camera is shifted from the measurement plane towards the background. However, since averaging is used in these images the focus is not very critical. Due to the flame being more out of focus here than in the commissioning campaign the flame becomes more spread in the averaging. For this reason, the centre of the flame cannot be seen in the image in Figure 7.10. Still, the trend is clear, the centroid moves downstream, and for a central jet equivalence of 1.2 and 1.5, the flame moves outside of the field of view. In Figure 7.11 the jet high case and the commissioning case do not overlap since the field of views in these cases do not match and therefore the images from the second campaign are biased downwards.

As the equivalence ratio is increased the mass flow of fuel increases as well as can be seen in Figure 7.4a and Figure 7.5a. If there is more fuel to burn it is expected that the flame becomes bigger and for the centroid to move further downstream. In the intensity contour plots, the area of highest intensity

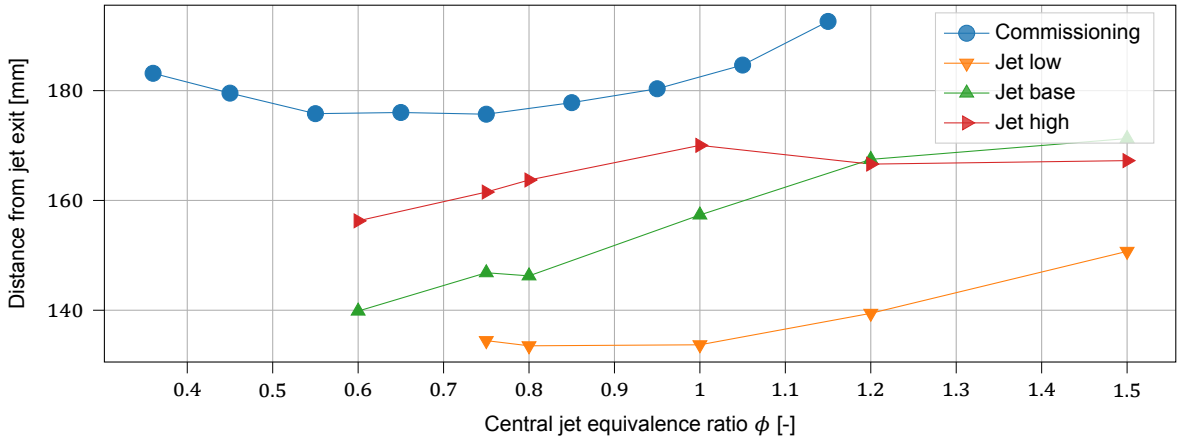

Figure 7.11: The location of the weighted centroid of the intensity as a function of the central jet equivalence ratio

can also be seen to move downstream, it is not just a growth of the flame. Additionally, under very lean conditions the centroid of the jet during the commissioning campaign can also be seen to move downstream with decreasing equivalence, even though the volume of fuel is decreasing. This suggests that there might be a chemistry effect at play and not just a change due to the amount of fuel burning. Spadaccini and Colket Iii, 1994 found that at very lean conditions the ignition delay of a methane flame under lean conditions was higher due to a lower concentration of hydrocarbons and therefore also a slower production of radicals. Approaching stoichiometry from the lean side they also observed an increase in ignition delay. This behaviour is unique to methane due to the primary hydrocarbon produced by methane being the methyl radical which is very stable. The authors state that this radical does not easily oxidise nor decompose to secondary radicals. This means that higher concentrations of this radical increase the ignition delay. They found the radical termination rate to increase with the square of the methyl concentration. The downstream movement of the highest intensity area might thus also be partially related to a decrease in the rate of reactions due to the higher methyl concentration.

More recent work by Sampat et al., n.d. also found this increase in ignition delay when approaching stoichiometry from the lean side. These authors modelled the autoignition of methane-air mixtures diluted by exhaust gas vitiation using an ideal gas constant pressure reactor model in Cantera. The authors looked at four different scenarios. Exhaust gasses were added to the methane-air mixture prior to ignition; in the radical vitiation case all radicals produced by the reaction were also added to the mixture (except NO_x and some related radicals). In the inert vitiation case only CO_2, CO, O_2, N_2 and H_2O are recirculated. Additionally, either a fixed mixture temperature was specified (non-adiabatic case), or the temperature was calculated based on an enthalpy balance between the recirculating gasses and fresh reactions (adiabatic case). The increased ignition delay was found to be negated when vitiated gasses were recirculated into the combustion chamber. In the adiabatic case both inert and radical vitiation results in a reversal of the trend. However, in the non-adiabatic case, the trend reversal only occurs when radicals are included in the vitiation. The trend reversal seen in the adiabatic case with inert vitiation is thus caused by an increase in the mixture temperature from the recirculating gasses. The a priori existence of radicals before combustion can thus cause the ignition delay to decrease when approaching stoichiometry from the lean side.

The difference between the work by Sampat et al., n.d. and the current combustor is that the current combustor has a fixed coflow composition; the pilot burners are fixed at a specified power and equivalence setting resulting in a consistent coflow composition and fixed flow rate of radicals. When the equivalence is increased the mass flow rate of fuel increases as well, which thus results in a lower radical-to-fuel ratio at higher equivalence ratios. The volume ratio of coflow-to-fuel about halves over the central jet equivalence range of 0.6 to 1.5 in the second campaign. It is thus possible that this observed trend reversal seen by Sampat et al., n.d. does not apply to the current combustor due to there being an insufficient amount of radicals to overcome the ignition delay increase due to a higher methane concentration and volume.

A contributing factor to the downstream movement might thus be due to the chemistry being slowed

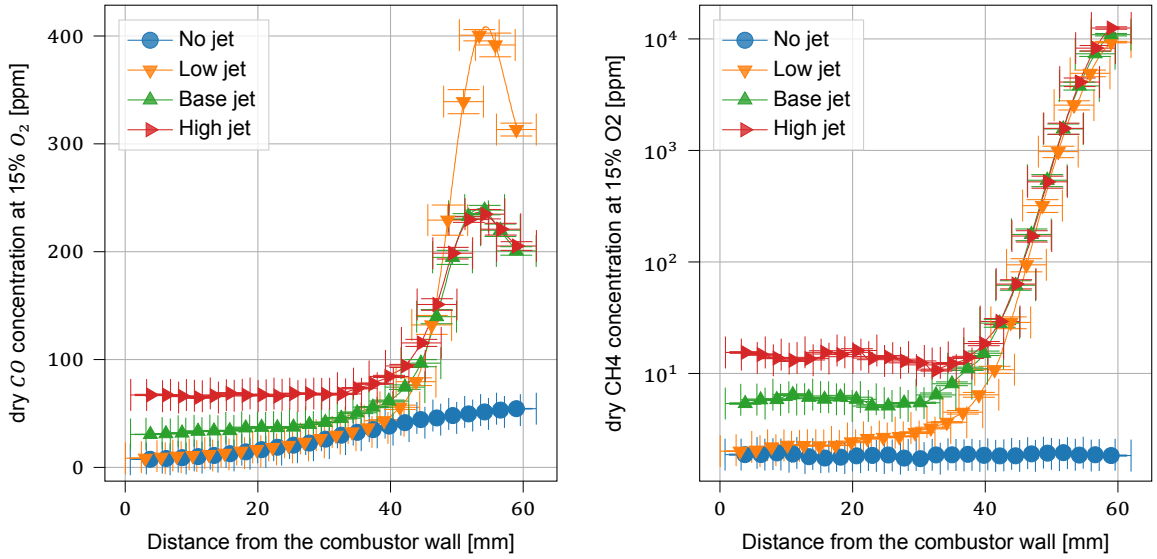

(a) Radial concentration of CO measured at port 1

(b) Radial concentration of CH_4 measured at port 1

Figure 7.12: Jets with $\phi_{cj} = 1.0$ from the second campaign.

down by higher methyl concentrations. It is important to note that the centroid location might not be directly related to the ignition delay, but is somewhat correlated to it. Ideally, the lift-off height should be calculated, but since there is no clear fixed flame front this is not possible with the current method. to decrease when approaching stoichiometry from the lean side.

7.6.2. State of the coflow

In the second campaign, the gas concentration and temperature were measured radially at port 1. A description of the collection method, as well as the method for calculating the error margins in the plots, is given in subsection 7.4.2 In Figure 7.12a the radial measurements of carbon monoxide are shown, in Figure 7.12b the methane concentrations are displayed. The centre of the combustion chamber is 62mm from the wall. In the CO plot the concentration of carbon monoxide is highest in the shear layer. This is where combustion takes place. The low jet case has the highest CO concentration peak, while the peaks for the base and high jet overlap. Looking at the coflow region a difference between all three jet cases can be seen. The concentration of carbon monoxide is highest for the high jet, followed by the base jet and then the low jet. The concentration for the low jet also matches the concentration measured when the central jet is turned off. This must mean that there is combustion occurring in the coflow with the base and high jet. In chapter 6 it was found that there is a recirculation zone in the coflow due to an insufficient volume flow of coflow gasses to feed the entrainment into the central jet. These increased CO concentrations compared to the no jet case are indicative of this recirculation zone also existing when combustion occurs. The methane measurements in Figure 7.12b show the same result. For the base and high jet case, there is still some methane left in the recirculation zone. Although, this concentration is really low at about 15 ppm for the high jet and about 8 ppm for the base jet.

Additionally, the CO concentration is not constant over the radius of the combustor when the jets are turned off. If the coflow was well mixed and uniform the concentration should be the same everywhere. Since in the traverse plane, the centre is the location closest to the pilot burners the concentration of carbon monoxide is highest here. It is thus clear from this result that the coflow is not uniform.

The radial temperature measurements in Figure 7.13 show a lower temperature in the coflow region for the jet cases compared to the no-jet case. The recirculation zone transports colder gas from downstream back upstream resulting in this lower temperature near the wall. This shows that, even though the low jet CO concentration was equal to the no-jet concentration, there is still a recirculation zone present. Although, no combustion occurs in this zone. Furthermore, the low jet case has the highest peak temperature, which is reached at the centreline. The base jet has the same temperature as the

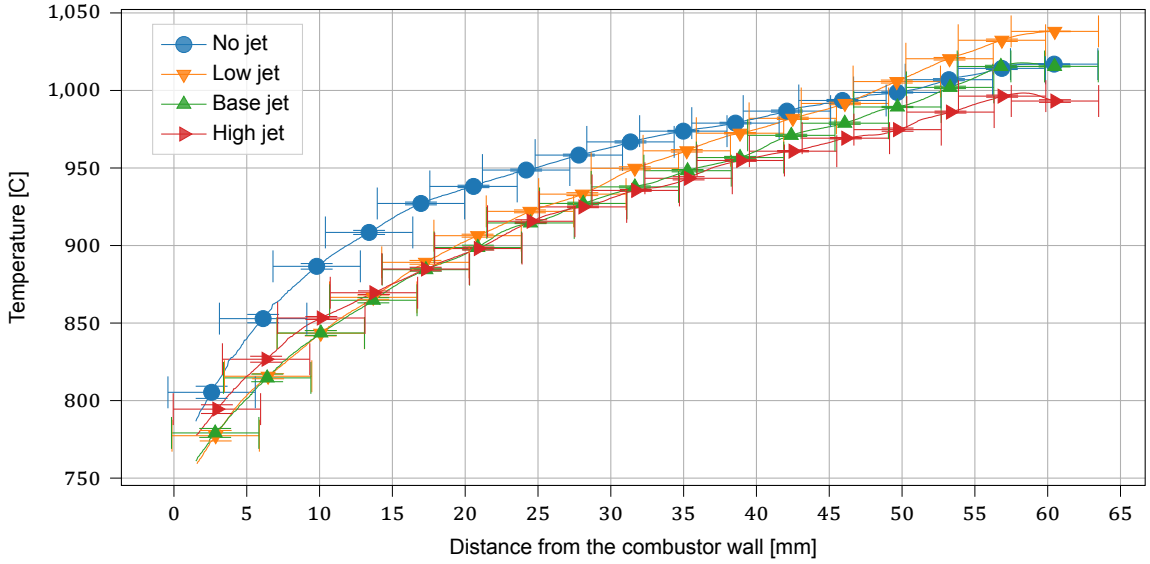

Figure 7.13: Radial temperature measurements from port 1, jets with $\phi_{cj} = 1.0$, from the second campaign.

no-jet case in the centre and the low jet case has the lowest temperature. This difference can partially be explained by the decrease in mixing temperature caused by the higher flow rate of the central jet but is also caused by the combustion zone being less compact at higher jet flow rates.

7.6.3. Detailed gas and temperature measurements

In the second campaign, gas composition measurements were taken at the centreline of the combustor at various locations downstream of the jet exit. In Figure 7.14a the NO concentration measured at the exhaust is shown as a function of the effective equivalence ratio. The exhaust measurements were taken for the entire range of equivalence ratios for the low and high jet velocities. Additionally, the NO concentration when the jet is off is also displayed as a reference. All jet cases have a lower NO concentration compared to the concentration in just the coflow. The cases with a low jet velocity have the highest NO concentration, then followed by the base jet velocity; The high-jet velocity has the lowest NO concentration at the exhaust. For the low jet, the NO concentration remains more or less constant with the changing effective equivalence. The base jet also doesn't vary much up to the richest case. The high jet case shows a constant decrease with increasing equivalence. It also is important to note again, that the normal volume flow rate in each jet case remains constant with the changing equivalence ratio. The resulting jet velocity should therefore also remain constant ensuring a constant residence time in the combustion chamber.

In Figure 7.14b the NO produced by the central jet is displayed. The method with which this value is computed is discussed in subsection 7.3.2. The trends as a function of equivalence ratio are very similar to those observed in Figure 7.14a. The low jet shows a more-or-less flat profile with increasing equivalence. While for the base jet velocity, a slight decrease is observed, until the richest case where a sudden drop is observed. The high jet velocity shows a much steeper decrease in NO concentration with increasing equivalence. With a low jet velocity, the central jet still produces a net positive in NO, though it is still much less than the concentration in the coflow. When these gasses mix this will then result in an overall lower NO concentration measured at the exhaust. The base jet and high jet velocity cases result in a net negative NO production after a central jet equivalence ratio of 0.75. This must mean that reburning is occurring. In these cases, the central jet is consuming NO from the coflow in greater quantities than what it is producing itself.

In Figure 7.15a and Figure 7.15b the concentration of methane and carbon monoxide are plotted at the exhaust of the combustor. For $\phi_{cj} = 1.0$, 1.2, and 1.5 in the high jet case there is still some methane left at the exhaust of the combustor. Also for the richest base jet case, there is notably more methane left at the exhaust, although it is still a relatively small concentration. In these cases, combustion is not yet fully complete. In the high jet case, the jet velocity is just too high and the volume of methane is too

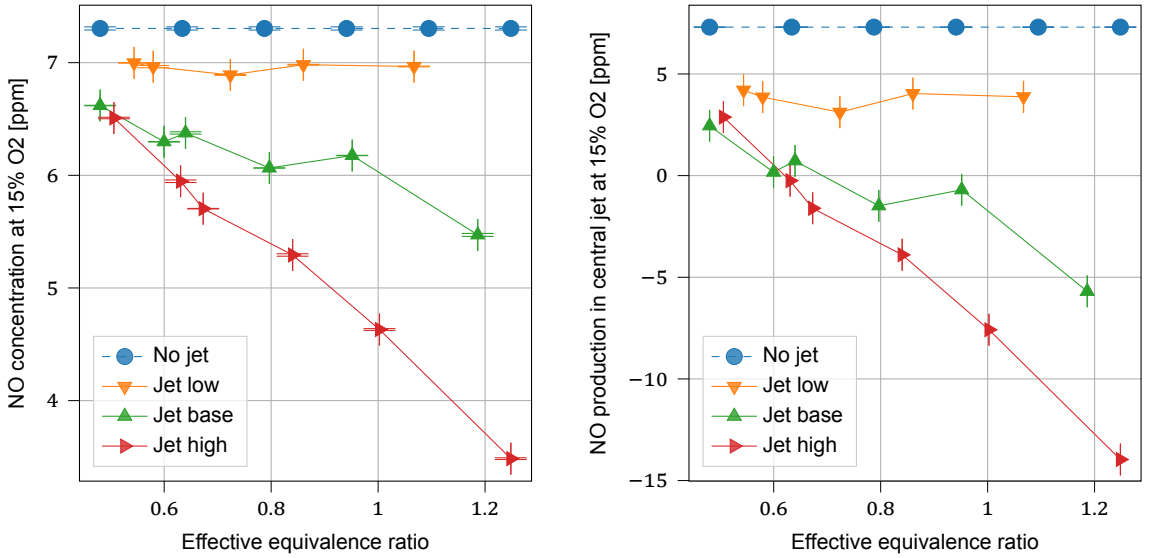

(a) NO concentration corrected at 15% O_2 measured at the exhaust for the effective equivalence ratio.

(b) Computed NO concentration corrected at 15% O_2 produced by the central jet.

Figure 7.14: Data from the second campaign. In both plots, the no-jet case is provided as a reference for the coflow conditions.

much to fully burn in time. The CO concentration can also be seen to increase when methane is left. The fact that combustion is not fully complete by the end of the combustion chamber indicates that the combustion zone is much longer as compared to the base jet case and the low jet case. The fact that combustion is not complete for the rich high jet velocity cases and the $\phi_{cj} = 1.5$ base jet case might also be linked to the steeper decline in NO.

In Figure 7.16, the CO concentration measurements from the centreline are plotted. For the base jet velocity measurements were taken for a range of equivalence ratios; for the jet high and jet low velocity streamwise measurements were taken only at a central jet equivalence of 1.0. Additionally, the CO concentration obtained when the central jet was turned off is also included. For the measurements, ports 1, 3, 5, 7, 10 and the exhaust connection were used. The location of these ports can be seen in Figure 7.1. The CO concentration can be inferred to be a progress variable for the progression of the combustion occurring in the central jet.

From Figure 7.16, it is seen that the low jet case has a steep CO concentration curve. Its concentration peaks at port 3, and then quickly drops. The high jet case shows a much slower increase in CO concentration. Its peak is reached at port 7. At the exhaust, the CO concentration is notably higher than in the other stoichiometric cases indicating that the combustion process does not fully complete in the combustion chamber. The stoichiometric base jet case lies somewhere between the low and high jet case. It peaks at port 5, and the concentration of CO reaches zero at the exit.

More interesting is the trend with the central jet equivalence ratio in the case jet case. The leanest case, ($\phi_{cj} = 0.6$), has a steep rise and then peaks at port 3. After that, it decreases slowly and only reaches zero at the exhaust. Increasing the central jet equivalence to 0.75 results in a decrease in the slope of CO. The peak also lays at port 3, but is lower than the peak for the $\phi_{cj} = 0.6$ case; though it is likely that the actual peak lays somewhere between ports 3 and 5. This trend continues with $\phi_{cj} = 0.8$; the slope slightly decreases. At port 3 a higher concentration is measured for the $\phi_{cj} = 0.75$ case, but at port 5 the concentration for $\phi_{cj} = 0.8$ is higher. This indicates that the peak concentration has likely also shifted downstream. For the stoichiometric case, the peak is further downstream and the slope is again smaller. The same goes for $\phi_{cj} = 1.2$ the slope has again decreased, but this time the peak concentration has increased again. Up to this point, the measured peak concentration has been decreasing. Although, for $\phi_{cj} = 0.75$ and $\phi_{cj} = 0.8$ the peak concentration likely lies somewhere between port 3 and 5 so it is hard to tell if the peak is indeed decreasing, but from $\phi_{cj} = 0.6$ and $\phi_{cj} = 1.0$ it seems to be reasonable to assume that it does. At an equivalence ratio of 1.5 the overall CO concentration is much higher at all ports. At the exhaust, the CO concentration doesn't go to zero. The central jet equivalence ratio case

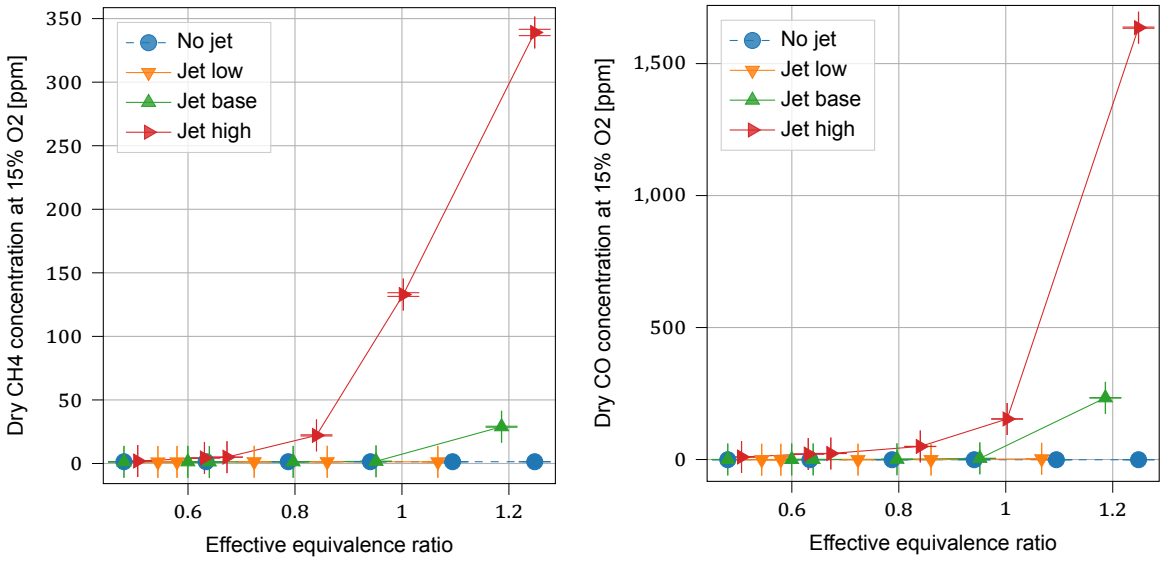

(a) Dry methane concentration at the exhaust corrected for 15% oxygen concentration.

(b) Dry CO concentration at the exhaust corrected for 15% oxygen concentration.

Figure 7.15

of 1.5 is also the only case for the base jet where the overall equivalence ratio, thus also including the coflow air, is rich. For the base jet with a central jet equivalence of 1.2, the overall equivalence is about 0.95, and for a central jet ratio of 1.5 the overall ratio is just below 1.2.

The observed downstream movement of the peak in CO concentration is interesting. As stated earlier the jet velocity remains constant when the equivalence ratio is changed, but the fuel volume increases. In the chemiluminescence images, it was also observed that the high intensity region moves downstream with increasing equivalence. It is possible that due to the increase in fuel volume, the peak in concentration is only reached further downstream. Though, the ignition delay and rate of reactions also influence when this peak is reached. The peak location not only changes but the magnitude of the peak can also be observed to decrease between $\phi_{cj} = 0.6$ and $\phi_{cj} = 1.0$. After stoichiometry, the peak increases again. This also results in a change in the slope of the CO concentration. A lower, further downstream peak results in a less steep slope. This slope is determined by the relative production and consumption of CO, so if the production increases relative to the consumption rate then a steeper slope is produced, while a relatively higher consumption compared to production results in a shallower slope. What can be concluded then is that the relative production of CO compared to its consumption is decreased with an increasing equivalence ratio.

There are several plausible explanations for this observed trend. It is possible that the increase in methyl concentrations results in an increase in the ignition delay and therefore also a slower rate of CO production as was discussed in subsection 7.6.1. This would explain both the change in peak concentration as well as the further downstream location. It is also possible that an increase in temperature with increasing equivalence just results in a relative increase in rate of CO oxidation, making the peak lower; an increase in fuel volume can then explain the peak laying further downstream. A counterargument to that point is the fact that the CO concentration peak in the low jet stoichiometric case is much higher than all other cases base jet cases while it also has the highest temperature, as can be seen in Figure 7.18. But, the oxygen concentration for this jet case is also the lowest, which could result in a relatively lower rate of CO oxidation to CO_2. In the end, these results cannot tell which mechanism is responsible for this behaviour. Further research is required into the underlying mechanisms and their possible connection to the ignition delay.

The wet NO concentration measurements from the centreline are given in Figure 7.17. In the no-jet case, the NO concentrations are higher than in all jet cases. At the first port, the NO concentration in all jet cases is very similar. At the bottom of the combustion chamber, a lower NO concentration can be expected as it takes some time for the nitric oxide to entrain into the jet from the coflow. After the first

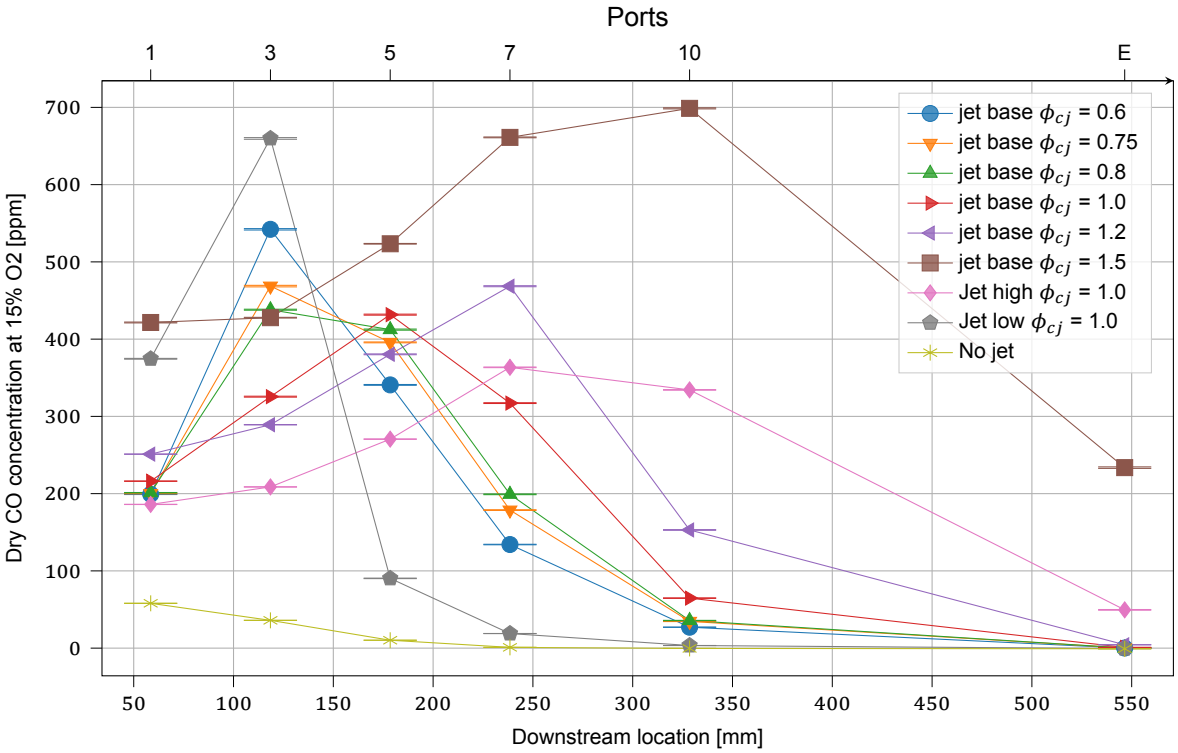

Figure 7.16: Streamwise centreline measurements of dry CO concentration corrected at 15% O_2 from the second campaign.

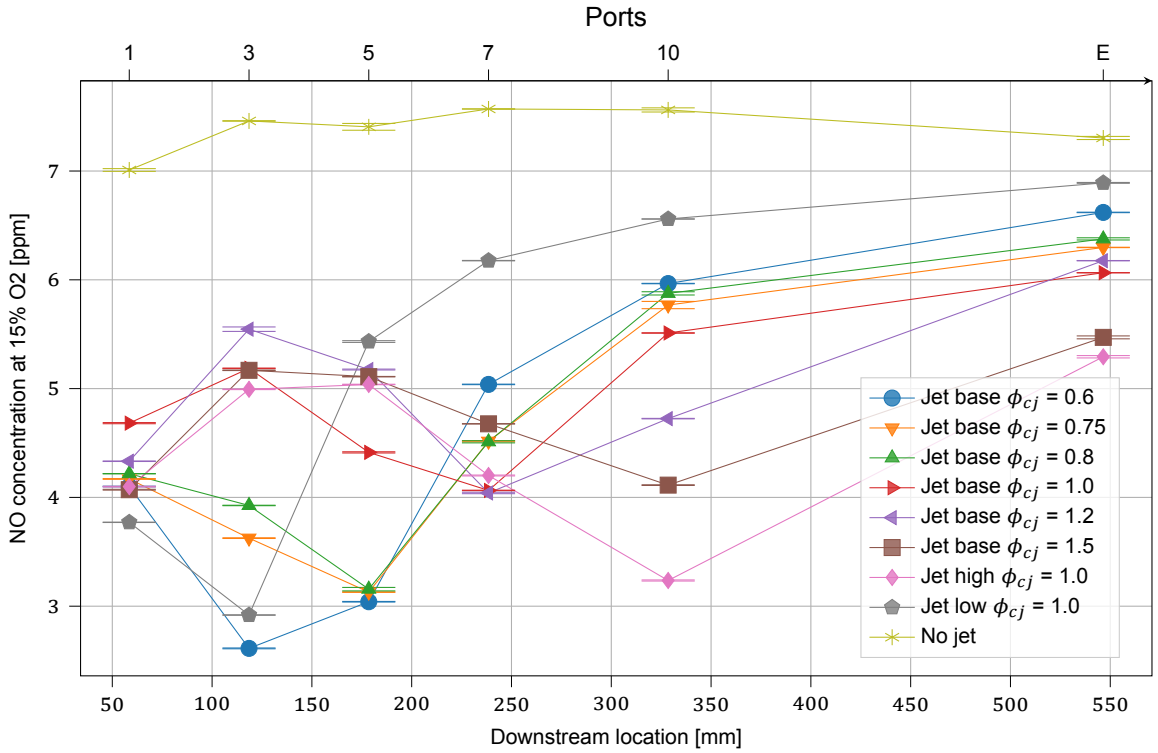

Figure 7.17: Streamwise centreline measurements of NO concentration corrected at 15% O_2

point, different trends are observed. What is most notable is that all jet cases show a decrease in the NO concentration at some point downstream. For the low jet case and the lean baseline cases, this decrease happens right after port 1, while for the high jet case and the stoichiometric and rich jet cases, this occurs after port 3 or 5 with an initial rise before that. Comparing the valleys in the NO plot with the peaks in the CO plot in Figure 7.16 shows a very good correlation between the results; a valley in nitric oxide concentration is always located close to a peak in carbon monoxide concentration. As the CO concentration starts to drop the NO concentration will start to rise again. The drop in NO is an indication of NO_x reburning occurring in the jet, while the rise at the start might be explained by NO_x production becoming dominant when the carbon radicals have all been consumed. The initial rise in NO observed in some jet cases could be explained by NO entraining at a faster rate than the rate at which the flame is reburning it, or by NO production in this region being more dominant than the consumption reactions.

From Figure 7.16 and Figure 7.17 it could be seen that the NO concentration reached a minimum around the point at which the CO concentration reaches a peak, only after this point does the NO concentration start to rise again. If the combustion zone is lengthened and the CO peaks further downstream then reburning is expected to continue for longer and there is less residence time left to produce NO again after that point. If this is the case one would expect a decrease in NO concentration at the exhaust with increasing equivalence, but this does not seem to be the case for the low jet.

In Figure 7.18 the temperature measurements from the centreline of the combustor are plotted. Since at the exhaust, cooling air is added the temperature measurement at this location might be inaccurate and has therefore not been included in the plot. It can be seen that the low jet case reaches the highest temperature of all measurements, but after reaching its peak shows a relatively quick cooling. From the CO measurements and the photographs, this flame was found to be the most compact. Even at the first port is the temperature of the low jet already higher than in all other cases. The mass flow rate in the central jet is the lowest therefore the mixing temperature between the jet and the coflow is the highest of the three jet flow rates. The high jet case has a similar temperature as the stoichiometric base jet case at the bottom of the combustor, but for the high jet the temperature has a much flatter profile; the slope towards the end of the combustor is less steep downwards. For the base jet case, the temperature increases with increasing equivalence ratio, as expected. Even at port 1, the richer flames have a higher temperature. The leaner cases also have a steeper slope downward by the end of the combustor. This is also expected since the rich cases can burn more fuel and the flames are therefore longer.

The higher temperature with increased equivalence might explain why the NO concentration profile is so flat for the low jet and base jet case. As the name suggests thermal NO_x is very temperature dependent [Warnatz et al., 2006]. A higher temperature would result in a faster rate of thermal NO_x production. Although, it is important to note that the temperature observed in the combustion chamber is well below the 1700K stated by Warnatz et al., 2006 below which thermal NO_x production is insignificant; other NO_x production pathways may be playing a more important role at the temperatures in the combustion chamber. One way in which one could tell if the thermal NO production rate is increased is by comparing the steepness of the NO concentration rise after the drop. When looking at the NO concentration for the low jet case, in Figure 7.17, after it reaches its minimum it shows a steeper increase in NO as compared to the other cases. However, for the base jet cases, this increase in steepness is not really visible for increasing central jet equivalence. For the base jet case, the leanest case shows the steepest slope in NO concentration after reaching its minimum. Likely, the jet is still entraining NO from the coflow after it has exhausted its fuel resulting in an initial steep increase. It is therefore hard to distinguish between the potentially still entraining NO and the NO being generated inside the central jet.

Though, it is probable that the higher temperature does indeed result in more thermal NO production, which would mean that there seem to be two opposing forces with increasing equivalence: The increased NO production due to increased temperature and a decrease in NO production due to a bigger flame. A longer combustion zone results in more NO being reburned, and also reduced the available residence time for the NO to build up again after the fuel has been consumed. For the low jet, it could be that the effect increased NO_x production due to the temperature increase is balanced with the increase in returning due to the increase in the combustion zone length, while with the base jet cases and the high jet cases the increasing flame size is more dominant. Though it must be noted that for the stoichiometric and rich high jet cases, the combustion zone becomes so long that the fuel does not have sufficient time in the combustor to fully burn.

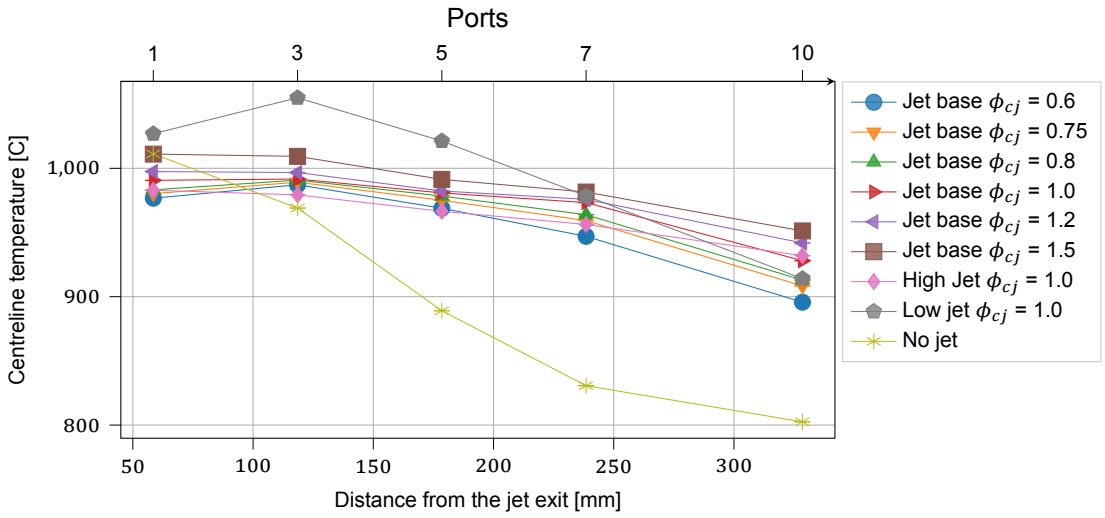

Figure 7.18: Streamwise centreline measurements of the temperature in the combustion chamber.

In Figure 7.19a the oxygen concentration measurements are shown at the exhaust of the combustion chamber. The markers denoted by the dotted line indicate the expected oxygen concentration based on the measured flow rates for that case. As can be seen, there is a linear offset between the oxygen concentration which is measured and the expected oxygen concentration based on the flow rates. In Equation 7.1.3 the working principle of the Magnos is explained. It is possible that interference from CO_2 is interfering with the oxygen measurements and producing an offset, though it seems that the difference is larger than what would be expected if CO_2 was interfering with the measurements.

Additionally, in Figure 7.19b the centreline measurements of the oxygen concentration are shown. What is most notable in this graph is the fact that the oxygen concentration near the bottom of the combustion chamber is different compared to the top of the combustion chamber in the no-jet case. This is further indicative of the flow not being uniform at the bottom of the combustion chamber. Furthermore, it can be seen that the low jet case has a lower oxygen concentration at the bottom of the combustor as compared to the base and high jet cases.

Furthermore, in Figure 7.20 the streamwise centreline concentration of NO_2 is shown. A large portion of the measurements is negative, meaning something went wrong when collecting this data. In Equation 7.1.3 the working principle of the LIMAS21 module, which measures the NO and NO_2 concentration, is discussed. In this section, it was found that the gas analyser employs wavelength comparison in the 200-500 nm range [ABB, 2004] to determine the NO_2 concentration, although no description for the exact methodology was found. It would be easy to discard these results as erroneous and therefore irrelevant, but comparing the NO_2 concentration trends with the trends in the NO measurements in Figure 7.17 shows an interesting correlation. For the cases where a trough in NO concentration is observed at port 3 a peak is observed in NO_2 concentration. The peaks in NO concentration at port 3 do not fully match up with the troughs in NO_2, but a decline is observed here; the trough for these cases is reached at port 5. Experiments by Song et al., 2019 showed that when methane combustion was doped with NO or NO_2 these gasses would have a catalytic effect at temperatures between 850K and 1100K. These radicals were found to enhance oxidation but were not consumed, only transformed into the other. Only above this temperature would reburning following the HCN pathway be detected. Although, looking at the temperature profile in Figure 7.18 shows that the temperature is above 1100K for all cases, so the results from these authors would predict reburning. It is likely that because the NO_2 concentration is derived from the NO concentration in some way that this correlation appears. Further investigation is required as to why these concentration measurements are negative.

7.6.4. Effect of added diluent

In Figure 7.21a and Figure 7.21b the streamwise centreline NO and CO concentrations are plotted for the base jet with added CO_2 or N_2 at 20 lnpm. Their respective no-jet cases and the regular base jet are also plotted. All the jets in this figure operated at a central jet equivalence of 1.0. At port

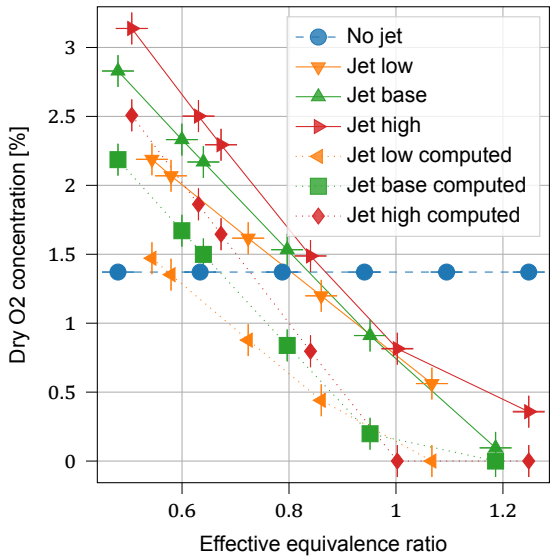

(a) Exhaust oxygen measurements, and the computed value based on the measured flow rates for each case. The no-jet case is displayed as a reference for the coflow conditions

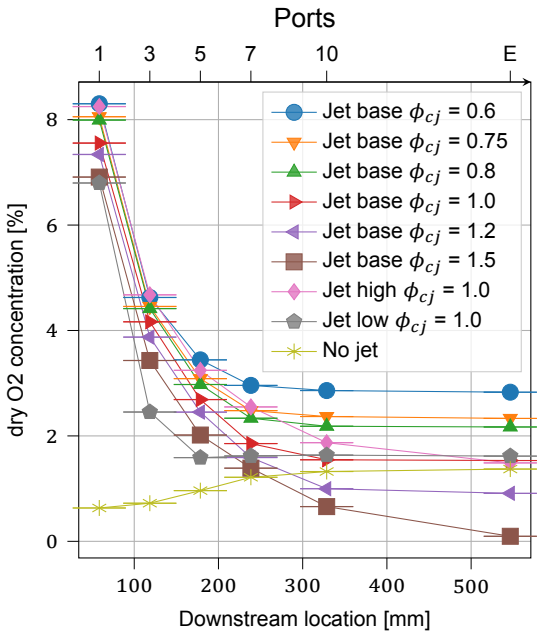

(b) Streamwise centreline oxygen concentration measurements

Figure 7.19: Oxygen concentration measurements from the second campaign

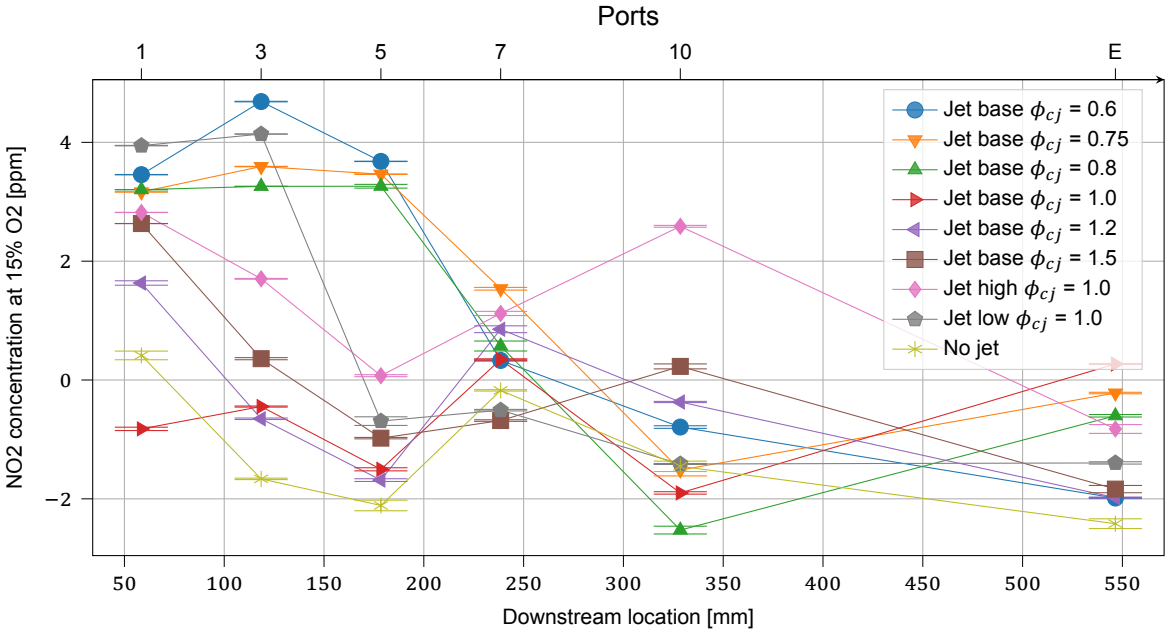

Figure 7.20: Streamwise centreline measurements of the NO_2 concentration corrected at 15% O_2

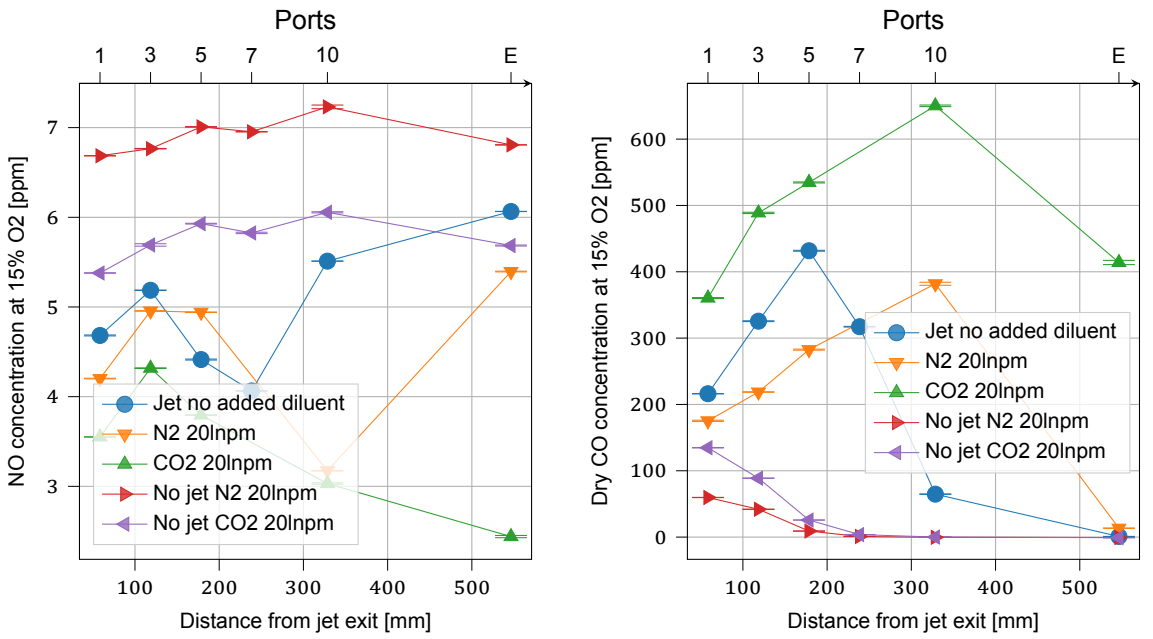

(a) Centreline NO concentration

(b) Centreline dry CO concentration

Figure 7.21: Base jet at ϕ_{cj} = 1.0 with 20lnpm of CO_2 or N_2 added to the coflow from the second campaign.

7 the measurements for the diluted jet are missing, the jet was erroneously not turned on when the measurements were taken. Looking at the streamwise behaviour of NO it can be seen that when diluting with N_2 the same trends are observed as with the normal base jet. An initial rise in NO followed by a drop, and then a rise again. Comparing this to the CO plot the valley in NO again also matches well with the CO peak, which are both reached at port 10. Looking at the CO_2 diluted case shows a different trend; the initial rise and then drop in NO are present but the NO concentration doesn't increase near the exhaust. At the exhaust, the CO concentration is also still notably higher as compared to the other cases at above 400 ppm. At the inlet, the concentration of CO is also notably higher. At high temperatures, CO_2 can decompose into CO which explains the increased concentrations at the inlet and exit of the combustion chamber [Park et al., 2002]. The fact that the NO concentration keeps dropping is indicative of reburning occurring till a much later downstream location. There could still be carbon-based reactions occurring.

Furthermore, looking at the NO and CO concentration in the no-jet cases shows that the extra dilution also affects the pilot flames. The CO concentration is higher when diluting with CO_2, likely due to the decomposition of the added CO_2. The CO concentration returns to zero at port 7, which is the same port where the N_2 diluted no-jet case also reports zero CO. Interestingly, the nitric oxide measured in the CO_2 diluted no-jet case is also lower than the N_2 diluted no-jet case. The mixing temperature of the pilot flue gasses and the carbon dioxide is lower than the mixing temperature of the pilot flue gasses with nitrogen which results in a sort of quenching behaviour for the production of thermal NO_x. One can also see that the jet case with CO_2 is translated downward compared to the N_2 case due to the reduced NO concentration in the coflow.

In Figure 7.22a and Figure 7.22b the streamwise centreline NO and CO concentration are plotted for the base jet, with the added diluent flow increased to 50 lnpm. Now for both the N_2 and CO_2 diluted case the rise in NO at the end of the combustion chamber is missing. Both keep showing a slow decline. For both cases, the CO concentration remains high at the exhaust as well. For the CO_2 diluted case there is little variation in CO over the length of the combustion chamber. The carbon-monoxide concentration at the inlet of the combustion chamber is much higher compared to the 20 lnpm case. The nitrogen diluted case and the no-jet cases do not have a notably higher CO at the inlet. In the nitrogen-diluted jet case, the CO concentration keeps climbing further downstream. The no-jet cases show a lower NO concentration in the coflow compared to the 20 lnpm cases. The increased flow rate of diluent and reduced power setting of the pilot burners has lowered the mixing temperature of the flue gas and the

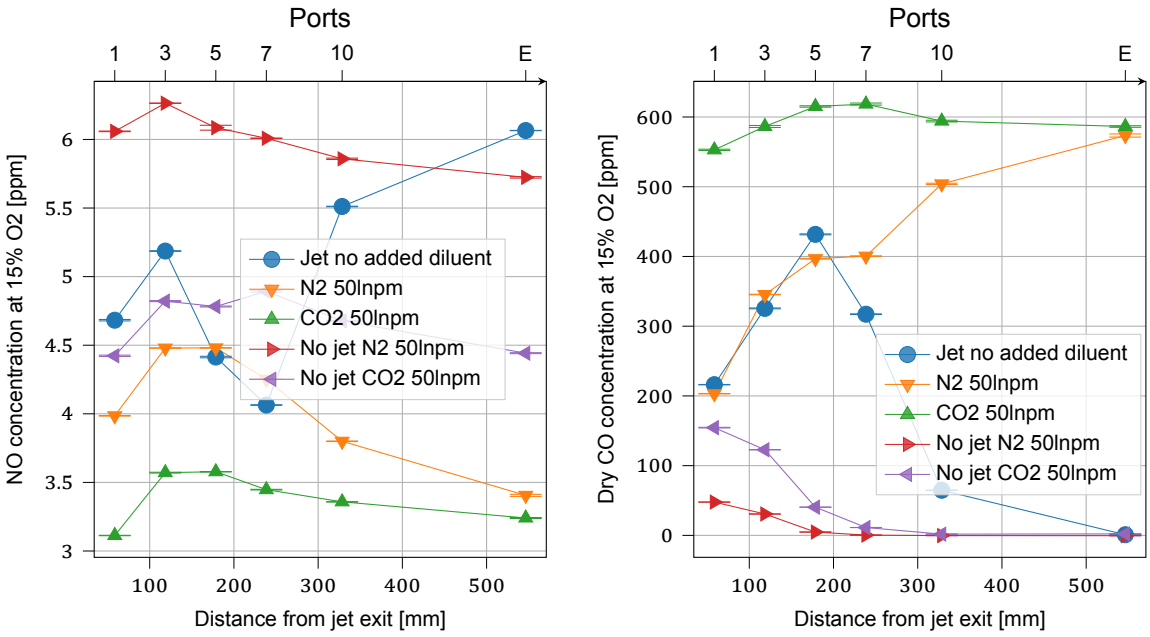

(a) Centreline NO concentration

(b) Centreline dry CO concentration

Figure 7.22: Base jet at ϕ_{cj} = 1.0 with 50lnpm of CO_2 or N_2 added to the coflow from the second campaign.

diluent and thus the thermal NO_x reactions have likely been reduced further than in the 20 lnpm case. Also here the CO_2 diluted case shows the lowest NO concentration.

The centreline measurements for methane are shown in Figure 7.23a and Figure 7.23b for 20 lnpm and 50 lnpm added diluent respectively. In Figure 7.23a the jet with added N_2 has less than 10 ppm of methane left in the flow at the exhaust, for the carbon-dioxide diluted jet there is still about 300 ppm left. This means that the combustion with CO_2 added is not complete yet. The lack of a rise in NO seen in Figure 7.21a can thus be explained by methane oxidation reactions still occurring at the exhaust. In Figure 7.23b both diluted jets are quenched before combustion can be completed. At the exhaust, the nitrogen-diluted jet still has about 1700 ppm methane in the flow while for the carbon-dioxide diluted jet about 2800 ppm remains. Between port 10 and the exhaust, virtually no change in concentration is measured. This does not mean that all reactions have ceased . In Figure 7.22b an increase in CO concentration is observed between port 10 and the exhaust for the nitrogen-diluted jet. Additionally, for both diluents, a decrease in NO is also observed between port 10 and the exhaust in Figure 7.22a.

In Figure 7.24a and Figure 7.24b the centreline temperature is shown for the two dilution flow rate cases. The increased diluent flow rate and reduced pilot power setting result in lower coflow temperatures. When adding CO_2 the temperature of the coflow and of the jet is lower than the N_2 diluted case due to its higher specific thermal capacity per volume. For the 20 lnpm diluted flow there is about a 50 K difference between the jets with the added diluent and the jet without the added diluent. For the 50 lnpm diluent flow, this difference is about 100 K. The temperature difference may also play a big role in the reduced NO_x production when additional inert diluent is added.

7.7. Discussion & Conclusion

From the chemiluminescence two main observations are made: The increased jet flow rate results in the combustion zone becoming more distributed and the peak intensity area moving downstream. Increasing the equivalence ratio has a similar effect. Both increasing the jet flow rate and increasing the equivalence ratio increase the volume of fuel being burned. Though, from Figure 7.5a it can be seen that the jet low case at stoichiometry has about an equal fuel flow rate as the leanest base jet case. Comparing these two cases in Figure 7.9a and Figure 7.9b shows that the leanest base jet combustion zone is more distributed than the stoichiometric low jet combustion zone. The CO, NO and temperature data in Figure 7.16, Figure 7.17 and Figure 7.18 also corroborate the observation that the $\phi_{cj} = 1.0$

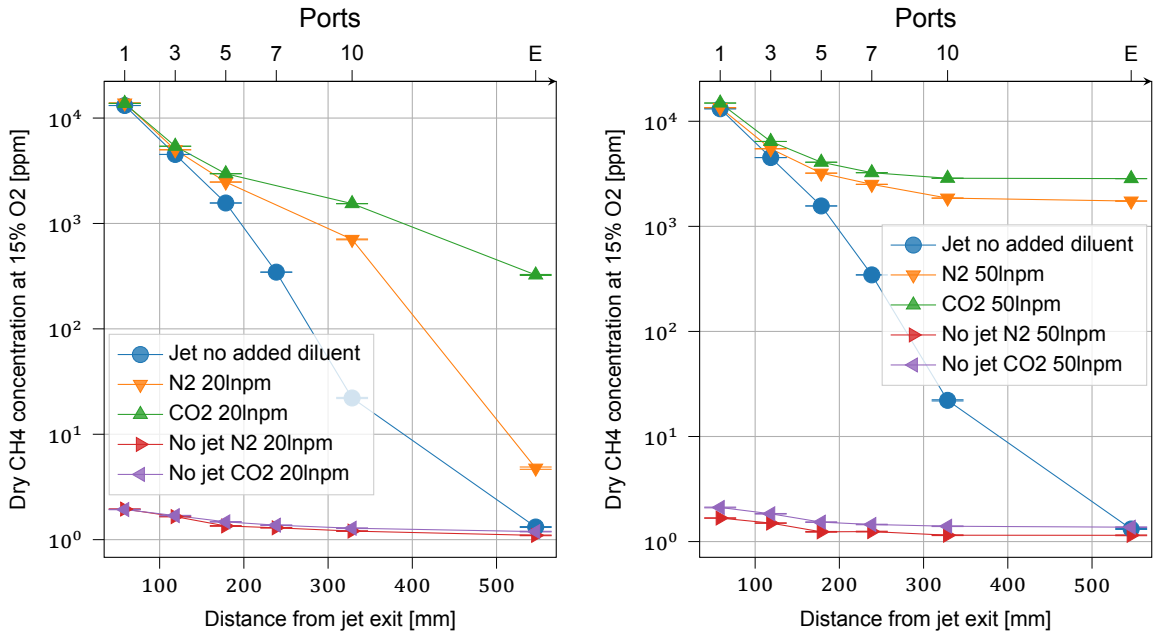

(a) With 20lnpm CO_2 or N_2

(b) With 50lnpm CO_2 or N_2

Figure 7.23: Centreline dry CH_4 concentration for the base jet at $\phi_{cj} = 1.0$

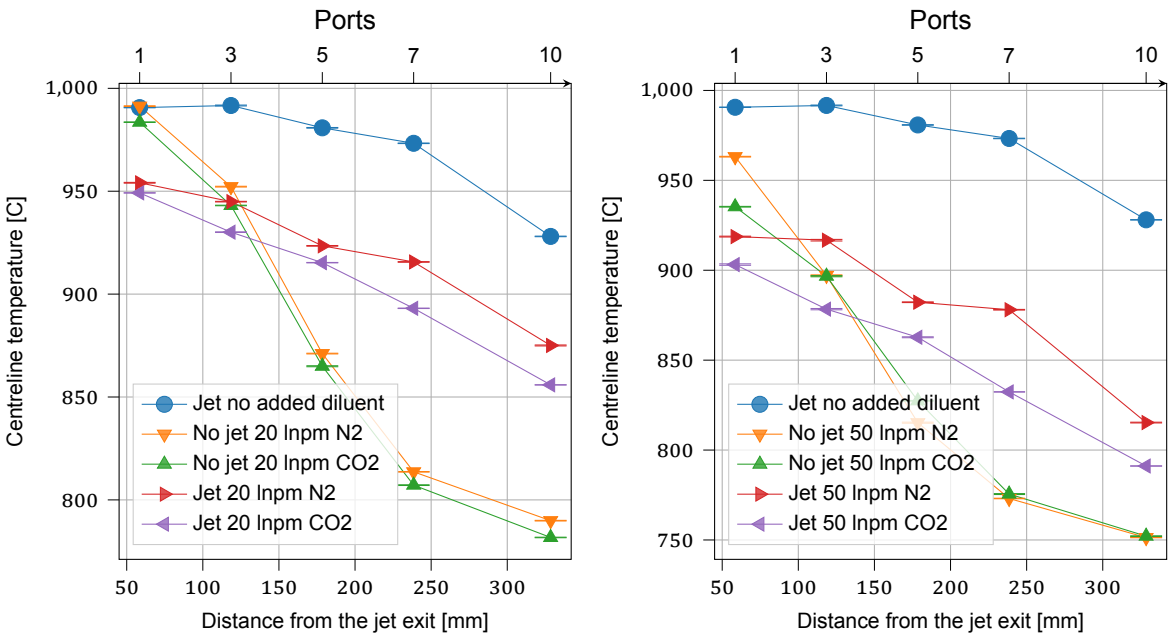

(a) With 20 lnpm CO_2 or N_2

(b) With 50 lnpm CO_2 or N_2

Figure 7.24: Centreline temperature measurements for the base jet at $\phi_{cj} = 1.0$

low jet combustion zone is more compact than the $\phi_{cj} = 0.6$ base jet combustion zone. Mi et al., 2009 found that, for a non-premixed jet, a lower jet momentum resulted in higher temperatures and NO_x concentrations. Although, the burner employed in their modelling and experiment is not a jet-in-hot-coflow setup. It uses recirculation to dilute the jet. A lower jet momentum resulted in a decrease in the recirculation of combustion products into the reactant jets. Ricou and Spalding, 1961 found that the ratio of entrained mass flow to initial jet mass flow is constant above a Reynolds of 25,000. Below this point, an increase is even observed. Nevertheless, the entrained mass flow ratio is mostly a function of downstream location. So if the jet speed is decreased and the ignition delay remains the same ignition will take place closer to the jet exit, where less diluent will have been entrained into the jet. Furthermore, because the mass flow in the jet is smaller and the mass flow and temperature in the coflow remain constant between cases, the mixing temperature of the low jet with the coflow is higher than the mixing temperature of the coflow with the base jet. This might also explain the faster rates of reaction.

The main observation that can be made is that jet speed can have a significant effect on the behaviour and NO_x emissions of flameless combustion. As was seen in Figure 7.14 the low jet speed consistently resulted in higher NO emissions. For the low jet, the central jet produced NO is independent of the equivalence ratio, while for the base jet cases and the high jet cases, a decrease is observed with increasing equivalence. The temperature increases with increasing equivalence, which might result in a higher thermal NO_x production. On the other hand the increased equivalence results in a larger and more distributed combustion zone, which consumes more NO. Additionally, the slower the jet speed the longer the residence time in the combustor, which is advantageous especially for the slow thermal NO_x pathway [Warnatz et al., 2006].

In the streamwise CO and NO measurements in Figure 7.16 and Figure 7.17 it could be seen that when CO was present in high concentrations the NO concentration would drop. This indicates that when there are still sufficient numbers of carbon radicals reburning will take place. Though, CO itself is probably not involved in the reburning. Glarborg et al., 1998 found that the reaction of the methyl radical with NO was the most important pathway for NO_x removal in methane combustion in vitiated conditions, followed by the reaction of $HCCO$ with NO. Both these pathways lead to HCN which then either decomposes to N_2 or back into NO. Measuring the hydrogen-cyanide concentrations directly will give an even better indication of where NO_x reburning occurs.

The lowest NO concentrations are measured at the exhaust when combustion could not be completed inside the combustion chamber. The high jet cases with an equivalence ratio equal to or above stoichiometry still had relatively high methane concentrations in the flow at the exhaust. In the base jet the richest case also still had methane in the exhaust gas mixture. Near the end of the combustor, an increase in NO concentration is always observed when combustion is complete at the exhaust. The increase in NO concentration can be explained either by entrainment of still unburned NO from the coflow into the jet region or by NO_x production in the jet exhaust. This region of increasing NO is not always observed when extra inert diluent is added. Only when diluting with 20 lnpm N_2 is it observed in Figure 7.21a, but diluting with CO_2 at the same flow rate it is not observed. With carbon-dioxide dilution the methane concentration at the exhaust was relatively higher as well. At a higher diluent flow rate of 50 lnpm, the NO rise is not observed for either diluent. At this rate of dilution, methane consumption stopped before reaching the exhaust, likely due to the temperature being too low to sustain methane oxidation. Though the NO concentration continued to drop. For the nitrogen diluted case, the CO concentration also continued to rise.

When diluting with extra CO_2 the measured NO concentration is lower than when diluting with N_2. The diluents were also found to affect the pilot burner exhaust. Adding CO_2 reduced the coflow temperature more than adding the same volume of nitrogen, due to the higher specific thermal capacity per volume of carbon dioxide. The pilot exhaust also contained less NO when diluting with carbon dioxide. The reduced temperature likely reduces thermal NO_x formation in the pilot exhaust. The diluents caused the combustion zone to elongate. The CO peak is only reached at port 10 in the 20 lnpm experiments. While the base jet without extra diluent reached its peak at port 5. The diluents also created a deeper trough in the streamwise NO concentration as compared to the jet without extra diluent. Though the difference between the N_2 diluted and undiluted jet is a lot smaller at the exhaust. In literature, CO_2 is found to influence the oxidation of methane in various ways. Park et al., 2002 found that CO_2 can decompose into CO which then actively reacts with hydrogen radicals reducing the pool of hydroxyl radicals [Westbrook

and Dryer, 1984]. Additionally, CO_2 has also been found to promote chain branching reactions at low temperatures due to its higher third body collisional efficiency as compared to N_2 when burning propane [Sabia, Lubrano Lavadera, et al., 2015]. At intermediate temperatures and temperatures above 1200K CO_2 was found to inhibit ignition by promoting methyl recombination reactions. From the current data, it cannot be said in what way the diluents exactly influence the combustion zone.

The CO peak concentration and slope decrease with increasing equivalence. Indicating that there is a relative change in the CO production and consumption reactions. The combustion zone is also elongated and more distributed at higher equivalence ratios. One plausible explanation concerns higher methyl radical concentrations. Spadaccini and Colket Iii, 1994 showed an increase in ignition delay when approaching stoichiometry from the lean side due to increasing methyl concentrations. This species does not easily oxidise or decompose to secondary radicals. Similarly Sampat et al., n.d. also observed an increase in ignition delay with increasing equivalence on the lean side, though this trend flipped when radicals were recirculated back into the flow. A reason why the current addition of radicals would not negate the effect of methyl is that the ratio of fuel-to-radicals stayed the same in the experiments by Sampat et al., n.d. In the present campaign, the amount of radicals remains the same while the fuel volume increases with increasing equivalence. Meaning the fuel-to-radical ratio decreases with increasing equivalence ratio. Which might mean that the inhibitory effect of methyl is not mitigated by the radicals. Though, the increase in fuel volume and changes in temperature might also play a role.

Finally, from the radial measurements it was found that the recirculation zone observed in the cold flow campaign is also present in these experiments. Combustion was found to occur in them for the base and high jet flow rates. Additionally, the NO concentration in the no-jet case is higher in the centre than near the walls indicating that the flow is not fully uniform. This might make it more difficult to model this setup.

8

Conclusion and recommendations for further research

In this report, the design of a jet-in-hot-coflow setup was discussed. Three experimental campaigns were performed with this setup, and these results have also been analysed. In this chapter, these results are summarised and concluded. First, the research questions derived from the research objective stated in the introduction are answered based on the data discussed in this report. Then the report is concluded and recommendations for future research are provided.

8.1. Research questions

The main objective of this thesis was to study the effect of vitiation on the formation of product species, and stability of flameless combustion, by designing a jet-in-hot-coflow burner and analysing a methane flame in flameless operation by diluting with hot vitiated gasses at various equivalence ratios, operating temperatures and dilution levels. In this report, the design of this combustor is discussed. In the end, three experimental campaigns were successfully performed: One cold flow PIV campaign and two combustion campaigns. In the combustion campaigns, the effect of CO_2, and N_2 were directly studied by adding them to the flow at two fixed rates. The effect of the equivalence ratio was studied over a wide range with three different jet flow rates. The different jet flow rates resulted in a change in the overall oxygen concentration as well. A change in temperature was achieved both by altering the jet flow rate and by adding additional inert gasses to the coflow. The research objective is broken down into research questions which will now be discussed.

"In what way does dilution with hot vitiated gasses influence the formation of secondary product species at various oxygen concentrations equivalence ratios and coflow temperatures" - In the combustion campaign dilution of the reactants was provided by flue gasses from the pilot burners and additional N_2 and CO_2 was added to the coflow to observe the influence of these gasses independently. The power and equivalence ratio of the pilot burners was changed to maintain a constant total coflow flow rate and maintain a constant oxygen concentration. When nitrogen was added the coflow had a higher temperature than when carbon dioxide was added. This can partly be explained by the fact that CO_2 has a higher specific thermal capacity per volume than N_2 [Chase, 1998]. The addition of CO_2 also resulted in a higher CO concentration in the coflow, but also a lower NO concentration. The higher CO concentration could be caused by the decomposition of CO_2 at high temperatures [Park et al., 2002], or it could be due to the lower temperature in the pilot flame reducing the rate at which CO is converted into CO_2. The lower NO output from the pilot burner is likely a direct effect of the lower mixing temperature and therefore also lower thermal NO_x production. The addition of these inert diluents is found to decrease the production of NO_x in all cases. The diluent made the combustion zone longer and reduced the temperature in the combustion chamber. It seems that the added diluent relatively enhanced NO_x reburning, but it is also possible that the reduced temperature resulted in less NO_x generation in the central jet itself. The addition of CO_2 resulted in the lowest NO_x concentration at the exhaust but also resulted in a higher CO and CH_4 concentration there. However, with nitrogen addition

at a flow rate of 20 lnpm, the combustion was complete at the exhaust. Increasing the flow rate of added diluent to 50 lnpm caused the oxidation of methane to cease at port 10 with either nitrogen or carbon dioxide. The temperature in the combustion chamber dropped too much for methane to continue to be consumed, but with nitrogen addition, CO was still produced beyond port 10. Additionally, NO consumption also continued beyond port 10 for both diluents as well.

In literature CO_2 addition is found to influence flameless combustion. Decomposition of CO_2 into CO causes it to compete for hydrogen radicals depleting that radical pool quicker [Park et al., 2002], [Westbrook and Dryer, 1984]. On the contrary CO_2 addition also has been found to promote branching reactions at low temperatures due to its higher third body collisional efficiency compared to N_2 [Sabia, Lubrano Lavadera, et al., 2015]. At intermediate temperatures and temperatures above 1200 K, it was found to inhibit ignition by enhancing methyl recombination reactions [Sabia, Lubrano Lavadera, et al., 2015]. With the current data, it is not clear if these effects are present, and to what extent they influence the flame shape or NO_x production. Controlling the temperature of the added diluent in such a way as to maintain the mixing temperature would be a good way to partially eliminate the effect of the temperature difference on the results.

NO addition was not directly studied, but it was present in the pilot burner exhaust. From the streamwise measurements, it is clear that the NO_x formed by the pilot burners is reburned. When the CO concentration in the central jet is sufficiently high the NO_x concentration was observed to drop. When the CO concentration peak has passed the NO concentration started to rise again. Either due to entrainment of, until that point unburned, NO or due to the production of NO.

While different total oxygen concentrations were tested it is not clear if this resulted in a different oxygen concentration in the combustion zone. The low-speed jet in the second combustion campaign had the lowest mixing oxygen concentration but also had the most compact combustion zone with the highest temperature peak. This might be counterintuitive to what one would expect as lower oxygen concentrations should lead to slower reactions and a more distributed combustion zone. Either the mixing temperature plays a more dominant role than the oxygen concentration at this point, or due to the slower jet speed ignition occurred closer to the jet exit where less diluent had entrained resulting in the flame seeing an effectively higher oxygen concentration on ignition. It is difficult to differentiate the effect of jet speed and the oxygen concentration in these results.

In the second campaign, for all jet speeds, a central jet equivalence range of 0.75 to 1.5 was tested, for the base and high jet case an additional measurement at 0.6 was taken. To keep the residence time in the combustion chamber constant the total central jet flow rate was fixed. An increase in equivalence thus also resulted in an increase in methane volume. What effect the equivalence had on the emissions depended on the jet speed. For the low jet, an increase in equivalence ratio did not result in more NO production in the central jet. With the base jet and high jet velocity, the NO concentration at the exhaust decreased with increasing equivalence. The increase in equivalence ratio results in a large and more distributed combustion zone, while also increasing the temperature. From the streamwise measurements, it can be seen that whenever the CO concentration is high NO will be consumed. A bigger or more distributed combustion zone will therefore consume more NO, while on the other hand, the increased temperatures might increase the NO production. It is possible that for the low jet velocity with increasing equivalence, these two effects are balanced, while for the base jet and high jet velocity, the consumption increase is dominant with increasing equivalence. For equivalence ratios equal to or above stoichiometry the high jet still has methane and carbon monoxide in the exhaust. In the base jet $\phi_{cj} = 1.5$ case there is also a heightened concentration of methane in the exhaust. Indicating that the flame has grown so much combustion cannot be completed inside the combustion chamber.

Effects of the coflow temperature on the formation of product species were not studied directly, but changing the central jet flow rate also resulted in a slight mixing temperature change of about 35K. Additionally, by adding additional diluent the coflow temperature was changed as well. A decrease in coflow temperature seemed to result in a lower pilot exhaust NO concentration. Though it is hard to tell to which degree this change is due to the chemical kinetic effects of adding CO_2 over N_2 as discussed earlier or if this is the direct result of lowering the coflow temperature.

"How does dilution of the coflow with hot vitiated gasses influence the physical characteristics of the combustion zone at various oxygen concentrations, equivalence ratios and coflow

temperatures?" - The combustion zone was observed to dance around, but the extent to which this occurred depended on the equivalence ratio and jet velocity. At low jet velocities, the combustion zone was much more concentrated in one location, while at higher jet speeds it was much more elongated and moved around much more. Similarly, at low equivalence ratios, the combustion zone was more compact compared to higher equivalence ratios. The jet velocity was kept constant with the changing equivalence ratio by keeping the total central jet volume flow rate constant. The volume of fuel being burned would then increase with increasing equivalence ratio which could play a role in making the combustion zone bigger, but the size and location of the combustion zone also depends on the ignition delay and rates of reaction. It is possible that a relative decrease in the rate of reactions occurs due to higher methyl concentrations. In literature, it has been shown that approaching stoichiometry from the lean side the ignition delay of methane increases due to the inhibitory effects of the methyl radical [Spadaccini and Colket Iii, 1994]. Though this cannot be determined from this data. Additional research is required to understand if this is indeed the case.

Adding additional CO_2 or N_2 also resulted in the combustion zone becoming more elongated. This is likely mainly caused by a decrease in temperature, slowing down the rate of reactions. Where CO_2 resulted in the largest temperature decrease it also resulted in the longest elongation. When providing 20 lnpm of CO_2, not all methane was consumed when it reached the exhaust. While for N_2 there was no methane left. Additionally, as discussed earlier there might be chemical kinetic effects at play, but it was not possible to obtain this from the data. When adding 50 lnpm of diluent combustion ceased between ports 8 and 10. Likely, the decrease in temperature was too large to sustain combustion.

Like stated before the low jet speed resulted in a more compact flame compared to the base and high jet speed. Looking purely at the oxygen concentration this was counterintuitive, as with the low jet flow rate the highest level of dilution should be achieved. But, as stated in the answer to the previous research question, it is possible that ignition occurred closer to the jet exit due to the lower jet speed. Here less diluent will have been entrained. The increase in the mixing temperature between the coflow and the central jet could even have resulted in a lower ignition delay; bringing ignition even closer to the jet exit.

"What are the operational limits of the designed setup and what are the characteristics of the flow field inside the combustor?" - During the cold flow campaign a recirculation zone was discovered. This occurred due to the coflow not providing a sufficiently large flow rate to feed the entrainment needs of the central jet. Additionally, the top foam disk was found to create a non-uniform flow. This disk was supposed to generate turbulence in the coflow to enhance mixing, but because it did not fit tightly around the central jet pipe small jets of gas were created by the gaps between the disk and the jet pipe. The remaining two disks were also found to be detrimental as they acted as heat sinks, dissipating substantial amounts of heat from the coflow.

The temperatures reached in the combustion chamber were also much lower than predicted by the heat transfer model. This is mainly due to the model not accurately accounting for the radiation coming off of the pilot burners and for the conduction inside the combustor walls. As well as due to making oversimplified assumptions about the flow inside the mixing duct. To be able to reach a high enough temperature in the combustion chamber all three disks were removed from the mixing ducts. The cylindrical mixing duct was also removed to reduce the flow distance to the combustion chamber and reduce heat losses. This resulted in the coflow being somewhat non-uniform. From the radial measurements, it was clear that the CO concentrations were higher at the centre of the combustion chamber, as compared to near the wall, since the centre was the point at which the traverse came closest to the pilot burners.

The pilot burners had to operate much beyond their designed maximum operating power to generate a sufficiently high temperature. This resulted in a smaller equivalence ratio range in which they could operate. Only an equivalence ratio range of 0.87 to 0.99 was possible; outside this range, the pilot burners would shut down. The equivalence ratio of the pilot burners determines the oxygen concentration in the coflow. Limitations on the equivalence ratio therefore also limit the achievable oxygen concentration range in the coflow.

For the main burner the minimum tested central jet equivalence ratio is 0.36. A flame was observed at that point and combustion was found to be complete. Decreasing the equivalence ratio further was not

possible due to reaching the minimum flow rate limit of the methane mass flow controller. A maximum equivalence ratio was not tested.

8.2. Conclusion & Recommendation for further research

In this report, the design of an enclosed jet-in-hot-coflow setup was presented, the flow characteristics in its combustion chamber were analysed using a PIV campaign, and it was demonstrated that the central jet could be successfully ignited by the hot flue gasses from the pilot burners. The obtained emissions data showed that the NO_x emissions of the central jet were indeed lower than the emissions coming from the pilot flames. The main combustion zone was also found to reburn some of the NO_x produced by the pilot burners. This setup has thus been demonstrated to achieve flameless operation and can now serve as a basis for further experimentation on the flameless regime.

Some requirements were generated as part of the design process of this combustion setup. The first requirement specified was that the combustor should be able to operate at various oxygen concentrations. This is indeed achieved with the current design. By either altering the central jet flow rate or by altering the pilot burner equivalence ratio the oxygen concentration can be changed. Furthermore, the combustor was able to withstand the temperatures inside the mixing duct and combustion chamber without a problem. Cooling of the central jet turned out not to be needed to prevent damage to the material; though cooling would probably be beneficial to have better control over the central jet temperature before it enters the combustion chamber. In the commissioning campaign, the weld inside the cooling jacket broke allowing gasses from the fuel line to enter the cooling jacket and visa versa. Since the fuel pipe inside the cooling jacket didn't heat up as much as the outside of the cooling jacket resulting in a difference in expansion. The central tube inside the cooling assembly should be redesigned such that the cooling jacket can expand without damaging it.

An area of improvement for the combustor setup is the pilot burners. The hot flue gasses from these burners were hot enough to ignite the main jet, but only after removing all the foam disks and removing a section of the mixing duct. This resulted in the coflow not being uniform or well mixed. Modelling combustion inside this combustor might thus be more difficult. The temperature reached in the combustion chamber is also relatively low, only at about 1000 $^{\circ}C$. Increasing the coflow temperature might lead to a more stable flame as the results from Sabia, Lubrano Lavadera, et al., 2015 and Sabia, Sorrentino, et al., 2015 show. Adding more pilot burners is difficult to fit into the coflow attachment at the bottom. Having an integrated burner inside the mixing duct would be a better solution. This can be as simple as using a perforated plate to anchor a premixed flame. Some sort of ignition system would then still be required to ignite this secondary burner. Designing an integrated burner would also make it possible to increase the volume flow rate in the coflow, which if increased enough, would eliminate the recirculation zone in the combustion chamber.

Precise temperature control was also not possible with the current setup. The temperature can be changed by altering the pilot burner power or adding additional nitrogen or carbon dioxide but this will result in a different coflow composition or flow rate. A pre-heating system which can heat the diluents or secondary burner air could be used to control the temperature independently of the coflow flow rate or composition.

There are some issues with the gas analyser. When measuring the NO_2 concentration the gas analyser registered negative concentrations. In previous experiments, this was blamed on the cooling of the probe causing water to condense inside the probe. During the experiments detailed in this report, the cooling was removed completely, and negative NO_2 concentrations were still observed. Additionally, a discrepancy between the expected oxygen concentrations and the measured oxygen concentrations is observed. A more thorough investigation needs to be done to understand what is the cause of these two effects.

Further research is also needed to better understand the effect of the changes in equivalence ratio on the ignition delay. The photographs taken in this campaign do not provide enough insight into the ignition behaviour and evolution of the flame. Because the flame is very dim a long exposure time is required to capture the flame. Just using a high-speed camera is therefore not possible. Using a system where an external source provides the light would make it possible to capture the flame at a higher frequency. Schlieren imaging would be an imaging method with which this can be achieved. From this the lift-off height can be measured, and compared to the results in the literature.

Bibliography

ABB. (2004). Measuring of nitrogen compounds in exhaust gases of engines. https://library.e.abb.com/public/ede9f8da570a7978c125768200385c63/Limas%2011HW%20Analyser.pdf

ABB. (2009). Advance optima continuous gas analyzers AO2000 series Operator's Manual.

Albrecht, H.-E., Borys, M., Damaschke, N., & Tropea, C. (2003). *Laser Doppler and Phase Doppler Measurement Techniques*. Springer Berlin Heidelberg. https://doi.org/10.1007/978-3-662-05165-8

Anderson, J. D. (2011). *Fundamentals of Aerodynamics* (5th). McGraw-Hill.

Arndt, C. M., Gounder, J. D., Meier, W., & Aigner, M. (2012). Auto-ignition and flame stabilization of pulsed methane jets in a hot vitiated coflow studied with high-speed laser and imaging techniques. *Applied Physics B: Lasers and Optics*, *108*(2), 407–417. https://doi.org/10.1007/s00340-012-4945-5

Arndt, C. M., Papageorge, M. J., Fuest, F., Sutton, J. A., Meier, W., & Aigner, M. (2016). The role of temperature, mixture fraction, and scalar dissipation rate on transient methane injection and auto-ignition in a jet in hot coflow burner. *Combustion and Flame*, *167*, 60–71. https://doi.org/10.1016/j.combustflame.2016.02.027

AZO Materials. (n.d.). Stainless Steel - Properties and Applications of Grades 310/310s Stainless Steel. https://www.azom.com/article.aspx?ArticleID=4392

Ball, C. G., Fellouah, H., & Pollard, A. (2012). The flow field in turbulent round free jets. https://doi.org/10.1016/j.paerosci.2011.10.002

Baukal, C., & Eleazer, P. (1998). Quantifying NOx for Industrial Combustion Processes. *Journal of the Air & Waste Management Association*, *48*(1), 52–58. https://doi.org/10.1080/10473289.1998.10463664

Benedict, L. H., & Gould, R. D. (1996). *Towards better uncertainty estimates for turbulence statistics* (tech. rep.). Springer-Verlag.

Boetcher, S. K. S. (2014). *Natural Convection from Circular Cylinders*. Springer International Publishing. https://doi.org/10.1007/978-3-319-08132-8

Bozzelli, J. W., & Dean, A. M. (1995). O + NNH: A possible new route for NOX formation in flames. *International Journal of Chemical Kinetics*, *27*(11), 1097–1109. https://doi.org/10.1002/kin.550271107

British Stainless Steel Association. (n.d.). Oxidation resistance of stainless steels. https://web.archive.org/web/20200807084144/https://www.bssa.org.uk/topics.php?article=107

Bronkhorst. (n.d.). What does Bronkhorst mean by ln/min or ls/min? https://www.bronkhorst.com/int/service-support-1/faq/flow-theory/what-does-bronkhorst-mean-by-ln-min-or-ls-min/

Brown, T. P., & Harrison, P. T. (2014). Crystalline silica in heated man-made vitreous fibres: A review. *Regulatory Toxicology and Pharmacology*, *68*(1), 152–159. https://doi.org/10.1016/j.yrtph.2013.11.014

Cabra, R., Chen, J. Y., Dibble, R. W., Karpetis, A. N., & Barlow, R. S. (2005). Lifted methane-air jet flames in a vitiated coflow. *Combustion and Flame*, *143*(4), 491–506. https://doi.org/10.1016/j.combustflame.2005.08.019

Cabra, R., Myhrvold, T., Chen, J. Y., Dibble, R. W., Karpetis, A. N., & Barlow, R. S. (2002). SIMULTANEOUS LASER RAMAN-RAYLEIGH-LIF MEASUREMENTS AND NUMERICAL MODELING RESULTS OF A LIFTED TURBULENT H 2 / N 2 JET FLAME IN A VITIATED COFLOW. *29*, 1881–1888.

Cavaliere, A., & De Joannon, M. (2004). Mild combustion. *Progress in Energy and Combustion Science*, *30*(4), 329–366. https://doi.org/10.1016/j.pecs.2004.02.003

Çengel, Y. A., & Ghajar, A. J. (2015). *Heat and Mass Transfer: Fundementals \& Applications* (5th). McGraw-Hill Education.

Chase, M. J. (1998). NIST-JANAF Themochemical Tables.

Cheong, K. P., Wang, G., Si, J., & Mi, J. (2021). Nonpremixed MILD combustion in a laboratory-scale cylindrical furnace: Occurrence and identification. *Energy*, *216*, 119295. https://doi.org/10.1016/j.energy.2020.119295

Colebrook, C. F. (1939). Turbulent Flow in Pipes, with particular reference to the Transition Region between the Smooth and Rough Pipe Laws." *Journal of the institution of civil engineers*, *11*(4), 3–175. https://doi.org/10.1680/ijoti.1939.13150

Dally, B. B., Karpetis, A. N., & Barlow, R. S. (2002). Structure of turbulent non-premixed jet flames in a diluted hot coflow. *Proceedings of the Combustion Institute*, *29*(1), 1147–1154. https://doi.org/10.1016/S1540-7489(02)80145-6

de Joannon, M., Sorrentino, G., & Cavaliere, A. (2012). MILD combustion in diffusion-controlled regimes of Hot Diluted Fuel. *Combustion and Flame*, *159*(5), 1832–1839. https://doi.org/10.1016/j.combustflame.2012.01.013

Dekking, F. M., Kraaikamp, C., Lopuhaä, H. P., & Meester, L. E. (2005). *A modern introduction to probability and statistics : understanding why and how*. Springer.

Derudi, M., Villani, A., & Rota, R. (2007). Sustainability of mild combustion of hydrogen-containing hybrid fuels. *Proceedings of the Combustion Institute*, *31 II*, 3393–3400. https://doi.org/10.1016/j.proci.2006.08.107

Dimotakis, P. E. (2000). The mixing transition in turbulent flows. *Journal of Fluid Mechanics*, *409*, 69–98. https://doi.org/10.1017/S0022112099007946

Dunn, M. J., Masri, A. R., & Bilger, R. W. (2007). A new piloted premixed jet burner to study strong finite-rate chemistry effects. *Combustion and Flame*, *151*(1-2), 46–60. https://doi.org/10.1016/j.combustflame.2007.05.010

Duwig, C., Li, B., Li, Z. S., & Aldén, M. (2012). High resolution imaging of flameless and distributed turbulent combustion. *Combustion and Flame*, *159*(1), 306–316. https://doi.org/10.1016/j.combustflame.2011.06.018

Egerton, G. (2021). ABB's Magnos28 Oxygen analyzer delivers unprecedented accuracy. https://new.abb.com/products/measurement-products/measurement-products-blog/magnos28-oxygen-analyzer-delivers-unprecedented-accuracy

Engineering Toobox. (2018). Methane - Thermal Conducitvity vs. Temperature and Pressure. https://www.engineeringtoolbox.com/methane-thermal-conductivity-temperature-pressure-d_2021.html

Engineering Toolbox. (2003a). Air - Dynamic and Kinematic Viscosity. https://www.engineeringtoolbox.com/air-absolute-kinematic-viscosity-d_601.html

Engineering Toolbox. (2003b). Roughness & Surface Coefficients. https://www.engineeringtoolbox.com/surface-roughness-ventilation-ducts-d_209.html

Engineering Toolbox. (2009). Air - Thermal Conductivity vs. Temperature and Pressure. https://www.engineeringtoolbox.com/air-properties-viscosity-conductivity-heat-capacity-d_1509.html

Engineering Toolbox. (2018a). Air-Prandtl Number. https://www.engineeringtoolbox.com/air-prandtl-number-viscosity-heat-capacity-thermal-conductivity-d_2009.html

Engineering Toolbox. (2018b). Methane - Prandtl number vs. Temperature. https://www.engineeringtoolbox.com/methane-prandtl-number-viscosity-heat-capacity-thermal-conductivity-d_2022.html

Engineering Toolbox. (2019). AISI 310 Stainless Steel - Properties. https://www.engineeringtoolbox.com/stainless-steel-310-properties-d_2167.html

Engineers edge. (2020). Standard pipe schedules pipe sizes chart table data. https://www.engineersedge.com/pipe_schedules.htm

European Commission and Directorate-General for Mobility and Transport and Directorate-General for Research and Innovation. (2011). *Flightpath 2050 : Europe's vision for aviation : maintaining global leadership and serving society's needs*. https://doi.org/10.2777/50266

Evans, M. J., Medwell, P. R., Wu, H., Stagni, A., & Ihme, M. (2017). Classification and lift-off height prediction of non-premixed MILD and autoignitive flames. *Proceedings of the Combustion Institute*, *36*(3), 4297–4304. https://doi.org/10.1016/j.proci.2016.06.013

Feng, S., Gao, D., Liao, F., Zhou, F., & Wang, X. (2016). The health effects of ambient PM2.5 and potential mechanisms. *Ecotoxicology and Environmental Safety*, *128*, 67–74. https://doi.org/10.1016/j.ecoenv.2016.01.030

Fenimore, C. P. (1971). Formation of nitric oxide in premixed hydrocarbon flames. *Symposium (International) on Combustion*, *13*(1), 373–380. https://doi.org/10.1016/S0082-0784(71)80040-1

Ferdman, E., Otugen, M. V., & Kim, S. (2000). Effect of Initial Velocity Profile on the Development of Round Jets. *Journal of Propulsion and Power*, *16*(4), 676–686. https://doi.org/10.2514/2.5627

FNV. (2010). Werken met isolatiematerialen.

Friehe, C. A., van Atta, C., & Gibson, C. (1972). Jet turbulence: Dissipation rate measurements and correlations. *ARGARD Conference Proceedings*, (93).

Glarborg, P., Alzueta, M., Dam-Johansen, K., & Miller, J. A. (1998). Kinetic Modeling of Hydrocarbon/Nitric Oxide Interactions in a Flow Reactor. *Combustion and Flame*, *115*(1), 1–27. https://doi.org/10.1016/S0010-2180(97)00359-3

Glarborg, P., Miller, J. A., Ruscic, B., & Klippenstein, S. J. (2018). Modeling nitrogen chemistry in combustion. https://doi.org/10.1016/j.pecs.2018.01.002

Gluck, S., Glenn, C., Logan, T., Vu, B., Walsh, M., & Williams, P. (2003). Evaluation of NOx Flue Gas Analyzers for Accuracy and Their Applicability for Low-Concentration Measurements. *Journal of the Air & Waste Management Association*, *53*(6), 749–758. https://doi.org/10.1080/10473289.2003.10466208

Goselink, N. (2022). An Experimental Investigation of the Operating Characteristics of a Flameless Combustor.

Haber, L. C., & Vandsburger, U. (2003). A global reaction model for oh* chemiluminescence applied to a laminar flat-flame burner. *Combustion Science and Technology*, *175*(10), 1859–1891. https://doi.org/10.1080/713713115

Harnby, N., Edwards, M. F., & Nienow, A. W. (1985). *Mixing in the process industries* (2nd). Butterworth-Heinemann.

Heanjia Super-Metals Co. Ltd. (n.d.). Stainless Steel 310/310S (UNS S31000/ UNS S31008). https://super-metals.com/wp-content/uploads/2015/03/SS-310.pdf

Hoor, P., Borken-Kleefeld, J., Caro, D., Dessens, O., Endresen, O., Gauss, M., Grewe, V., Hauglustaine, D., Isaksen, I. S., Jöckel, P., Lelieveld, J., Myhre, G., Meijer, E., Olivie, D., Prather, M., Schnadt Poberaj, C., Shine, K. P., Staehelin, J., Tang, Q., … Sausen, R. (2009). The impact of traffic emissions on atmospheric ozone and OH: Results from QUANTIFY. *Atmospheric Chemistry and Physics*, *9*(9), 3113–3136. https://doi.org/10.5194/acp-9-3113-2009

Hottel, H. (1954). Radiant Heat Transmission. In W. McAdams (Ed.), *Heat transmission* (3rd). McGraw-Hill.

Howell, G. W., & Weathers, T. M. (1970). *Aerospace Fluid Component Designers' Handbook* (Revision D, Vol. 1).

Hussein, H. J., Capp, S. P., & George, W. K. (1994). Velocity measurements in a high-Reynolds-number, momentum-conserving, axisymmetric, turbulent jet. *Journal of Fluid Mechanics*, *258*, 31–75. https://doi.org/10.1017/S002211209400323X

Iavarone, S., & Parente, A. (2020). NOx Formation in MILD Combustion: Potential and Limitations of Existing Approaches in CFD. https://doi.org/10.3389/fmech.2020.00013

ICAO. (2016). ICAO Engine Exhaust Emissions Databank, version 23. https://doi.org/Doc9646-AN/943

Innocentini, M. D. M., Salvini, V. R., Macedo, A., & Pandolfelli, V. C. (1999). *Prediction of Ceramic Foams Permeability Using Ergun's Equation* (tech. rep.).

Iwasaka, M. (2009). Effects of gradient magnetic fields on CO2 sublimation in dry ice. *Journal of Physics: Conference Series*, *156*, 012029. https://doi.org/10.1088/1742-6596/156/1/012029

Kaneko, S., Inada, F., Nakamura, T., & Kato, M. (Eds.). (2008). *Flow Induced Vibrations*. Elsevier. https://doi.org/10.1016/B978-0-08-044954-8.X0001-0

Kasap, S. (2001). Thermoelectric Effects in Metals. *Department of Electrical Engineering. University of Saskatchewan, Canada*, 1–11.

Kathrotia, T. (2011). *Reaction Kinetics Modeling of OH*, CH*, and C2* Chemiluminescence* (Doctoral dissertation). Ruprecht-Karls-Universitat. Heidelberg.

Kazangas, D., Skevis, G., & Kaiktsis, L. (2021). Effects of NOx-SOx Addition on Methane Ignition: Toward a Kinetic Understanding for Marine Engine Applications. *Journal of Energy Engineering*, *147*(3), 04021007. https://doi.org/10.1061/(asce)ey.1943-7897.0000752

Khalil, A. E., & Gupta, A. K. (2017). The role of CO2on oxy-colorless distributed combustion. *Applied Energy*, *188*, 466–474. https://doi.org/10.1016/j.apenergy.2016.12.048

Klein Tools. (n.d.). Emissivity Chart. http://www.kleintools.com/sites/kleintools/files/instructions/KleinTools-Emissivity-Chart.pdf

Kreith, F., Manglik, R. M., & Bohn, M. S. (2011). *Principles of Heat Transfer* (7th). Cengage.

Kumar, S., Paul, P. J., & Mukunda, H. S. (2002). STUDIES ON A NEW HIGH-INTENSITY LOW-EMISSION BURNER. *29*, 1131–1137.

Lee, D. S., Fahey, D. W., Forster, P. M., Newton, P. J., Wit, R. C., Lim, L. L., Owen, B., & Sausen, R. (2009). Aviation and global climate change in the 21st century. *Atmospheric Environment*, *43*(22-23), 3520–3537. https://doi.org/10.1016/j.atmosenv.2009.04.024

Lemonis, M. E. (2020). Moment of Inertia of a Trapezoid. https://calcresource.com/moment-of-inertia-trap.html

Li, P. F., Mi, J. C., Dally, B. B., Wang, F. F., Wang, L., Liu, Z. H., Chen, S., & Zheng, C. G. (2011). Progress and recent trend in MILD combustion. *Science China Technological Sciences*, *54*(2), 255–269. https://doi.org/10.1007/s11431-010-4257-0

McEnally, C. S., & Pfefferle, L. D. (1999). Experimental study of nonfuel hydrocarbon concentrations in coflowing partially premixed methane/air flames. *Combustion and Flame*, *118*(4), 619–632. https://doi.org/10.1016/S0010-2180(99)00017-6

Medwell, P. R., & Dally, B. B. (2012a). Effect of fuel composition on jet flames in a heated and diluted oxidant stream. *Combustion and Flame*, *159*(10), 3138–3145. https://doi.org/10.1016/j.combustflame.2012.04.012

Medwell, P. R., & Dally, B. B. (2012b). Experimental observation of lifted flames in a heated and diluted coflow. *Energy and Fuels*, *26*(9), 5519–5527. https://doi.org/10.1021/ef301029u

Medwell, P. R., Kalt, P. A., & Dally, B. B. (2007). Simultaneous imaging of OH, formaldehyde, and temperature of turbulent nonpremixed jet flames in a heated and diluted coflow. *Combustion and Flame*, *148*(1-2), 48–61. https://doi.org/10.1016/j.combustflame.2006.10.002

Medwell, P. R., Kalt, P. A., & Dally, B. B. (2008). Imaging of diluted turbulent ethylene flames stabilized on a Jet in Hot Coflow (JHC) burner. *Combustion and Flame*, *152*(1-2), 100–113. https://doi.org/10.1016/j.combustflame.2007.09.003

Megson, T. (2012). *Aircraft structures for Engineering Students* (5th). Butterworth-Heinemann.

Mi, J., Li, P., Dally, B. B., & Craig, R. A. (2009). Importance of initial momentum rate and air-fuel premixing on moderate or intense low oxygen dilution (MILD) combustion in a recuperative furnace. *Energy and Fuels*, *23*(11), 5349–5356. https://doi.org/10.1021/ef900866v

Miller, R. W. (1996). *Flow Measurement Engineering Handbook* (3rd). McGraw-Hill.

Mills, A. (2014). *Basic Heat and Mass Transfer* (2nd). Pearson Education Limited.

Nori, V., & Seitzman, J. (2008). Evaluation of chemiluminescence as a combustion diagnostic under varying operating conditions. *46th AIAA Aerospace Sciences Meeting and Exhibit*, (January), 1–14. https://doi.org/10.2514/6.2008-953

Oberlack, M., Arlitt, R., & Peters, N. (2000). On stochastic Damköhler number variations in a homogeneous flow reactor. *Combustion Theory and Modelling*, *4*, 495–509. https://doi.org/10.1088/1364-7830/4/4/307

Oldenhof, E., Tummers, M. J., van Veen, E. H., & Roekaerts, D. J. (2010). Ignition kernel formation and lift-off behaviour of jet-in-hot-coflow flames. *Combustion and Flame*, *157*(6), 1167–1178. https://doi.org/10.1016/j.combustflame.2010.01.002

Oldenhof, E., Tummers, M. J., van Veen, E. H., & Roekaerts, D. J. (2011). Role of entrainment in the stabilisation of jet-in-hot-coflow flames. *Combustion and Flame*, *158*(8), 1553–1563. https://doi.org/10.1016/j.combustflame.2010.12.018

Panchapakesan, N. R., & Lumley, J. L. (1993). Turbulence Measurements in Axisymmetric Jets of Air and Helium. Part 1. Air Jet. *Journal of Fluid Mechanics*, *246*, 197–223. https://doi.org/10.1017/S0022112093000096

Park, J., Kim, S. G., Lee, K. M., & Kim, T. K. (2002). Chemical effect of diluents on flame structure and NO emission characteristic in methane-air counterflow diffusion flame. *International Journal of Energy Research*, *26*(13), 1141–1160. https://doi.org/10.1002/er.841

Perpignan, A. A., Gangoli Rao, A., & Roekaerts, D. J. (2018). Flameless combustion and its potential towards gas turbines. *Progress in Energy and Combustion Science*, *69*, 28–62. https://doi.org/10.1016/j.pecs.2018.06.002

Pirozzoli, S., Modesti, D., Orlandi, P., & Grasso, F. (2018). Turbulence and secondary motions in square duct flow. *Journal of Fluid Mechanics*, *840*, 631–655. https://doi.org/10.1017/jfm.2018.66

Pitsch, H., & Fedotov, S. (2001). Investigation of scalar dissipation rate fluctuations in non-premixed turbulent combustion using a stochastic approach. *Combustion Theory and Modelling*, *5*(1), 41–57. https://doi.org/10.1088/1364-7830/5/1/303

Popa, D., & Udrea, F. (2019). Towards Integrated Mid-Infrared Gas Sensors. *Sensors*, *19*(9), 2076. https://doi.org/10.3390/s19092076

Pope, S. B. (2013). *Turbulent Flows* (10th ed.). Cambridge University Press.

Raffel, M., Willert, C. E., Wereley, S. T., & Kompenhans, J. (2007). *Particle Image Velocimetry A Practical Guide*. Springer.

Ricou, F. P., & Spalding, D. B. (1961). Measurements of entrainment by axisymmetrical turbulent jets. *Journal of Fluid Mechanics*, *11*(1), 21–32. https://doi.org/10.1017/S0022112061000834

RS. (n.d.). RS Pro Superwool 607 Fibre Thermal Insulating Sheet, 1800mm x 610mm x 50mm. https://docs.rs-online.com/86a3/0900766b815844df.pdf

RS Components SAS. (2020). Veiligheidsblad: Superwool plus blanket.

Rüdiger, W., Rathke, C., Ohland, M., & Crevatin, M. (2008). *High-technology workhorse: Advancing contemporary modular gas analyzer technology with the Uras26 photometer* (tech. rep.). https://library.e.abb.com/public/445a35571d72713fc12573d1006ee22e/ABB%20SRIA%201_06_HighTechnologyWorkhorse.pdf

Sabia, P., Sorrentino, G., Chinnici, A., Cavaliere, A., & Ragucci, R. (2015). Dynamic behaviors in methane MILD and oxy-fuel combustion. Chemical effect of CO2. *Energy and Fuels*, *29*(3), 1978–1986. https://doi.org/10.1021/ef501434y

Sabia, P., & de Joannon, M. (2020). Critical Issues of Chemical Kinetics in MILD Combustion. *Frontiers in Mechanical Engineering*, *6*(March), 1–10. https://doi.org/10.3389/fmech.2020.00007

Sabia, P., Lubrano Lavadera, M., Giudicianni, P., Sorrentino, G., Ragucci, R., de Joannon, M., Lubrano, M., Giudicianni, P., Sorrentino, G., & Ragucci, R. (2015). CO2 and H2O effect on propane auto-ignition delay times under mild combustion operative conditions. *Combustion and Flame*, *162*(3), 533–543. https://doi.org/10.1016/j.combustflame.2014.08.009

Sampat, R., Schrijer, F., & Rao, A. G. (n.d.). Autoignition of Lean Methane-Air mixtures with exhaust gas vitiation.

Shin-Etsu Quartz Products. (n.d.). For use in high temperature process applications. https://www.sqp.co.jp/e/products/usage/thermal.html

Song, Y., Marrodán, L., Vin, N., Herbinet, O., Assaf, E., Fittschen, C., Stagni, A., Faravelli, T., Alzueta, M. U., & Battin-Leclerc, F. (2019). The sensitizing effects of NO 2 and NO on methane low temperature oxidation in a jet stirred reactor. *Proceedings of the Combustion Institute*, *37*(1), 667–675. https://doi.org/10.1016/j.proci.2018.06.115

Sorrentino, G., Sabia, P., De Joannon, M., Cavaliere, A., & Ragucci, R. (2016). The Effect of Diluent on the Sustainability of MILD Combustion in a Cyclonic Burner. *Flow, Turbulence and Combustion*, *96*(2), 449–468. https://doi.org/10.1007/s10494-015-9668-3

Spadaccini, L. J., & Colket Iii, M. B. (1994). IGNITION DELAY CHARACTERISTICS OF METHANE FUELS. *Progress in Energy and Combust Science*, *20*, 431–460.

Special Metals Corporation. (2008). INCONEL ALLOY 600. https://www.specialmetals.com/documents/technical-bulletins/inconel/inconel-alloy-600.pdf

Systech Instruments. (n.d.). Paramagnetic Cells. https://industrialphysics.com/knowledgebase/articles/paramagnetic-cells-technology-for-our-paramagnetic-o2-analyser/

The Engineering ToolBox. (2004). STP - Standard Temperature and Pressure and NTP - Normal Temperature and Pressure. https://www.engineeringtoolbox.com/stp-standard-ntp-normal-air-d_772.html

thyssenkrupp Materials Ltd. (2017). *Stainless Steel 1.4845 Material Data Sheet* (tech. rep.). https://www.thyssenkrupp-materials.co.uk/stainless-steel-310-14845.html

Tropea, C., Yarin, A. L., & Foss, J. F. (2007). *Handbook of Experimental Fluid Mechanics*. Springer-Verlag.

U.S. EPA L U - U S Environmental Protection Agency. (2016). Integrated science assessment for oxides of nitrogen (final report). *Washington D.C.: Contract No.: EPA/600/R-08/071*. http://ofmpub.epa.gov/eims/eimscomm.getfile?p%7B_%7Ddownload%7B_%7Did=526855

Wang, F., Li, P., Mei, Z., Zhang, J., & Mi, J. (2014). Combustion of CH4/O2/N2 in a well stirred reactor. *Energy*, *72*, 242–253. https://doi.org/10.1016/j.energy.2014.05.029

Warnatz, J., Maas, U., & Dibble, R. (2006). *Combustion* (4th). Springer.

Westbrook, C. K., & Dryer, F. L. (1984). Chemical kinetic modeling of hydrocarbon combustion. *Progress in Energy and Combustion Science*, *10*(1), 1–57. https://doi.org/10.1016/0360-1285(84)90118-7

Worthington, B., & von-Hoersten, H. (n.d.). *Novel Differential Ultra-Violet Resonance Absorption Gas Analyzer for NOx Measurements in Continuous Emission Monitoring Systems* (tech. rep.).

Wünning, J. A., & Wünning, J. G. (1997). Flameless oxidation to reduce thermal no-formation. *Progress in Energy and Combustion Science*, *23*(1), 81–94. https://doi.org/10.1016/s0360-1285(97)00006-3

Ye, J., Medwell, P. R., Dally, B. B., & Evans, M. J. (2016). The transition of ethanol flames from conventional to MILD combustion. *Combustion and Flame*, *171*, 173–184. https://doi.org/10.1016/j.combustflame.2016.05.020

Yin, F., & Gangoli Rao, A. (2017). Performance analysis of an aero engine with inter-stage turbine burner. *Aeronautical Journal*, *121*(1245), 1605–1626. https://doi.org/10.1017/aer.2017.93

Zeldovich, Y. (1946). The Oxidation of Nitrogen in Combustion and Explosions. *Acta Physicochimica U.S.S.R*, *21*, 577–628.

A

Error margins cold flow results

A.1. Velocities

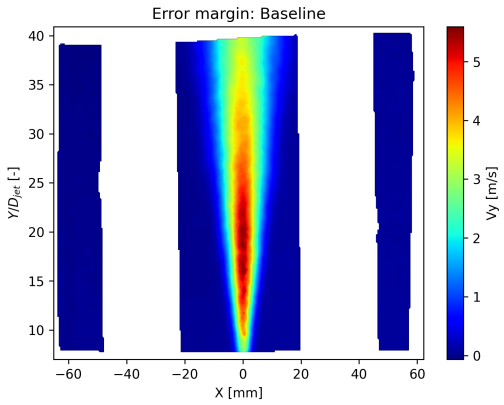

Figure A.1: Error margins 95% confidence interval of vertical velocity, in the baseline Vertical enclosed - single window view.

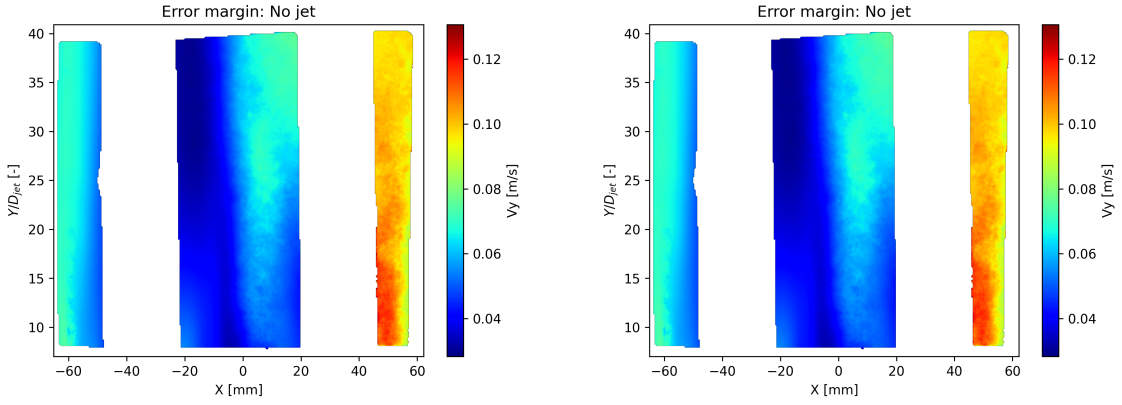

(a) Both pilot burners open

(b) left pilot burner closed

Figure A.2: Error margins 95% confidence interval of vertical velocity when the jet is off. Vertical enclosed - single window view.

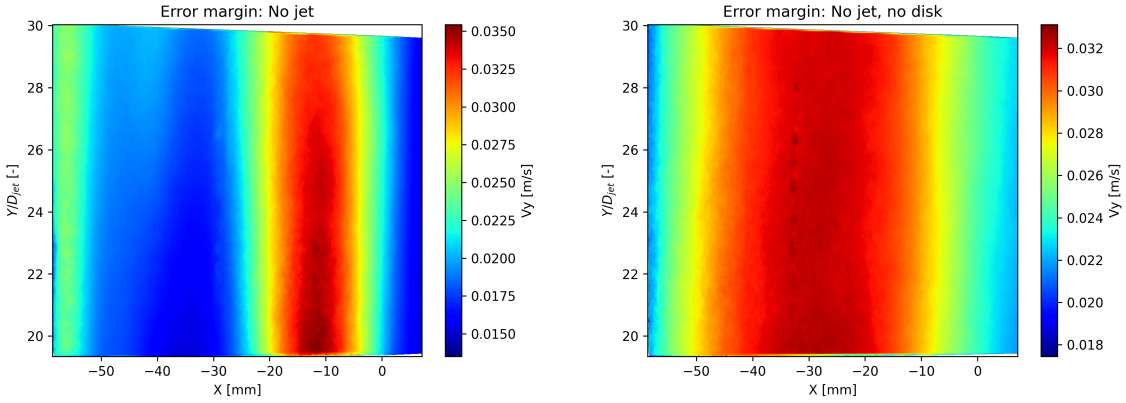

(a) With top disk (b) Without top disk

Figure A.3: Error margins 95% confidence interval of vertical velocity when the jet is off. Vertical enclosed - two window view.

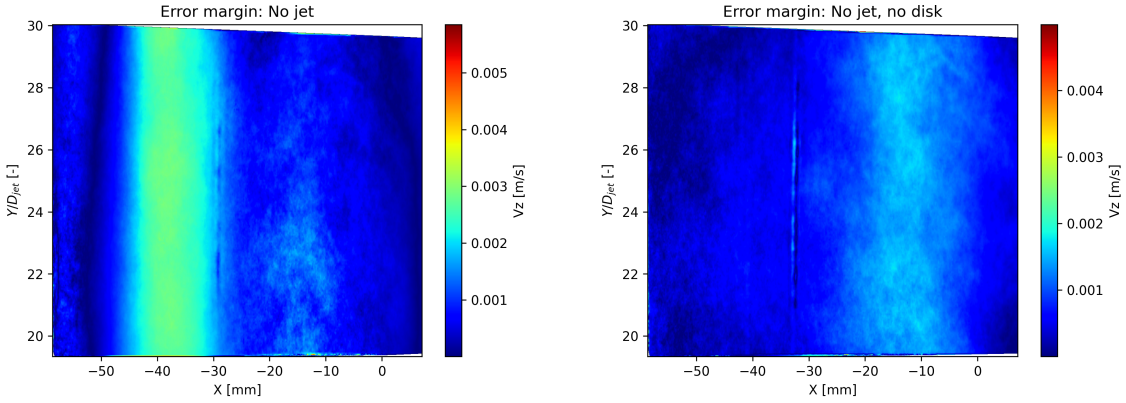

(a) With top disk (b) Without top disk

Figure A.4: Error margins 95% confidence interval of the velocity in the Z-direction when the jet is off. Vertical enclosed - two window view.

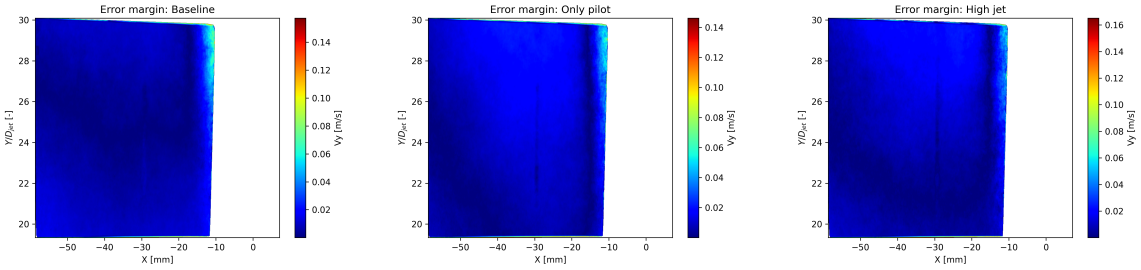

(a) Baseline (b) Left pilot off (c) High pilot

Figure A.5: Error margins 95% confidence interval of vertical velocity in the coflow with the central jet on. Vertical enclosed - two window view.

A.2. Reynolds shear stress

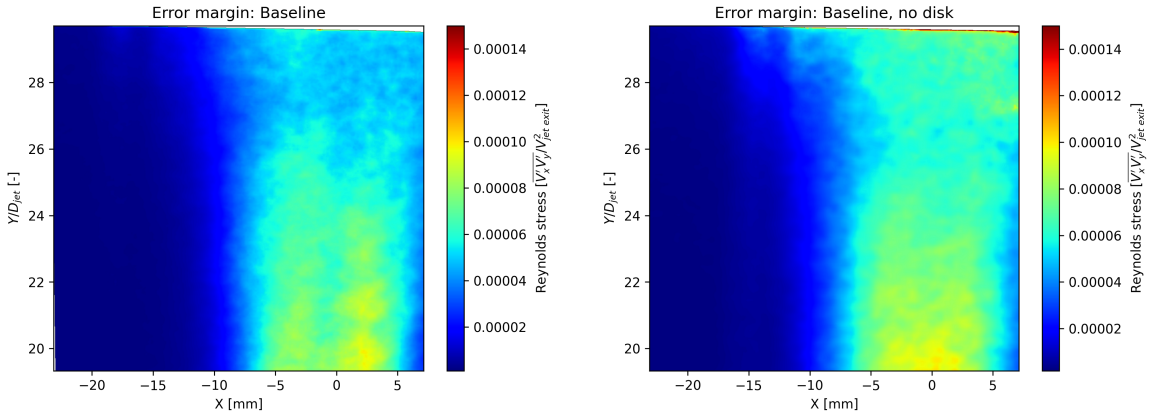

(a) With top disk (b) Without top disk

Figure A.6: Error margins 95% confidence interval of the Reynolds shear stress. Baseline, vertical enclosed - two window view.

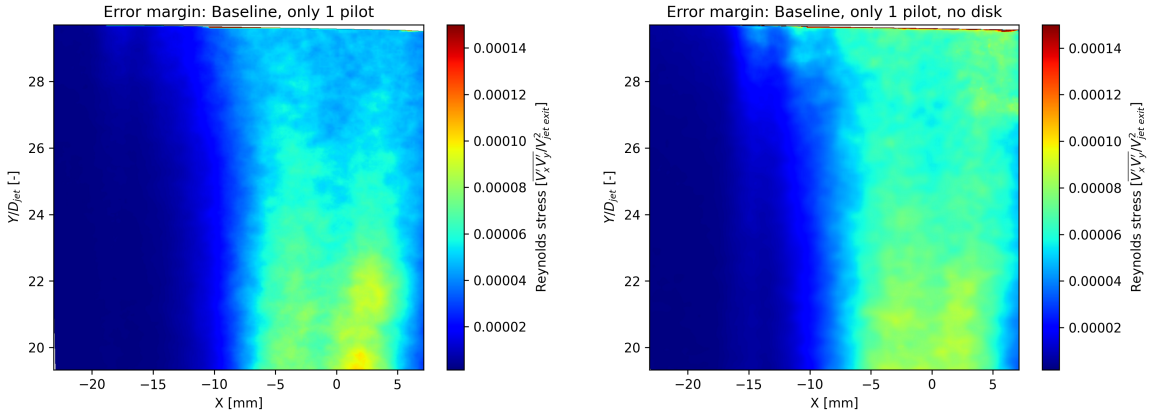

(a) With top disk (b) Without top disk

Figure A.7: Error margins 95% confidence interval of the Reynolds shear stress. Left pilot closed, vertical enclosed - two window view.

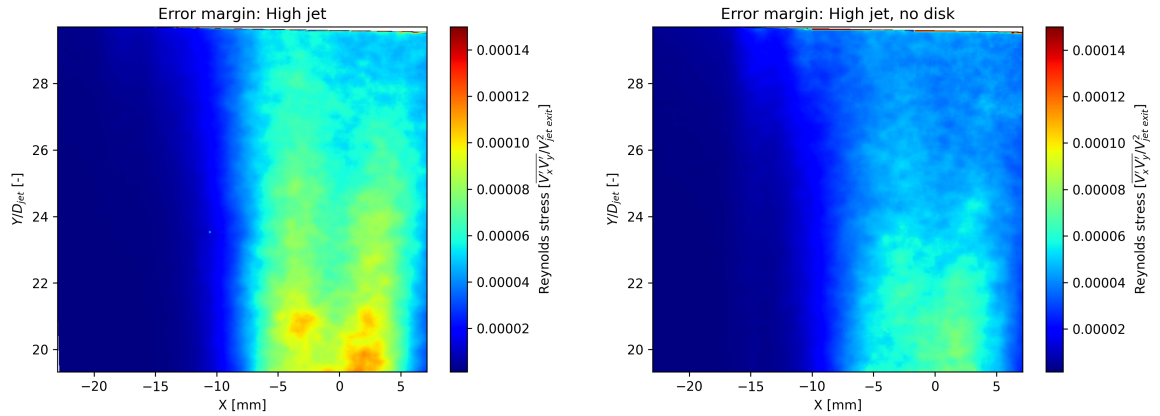

(a) With top disk (b) Without top disk

Figure A.8: Error margins 95% confidence interval of the Reynolds shear stress. High jet, vertical enclosed - two window view.

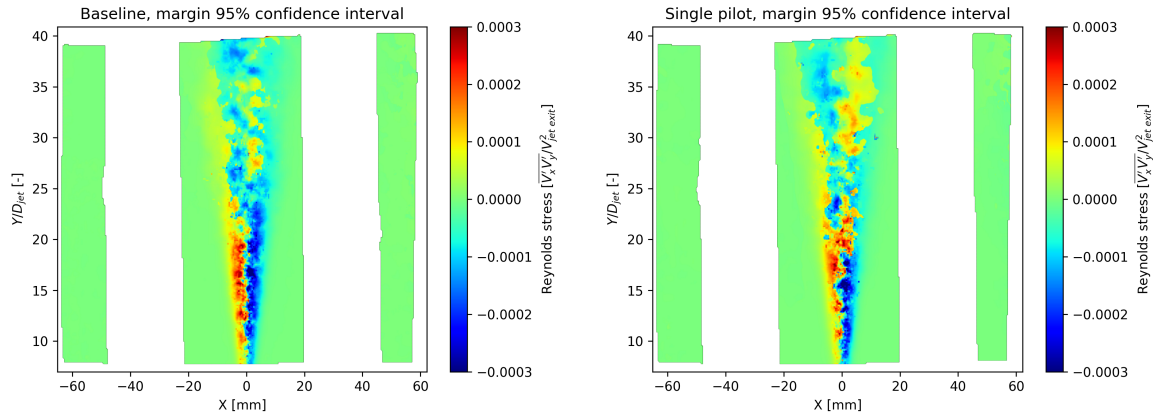

(a) Baseline case (b) Left pilot closed

Figure A.9: Error margins 95% confidence interval for the Reynolds stress of the enclosed - single window view

B

Thermocouple placement

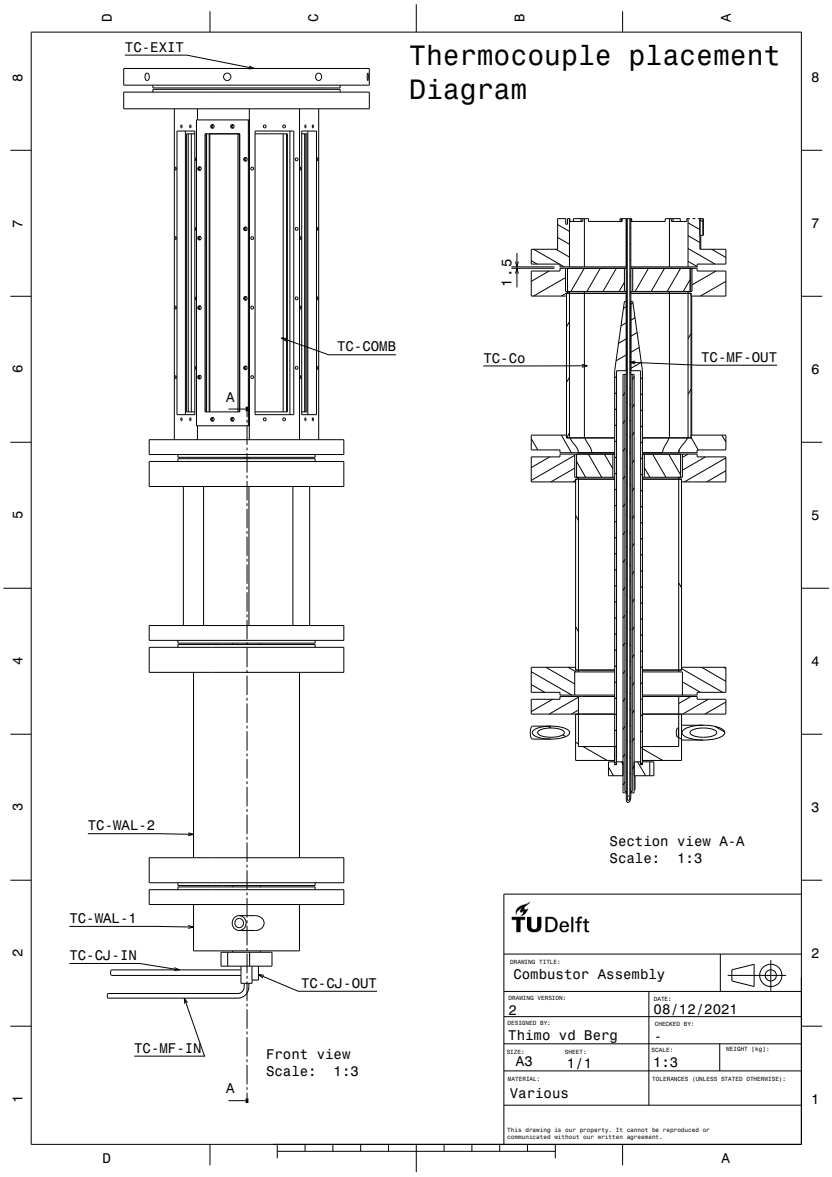

C

Process and instrumentation diagram

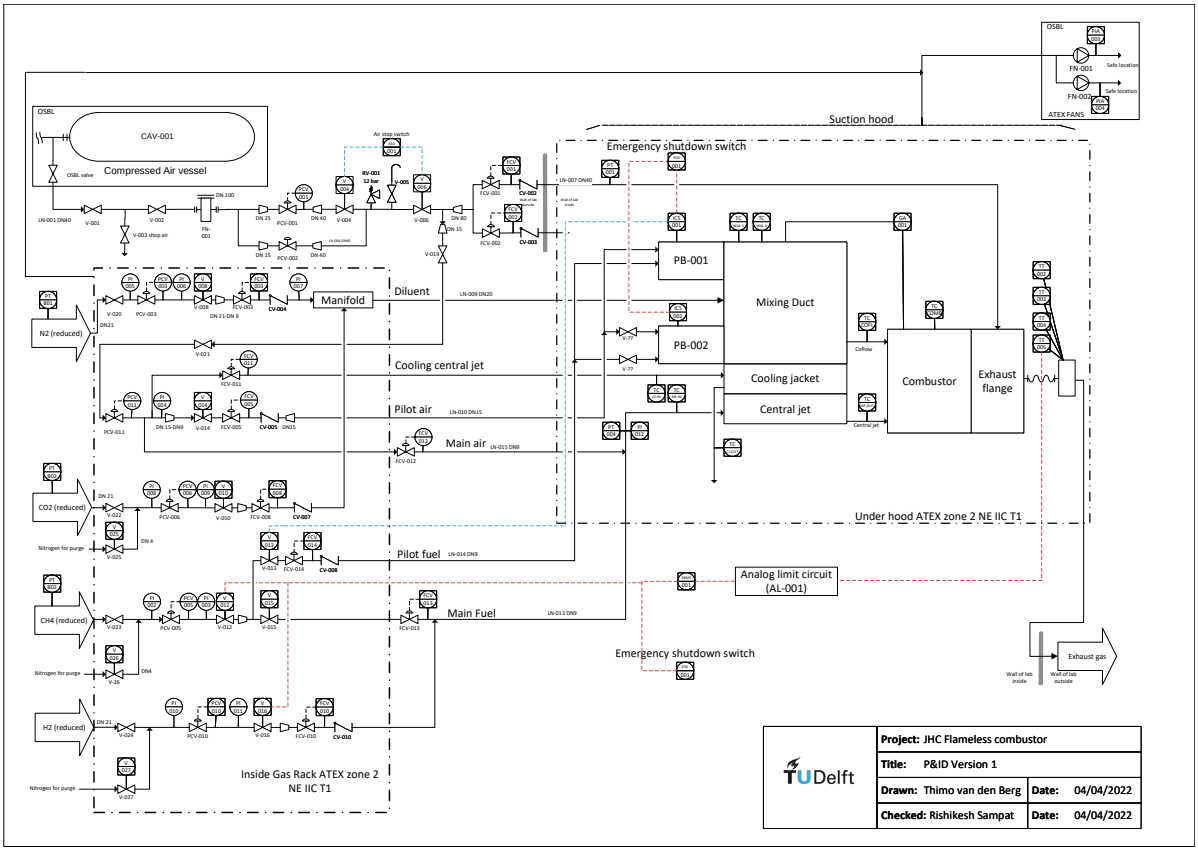

D

Engineering drawings

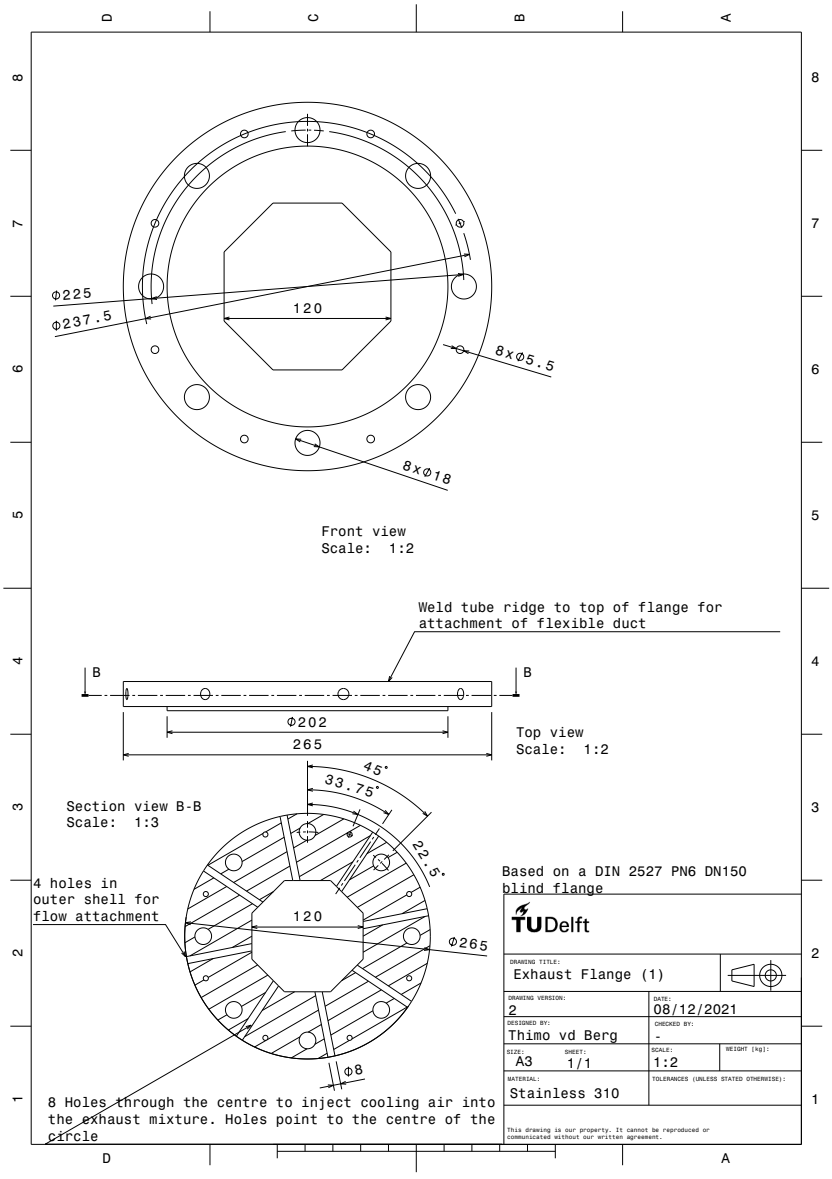

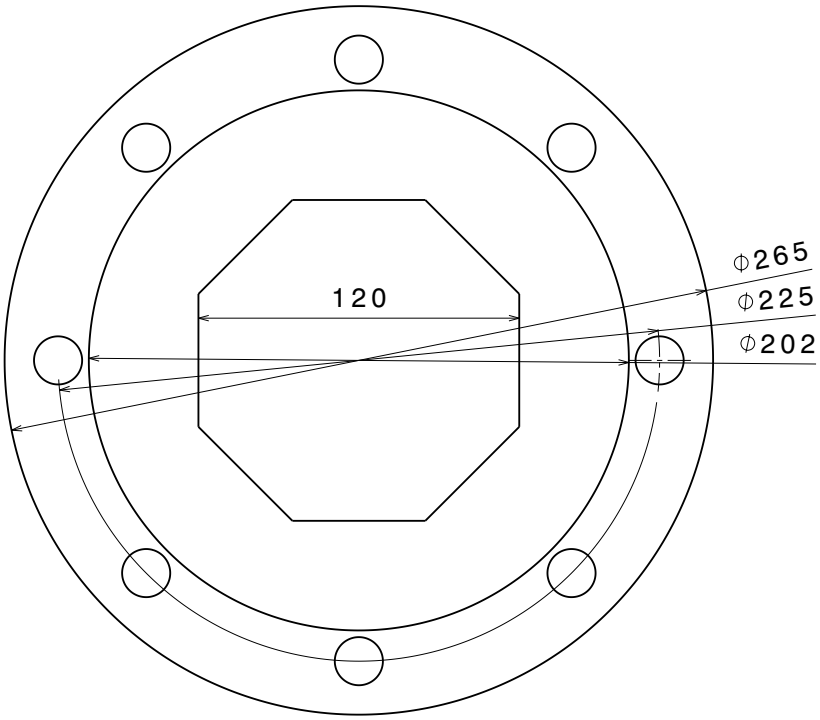

Bottom view
Scale: 1:2

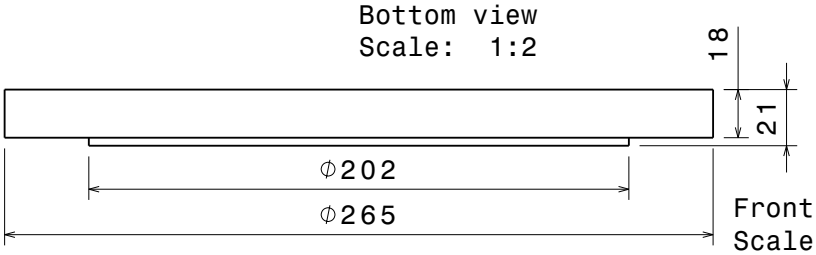

Front view
Scale: 1:2

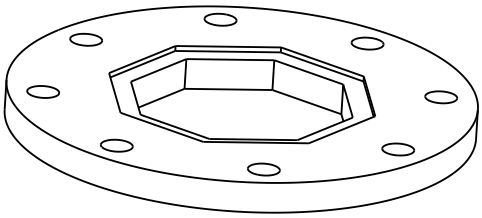

Isometric view
Scale: 1:3

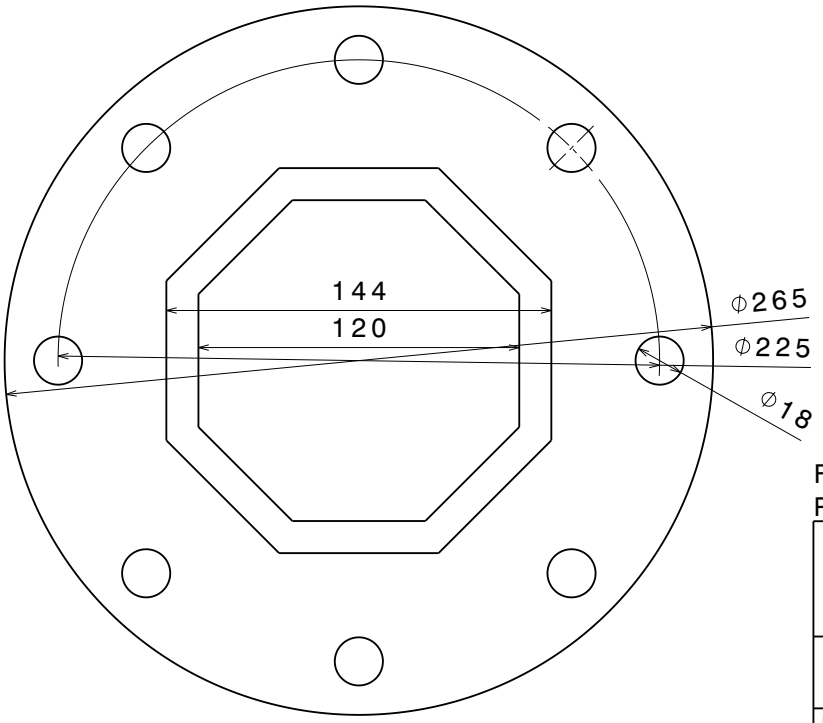

Top view
Scale: 1:2

Flange is based on a blind DIN2527
PN6 DN 150 flange

TU Delft

DRAWING TITLE: DN150 Octagonal Flange (2)		
DRAWING VERSION: 2	DATE: 08/12/2021	
DESIGNED BY: Thimo vd Berg	CHECKED BY: -	
SIZE: A3 SHEET: 1/1	SCALE: 1:2	WEIGHT [kg]:
MATERIAL: Stainless 310	TOLERANCES (UNLESS STATED OTHERWISE):	

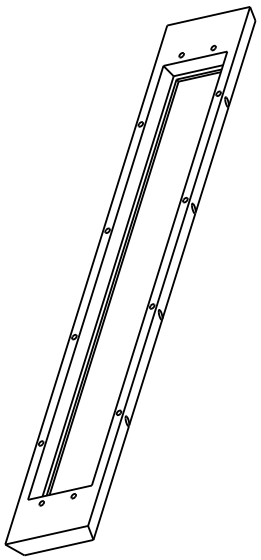

Isometric view
Scale: 1:3

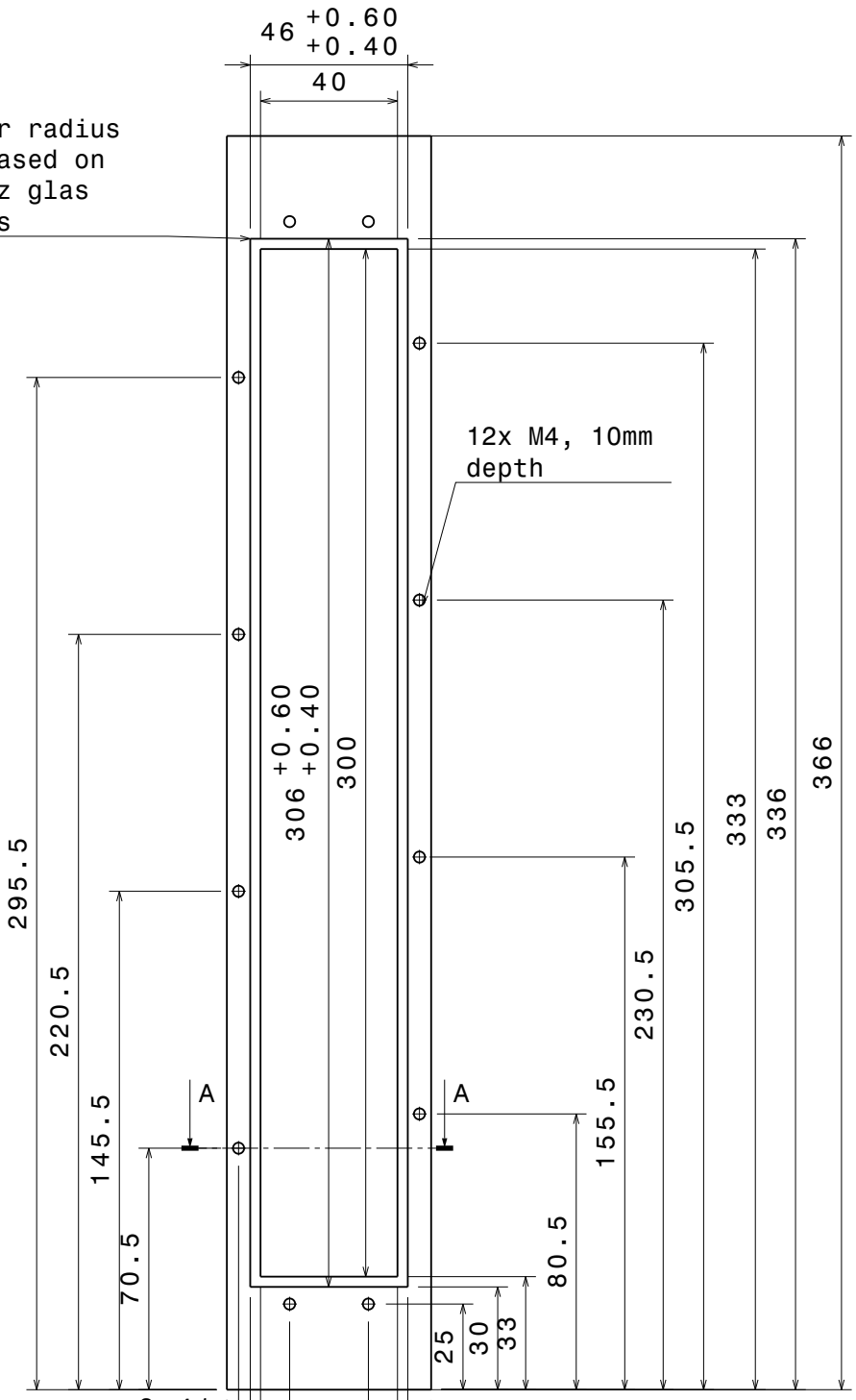

Front view
Scale: 2:3

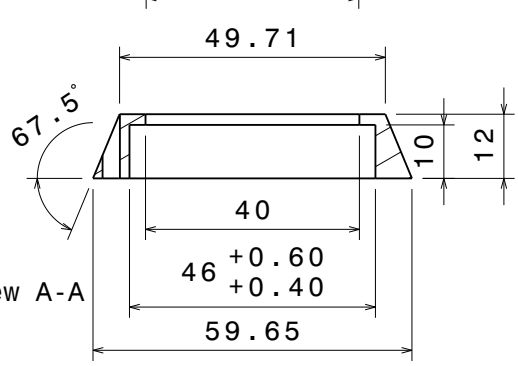

Section view A-A
Scale: 1:1

TU Delft

DRAWING TITLE: Combustor Frame (3)	
DRAWING VERSION: 2	DATE: 08/12/2021
DESIGNED BY: Thimo vd Berg	CHECKED BY: -
SIZE: A3 SHEET: 1/1	SCALE: 2:5 WEIGHT [kg]:
MATERIAL: Stainless 310	TOLERANCES (UNLESS STATED OTHERWISE):

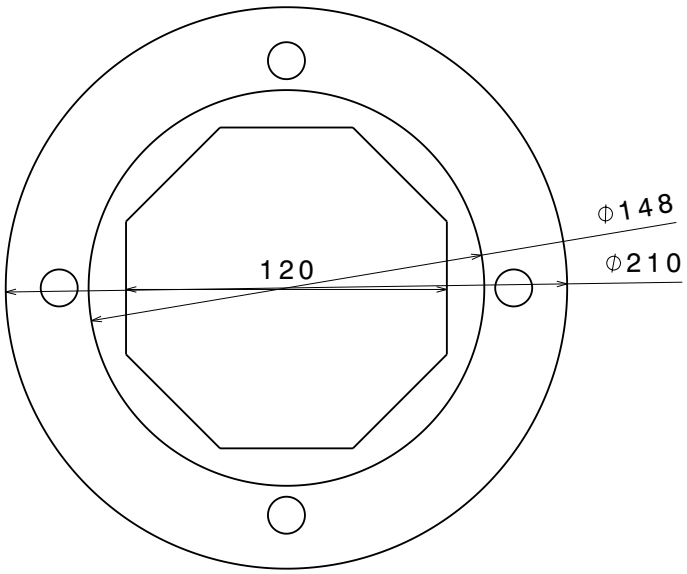

Bottom view
Scale: 1:2

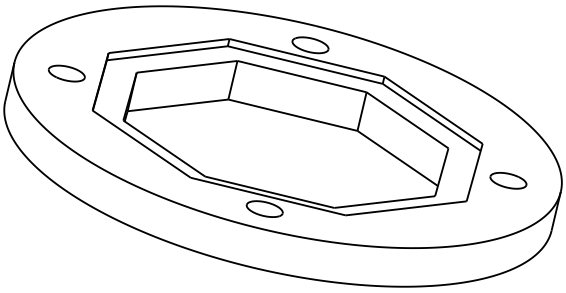

Isometric view
Scale: 1:2

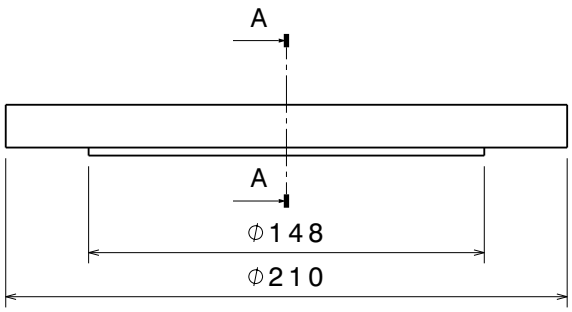

Front view
Scale: 1:2

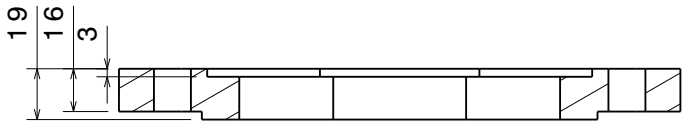

Section view A-A
Scale: 1:2

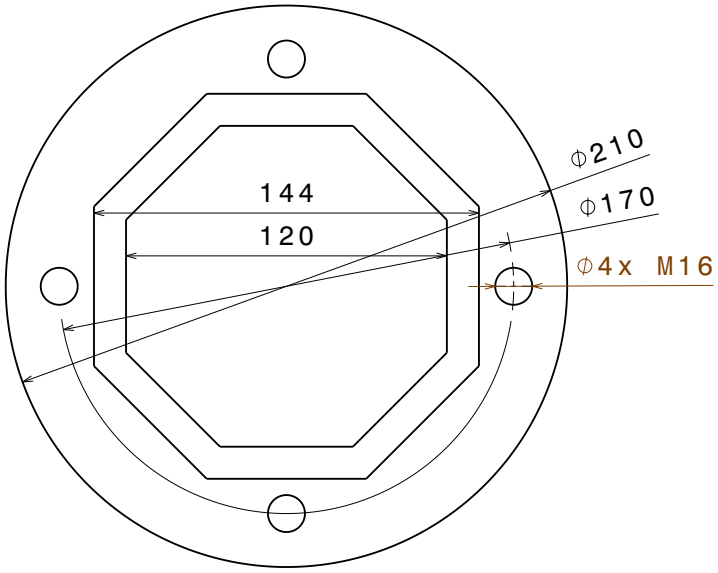

Top view
Scale: 1:2

Flange is based on a blind DIN 2527 PN6 DN100 flange.

TU Delft

DRAWING TITLE: Thin Octagonal Flange (4)	
DRAWING VERSION: 2	DATE: 08/12/2021
DESIGNED BY: Thimo vd Berg	CHECKED BY: -
SIZE: A3 SHEET: 1/1	SCALE: 1:2 WEIGHT [kg]:
MATERIAL: Stainless 310	TOLERANCES (UNLESS STATED OTHERWISE):

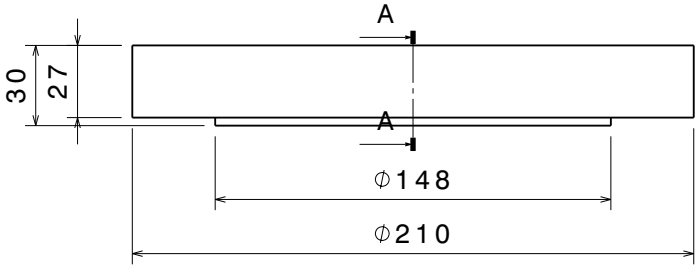

Front view
Scale: 1:2

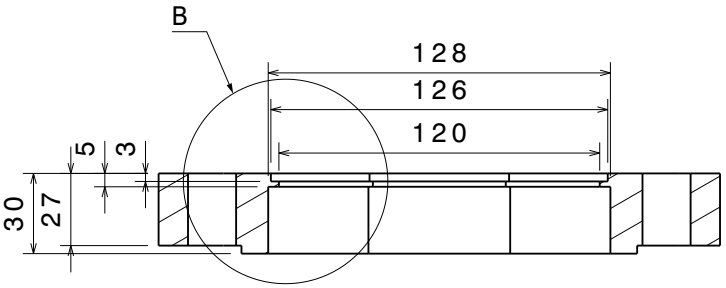

Section view A-A
Scale: 1:2

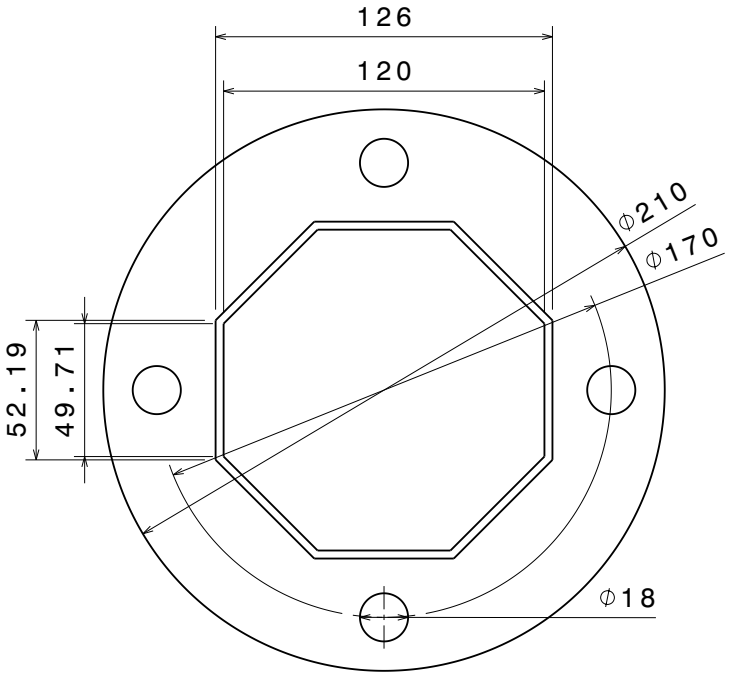

Top view
Scale: 1:2

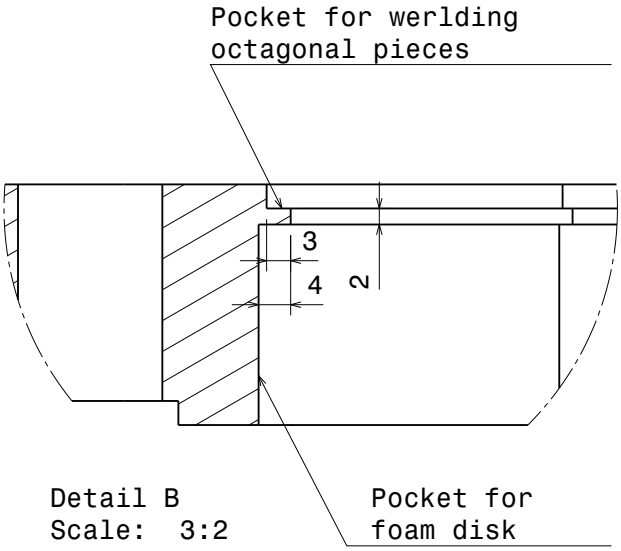

Detail B
Scale: 3:2

Flange is based on a blind DIN 2527 PN6 DN100 flange.

Final dimensions dependant on ceramic disk margins

TUDelft

DRAWING TITLE: Thick Octagonal Flange (5)		
DRAWING VERSION: 2	DATE: 08/12/2021	
DESIGNED BY: Thimo vd Berg	CHECKED BY: -	
SIZE: A3 SHEET: 1/1	SCALE: 1:2	WEIGHT [kg]:
MATERIAL: Inconel 600	TOLERANCES (UNLESS STATED OTHERWISE):	

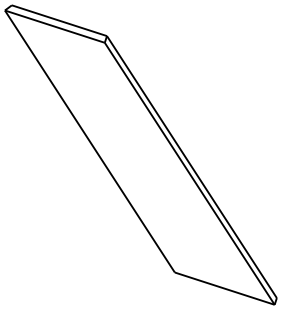

Isometric view
Scale: 1:2

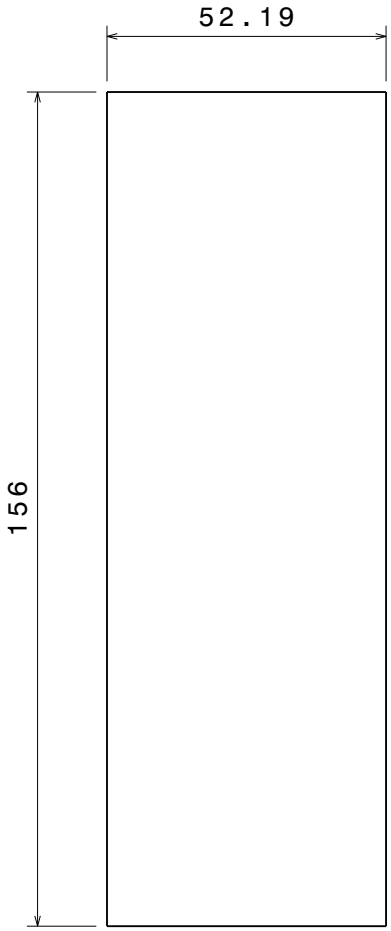

Front view
Scale: 1:1

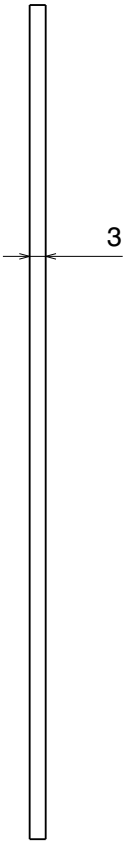

Left view
Scale: 1:1

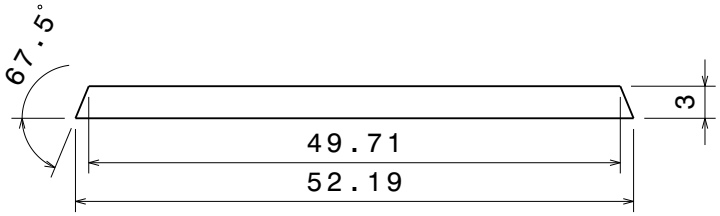

Top view
Scale: 2:1

TUDelft

DRAWING TITLE: Octagonal Duct Plate (6)	
DRAWING VERSION: 2	DATE: 30/11/2021
DESIGNED BY: Thimo vd Berg	CHECKED BY: -
SIZE: A3 SHEET: 1/1	SCALE: 1:1 WEIGHT [kg]:
MATERIAL: Inconel 600	TOLERANCES (UNLESS STATED OTHERWISE):

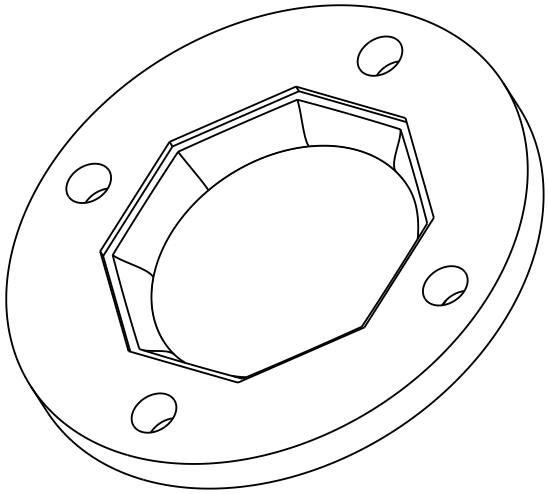

Isometric view
Scale: 1:2

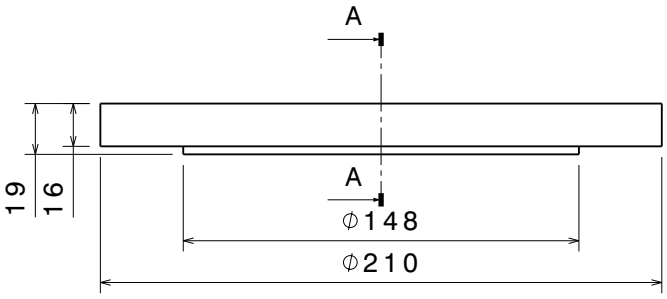

Front view
Scale: 1:2

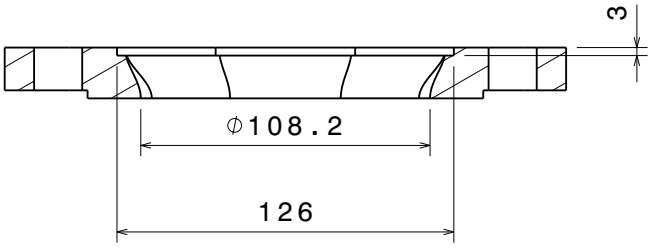

Section view A-A
Scale: 1:2

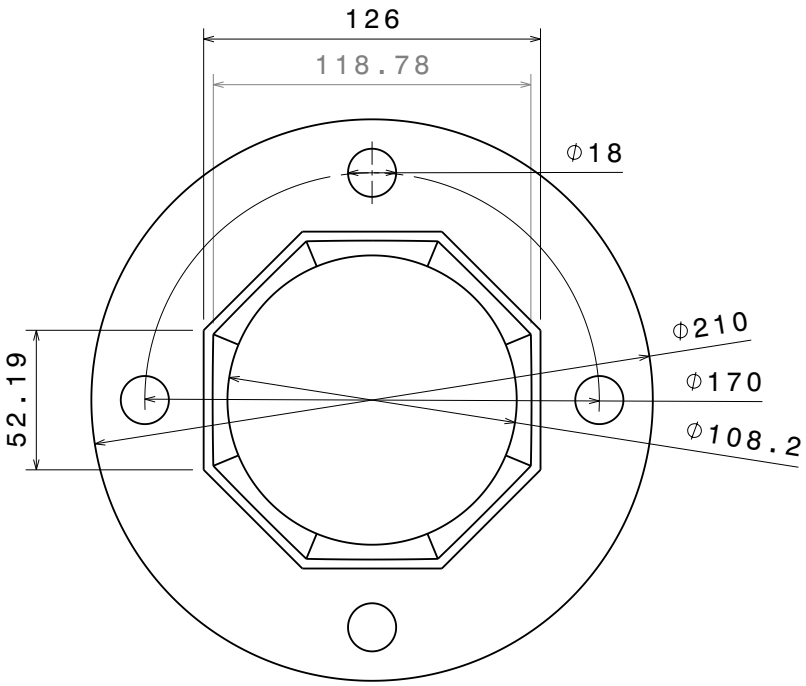

Top view
Scale: 1:2

Flange is based on a blind DIN 2527 PN6 DN100 flange

TUDelft

DRAWING TITLE: Circular to Octagonal Flange (7)		
DRAWING VERSION: 2	DATE: 08/12/2021	
DESIGNED BY: Thimo vd Berg	CHECKED BY: -	
SIZE: A3 SHEET: 1/1	SCALE: 1:2	WEIGHT [kg]:
MATERIAL: Inconel 600	TOLERANCES (UNLESS STATED OTHERWISE):	

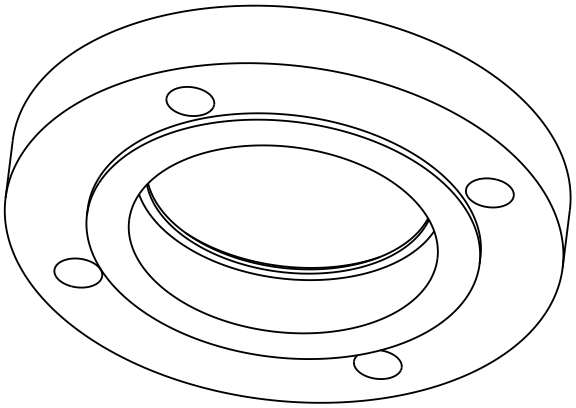

Isometric view
Scale: 1:2

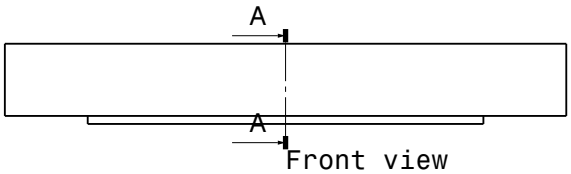

Front view
Scale: 1:2

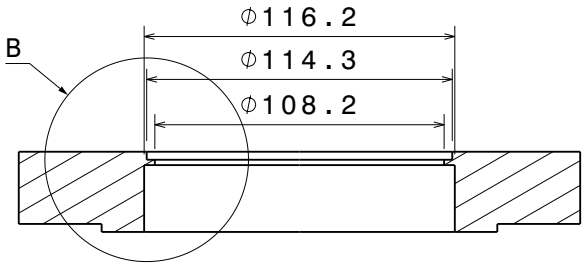

Section view A-A
Scale: 1:2

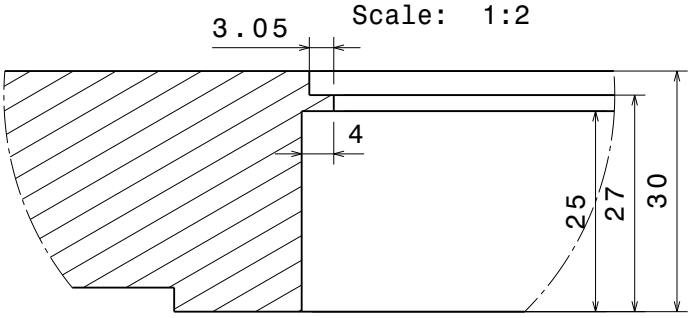

Detail B
Scale: 3:2

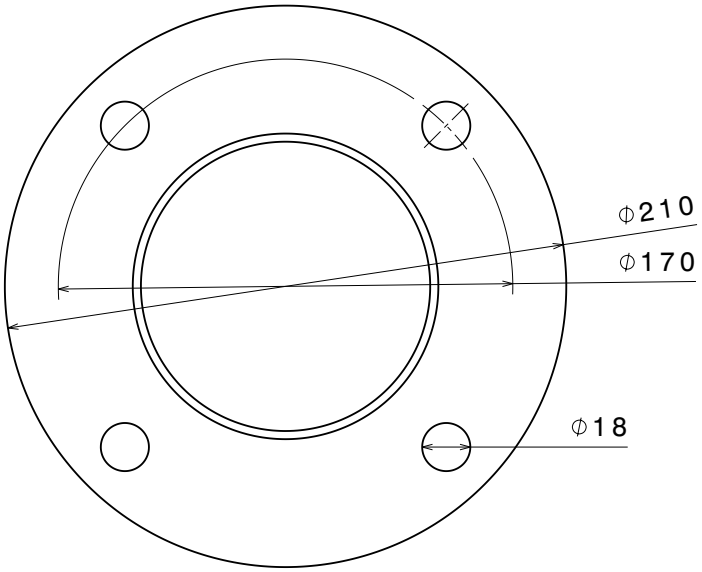

Top view
Scale: 1:2

Flange is based on blind DIN 2527 PN6 DN100 flange

Final dimensions dependant on ceramic disk margins

TUDelft

DRAWING TITLE: Thick Circular Flange (8)		
DRAWING VERSION: 2	DATE: 08/12/2021	
DESIGNED BY: Thimo vd Berg	CHECKED BY: -	
SIZE: A3 SHEET: 1/1	SCALE: 1:2	WEIGHT [kg]:
MATERIAL: Inconel 600	TOLERANCES (UNLESS STATED OTHERWISE):	

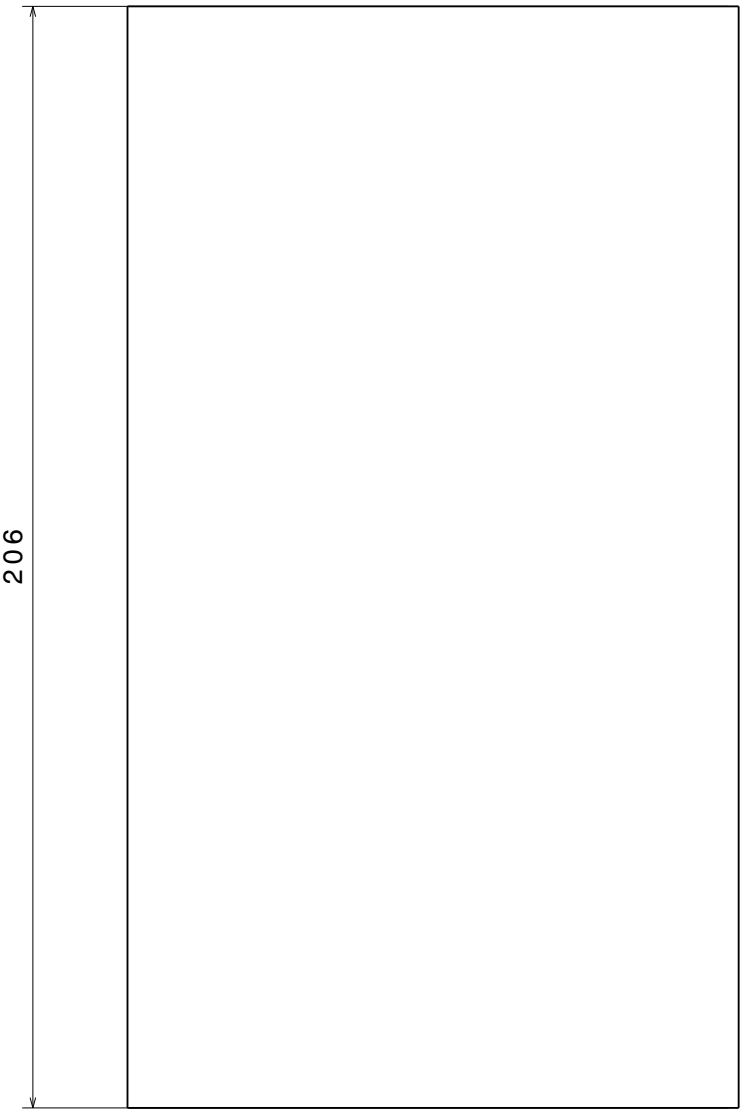

Front view
Scale: 1:1

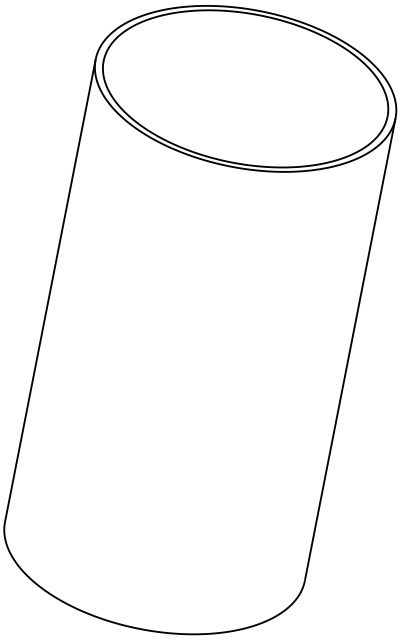

Isometric view
Scale: 1:2

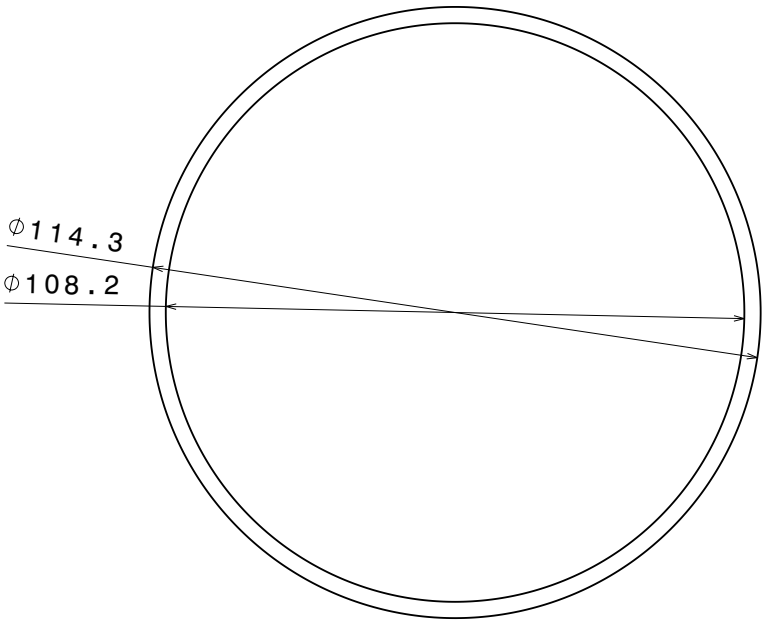

Top view
Scale: 1:1

TU Delft

DRAWING TITLE: Duct (9)	
DRAWING VERSION: 2	DATE: 08/12/2021
DESIGNED BY: Thimo vd Berg	CHECKED BY: -
SIZE: A3 SHEET: 1/1	SCALE: 1:2 WEIGHT [kg]:
MATERIAL: Inconel 600	TOLERANCES (UNLESS STATED OTHERWISE):

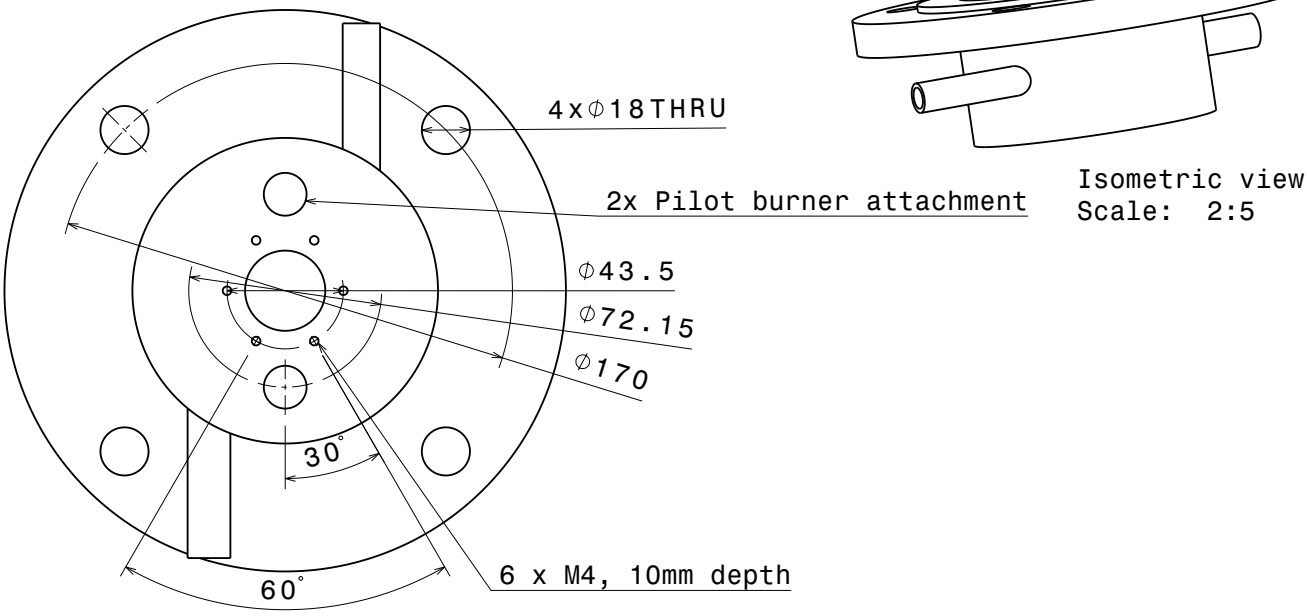

Isometric view
Scale: 2:5

Bottom view
Scale: 1:2

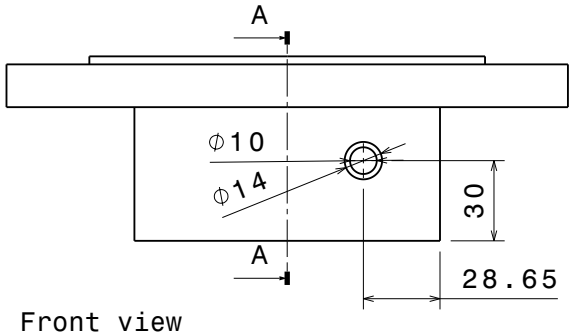

Front view
Scale: 1:2

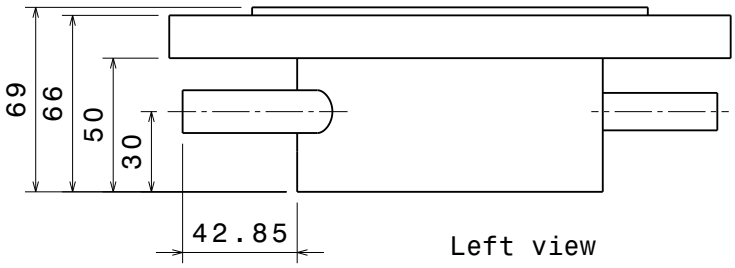

Left view
Scale: 1:2

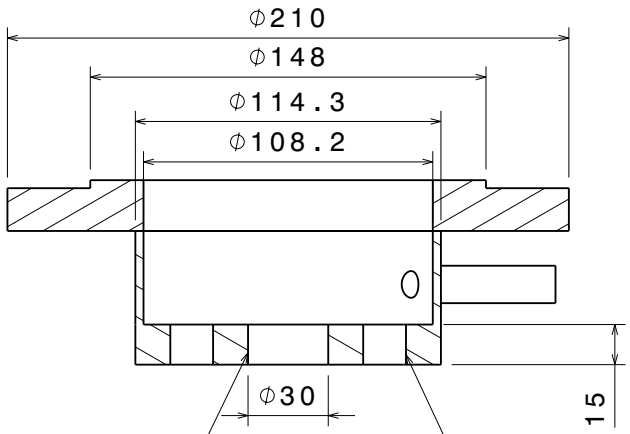

Section view A-A
Scale: 1:2

Must be able to fit welded cooling assembly

2 x Pilot burner attachment

TU Delft

DRAWING TITLE: Coflow Attachment (10)	
DRAWING VERSION: 2	DATE: 08/12/2021
DESIGNED BY: Thimo vd Berg	CHECKED BY: -
SIZE: A3 SHEET: 1/1	SCALE: 1:2 WEIGHT [kg]:
MATERIAL: Stainless 310	TOLERANCES (UNLESS STATED OTHERWISE):

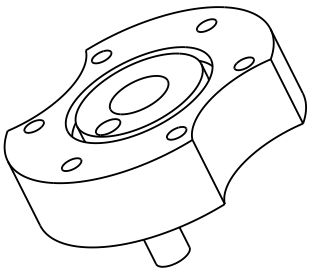

Isometric view
Scale: 1:1

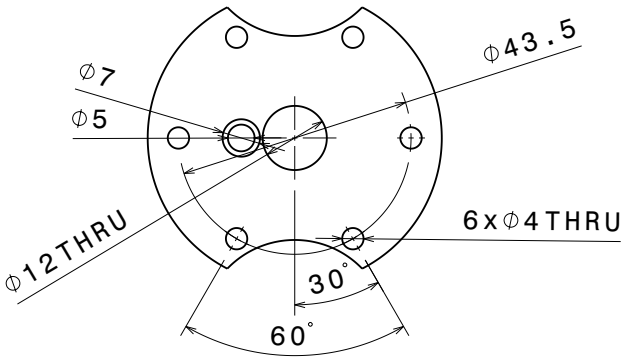

Bottom view
Scale: 1:1

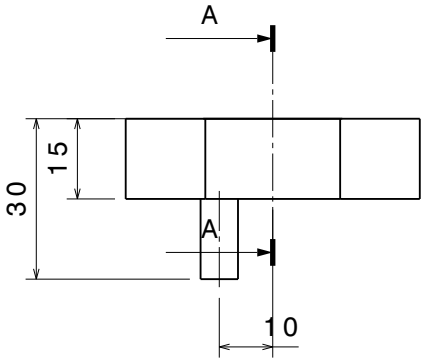

Front view
Scale: 1:1

Groove for fuel jacket

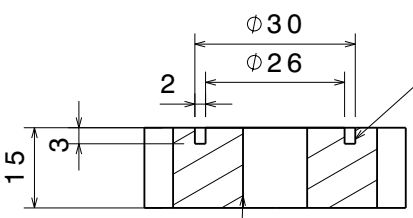

Fuel tube must fit through and be welded

Section view A-A
Scale: 1:1

Same as pocket on other side

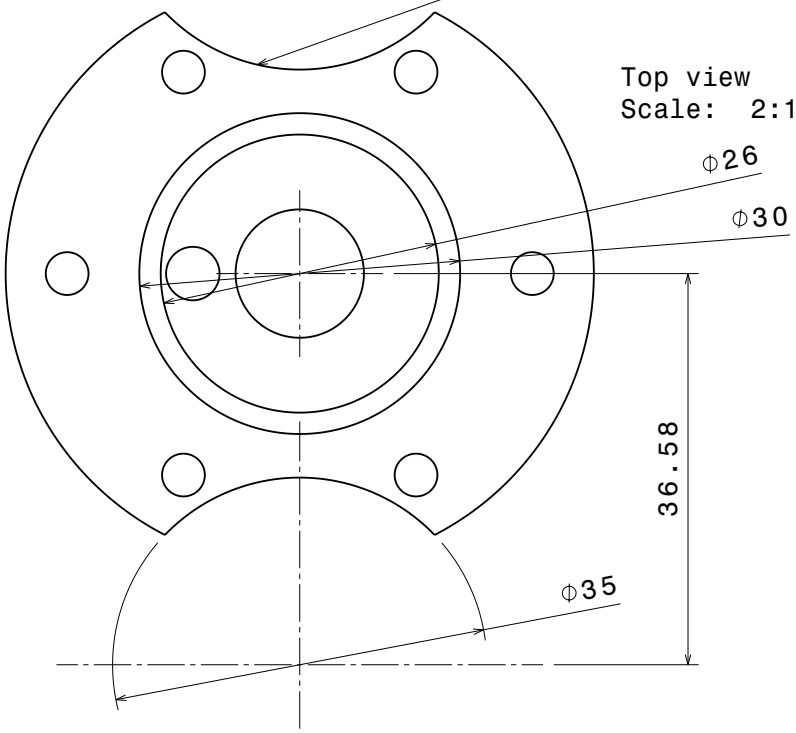

Top view
Scale: 2:1

TUDelft	
DRAWING TITLE: Cooling Exit (11)	
DRAWING VERSION: 2	DATE: 08/12/2021
DESIGNED BY: Thimo vd Berg	CHECKED BY: -
SIZE: A3 SHEET: 1/1	SCALE: 1:1 WEIGHT [kg]:
MATERIAL: Stainless 310	TOLERANCES (UNLESS STATED OTHERWISE):

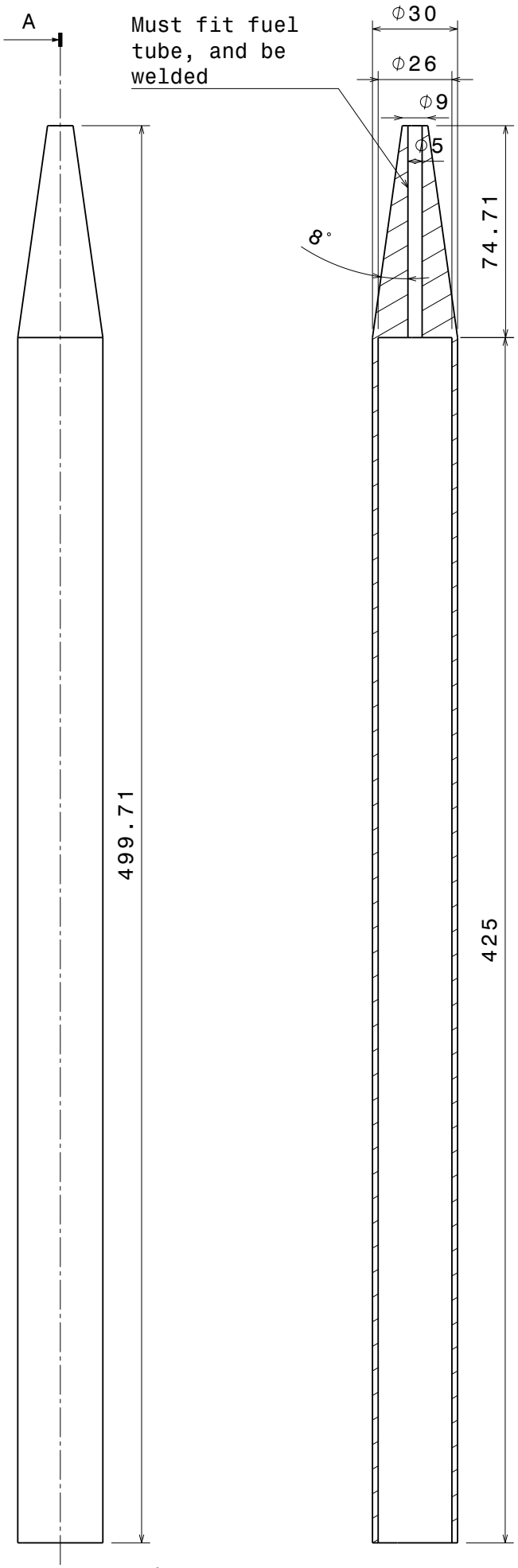

Front view
Scale: 2:3

Section view A-A
Scale: 2:3

TU Delft

DRAWING TITLE: Cooling Jacket (12)	
DRAWING VERSION: 2	DATE: 08/12/2021
DESIGNED BY: Thimo vd Berg	CHECKED BY: -
SIZE: A3 SHEET: 1/1	SCALE: 2:3 WEIGHT [kg]:
MATERIAL: Stainless 310	TOLERANCES (UNLESS STATED OTHERWISE):

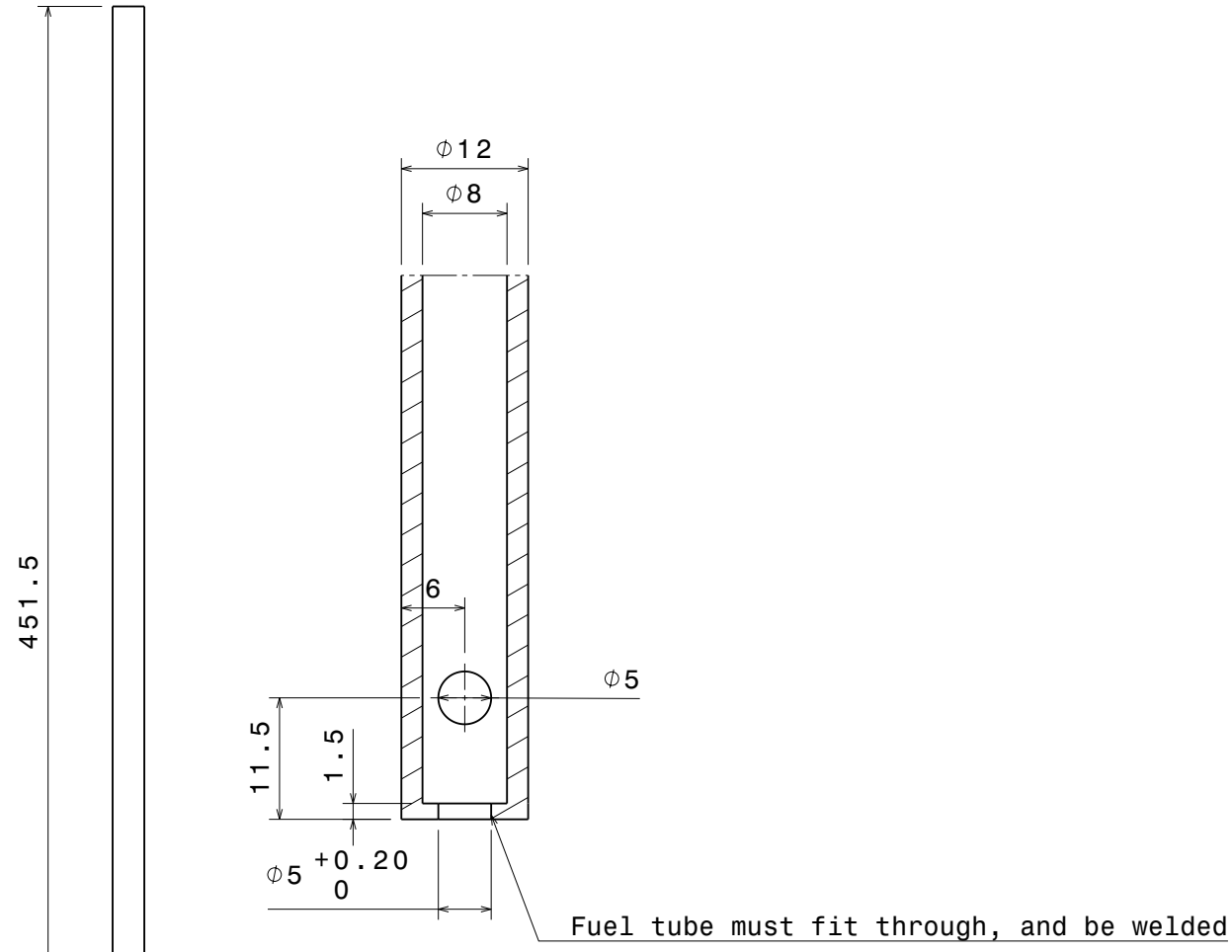

Section view B-B
Scale: 2:1

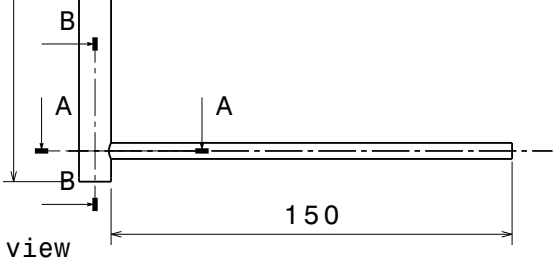

Front view
Scale: 1:2

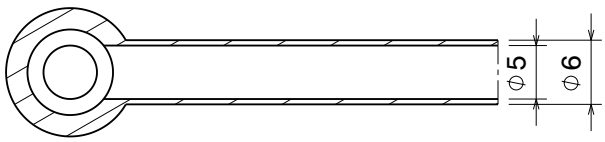

Section view A-A
Scale: 2:1

TU Delft

DRAWING TITLE: Cooling Channel (13)		
DRAWING VERSION: 2	DATE: 08/12/2021	
DESIGNED BY: Thimo vd Berg	CHECKED BY: -	
SIZE: A3 SHEET: 1/1	SCALE: 1:2	WEIGHT [kg]:
MATERIAL: Stainless 310	TOLERANCES (UNLESS STATED OTHERWISE):	

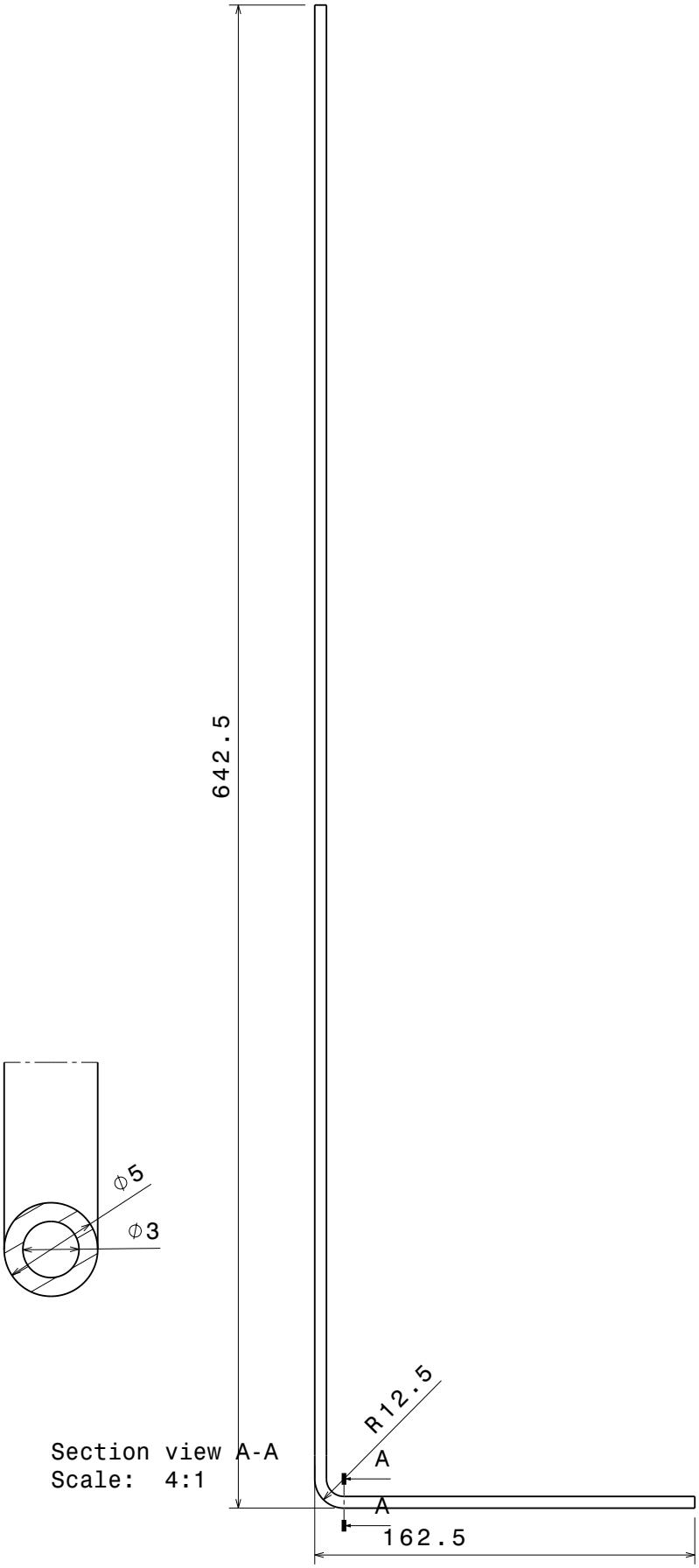

Front view
Scale: 1:2

Section view A-A
Scale: 4:1

TU Delft

DRAWING TITLE: Fuel Pipe (14)	
DRAWING VERSION: 2	DATE: 08/12/2021
DESIGNED BY: Thimo vd Berg	CHECKED BY: -
SIZE: A3 SHEET: 1/1	SCALE: 1:2 WEIGHT [kg]:
MATERIAL: Stainless 310	TOLERANCES (UNLESS STATED OTHERWISE):

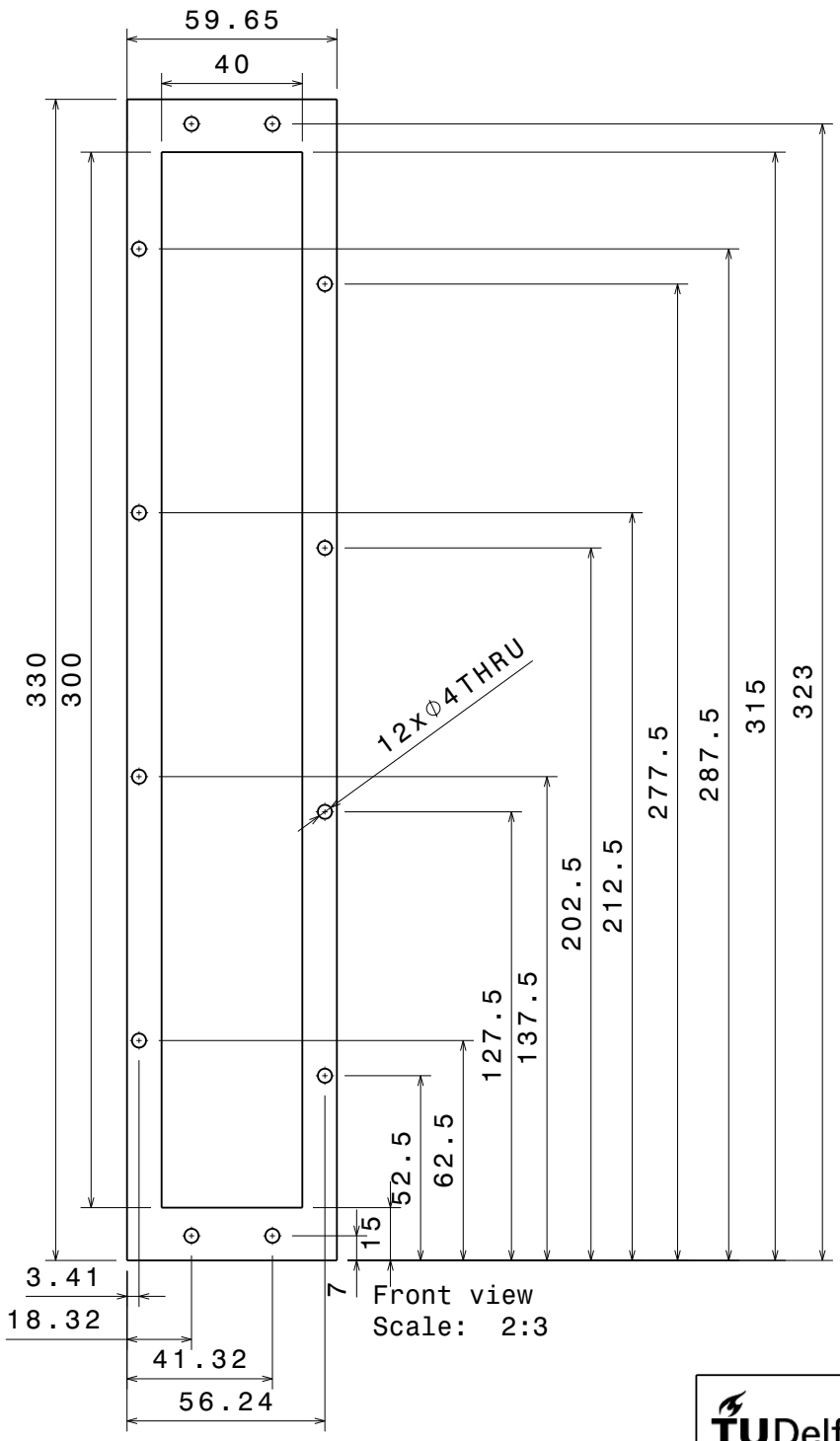

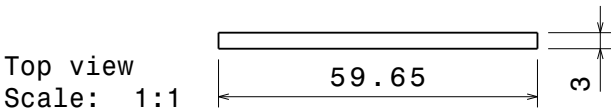

TUDelft

DRAWING TITLE: Window Plate (15)	
DRAWING VERSION: 2	DATE: 08/12/2021
DESIGNED BY: Thimo vd Berg	CHECKED BY: -
SIZE: A3 SHEET: 1/1	SCALE: 1:2 WEIGHT [kg]:
MATERIAL: Stainless 310	TOLERANCES (UNLESS STATED OTHERWISE):